UNIVERSITÀ DEGLI STUDI DI BRESCIA

PH.D. PROGRAM IN
CIVIL AND ENVIRONMENTAL ENGINEERING

CURRICULUM
MATHEMATICAL METHODS AND MODELS FOR ENGINEERING

Scientific Disciplinary Sector
ICAR/08 Structural mechanics

XXX CYCLE

A theory for the analysis of electro-chemo-mechanical systems and its application to Li-ion batteries

Advisor:
Prof. Alberto Salvadori

Ph.D. Candidate:
Marco Magri

Sommario

Questa tesi ha per oggetto la modellazione teorica e numerica di sistemi elettro-chemo-meccanici, con particolare applicazione alle batterie agli ioni di litio.

Studi di carattere teorico e numerico non solo permettono di comprendere il reale comportamento delle batterie agli ioni di litio, ma possono offrire un valido strumento a supporto delle indagini sperimentali per la progettazione di nuove architetture e soluzioni tecnologiche.

Le batterie sono dispositivi intrinsecamente multi-scala, sia nello spazio che nel tempo. Infatti le caratteristiche macroscopiche (ad esempio lo spessore di una singola cella elettrochimica) sono maggiori, di alcuni ordini di grandezza, delle dimensioni delle particelle che formano la microstruttura di un elettrodo poroso. Per di più, i processi che caratterizzano l'intercalazione di ioni litio negli elettrodi avvengono addirittura a scala atomistica.

Nel Capitolo 1 è esaminata l'abbondante letteratura riguardante la modellazione delle batterie agli ioni di litio. In particolare, sono analizzate dettagliatamente le diverse tecniche di modellazione a livello microscopico e macroscopico, nonchè le più recenti tecniche di modellazione multi-scala.

Il Capitolo 2 analizza il ruolo della saturazione nella modellazione degli elettroliti liquidi. Recenti analisi numeriche mostrano chiaramente che la concentrazione di ioni litio può eccedere metà del limite di saturazione, specialmente nella regione vicino agli elettrodi. Questa osservazione mette in discussione l'ipotesi di soluzioni infinitamente diluite, largamente utilizzata in letteratura, e suggerisce l'adozione di una teoria più appropriata per soluzioni saturabili. Da questo studio conseguono due importanti risultati. In prima analisi la saturazione non ha alcun effetto sulla diffusività degli ioni in soluzione. D'altra parte, la saturazione impatta fortemente lo sviluppo del potenziale elettrico nell'elettrolita con differenze anche del 40 % rispetto al caso di soluzioni infinitamente diluite.

La risposta chemo-meccanica di *active particles* costituenti gli elettrodi porosi è analizzata nei Capitoli 3, 4 e 5. Innanzitutto, una teoria generale per processi accoppiati di trasporto di massa, calore, meccanica e reazioni chimiche con intrappolamento è proposta nel Capitolo 3. Questa teoria si fonda sulla termodinamica di non-equilibrio nell'ipotesi di deformazioni e spostamenti infinitesimi. Le equazioni di bilancio sono formulate in termini di bilancio di massa, bilancio della quantità di moto e del momento angolare, conservazione dell'energia e bilancio di entropia. Le relazioni costitutive, necessarie per l'identificazione delle equazioni governanti, sono ricavate a partire dalle restrizioni termodinamiche e dalla scrittura dell'energia libera di Helmholtz.

Nel Capitolo 4 si studia l'impatto dell'intrappolamento di ioni litio nella litiazione e delitiazione di una particella sferica. Si evince che una reazione chimica può indurre una energia libera non-convessa, proprio come nei materiali che mostrano trasformazioni di fase. Inoltre, i risultati numerici dimostrano che l'intrappolamento di ioni litio nella *particle* può simulare le peculiarità di un processo di transizione di fase del materiale ospitante.

Un modello chemo-meccanico per la risposta di *active particles* di $LiCoO_2$ è proposto nel Capitolo 5. Il litio cobalto ossido Li_xCoO_2 mostra una transizione di fase del primo ordine tra $x = 0.75$ and $x = 0.93$. Durante questa transizione di fase, la diffusione degli ioni litio nel materiale ospitante è influenzata dalla formazione dell'interfaccia che separa le due fasi coesistenti. Inoltre, la transizione di fase influenza la risposta meccanica della *particle*, inducendo un ingente stato di sollecitazione in corrispondenza dell'interfaccia. Allo scopo di cogliere queste evidenze sperimentali, il modello analizzato nel Capitolo 4 è stato leggermente modificato, introducendo una legge di evoluzione dei siti per l'intrappolamento nel materiale ospitante.

Il Capitolo 6 affronta la modellazione dell'intero elettrodo poroso. Tale componente è idealizzato come un sistema a tre-fasi composto da *active particles*, *conductive particles* ed elettrolita. Le leggi di bilancio e le condizioni di interfaccia sono state enunciate per ogni fase. Le relazioni costitutive, ricavate dalle leggi della termodinamica, completano il sistema di equazioni governanti. Tale modello è stato opportunamente validato mediante simulazioni numeriche.

Abstract

This thesis investigates the behavior of electro-chemo-mechanical systems through theoretical and numerical analysis, with particular application to Li-ion batteries.

Theoretical and numerical studies not only provide a better understanding of the intimate behavior of actual batteries under operational and extreme conditions, but they may tailor new materials and shape new architectures in a complementary way to experimental approaches. Modeling can therefore play a very valuable role in the design and lifetime prediction of energy storage materials and devices.

Batteries are inherently multi-scale, in space and time. The macrostructural characteristic lengths (the thickness of a single cell, for instance) are order of magnitudes larger than the particles that form the microstructure of the porous electrodes, which in turn are scale-separated from interface layers at which atomistic intercalations occur.

In Chapter 1, a comprehensive overview and description of computational models and methods proposed in recent years for batteries is provided. In particular, multi-physics modeling concepts, methodologies, and simulations at different scales, as well as scale transition strategies are revised.

Chapter 2 focuses on the role of saturation in liquid electrolytes. Recent computational simulations of ionic conductivity across the electrolyte of commercial batteries have shown that the concentration of ions exceeds half the saturation limit near the electrodes. This observation implies that the widespread assumption of infinite dilution far from saturation is questionable. An important result is found, that saturation has no effect on the diffusivity, whereby the condition of electroneutrality is well approximated in the solution. However saturation affects the electric potential up to 40 % near the electrodes for all charge rates.

The chemo-mechanical response of active particles of porous electrodes is investigated in Chapters 3, 4, and 5. A general framework for coupled mass and heat transport, mechanics, and chemical reactions with trapping is first provided in Chapter 3. It is rooted in non-equilibrium rational thermodynamics and assumes that displacements and strains are small. Balance laws for mass, linear and angular momentum, energy, and entropy are stated. Thermodynamic restrictions are identified, based on an additive strain decomposition and on the definition of the Helmholtz free energy. Constitutive theory and chemical kinetics are studied in order to finally write the governing equations for the multi-physics problem.

In Chapter 4 the impact of trapping of Li ions in investigated on a spherical particle upon lithiation and delithiation. A chemical reaction may induce a non-convex free energy with multiple equilibrium configurations, as expected in phase segregating materials. In addition, numerical analysis on the transient response of the particle, show that trapping of Li ions may simulate the typical features of a phase-transition.

A chemo-mechanical model of the response of $LiCoO_2$ particles is proposed in Chapter 5. A strong first-order phase transition has been measured between $x = 0.75$ and $x = 0.93$ in Li_xCoO_2. During this phase-change, lithium diffusion in the electrode is influenced by the formation of a phase boundary separating two coexisting phases. The phase-transition has impact on the mechanical response as well. Indeed a state of stress results from the lattice parameter mismatch at the phase-interface. In order to meet the experimental evidence, a slightly modification of the model analyzed in Chapter 4 is proposed here. In particular the trap density will be considered non-constant during the process in order to simulate the phase diagram of $LiCoO_2$.

Chapter 6 focuses on the microscopic modeling of a porous electrode compound. The electrode microstructure is idealized here as a three-phase media made of active particles, conductive particles, and electrolyte. Balance laws and interface conditions are derived for any component. Constitutive relations, derived from thermodynamic principles, complete the set of governing equations. Validation of the numerical algorithms descending from them have been carried out.

Contents

Chapter 1

Literature Review

1.1 Introduction

Greenhouse gas reduction strategies call for developing and deploying innovative technologies. Industrial production of high capacity energy storage devices is one of the major challenges to achieve a low-carbon global economy in the long-term. Li-ion batteries, LIBs, currently have the highest energy storage density of any rechargeable battery technology [1]. The present commercial realities, however, are not yet at such a technological level to meet the requirements of ambitious actions to tackle climate change, as for powering Electric Vehicles (EVs) to displace fossil fuel transport systems.

Since the commercial spreading begun by Sony in 1991 [2], Li-ion battery cells have been widely used to supply electric portable devices such as mobile phones, laptop computers and cameras. Being the latter characterized by limited lifetime, battery aging was not a central topic. The expected use of LIBs for high-power and high-capacity demanding systems, as EVs [3], and for storage systems for renewable energy sources makes contained capacity fading and power loss nowadays priorities for the world-wide research community. Whereas experimental studies are the backbones of batteries investigation, modeling can provide fundamental contributions, particularly in tailoring material performances and degradation.

Research activities carried out worldwide over the last few years call attention to the multi-scale and multi-physics modeling of storage cells [4] to predict conditions to develop the next generation of batteries for higher capacity and longer cycling life. Computational simulations, based on rigorous theoretical modeling and coupled to validation and quantification of the uncertainties, have the potential to enhance batteries' performances, tailor architectural configurations toward optimal functioning of energy storage devices, and shape new materials for greater capacity and power release. Accurate reviews of battery management systems in electric vehicles [5], of prognostics and health monitoring [6], of prominent phenomena occurring during common operations as well as of the material response to solicitations and of the aging mechanism [7] have been recently published. Apparently though, a careful account of the broad literature on computational modeling and simulations appears not to have been considered yet, with a few exceptions [8].

This paper aims at filling this gap, by providing a comprehensive overview and description of computational models and methods proposed in recent years for batteries. Modeling of composite electrodes and electrolytes - either solid or liquid, of core functioning of cells, of intercalation of lithium ions in active materials and their multi physic description, with special emphasis on mechanical behavior and failure will be reviewed and discussed. The main target is to underline the efforts of the scientific community in modeling and simulating Li-ion batteries, by no means presuming to be exhaustive of the widespread literature available on the topic.

Current challenges - including the lack of full 3D multi-scale modeling of the multi-physics processes from atomistic to continuum, of hot spots generation, phase-segregations and mechanical failure - are also identified and approaches to address them are devised.

The chapter is organized as follows. Section 1.2 illustrates basic concepts of Li-ion batteries, highlighting the multi-physics processes that occur at different length and time scales. Sections 1.3-1.5 are the core of this

review and examine several computational models for the processes of section 1.2 that have been developed in recent years. Macroscopic models 1.3, microstructural models 1.4 as well as multiscale models 1.5 are separately dealt with.

1.2   Processes, modeling, simulations.
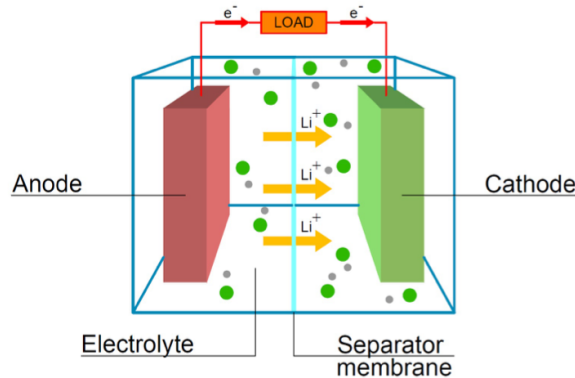
Figure 1.1: *Sketch of a Li-ion battery cell with porous electrodes. Additives are used to create conductive networks in both electrodes, to increase the electronic conductivity. Additives include large (graphite) and small (carbon black) conductive particles, which are bound to the active particles that host Lithium by a polymer binder.*

An electrochemical cell consists of two electrodes, a separator and, for liquid electrolytes, an electrolytic solution. Electrons flow externally and through the electrodes, facilitated by a network of conductive particles. Mass and positive charges are transported in form of ions through the electrolyte from one electrode to the other, to bring reactants to the interfaces where intercalation reactions occur. A sketch of a LIB cell is depicted in Figure 1.1, whereas Figure 1.2 illustrates the main processes that take place during operations. As shown in Figure 1.3, each process requires its own modeling.

As already pointed out [9], the term *battery modeling* is shared by different approaches, each of which makes use of its own methodology to achieve specific targets. Some models for instance define the battery as a *black box*, aiming at empirically describing its system-level characteristics, such as capacity, efficiency, and voltage. Peukert's law, which correlates the rate of discharge and the capacity, falls into this class [10, 11]. Other mathematical models study the non-linear capacity/recovery effects in LIBs in a similar way [12, 13, 14]. *Equivalent circuit models* simulate the battery with combination of variable voltage sources, resistors, and capacitors [15, 16]. Several of these models have been developed in the literature [17], including Thevenin equivalent circuit models [18], impedance-based models [19], and runtime-based models [20]. A recent review can be found in [21].

Although those models have been quoted here for the sake of completeness, the present review focuses on the multi-scale and multi-physics modeling of the processes that take place during charge/discharge, from the atomistic size up to the cell size. This choice has a sound motivation, since theoretical and computational modeling not only provide the ability of understanding the microscopic behavior of batteries under operational and extreme conditions, but they may also be tailored to devise and shape new materials as well as new architectures in a way complementary to the experimental approaches. Modeling of multi-scale and multi-physics processes taking place during charge/discharge can therefore play the most valuable role for battery design and lifetime prediction.
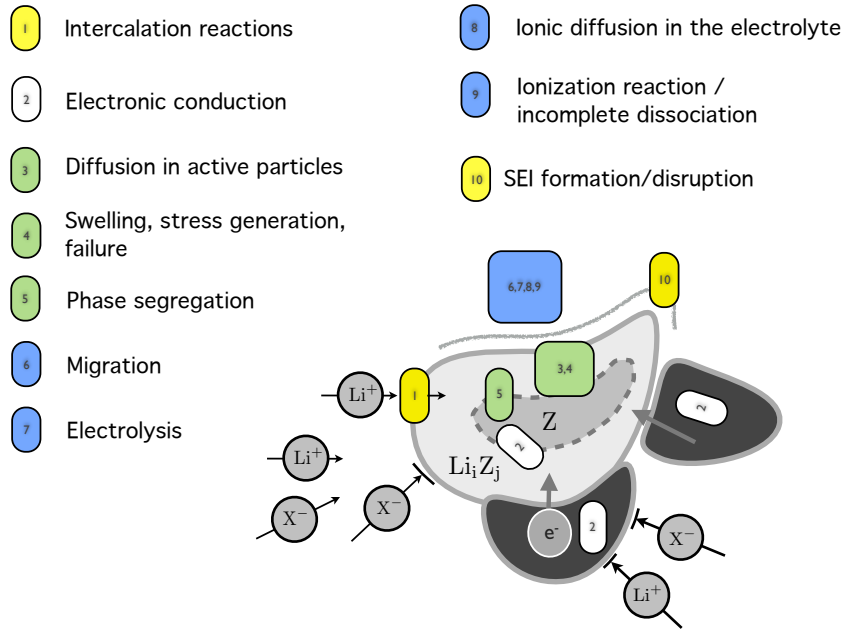
Figure 1.2: *A list of processes that take place in a battery during normal operation.*
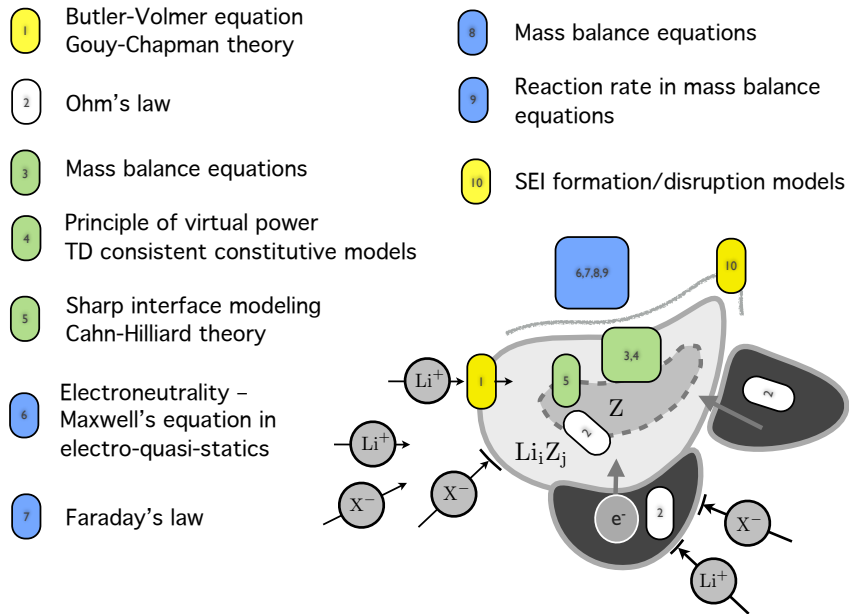
Figure 1.3: *A list of models for the processes that take place in a battery during normal operation.*

Any rigorous model of physical phenomena stems from a few pillars. They are, in order: the balance (or continuity) equations; the thermodynamic analysis, in terms of energy and entropy balance; the constitutive theory and specifications; in the presence of large deformations, objectivity shall also be properly investigated.

Governing equations result from this fundamental sequence of tasks. Scientific rigor claims that this sequence shall be respected, but this is unfortunately not always the case in the literature on battery modeling. In particular, from the second law of thermodynamics restrictions arise that constitutive modeling should account for [22, 23, 24, 25, 26]. Furthermore, in multi-scale approaches, the so called Hill-Mandel condition must be considered, to guarantee that energy is neither artificially created nor annihilated in the scale transitions.

Despite many progresses have been made in the last decades, modeling the complex microstructure of a battery still represents an open challenge. The different nature of the phenomena involved (mechanical, electrical, electrochemical, and thermal) and the interactions among them lead to complex mathematics with a very high number of unknown fields (displacements, electric potential, concentrations, temperature). Moreover all the fields are coupled through non-linear constitutive relations, thus leading to non linear partial differential equations that require iterative algorithms to be numerically solved. As a further complexity in order to achieve predictive capabilities, several parameters usually must be calibrated. Uncertainties in the measurement of those parameters are significantly high for LIBs [27, 28].

Mass transfer entails a description of the movement of mobile ionic species. In the absence of *convection*, as usually assumed under operation conditions, movement of species is governed by *diffusion*, driven by gradients of concentration, or by *migration*, driven by an electric field. The intercalation reactions taking place at the electrode-electrolyte interfaces, can be either described by Butler-Volmer-type equations or by more complex analysis [29, 30, 9] of the phenomena that occur in the atomistic-size layers, termed after Stern and Gouy-Chapman.

Both negative - carbonaceous, mainly graphite, (C) - and positive - $LiCoO_2$ (LCO), $LiNiO_2$ (LNO), $LiFePO_4$ (LFP), and $LiMn_2O_4$ (LMO) - electrodes intercalation materials exhibit phase transition [31, 32]. In some cases the transition is sharp (e.g. from crystalline to amorphous in Silicon) and can be clearly defined by an atomically thick boundary [33] where a chemical reaction takes place. The material properties may change among phases, thus leading to unexpected stress scenario which are under intense study. The reaction rate at the front has been detected as one of the limiting factors for the electrode charge/discharge rate.

Modeling power loss and capacity fade with electrochemical cycling - either in operating or non operating conditions - is becoming a major branch of research [34, 35, 36, 37, 38], especially in connection with high-power and high-density cells that are prone to rapid degradation. The main mechanisms of aging can be categorized in four groups, namely: surface film formation (solid electrolyte interphase (SEI), Lithium plating), bulk changes (phase segregation), mechanical effects due to lithiation (fracturing, dissipation, grinding), and parasitic reactions (corrosion, binder degradation). An up to date review of the literature on aging of Lithium-ion batteries for electric vehicles can be found in [3], with special emphasis on physicochemical transformations. Recent publications on aging and degradation accentuated the role of mechanical detrimental effects. Although individual mechanism strongly depend on the materials in the cell, general effects can be pointed out. Phase-segregation and large volume changes in the active particles are associated with the intercalation of Li in the hosting storage materials. Swelling induce inelastic effects, micro-cracks and particle fracture, decrepitation or pulverization, loss of integrity and loss of electric contact with the current collector, finally leading electrodes to die.

Functional materials for energy conversion and storage exhibit strong coupling between electrochemistry and mechanics [39, 40]. Volume expansion and fracturing of composite electrode components may occur during battery standard operations. Active materials in composite electrodes experience swelling and shrinking during cycling due to Li-ions insertion and extraction. Volume changes reported in the literature range between 6.5% for LMO [41] and about 10% for carbonaceous materials [42, 43]. Such an amount of deformation may induce stress which in turn cause fracture and detachment of particles from the conductive network. In this regard, experimental data have been reported for various active materials:, such as LCO [44], LMO [45, 46], LFP [47, 48] and C [49, 50, 43, 51]. The problem is even more relevant in materials with large storage capacity materials. For instance, the tremendous volume change experienced by Li-alloys, e.g., up to 300% for Li-Si [52] causes fracturing after a small number of cycles.

Deformations in composite electrodes may cause contact loss among their different components accompanied by irregular SEI growth that can modify the porosity of the solid matrix and reduce the overall ionic conductivity.

Temperature influences drastically the performance of batteries under operation conditions. In extreme conditions, temperature increase can initiate a sequence of detrimental effects, known as thermal runaway, that may lead to a destructive result. Three paradigmatic mechanisms for thermal runaway have been recently either experimentally discovered or numerically envisaged. The first mechanism [34, 53] relates to deposition of metallic Lithium during charging, which may compromise cell safety because of dendritic growth and internal short-circuiting. The deposition reaction occurs upon overcharge, fast charge, or at low temperature. Thermally induced mechanisms have been experimentally investigated in [54] in the presence of an external heat source, as for the failure of neighboring cells. They are fueled by the continuous exothermic decomposition and reformation of the solid electrolyte interphase layer at negative electrode/electrolyte interface, inducing a complex chain of events up to battery explosion. Drops in concentrations at the same location, which have been predicted in the presence of fast charge/discharge processes [55, 56], can trigger a similar series of events. Modeling and simulation of those mechanisms involve complex physical processes coupled across a wide range of length and time scales.

1.3 Macroscopic models

Although multi-physics phenomena described in figure 1.2 take place at the length scale of the electrode particles - namely three order of magnitudes below the battery cell size - or even at smaller scales, boundary conditions that drive the response of batteries cannot be identified from experimental observations at those scales. Boundary conditions are more naturally defined at the battery cell scale, and they depend upon the process (galvanostatic/potentiostatic, charge/discharge) and upon the geometry of the cell (cylindrical, pouch, others). The former remark, together with the quest of feasibility of numerical simulations for the models described in figure 1.3 at the finest scale with the state of the art of high performance computing, lead to the conclusion that the computational modeling of batteries must unavoidably be treated via multi-scale approaches. Nevertheless, a large amount of research in batteries focused on one-dimensional, single scale modeling, accounting *in the best possible way* for the underlying microstructure.

1.3.1 Macroscopic models for liquid electrolytes and separators

In liquid-electrolyte batteries, the inter-electrode medium is a composite structure formed by the electrolyte and a separator membrane, that includes a network of interconnected and irregular pores. Most liquid electrolyte models concern a *single* binary electrolyte, i.e. a solution of a binary salt, say LiX where X can for instance [59] be PF_6, plus a solvent in which the ionic concentration varies in the cell. Mass transfer in an electrolytic solution requires a description of the motion of mobile ionic species Li^+ and X^- which is due to diffusion, migration, and advection. Even though the latter contribution might be relevant for some electrochemical systems [60, 61], especially under abuse or extreme conditions [62], advection is usually neglected in LIBs models.

In many cases, the ionic transport is described assuming the electrolyte as an ideal infinitely diluted solution. Under this hypothesis the energetic interactions between different species are neglected; hence, the flux of a species is proportional to the gradient of its own electrochemical potential [63]. For systems involving n different species, the set of n mass balance equations contains $n + 1$ unknowns, typically n mass concentrations plus the electric potential. An additional equation is mandatory and the most common selection in battery modeling is the *electroneutrality* condition [64].

Electroneutrality can be defined as follows: over macroscopic distances the difference in concentrations of the ionic species is small compared to the ionic concentrations [65] and can be neglected. Such an assumption is valid at material points "far" from the electrode/electrolyte interfaces, where high electric fields separate positive and negative charges across very narrow layers.

Noteworthy, electroneutrality is not a fundamental law, but rather an approximation towards the solution, which can lead to paradoxes if not consciously adopted. *Dickinson et al.* [66] have shown that electroneutrality does not constrain in any way the electric field to satisfy Maxwell's equations. *Danilov and Notten*
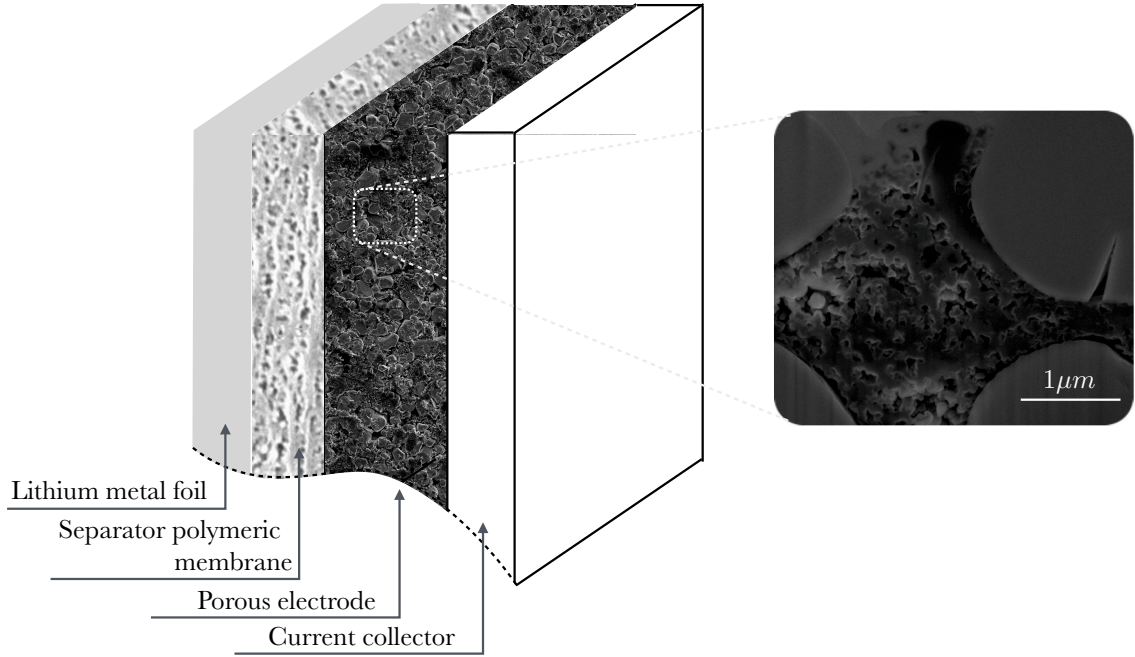
Figure 1.4: *Sketch of a Lithium metal/liquid electrolyte separator/porous insertion electrode cell and a FIB-SEM image of a $LiCoO_2$ commercial electrode. Large active particles are clearly visible, together with the carbon additive particles that form a microporous structure between them. Separator scanning electrode microscope images can be found for instance in [57, 58].*

[63], while discussing numerical simulations stemming from the electroneutrality assumption, pointed out an unjustified electric field in spite a good estimation of the ionic concentration. More general formulations that do not account for electroneutrality in the set of balance equations are required in multi-scale approaches [67, 68, 55, 56]. Their description is thus postponed to section 1.5.

Separators have to be designed to prevent internal short circuiting while providing a path for ionic conduction in the liquid electrolyte throughout its open porous structure. Examples of separators are microporous polymer membranes, non-woven fabric mats, and inorganic composite membranes. Although the separator does not participate in the electrochemical reaction it influences the performance of Li-ion battery cells, as experimentally observed by *Djian et al.* [69].

Morphological features are macroscopically accounted for through global parameters, such as *porosity* and *tortuosity*. The former quantifies volume fraction occupied by the pores; the identification of an optimal value is a compromise between the minimization of the ionic resistance, enabling high-specific battery power (high porosity and large mean pore size), and the limitations dictated by the mechanical resistance of the membrane, preventing the risk of inner battery electrical shorting (thick membrane and low porosity). The tortuosity is a measure of how the conductive pathways deviate from an ideal condition of straight channel of uniform cross section. Increasing tortuosity also increases the mean path length of ions, eventually favoring undesired effects [70]. Many attempts can be found in the literature [71, 72, 73, 74, 75] to relate porosity and tortuosity to effective *conductivity* and *diffusivity* of inhomogeneous media. The influence of the underlying microstructure onto macroscopic material properties is a goal of homogenization theories, which will be discussed in section 1.5.

As the integrity of the separator is crucial to the performance and safety of batteries, stress analyses for the separator can be found in literature [58, 76], taking also into account the SEI layer and its growth as one of the main degradation mechanisms [77].

1.3.2 Macroscopic models for solid electrolytes

Solid electrolytes are of increasing interest due to their possible application in power microelectronic devices, such as micro-electomechanical systems (MEMS), remote sensors, self powered integrated circuits and health care implants [78, 79, 80]. Despite a generally limited ionic conductivity, up to three orders of magnitude smaller than conventional liquid electrolytes [81], their application is characterized by undeniable advantages: safety, high energy density due to usage of a pure Lithium metal anode is enabled yet ensuring stability, no need for casting, no leakage, resistance to shock and vibration, resistance to pressure and temperature variations, electrochemical stability [82, 83, 81, 84].

Inorganic glasses, with particular reference to lithium phosphorus oxynitride (LiPON), find application in many solid state thin-film lithium batteries [85]. A widespread example is the Li/LiPON/LiCoO$_2$ system, investigated by Fabre et al. [83] and Danilov et al. [86]. LiPON solid electrolyte is a glass-forming system in which immobile, oxygen-binded Lithium is transferred to mobile Lithium by means of a ionization reaction, during which a negative charge is released. This process was described by Danilov et al., who made use of the Nernst-Plank equation and the electroneutrality assumption to describe mass transport of Li-ion and negative charges during a battery subjected to a discharge process. A simplified approach was pursued by Fabre et al., who assumed the ionic concentration to be uniform in the bulk electrolyte during both charge and discharge processes. The mobile charges being exclusively Li-ions, Ohm's law was used to relate the current density to the electric potential distribution across the LiPON. The effect of temperature on the input parameters of the model was also studied.

Polymer electrolyte find application in three-dimensional [78] and flexible [87] batteries. Ionic transport in these materials is related to the segmental motion of the polymer chains. The repeated association and dissociation of the ions with the polymer segments and the continuous rearrangement of the latter allow ions to be transferred from one electrode to the other [88]. As the motion of the polymer chains is enhanced at temperatures above the glass transition temperature, higher ionic conduction are also observed at higher temperatures [82]. For reviews on the ionic transport mechanisms in polymer electrolytes, their dependence on temperature and modeling approaches at different scales the reader is referred to [89, 90].

Solid electrolyte have recently modeled from a continuum level perspective by Natsiavas et al. [91]. The latter investigated the effect of pre-stresses on the dendrites formation of lithium metal anode either in contact with LiPON electrolyte or dioxolane-dimethoxy ethane, a soft polymer. In both cases the electrolyte was modeled as a linear elastic material undergoing small deformations. A continuum model for diffusion of multiple charged species in a solid medium in the presence of stress, electrostatic and chemical potential gradient was developed by Bucci et al. [92]. The model, applied for the investigation of the effect of mechanical stress in kinetic demixing and ambipolar diffusion (both phenomena are peculiar of solid oxide fuel cell) is also amenable for solid electrolyte modeling.

1.3.3 Macroscopic models for porous electrodes

For porous heterogeneous electrodes, one-dimensional macroscopic mathematical models reflect reality only in an average sense, that must be properly defined. Porous electrodes are in fact multi-phase structures, which include a network of interconnected and irregular pores and channels [58]. They consist of active particles bound by a polymer to a network of conducting particles, see Figure 1.4. Storage materials are subjected to Lithium intercalation, while conducting particles provide a conductive path that enhances the electronic mobility from the current collector to the active particles surface. Lithium transport in form of ions takes place in the electrolytic solution. The porous configuration increases the effective interfacial area per unit volume between the electrolyte and the active material, favoring the intercalation of lithium. The rate at which the latter occurs depends on the structure and on the material properties of the phases of the composite electrodes [64]. These factors influence the potential drop and concentration changes in both the solution and solid phases [93].

From the seminal works by $Newman$ and coworkers [94, 95] a multitude of models based on the so-called *porous electrode theory* have been applied to the insertion electrodes. The approach circumvents the description of the complex microstructural geometry and processes, by considering *macroscopic* averaged quantities *"over a region of the electrode small with respect to the overall dimensions but large compared to the pore structure"* [64]. Two components, occupying different domains, are considered: an homogeneous

separator - in which only the electrolytic solution is present - and multi-component *porous electrodes* - in which the electrolytic solution and the solid matrix are treated as superposed continua, ensuring connectivity between all points of the electrode [96] - both present at any point of the domain.

The model entails a set of partial differential equations, which describe the processes at the cell scale in an averaged, phenomenological way. The unknown fields are: the molar concentration c_i of species i (both in the separator and in the porous electrodes); the electric potentials ϕ_e and ϕ_s of the electrolyte and of the solid phase respectively. The fields are assumed to be continuous functions in time and space. Porosity ϵ accounts for the void volume fraction, filled by the electrolytic solution. It equals unity in the separator and is strictly smaller than one in the porous electrodes [97, 98].

Mass conservation equation

$$\frac{\partial \, \epsilon \, c_i}{\partial t} + \text{div} \left[\vec{h}_i \right] = R_i \,, \tag{1.1}$$

is enforced to any mobile species i in the electrolytic solution. It relates variations of the molar concentration to the molar mass flux $\vec{h}_i$ and to the mass supply R_i. The latter is identically equal to zero in the separator (unless chemical reactions are explicitly considered) while it macroscopically accounts for the microscopic pore-wall flux density in the porous electrodes [64].

The current $\vec{i}$ is defined as the charge flux density per unit area. It coincides with the electrolytic current $\vec{i}_e$ within the separator where the ions are the only mobile charged species, and with the sum $\vec{i}_e + \vec{i}_s$ in the porous electrodes. Charge conservation is ensured being $\vec{i}_s$ the amount of current carried by the electrons in solid phase within porous electrodes.

By imposing the electroneutrality condition

$$\sum_i z_i \, c_i = 0 \,, \tag{1.2}$$

where z_i is the charge number of species i, the net charge is always zero and the total current density satisfies the charge balance equation

$$\text{div} \left[\vec{i} \right] = 0 \,, \tag{1.3}$$

both in the separator and in the porous electrodes.

Constitutive assumptions relate the mass fluxes $\vec{h}_i$, the current densities $\vec{i}_e$ and $\vec{i}_s$ and the bulk terms R_i to the molar concentrations c_i and the electric potentials ϕ_e and ϕ_s, which are the thermodynamic variables and the unknown fields of the model. Faraday's law relates the electrolytic current density to the ionic mass fluxes in the electrolyte, whereas Ohm's law is assumed to govern the movement of electrons in the matrix phase. Either dilute, moderately-dilute or concentrated solution theories may be adopted, leading to thermodynamic scenarios characterized by an increasing degree of mathematical complexity. For the sake of brevity, the reader is addressed to specific literature [63, 97, 98, 99, 64, 100] for the explicit expressions of the constitutive equations.

The macroscopic physical properties that enter the constitutive equations assume the meaning of averaged micro-structural features within the porous electrode. For example, the effective ionic diffusivity in random porous structures intrinsically accounts for the porosity and the for the deviation of paths within pores from being straight channels (tortuosity) [75].

A Butler-Volmer type kinetic expression was introduced to account for the kinetics of the charge-transfer processes at the electrode in place of the assumption of infinitely fast insertion [100, 97]

$$i_n = i_0 \left[\exp\left(\frac{\alpha_a \, F \, \eta}{RT} \right) - \exp\left(-\frac{\alpha_c \, F \, \eta}{RT} \right) \right] \,, \tag{1.4}$$

i_0 is the exchange current density, whose value varies with the concentrations of reactants and products, temperature, and the nature of the electrode-electrolyte interface; α_a and α_c, called apparent transfer coefficients, express how an applied potential favors one direction of reaction over the other (their values range in literature between 0.2 and 2); $\eta = \phi_s - \phi_e - U$ is the surface overpotential and U is the open-circuit potential, corresponding to thermodynamic equilibrium conditions (zero net transfer current density). The mass supply R_i is related to the average transfer current density i_n.

The open-circuit potential U is related to the state of charge. The so-called *pseudo-2D models* [101, 102] have been introduced to investigate such a dependency. The etymology of this class of models arises from the two "unrelated" dimensions that are involved, namely the cell and the active-particles. The latter have been assumed as spherical (with rather few exceptions, e.g. [103, 100]) of constant radius upon intercalation of external species.

Porous electrode theory has been applied with an increasing degree of complexity over time, since enhanced available computational tools became available. In particular, modeling of electrodes attempted to account for the fine microstructure within the porous electrode theory, with strategies sometimes formulated on a phenomenological rather than a solid theoretical ground.

The modeling of full-cells composed by Lithium metal/solid polymer separator/insertion positive electrode and simulation of galvanostatic charge/discharge processes pursued by *Doyle et al.* [97] enhanced previous approaches [103, 100], accounting for interactions of the battery components. Concentrated solution theory was used to describe transport process occurring in the electrolyte.

The "constitutive" relation between the open-circuit potential and the state of charge controls the current distribution inside the porous electrode. Materials characterized by significant changes in open circuit potential for limited variation of the state of charge (e.g. carbonaceous materials) lead to more uniform current profiles in the porous electrode compared to materials exhibiting this dependence to a limited extent (e.g. LMO),[98] and hence to a better utilization [34].

Intercalation materials were regarded as perfectly conductive and interested by Fickian solid diffusion, as in [103, 100, 97, 96]. Constant physical properties were used for all the components. Film resistances on both electrodes was introduced by *Doyle et al.* [104].

All the models described above share some fundamental *hypotheses*. The electrolyte consists of a binary salt in a single solvent [100, 97, 96, 98], a picture recently questioned under high C-rates [105, 106]. Side reactions (e.g. SEI layer formation and electrolyte decomposition) have not been considered, therefore the amount of Lithium during all processes is conserved, which contrasts experimental observations [34]. Volume changes due to intercalation have not been accounted for, therefore the models do not account for mechanical effects that strongly contribute to degradation [107].

Numerical simulations with the porous electrode theory have been carried over a wide range of materials and configurations [97, 98, 108, 104, 105, 109, 110]. Outcomes, in terms of concentration profiles and pore wall flux distribution within composite electrodes during charge/discharge processes, provided meaningful insights on battery design and optimization. As observed by *Doyle et al.* [97], cell optimization relates to battery configuration, energy and power density requirements of the system, and cost of components. Whereas thinner electrodes limit electrolyte depletion and allow for higher specific power, thicker electrodes increase specific energy by reducing the number of cells in the battery stack and the volume fraction of inactive components [105].

The robustness of the Pseudo-2D approach is assessed by the number of recent models that stem from it, as [101, 111, 112]. Pseudo-2D models also present limitations: typically, the large amount of material parameters requires remarkable experimental efforts. The main drawback though relates to microscopic approximations. Pseudo-2D models do not allow describing in detail the processes taking place at the finest scale, which can have a significant impact on the overall battery response [99]. The capacity fade due to active particles fracturing and decrepitation, the porosity change caused by SEI formation or reaction products deposition have already been remarked. A thorough discussion on the applicability of macroscopically homogeneous models to Lithium-ion battery description can be found in [113], where a poor predictive capacity is highlighted for high C-rates.

Macroscopic battery models that do not make use of Newman's porous electrode theory have been published, too. In general, they replace the porous structure with aggregates of solid-phase particles, which are directly embedded in the electrolytic phase [114, 115, 116]. Mechanical stress generation was in few cases accounted for in the solid-phases [99, 116].

Despite the formulation was derived in 3D, the numerical implementation was often restricted to 2D [99, 114, 116]. Three-dimensional simulations were developed in [115], where a half-cell Lithium battery

was modeled on a LMO spherical particles array. Numerical analyses suggest that small sized particles and regular arrangement ensure higher capacity, especially when active materials are characterized by low diffusivity.

Macroscopic models for *solid (non porous) electrodes* have also been studied. The geometry of the cell is idealized as blocks stacked in order to reproduce the sequence of the battery components, idealizing the battery with a one-dimensional structure [30, 86, 83].

1.4   Microscopic phenomena and their modeling

Several models have been proposed to investigate the microscopic response of electrodes during intercalation, in order to provide design criteria for enhancing electrodes performance. In fact, the response of the electrodes upon Lithium uptake and release during batteries charge and discharge depends on the thermo-chemo-mechanical properties of the compound of active and conductive particles. The micro-structural composition and the geometrical configuration are of paramount relevance for the intercalation process and the performances of the electrodes.

Since the cell is first assembled, charges are localized at the interfaces between electrodes and electrolyte, causing an intense electric field to develop in an *adsorption* layer (named after Stern [117]) with atomic-scale dimensions adjacent to the interface, together with a more diffuse region of charge (known as the Gouy-Chapman layer [118, 119]) in the electrolyte [120]. These regions together (in the order of 10 to 20nm according to the literature [64]) define a so-called *electric double layer*. An exhaustive dissertation about the electric double layer can be found in classical books [29, 64] as well as in more recent literature, among which *Bazant and co-workers* publications deserve special merit [65, 121, 122].

In Li-ion battery modeling literature, the double layer is generally assumed as infinitesimally narrow, with a few exceptions [123]. Local electroneutrality is generally assumed in the electrolyte and a discontinuity in the potential across the electrode/electrolyte boundary is allowed for (see among others [60, 61, 63, 116, 112]). Butler-Volmer equation [124, 125, 126] is used to relate the intercalation flux to the potential discontinuity between the electrode and the points in the solution immediately beyond the ideally narrow double layer [127, 128, 129, 99, 116]. *Streeter and Compton* [130] critically discuss the *electroneutrality* and the *negligibly small double layer* approximations, arguing that they are appropriate only if the active particles of the electrode are much larger than the electric double layer. *Dreyer et al* [131] formulated a continuum model of the layer, including solvation effects of the dissociated ions, as well as the mechanical effects. *Landstorfer and Jacob* [9] discuss weak and strong electroneutrality conditions and split the electrochemical intercalation-deintercalation process in three simple reactions, in order to define appropriate boundary conditions. That paper also accounts for a large bibliography on the mathematical modeling of intercalation, to which we further address the interested reader.

An accurate *morphology* reconstruction is a crucial information for micro-scale analysis. This statement applies to localized phenomena, like hot spot formation, as well as to ensemble averaged material properties, which have been shown to be extremely sensitive to the size, shape, and particle distribution within a Representative Volume Element [132].

Accurate reconstructions of the connectivity and of the internal structure of electrodes is a very hard task: binder, active, and conductive particles give rise to tangled and intricated geometries. The complexity of the morphology of electrodes and separator restricted the focus of most publications to the behavior of a single particle, disregarding the influence of the electrode microstructure [133, 134, 135, 136, 137, 138, 139, 140, 141, 142, 143, 144].

The microscopic arrangement of active particles, carbon, binder and pores can be recovered from statistical analyses of 2D cross sections of the electrode achieved through scanning electron microscope with focused ion beam. The particle geometry can either be a simplified abstraction of reality - for example using cluster of spherical [74, 145] or ellipsoidal [146] particles that yet represent challenges for computational discretization [147, 148] - or be digital reconstruction of realistic morphology [149, 150, 151, 152, 153, 154, 155] - generally restricted to single-particle analyses.

In recent years major progresses have been made in the area of X-ray computed tomography [156, 157, 158, 159] and focused ion beam scanning electron microscopy [149, 160, 151, 161, 162, 163], paving the way to numerical simulations on realistic three dimensional microstructures. They involve high computational costs [151, 147, 148] and are feasible only in a high performance computing environment.

Modeling *temperature evolution* in Li-ion battery cells is important in operation conditions [9, 164, 165, 166, 111], to dictate parameters for cooling devices design, but even more under abuse or extreme conditions, to predict and control thermal runaway [54, 167]. A recent review can be found in [168].

Whereas operating temperature ranges may vary upon different applications and related national standards, it is generally established that an increase of temperature, either because of external conditions or during fast charge/discharge [69], boosts degradation mechanisms. In general, temperature affects ion mobilities, SEI formation and dissolution, interface reactions - eventually promoting undesired side effects. Accounting for the influence of temperature in modeling is extremely complex mostly because: i) temperature affects transport properties of materials, interface kinetics, electrical and mechanical properties in ways that are difficult to capture experimentally and reproduce numerically [169], even though the general thermodynamic framework that lays the ground of every rigorous theory is nowadays well established [170]; ii) numerical treatment of multi-physics problems in coupled chemo-electro-thermo-mechanics are not completely understood [171]; ii) temperature in the cell may increase after the formation of very localized hot-spots, which are related to the speed of charge/discharge [152].

A few attempts only accounted for realistic microstructure of porous electrodes considering the temperature field and the hot spots formation under extreme conditions in a multi-scale and multi-physics framework [170, 62, 153].

Notwithstanding the large number of publications focused on Lithium-ion battery, the modeling of the detrimental effects related to *aging mechanisms* is a relatively recent topic[172]. *Arora et al.* [34], browsing the most relevant capacity fade mechanisms concerned with side reactions in Li-ion batteries, observed that the only model on the topic available at that time was provided in *Darling and Newman* [173]. The latter represents the first attempt of simulating aging process in a physical model, as recently remarked also by *Barré et al.* [7].

Aging affects electrolyte, composite electrodes, as well as the electrode/electrolyte interfaces. Many different factors concur to capacity decrease and power fading of Lithium-ion batteries both during storage and charge/discharge cycling. Calendar aging is monitored in terms of capacity loss, impedance rise, state of charge and state of health [37]; it has been proved to be sensible to storage conditions, especially temperature and state of charge [7]. Cycle aging may be detected through capacity fade, impedance rise and overpotential that can be measured during cycling [37]. Various studies have experimentally shown that it is enhanced by larger amount of charge variation during cycles [174, 175], high charging/discharging voltage [176] and current peaks [7]. Calendar and cycle aging coexist during the whole battery lifetime. An example of estimation and comparison between their relevance on the performance of a C/LFP cell can be found in *Safari and Delacourt* [177].

The processes by which Lithium is either produced or consumed within a battery cell include Lithium deposition, electrolyte decomposition, active material dissolution, phase changes in the insertion electrode materials, and passive film formation over the electrode and current collector surfaces. Often they are collectively termed *side reactions* [34]. The interaction among any of the processes mentioned above is favored by the similar timescales over which they occur, making difficult their specific identification. Moreover most of them are strongly related to the peculiar features of the cell (shape, microstructure, material components).

Detrimental effects may also descend from other processes, such as interaction between binder polymer with active and conductive particles, current collector corrosion and plating, gas formation within the cell [7, 3, 37].

The most relevant aging mechanism for carbon anodes is attributed to phenomena occurring at the electrode/electrolyte interface, where a passivating layer, termed *solid electrolyte interface (SEI)*, prevents further interfacial reactions yet allowing the Lithium ion migration [31, 178]. Notwithstanding the protective function attributed to the SEI, its formation entails a capacity loss as a consequence of the irreversible consumption of Lithium ions. The process is more pronounced during the first few cycles [179]. Among the

factors affecting the SEI layer's evolution, a strong dependence on temperature and state of charge has been proved to exist for its morphology, composition and Lithium ionic conductivity [7, 37]. Continuum theory for the growth of an SEI layer have been recently proposed by many authors [128, 180, 181, 182, 183, 184, 77, 185, 186, 187, 188, 189, 190, 191].

1.4.1 The modeling of micro-mechanical effects.

Since *mechanical effects* are among the most important mechanisms of capacity fade and impedance growth in Lithium-ion batteries [34], the stress generation during Lithium diffusion in active materials has been widely investigated. The intercalation process is generally modeled as a multicomponent system [192, 193], which comprises Lithium diffusing in a hosting material lattice. Atomic diffusion in solids is much slower than deformation [194], therefore mechanical equilibrium is postulated at all instants.

High capacity electrode materials, such as Silicon and Tin, manifest huge expansions when lithiated. Storage particles develop non-uniform Lithium concentration profiles, which cause differential strains and originate a stress field within the particle (referred to as *chemical stresses* [143] or *diffusion-induced stresses* [133]). Many efforts have been made in the last decade in order to understand and model the *stress evolution in active particles* [195]. Modeling involves multi-physics description of the processes as they entails coupling among mechanics, transport, and thermo-electro-chemical kinetics. Lithiation influences material parameters [107] and may lead to phase segregation, too, which causes lattice mismatch within the particle.

It has been observed that both anodic and cathodic materials may fracture during charging/discharging operations. Some electrode materials, such as Lithium-alloys, undergo *decrepitation*, i.e. fracturing in many small parts, caused by large deformations during lithiation [196]. Cracks have been observed even in active materials that undergo small deformations when lithiated, as for $LiCoO_2$, $LiMn_2O_4$, and $LiFePO_4$ [197].

To predict the onset of fracture in electrode particles, many authors [198, 199, 196, 200, 201, 202, 197, 203] resorted to linear-elastic fracture mechanics [204, 205, 206, 207]. A pre-existing flaws population in the particles was assumed and Griffith's criterion used to investigate the effects of charging rate and fracture toughness on the failure of particles of different sizes. Assumptions have been often taken upon the most dangerous flaw orientation, which might be incorrect [208]. Alternatively, some authors adopted cohesive models for crack nucleation inside the electrode [209, 210, 127] or phase-field methods [211, 212, 213, 214, 215, 216, 217, 218, 219].

Other studies lead to design criteria in order to avoid particle fracturing based on the stresses generated inside the electrode. For example tensile stresses [135, 220] or von Mises equivalent stresses [143] have been taken as measures of the distance to the onset of fracture.

In what follows, homogeneous material formulations and phase segregation models will be separately described.

1.4.1.1 Lithiation models in homogeneous particles.

It is common in literature to idealize the geometry: particles are either modeled as spheres [133, 134, 220, 135, 136, 139, 141, 221], cylinders [210, 222], or thin films [209, 30]. Chemo-mechanical features are also simplified: materials are often taken to be isotropic with properties (Young's modulus, Poisson's ratio, diffusivities) insensitive to Lithium content [133, 134, 137, 139, 141, 142, 143].

Since Lithium transport is severely influenced by the deformation of the hosting material and vice-versa, diffusion and mechanics are entangled processes. Accordingly, the thermodynamic forces that drive Lithium diffusion shall be mathematically coupled to mechanical deformation. The coupling is usually described in analogy with thermo-mechanics, i.e. the variation of solute atoms concentration in the hosting material causes a pure volumetric deformation: the partial molar volume plays the same role of the thermal expansion coefficient [223, 224, 225, 226].

Whereas most early models neglected the role of mechanics, a few recent ones couple the mass transport to the mechanics in a one-directional way. In those models, the driving force for the diffusion is solely the concentration gradient, therefore the Lithium concentration can be evaluated by solving the transport
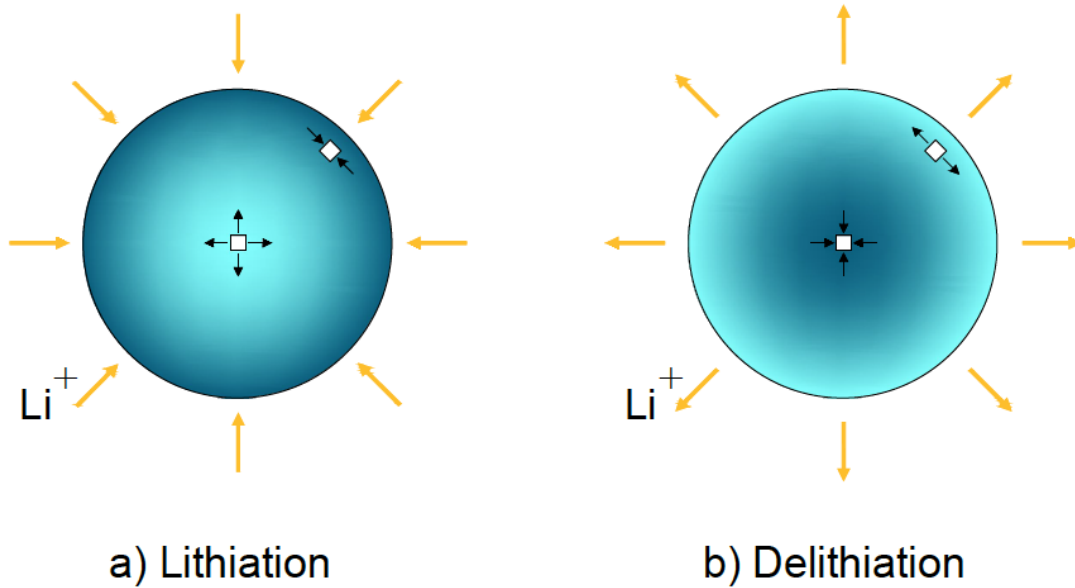
Figure 1.5: *Schematic of particle expansion during Lithium insertion (e.g., during charge) and contraction during Lithium extraction (e.g., during discharge). Arrows pointing toward each other indicate regions of compression in the particle, while arrows pointing away from each other indicate regions of tension. [135].*

problem, while the chemical stresses can be computed afterwards. For linear-elastic material with parameters independent upon Lithium concentration, analytical solutions are attainable for simple geometries. This approach was taken in [133, 134], to investigate the critical factors that influence the overall response of active materials. Diffusion induced stresses were computed in spherical active particles under either galvanostatic or potentiostatic control, as well as under more realistic boundary Butler-Volmer kinetics. It was shown that during lithiation the Lithium concentration decreases from the outer surface to the center, inducing the outer shell to swell and generating compressive hoop stresses near the particle surface and tensile stress into the inner core, in view of geometrical compatibility, as described in Figure 1.5. The opposite during delithiation. The stress magnitude was found to depend on the charge/discharge rate [141] and on the particle size.

The effects of surface mechanics in nano-sized spherical particles were studied in [194, 221], in order to design particle of longer cyclability. It resulted that the magnitude and distribution of stresses can be significantly affected by surface mechanics if the particle is in the nanometer range. Such an approach was applied to nanowire electrodes [137], too.

Two-way coupling was considered in more recent papers. The mass flux is modeled as dependent on both concentration and hydrostatic pressure gradients, as in the inspiring framework of *Larche and Cahn* [227, 228]. Some authors assumed that particles remain linear-elastic during the whole process [139, 229, 230, 142, 143]. This assumption is reasonable for electrodes with moderate swelling, as LiC, LMO. *Zhang* and co-workers simulated the charging/discharging process of $Li_xMn_2O_4$ for $0 \leq x \leq 1$ and captured the range in which phase transitions occur as a function of the state of charge. The stress generation in three-dimensional ellipsoidal particles with different aspect ratios was evaluated through numerical simulations [143]. The numerical outcomes suggest that larger aspect ratio and smaller particle size may reduce the intercalation induced stresses.

The influence of particle morphology has been simulated in [230] after digitalization of real particles. The maximum von Mises stress induced by the lithiation in a digitalized particle turned out to be one order of magnitude higher than the one predicted on idealized shapes.

Miehe and Dal [140] proposed a computational theory accounting for electro-chemo-mechanical inter-

13

action of Silicon particles. Numerical simulations shown significant discrepancy between small and finite strains approaches, pointing out the importance of large strains theory in modeling materials with significant swelling.

Silicon thin-films and particles show a markedly inelastic behavior during charge/discharge. Plasticity seem to infer a specific failure mechanism, since for spherical particles the initial compressive hoop stress in the outer shell during intercalation may even reverse [136]. The Lithium transport problem was coupled to plasticity models at infinitesimal [203] as well as at finite strains [231, 30, 127, 128, 136, 222, 232, 233, 234, 144].

Bower and co-workers [30] developed a general model that accounts for finite strains and plastic flow in electrodes materials. A Silicon thin-film was studied and compared with experimental evidences [235]. *Cui et al.* [136] focused on the chemical potential in the framework of finite strains and plastic flow as well. They proposed a chemical potential that extends the formulation of Larché-Cahn. Numerical examples on spherical Silicon particles emphasized the role of plastic flow in the lithiation process.

1.4.1.2 Models accounting for phase-segregation

Multi-phase models aim at investigating the behavior of particles in which phases co-exist because of lithiation. They essentially differ for Lithium content and for the crystal structure, which is transformed after intercalation [236]. The thickness of the physical region that separates distinct phases, the so-called *phase boundary*, varies upon materials. For instance, crystalline Silicon reacts with Lithium forming an amorphous phase with atomically sharp reaction front - about 1nm thick [33]. Experimental evidences for $LiFePO_4$ show a wider phase boundary, of several nanometers [237, 238].

The widespread class of so-called *sharp-interface models* splits particles in two distinct regions and idealizes the phase boundary to a zero-thickness interface. The class of *phase-field models*, usually stemming from the Cahn-Hilliard theory [239], smears the phase boundary in a narrow region of finite thickness, avoiding localized discontinuities. Alternative models recover discontinuous concentration profiles without recourse to any of the methods above. A review of modeling methods for phase boundary can be found in *Thornton et al.* [240].

Sharp-interface models [241, 242, 243] shown the ability to reproduce the observed voltage plateau [107] in the discharge profile of iron-phospate [241] and Lithium cobalt oxide [243] electrodes. To account for the phase transition, electrodes were modeled with the so called *shrinking-core* particle approach[242], which idealizes active particles as spheres with two distinct phases occupying the outer shell and the inner core, respectively[241]. The interface location is one of the unknowns of the problem and evolves in the radial direction driven by the Lithium transport in the Li-rich phase and on the concentration gap at the interface. Mechanical effects are included in the shrinking-core approach [220, 138, 112]. Particles have been modeled as linear-elastic bodies with different chemo-mechanical properties between the two phases. The onset of chemical stresses was modeled with the analogy to thermal stresses as in the single-phase models, therefore the stress field affects the phase-boundary kinetics. These models are capable to predict the rise of tensile stresses in the core-phase and compressive hoop stress in the outer shell during lithiation. Differently from single-phase models, the hoop stress can be discontinuous at the phase-boundary. The interfacial stress discontinuity depends upon the interface location, equilibrium concentration, and the material properties of the two phases.

In the *phase-field models* the dynamics of phase-segregation is ruled by the free-energy of the system. Differently from the Fickian description of diffusion, the Helmholtz free energy includes an interface energy, related to the gradient of concentration. Phase-segregation is not imposed *a priori* via sharp interfaces but arises as a consequence of the thermodynamic evolution of the system[244].

Early works applied the conventional Cahn-Hilliard phase-field model to describe phase separation in $LiFePO_4$ electrodes [245, 246, 247]. In particular *Singh et. al* [245] showed the ability of this theory to model the anisotropic ionic mobility in single crystals. The Cahn-Hilliard theory was extended in order to assess the conditions for phase-segregation in electrode particles. The total free energy was modeled accounting for additional terms, such as the strain and surface energies. In this way *Tang et al.* [248, 249] and *Cogswell and Bazant* [250] investigated the effect of particle size, mechanics, and applied overpotential in the phase transition pathways of storage particles.

14

Anand and co-workers [251] developed a general thermodynamically consistent theory that couples the Cahn-Hilliard theory with large elasto-plastic deformation mechanics. Simulations show the phase-transformation of a three dimensional LiFePO$_4$ spheroidal particle [252].

Basic computational aspects of phase-segregation modeling in electrodes have been recently dealt with in [253].

Stress evolution in two-phase electrodes was also modeled alternatively. A sharp-interface was reproduced either creating a series of step-like concentration profiles [254], by choosing a concentration dependent parameters [255], or making recourse to the concept of Lithium traps [256, 257]. Active particles, mostly idealized as spheres, were assumed to deform visco-plastically, to mimic the mechanics of lithiated Silicon. *Huang et al.* [254] showed that the initial compressive hoop stress in the lithiated shell could be reversed if the material undergoes plastic deformations. *Yang et al.* [255] adopted a concentration dependent diffusivity and imposed that Li diffusivity in the lithiated region is much larger than in the pristine core. This induces the concentration profile to assume a typical pattern of a two-phase system, with interface tracking controlled by diffusion. *Drozdov* [256, 257] assumes that Lithium within the particle is separated in mobile and alloyed. The latter is treated as a kinetic process, which ultimately permits to recover a sharp interface.

More recent models of lithiation in Silicon describe the phase-boundary kinetics [32, 258, 259] and the observed anisotropy in intercalation [260]. Crystalline Silicon becomes amorphous upon lithiation, and diffusion through the amorphous phase has been observed to be faster than the reaction at interface [259]. Therefore the phase-boundary motion, differently from the shrinking-core models, shall not be controlled by Lithium diffusion. *Zhao et al.* [259] formulated the driving force of the reaction between pristine Silicon and Lithium at the interface including the effects of the stress field. By simple benchmarks they showed that the interface motion could be inhibited by the stress field generated in the particle. With a more general approach *Cui and co-workers* [258] developed a two-phase model for Silicon particles accounting for diffusion in both phases, stress generation and phase-boundary kinetics. The kinetics of reaction at interface and diffusion in both phases are concurrent processes. Their numerical results showed the impact of different ratios between rates of interface kinetics and bulk diffusion in Lithium distribution and stress generation.

1.5 Multiscale models

Intercalation, swelling, and eventually the mechanical failure originate at a scale three order of magnitudes smaller than the battery cell scale, at which ion mobility is usually modeled. Since modeling a whole battery cell at the nano-scale is computationally unfeasible, nano-scale effects are incorporated into the micro-scale problem through *homogenization* approaches and constitutive models that are derived from multiscale approaches. They frame on a representative volume element (RVE), in which the relevant features of the microscopic morphology are accounted for. The proper selection of the RVE is a fundamental ingredient, as usual in the theory of composite materials. According to [261], an RVE may be defined in two different ways. It can be considered as the smallest microstructural volume for which the averages of properties represent with "sufficient accuracy" the mean macroscopic response. Accordingly, RVE's size is influenced by the material behavior of the microstructural components. A second definition requires the RVE to be statistically representative of the microstructure, that is to essentially include a sampling of all possible microstructural configurations occurring in the composite. This definition leads to significantly larger RVEs than in the former case, as the microstructural element must incorporate several kinds of material heterogeneities. Based on this definition, statistical methods have been presented to determine the size of the RVE and the number of inclusions to consider [262, 263, 264, 265].

Representative models of the battery microstructure were based on experimentally obtained statistical information. The three dimensional microstructure of a graphite porous electrode was reconstructed recurring to tomographic techniques[157]. The minimum RVE size was calculated as $43 \times 60 \times 60\mu$m after evaluating several geometrical parameters (e.g. porosity, pore and particle size distribution) and extracting the relative standards deviations. An estimate of the characteristic dimensions of a cubic RVE for LiCoO$_2$ electrodes was derived in [149], resulting in an edge of $\approx 30\mu$m. A similar approach [266] was employed for LiFePO$_4$ electrodes, $5 \times 5 \times 15\mu$m.

Ferguson and Bazant [267] made use of *Wiener* and *Hashin-Shtrikman* bounds to characterize the electrical conductivity and tortuosity of porous media, while an asymptotic multiscale expansion was pursued by *Schmuck and Bazant* [268].

Wieser et al. [155] made use of 3D imaging at different scales and homogenization techniques to estimate effective transport properties of ionic species within porous electrodes. The authors identified a micrometer porosity for the composite electrodes - made up by solid active material, additives and open pores filled by the liquid electrolyte - and a nanometer porosity within the additives - a mixture of carbon conductive particles and polymeric binder. A lithium metal/separator/graphite-based porous electrode half-cell was simulated showing that the impact of additives nanometer porosity on transport limitation is negligible.

Awarke et al. [145] attempted to quantify the impact of changes in the arrangement of solid particles within Li-ion battery electrode on the conductivity and tortuosity of a LiFePO$_4$ based cathode. A Finite Element Method (FEM) was used to analyze RVEs made up by spherical particles with various arrangements representing the same porous agglomerate under different mechanical and electrical loading conditions. Volume averages have been used to compute effective macroscopic properties (elastic tensor, volume expansion coefficient and electrical conductivity) which have in turn been adopted in numerical analyses on a cathode sample.

Lee et al. [269] adapted the variational multi-scale principle to a Li-ion battery system, in order to improve the predictions of battery performance by including multiphysics phenomena among the particle aggregates in the electrode. The role of the microstructure was highlighted, in terms of particle shape, tortuosity, and material composition.

A continuum model for Li-ion battery accounting for electrochemical and mechanical effects at multiple scales was presented by *Golmon and coworkers* [270] . Transport processes and battery deformation have been modeled at the cell scale, where the mechanical interactions with surrounding layers was considered through tractions boundary conditions. A single spherical active particle was analyzed to account for the microscopic evolution of the system both in terms of intercalated Lithium (state of charge) and chemically induced local stresses. The macroscopic pore wall flux was related to the microscale following Newman's porous electrode theory, while the Mori-Tanaka effective-field theory was used to relate mechanical properties between scales. Both scales were idealized to one-dimensional problems as in pseudo-2D models. The electrochemical and mechanical performance of half-cell have been studied by varying the electrochemical properties, the cathode particle radius, the porosity of the cathode, the discharge current density and the mechanical boundary conditions. The model has been further applied to design optimization of a Li-foil/separator/porous electrode battery [271] and to a battery cell in which both electrodes were porous [272].

Volume averaging techniques that are applicable to the entire cell with arbitrary 3D electrode configuration have been recently proposed [273].

Gupta et al. [146] proposed an electrochemical model for porous electrodes that accounts for two different scales. At the microscopic scale an RVE made up by an electrolyte and a solid matrix domain was identified for the porous electrode. Governing equations for Lithium and electric charges were written over each domain moving from conservation equations typical of continuum models. The cell scale governing equations differ from the ones detailed in [67, 68] because the volume-averaged fluxes have been explicitly provided through the introduction of effective transport properties, such as the Bruggeman's equation [72]. This approach differs from pseudo-2D models because all the macroscopic variables have been derived from microscopic volume averaging.

In recent contributions, [67, 68] a computational homogenization (CH) technique was tailored to Li-ion batteries by using a multiscale scheme with a complex multi-particle RVE idealizing active particles in the composite electrodes as network solids following Larche and Cahn [227], with the lattice material assumed as insoluble in the electrolyte. The CH technique is based on the solution of nested boundary value problems, one for each scale. A complete set of equations and boundary conditions governing the stress, electric, chemical, and electrochemical potentials was derived [67] for the whole battery cell for both scales following non-equilibrium thermodynamics of porous electrodes [267, 64]. Use of the Butler-Volmer equation was made to describe the intercalation kinetics accounting for the flux of Lithium between the particles and the electrolyte, which at the macro scale was modeled as a bulk supply. At such a scale, transport and stress evolution were modeled via volume averaged conservation equations.

In the rigorous mathematical formulation of multi scale modeling - see [274, 275] - the micro to macro

scale transition requires conservation of power expenditure between both scales, thus assuring that energy is neither artificially generated nor artificially dissipated across the scales. If electro-neutrality is used in place of Maxwell's equations, recovering the energy description of the electromagnetic interactions is not possible. Therefore, electroneutrality assumption (1.2) cannot be used in multi scale approaches [68]. In the approach proposed in [67, 68], rather then imposing the electroneutrality condition as an equation to be fulfilled, the impact that it has on the fundamental balance laws was investigated. Lorentz forces were thus neglected, whereas it was shown that electroneutrality has no influence on Maxwell's law.

A rigorous analysis of general principles of non-equilibrium thermodynamics [24, 276] has been performed in [55, 56]. The electrochemical potential was defined moving from the rate at which power is expended on a material region, in terms of mechanical contribution as well as of the power due to mass transport and to electromagnetic interactions. All processes were taken to be isothermal. The entropy imbalance with the Coleman-Noll procedure provide thermodynamic restrictions, satisfied by the usual Fickian description of diffusion and migration in terms of electrochemical potential, defined as in [22, 23]. Infinitely dilute solutions as well as solutions close to saturation have been numerically simulated.

A mixture theory has been presented in [131] for a liquid solvent containing (completely) dissociated ions. Electro-mechanical interaction has been explicitly taken into account by introducing the Lorentz contribution within the balance of forces and a chemical potential dependence on pressure. The effect of solvation was also considered in the definition of entropy of mixing. A fully coupled model for charge, species and thermal transport in Li-ion batteries has been developed by *Latz and coworkers* [170]. The formulation, based on general principles of non-equilibrium thermodynamics, makes use of charge neutrality assumption for both electrolyte and active particles. Electrical, chemical and thermal interactions between electrolyte and active particle were taken into account by proper interface conditions.

1.6 Conclusions

The relevance and timeliness of modeling and simulations in the field of energy storage materials [277] is made evident by the intense flow of scientific publications. A review of this abundant literature may reveal thus useful, although keen to become soon obsolete. An effort was provided in this note, moving from the inherent multi-scale nature of Li-ion batteries.

Continuum thermo-chemo-electro-mechanical models have been discussed at different scales and multi-scale approaches have been analyzed as well. This study illustrated the progresses made since the pioneering publications, and made clear that modeling is becoming more and more accurate and predictive and, with the availability of high performance computing, it can integrate experimental campaigns in discovering new materials and developing new architectures.

The non-equilibrium thermodynamics, coupled with rigorous scale transitions, is the appropriate theoretical background for multi-scale and multi-physics modeling. The future scientific endeavors will stem from this fundamental framework. They are expected to finalize the three-dimensional multi-scale approaches currently in progress into high-performance computing scalable codes, in order to investigate major concerns in current batteries technology as the behavior at high C-rates and voltages, which may lead to thermal runaway fueled by side reactions. A clear understanding of these phenomena may provide significant progresses in batteries safety, particularly under abuse or extreme conditions.

Several aging phenomena in batteries require further scientific investigations. These study may address some fundamental problems of electrode chemo-mechanical instabilities that have so far limited the power, energy, and durability of advanced batteries. The modeling of Lithium deposition and dendritic growth, for instance, is particularly relevant for the safe use of Lithium metal anodes yet lags behind the experimental evidences, in spite of recent investigations[91]. Co-designed experiments and simulations may pave the way to a deeper understanding of these limiting phenomena.

The predictive ability of modeling and simulations relies on the realistic reconstruction of three-dimensional porous electrode. Evident progresses have been made in this recent years, particularly in the field of X-ray tomography. The required accuracy of the electrode reconstruction is strictly related to the targeted processes, so that the classical statistical paradigms of homogenization may not always be applicable successfully.

This review did not focus on atomistic simulations. A major challenge of the future investigations will concern the incorporation of quantum mechanics and molecular dynamics into coarser scales formulations. As pointed out also in [278, 8], it will become more and more important to develop multi-scale models that account for a realistic chemical environment by means of coupling discrete and continuum approaches. This seems to be particularly relevant in the modeling the interface phenomena, that take place in atomistic-size narrow layers.

Modeling unavoidably requires identification of material parameters, most of which can hardly be measured experimentally[279] especially in operating conditions [280]. Severe procedures of calibration must be put in place in order to ensure that modeling indeed achieves predictive science capability. In this regard, computational modeling and simulations may take advantage of the most recent achievements in the fields of uncertainty quantification and sensitivity analysis.

Part I

Electrolyte

Chapter 2

Modeling saturation of species in battery electrolytes

2.1 Introduction

Consider an electrochemical cell with a binary ionic electrolyte (say LiX, where X can for instance be PF_6, consisting of two ions, a cation (Li^+) and an anion (X^-)). In the absence of convection, ions are transported by migration and diffusion across the electrolyte from one electrode to the other, to bring reactants to the interfaces so that electrochemical charge transfer reactions can take place. Modeling the kinetics of mobile ionic species in the electrolyte is thus required in order to perform predictive computational simulations of electrochemical cells.

Ionic species kinetics was recently considered in [55]. That paper presents a formulation based on: i) the mass continuity equation for the cations Li^+ and anions X^-, in terms of their concentrations c_{Li+} and c_{X-}; ii) Maxwell's equations, to model the evolution in time and space of the electric field, since ionic transport entails movement of mass as well as of charge. Electroneutrality was not used as a fundamental law and electro-magnetics was explicitly taken into account via the *electro-quasi-static* formulation [281] of Maxwell's equations. A one-dimensional application to ionic transport in Li-ion batteries electrolyte, inspired by [63], was performed.

While the outcome matches the results published in [63], it turned out that ionic concentrations near the electrodes can be higher than half of the *saturation limit* in the electrolyte solution. Therefore the usual and widespread simplified form of the chemical Helmholtz free energy density due to mixing of the species[1] does not seem to be suitable for commercial Li-ion batteries. The significant role played by the saturation contribution in the Helmholtz free energy density is therefore investigated in detail in this chapter.

Mass and force balance as well as Faraday's and Maxwell's equations are recalled briefly in Section 3.2. Balance laws are considered to be not affected by the saturation[2], i.e. there is no supply of species and the degree of dissociation of the binary salt in the solution is complete. The latter condition may not be satisfied in reality *when concentrations are close to the saturation limit*. In those cases it is known from literature that the degree of dissociation of Li-salts dissolved in an organic solvent is incomplete. Modeling the dissociation rate would require a bulk term in the mass balance equations and an additional mass balance equation for the undissociated salt [63]. The numerical analyses in [55] reveal that concentration peaks exceed 50% of the saturation limit. Concentrations are therefore too high to neglect the role of saturation but they are nevertheless sufficiently far from saturation to assume complete dissociation of the Li-salt.

A rigorous analysis of general principles of thermodynamics is performed in Section 3.3 following the approach described in [24, 276] for processes in thermal equilibrium. The entropy imbalance and the Coleman-Noll procedure provide thermodynamic restrictions which are satisfied by the usual Fickian description of diffusion and migration in terms of the electrochemical potential, as defined in [22, 23]. Dilute solutions have been implemented taking into account the saturation limit. The formulation does not consider mixing

---

[1] That was used implicitly in [63] and explicitly in [55].
[2] It mainly affects the constitutive equations.

with interactions (regular solutions) nor concentrated solutions (modeled by the Maxwell-Stefan equations of multicomponent diffusion - see appendix 2.B). Extension to those conditions, although out of the scope of the present contribution, appears to be straightforward.

A weak form of the governing equations, in the framework of small displacements and strains, has been derived in Section 3.6 in terms of the selected thermodynamic fields, namely concentrations, displacements, and the electric potential. A one-dimensional application to ionic transport in Li-ion batteries, inspired by [63], is performed thereafter. Results with and without saturation are compared, and the role of saturation is clearly identified.

2.2 Balance laws

2.2.1 Mass balance

The mass balance equation may be written as follows

$$\frac{\partial c_\alpha}{\partial t} + \text{div} \left[\vec{h}_\alpha \right] = 0 \,. \tag{2.1}$$

In this equation, c_α is the *molarity* (i.e. the number of moles per unit volume) of a generic species α; $\vec{h}_\alpha$ is the mass flux in terms of moles, i.e. the number of moles of species α measured per unit area per unit time. In the problem at hand, eq. (2.1) applies to ions Li^+ and X^-, i.e.

$$\frac{\partial c_{\text{Li}^+}}{\partial t} + \text{div} \left[\vec{h}_{\text{Li}^+} \right] = 0 \,, \tag{2.2a}$$

$$\frac{\partial c_{\text{X}^-}}{\partial t} + \text{div} \left[\vec{h}_{\text{X}^-} \right] = 0 \,. \tag{2.2b}$$

Concentrations are defined in space $\vec{x} \in V$ and time $0 \le t \le t_f$, i.e. $c_\alpha = c_\alpha(\vec{x}, t)$. Functional dependence however is specified when necessary only, to enhance readability.

2.2.2 Faraday's law

Charges in the electrolyte solution are transported by dissociated ions. Therefore, the charge density ζ is related to the concentration of ions, by the following identity

$$\zeta = F \sum_\alpha z_\alpha c_\alpha \,, \tag{2.3a}$$

$F = 96485.3383 \text{ C mol}^{-1}$ is Faraday's constant and z_α is the number of electrons transferred per ion α, typically $+1$ for Li^+ cations and -1 for X^- anions. The flux of mass in balance (2.1) of each species contributes to a current density $\vec{i}$ in view of Faraday's law of electrolysis

$$\vec{i} = F \sum_\alpha z_\alpha \vec{h}_\alpha = F \left(\vec{h}_{\text{Li}^+} - \vec{h}_{\text{X}^-} \right) \,. \tag{2.3b}$$

2.2.3 Maxwell's equations for electro-quasi-statics

Gauss's laws

$$\text{div} \left[\vec{D} \right] = \zeta \,, \tag{2.4}$$

$$\text{div} \left[\vec{B} \right] = 0 \,, \tag{2.5}$$

relate the electric displacement and magnetic fields ($\vec{D}$ and $\vec{B}$ respectively) emanating from a distribution of electric charge ζ. Maxwell-Faraday's law of induction describes the reciprocal interactions between magnetic and electric field $\vec{E}$, in the form

$$\text{curl} \left[\vec{E} \right] = -\frac{\partial \vec{B}}{\partial t} \,. \tag{2.6}$$

In view of (2.6), the electric field can be written in terms of a so-called "magnetic potential" $\vec{A}$ and of an electrostatic potential ϕ as

$$\vec{E} = -\nabla \left[\phi \right] - \frac{\partial \vec{A}}{\partial t} \,,$$

In the framework of electro-quasi-statics [281], assumed henceforth as an approximation of the full Maxwell's equations, the magnetic potential $\vec{A}$ is time-independent. Accordingly, the electric field is irrotational

$$\vec{E} = -\nabla \left[\phi \right] \,, \tag{2.7}$$

Finally, Ampère's law (with Maxwell's correction)

$$\frac{\partial \vec{D}}{\partial t} + \vec{i} = \mathrm{curl} \left[\vec{H} \right] \,, \tag{2.8}$$

relates the electrical current and the time variation of the electric displacement field to the *magnetizing field* $\vec{H}$. After application of the divergence operator and of Faraday's law (2.3b), the following equation results

$$\mathrm{div} \left[\frac{\partial \vec{D}}{\partial t} + F \left(\vec{h}_{\mathrm{Li}^+} - \vec{h}_{\mathrm{X}^-} \right) \right] = 0 \,, \tag{2.9}$$

Note that the effect of the latter in Ampère's law cannot be disregarded even in the simplified framework of electro-quasi-statics, see [68].

2.2.4 Balance of momentum

The usual balance of forces:

$$\mathrm{div} \left[\boldsymbol{\sigma} \right] + \vec{b} = \vec{0} \,, \tag{2.10}$$

and the symmetry of the stress tensor $\boldsymbol{\sigma}$ emanate from the principle of virtual power [24]. The electrostatic bulk force $\vec{b}_\zeta = \zeta \, (\vec{E} + \vec{v} \times \vec{B})$ characterizing the interaction of a moving charge density ζ with velocity $\vec{v}$ in an electric field $\vec{E}$ and magnetic field $\vec{B}$ enters balance equation (2.10). Those electrostatic forces are the only interactions between flowing ions and the hosting material. In view of of the electroneutrality assumption, see [55, 68], there is no coupling between flow and forces, i.e. $\vec{b}_\zeta \sim \vec{0}$. The balance of forces is taken henceforth as homogeneous

$$\mathrm{div} \left[\boldsymbol{\sigma} \right] = \vec{0} \,. \tag{2.11}$$

2.3 Thermodynamics

2.3.1 First law

The balance between the internal energy ($\mathcal{U}$) of a material region $\mathcal{P}$, the mechanical external power ($\mathcal{W}$) expended on $\mathcal{P}$, the heat transferred ($\mathcal{Q}$) in $\mathcal{P}$, and the power due to mass ($\mathcal{T}$) and electromagnetic ($\mathcal{E}$) interactions exchanged on $\mathcal{P}$ for the problem at hand, for *quasi-static interactions*, reads

$$\frac{\partial \mathcal{U}}{\partial t}(\mathcal{P}) = \mathcal{W}(\mathcal{P}) + \mathcal{Q}(\mathcal{P}) + \mathcal{T}(\mathcal{P}) + \mathcal{E}(\mathcal{P}) \,, \tag{2.12}$$

It is assumed that these processes occur with *their distinctive contributions* in the balance, in particular *the energies due to charges and mass transfer are additively treated* as two separate processes. The individual contributions are: i) a mechanical contribution due to body forces $\vec{b}$ and surface forces $\vec{p}$ that spend power against velocities $\vec{v}$;

$$\mathcal{W}(\mathcal{P}) = \int_{\mathcal{P}} \vec{b} \cdot \vec{v} \, \mathrm{d}\Omega + \int_{\partial \mathcal{P}} \vec{p} \cdot \vec{v} \, \mathrm{d}\Gamma \,, \tag{2.13a}$$

ii) a heat contribution where the scalar s_q is the heat supplied by external sources and $\vec{q}$ is the heat flux vector;

$$\mathcal{Q}(\mathcal{P}) \quad = \quad \int_{\mathcal{P}} s_q \, \mathrm{d}\Omega - \int_{\partial\mathcal{P}} \vec{q} \cdot \vec{n} \, \mathrm{d}\Gamma \,, \tag{2.13b}$$

iii) a mass flux contribution with the scalar μ denoting the *chemical* potential, the scalar s_α the supply of species ($\alpha = \mathrm{Li}^+, \mathrm{X}^-$) and $\vec{h}_\alpha$ the mass flux vector;

$$\mathcal{T}(\mathcal{P}) \quad = \quad \sum_\alpha \left\{ \int_{\mathcal{P}} \mu_\alpha \, s_\alpha \, \mathrm{d}\Omega - \int_{\partial\mathcal{P}} \mu_\alpha \, \vec{h}_\alpha \cdot \vec{n} \, \mathrm{d}\Gamma \right\} \,, \tag{2.13c}$$

iv) an electromagnetic contribution with the energy flux vector $\vec{E} \times \vec{H}$ generated by the electric and magnetizing fields[3].

$$\mathcal{E}(\mathcal{P}) \quad = \quad - \int_{\partial\mathcal{P}} (\vec{E} \times \vec{H}) \cdot \vec{n} \, \mathrm{d}\Gamma \,. \tag{2.13d}$$

A specific (per unit volume in the reference body, see [24]) internal energy u is usually defined as

$$\mathcal{U}(\mathcal{P}) = \int_{\mathcal{P}} u \, \mathrm{d}\Omega \,,$$

in order to write the local form of the first principle. Standard application of the divergence theorem and of mass balances (2.1) leads from (2.13) to

$$\mathcal{W}(\mathcal{P}) \quad = \quad \int_{\mathcal{P}} \boldsymbol{\sigma} : \frac{\partial \boldsymbol{\varepsilon}}{\partial t} \, \mathrm{d}\Omega \,, \tag{2.14a}$$

$$\mathcal{Q}(\mathcal{P}) \quad = \quad \int_{\mathcal{P}} s_q - \mathrm{div}\,[\vec{q}] \, \mathrm{d}\Omega \,, \tag{2.14b}$$

$$\mathcal{T}(\mathcal{P}) \quad = \quad \sum_\alpha \int_{\mathcal{P}} \mu_\alpha \frac{\partial c_\alpha}{\partial t} - \vec{h}_\alpha \cdot \nabla\,[\mu_\alpha] \, \mathrm{d}\Omega \,, \tag{2.14c}$$

$$\mathcal{E}(\mathcal{P}) \quad = \quad \int_{\mathcal{P}} \left(\frac{\partial \vec{D}}{\partial t} + \vec{\imath} \right) \cdot \vec{E} \, \mathrm{d}\Omega \,. \tag{2.14d}$$

The electromagnetic contribution (2.14d) comes out under the assumption of electro-quasi-statics and in view of Ampère's-Maxwell's law (2.8). Since the energy balance (2.12) must hold for all regions $\mathcal{P}$, the global energy balance (2.12) can be written in a so-called "local form" at any point $\vec{x} \in \mathcal{P}$

$$\frac{\partial u}{\partial t} = \boldsymbol{\sigma} : \frac{\partial \boldsymbol{\varepsilon}}{\partial t} + s_q - \mathrm{div}\,[\vec{q}] + \left(\frac{\partial \vec{D}}{\partial t} + \vec{\imath} \right) \cdot \vec{E} + \sum_\alpha \mu_\alpha \frac{\partial c_\alpha}{\partial t} - \vec{h}_\alpha \cdot \nabla\,[\mu_\alpha] \,. \tag{2.15}$$

A different form can be given to equation (2.15), in terms of the *electrochemical potential*

$$\overline{\mu}_\alpha = \mu_\alpha + F \, z_\alpha \, \phi \,. \tag{2.16}$$

It has been derived in [55] and summarized in Appendix 2.A for the sake of brevity. The internal energy u is written as a function of the state variables, namely the entropy η, the concentrations c_α, the electric displacement field $\vec{D}$, and the kinematic variables *in terms of the small strain* tensor $\boldsymbol{\varepsilon}$, i.e.

$$\frac{\partial u}{\partial t} = \frac{\partial u}{\partial \eta} \frac{\partial \eta}{\partial t} + \frac{\partial u}{\partial \boldsymbol{\varepsilon}} : \frac{\partial \boldsymbol{\varepsilon}}{\partial t} + \frac{\partial u}{\partial \vec{D}} \cdot \frac{\partial \vec{D}}{\partial t} + \sum_\alpha \frac{\partial u}{\partial c_\alpha} \frac{\partial c_\alpha}{\partial t} \,. \tag{2.17}$$

---

[3] $\vec{E} \times \vec{H}$ is an energy flux vector results from Poynting's theorem (see also [276, 22]).

$$\mathcal{E}(\mathcal{P}) \quad = \quad - \int_{\partial\mathcal{P}} (\vec{E} \times \vec{H}) \cdot \vec{n} \, \mathrm{d}\Gamma = - \int_{\mathcal{P}} \mathrm{div}\left[\vec{E} \times \vec{H} \right] \mathrm{d}\Omega = \int_{\mathcal{P}} \vec{H} \cdot \mathrm{curl}\left[\vec{E} \right] - \mathrm{curl}\left[\vec{H} \right] \cdot \vec{E} \, \mathrm{d}\Omega \,.$$

After substitution of the curls from Maxwell's equations, Poynting's theorem results.

2.3.2 Second law

A local form of the entropy imbalance can be derived from the Clausius-Duhem inequality in terms of the referential entropy η and of the absolute temperature T [24]

$$\frac{\partial \eta}{\partial t} - \frac{s_q}{T} + \mathrm{div} \left[\frac{\vec{q}}{T} \right] \geq 0 \,, \tag{2.18}$$

By noting that

$$\mathrm{div} \left[\frac{\vec{q}}{T} \right] = \frac{1}{T} \mathrm{div} \left[\vec{q} \right] - \frac{1}{T^2} \vec{q} \cdot \nabla \left[T \right] \,,$$

equation (2.18) can be expressed in terms of internal energy, exploiting equations (2.15) and (2.17). The entropy imbalance yields

$$\frac{\partial \eta}{\partial t} \left(T - \frac{\partial u}{\partial \eta} \right) + \frac{\partial \boldsymbol{\varepsilon}}{\partial t} : \left(\boldsymbol{\sigma} - \frac{\partial u}{\partial \boldsymbol{\varepsilon}} \right) + \frac{\partial \vec{D}}{\partial t} \cdot \left(\vec{E} - \frac{\partial u}{\partial \vec{D}} \right) + \sum_\alpha \frac{\partial c_\alpha}{\partial t} \left(\mu_\alpha - \frac{\partial u}{\partial c_\alpha} \right) +$$

$$+ \vec{i} \cdot \vec{E} - \sum_\alpha \vec{h}_\alpha \cdot \nabla \left[\mu_\alpha \right] - \frac{1}{T} \vec{q} \cdot \nabla \left[T \right] \geq 0 \,, \tag{2.19}$$

Term $\vec{i} \cdot \vec{E}$ is the Joule effect. In view of Faraday's law, straightforward algebra allows to write

$$\vec{i} \cdot \vec{E} - \sum_\alpha \vec{h}_\alpha \cdot \nabla \left[\mu_\alpha \right] = - \sum_\alpha \vec{h}_\alpha \cdot \nabla \left[\overline{\mu}_\alpha \right] \,,$$

taking into account (2.16).

By applying the Coleman-Noll procedure, inequality (2.19) must hold for all constitutive processes [24, 26], giving rise to the following thermodynamic restrictions

$$T - \frac{\partial u}{\partial \eta} = 0 \,, \qquad \boldsymbol{\sigma} - \frac{\partial u}{\partial \boldsymbol{\varepsilon}} = 0 \,, \qquad \mu_\alpha - \frac{\partial u}{\partial c_\alpha} = 0 \,, \qquad \vec{E} - \frac{\partial u}{\partial \vec{D}} = 0 \,,$$

$$\vec{h}_\alpha \cdot \nabla \left[\overline{\mu}_\alpha \right] \leq 0 \,, \qquad \frac{1}{T} \vec{q} \cdot \nabla \left[T \right] \leq 0 \,. \tag{2.20}$$

Different thermodynamic potentials can be considered rather than the internal energy u. A classical one is the specific *Helmholtz free energy*

$$\psi(T, \boldsymbol{\varepsilon}, c_\alpha, \vec{E}) = u(\eta, \boldsymbol{\varepsilon}, c_\alpha, \vec{D}) - T \, \eta - \vec{E} \cdot \vec{D} \,,$$

that will be used henceforth in the assumption of processes in thermal equilibrium. Thermodynamic restrictions then read

$$\boldsymbol{\sigma} - \frac{\partial \psi}{\partial \boldsymbol{\varepsilon}} = 0 \,, \qquad \mu_\alpha - \frac{\partial \psi}{\partial c_\alpha} = 0 \,, \qquad \vec{D} + \frac{\partial \psi}{\partial \vec{E}} = 0 \,, \qquad \vec{h}_\alpha \cdot \nabla \left[\overline{\mu}_\alpha \right] \leq 0 \,, \qquad \frac{1}{T} \vec{q} \cdot \nabla \left[T \right] \leq 0 \,. \tag{2.21}$$

2.4 Constitutive theory

The processes are taken to be thermodynamically uncoupled and the Helmholtz free energy density ψ is decomposed in three separate parts

$$\psi(\boldsymbol{\varepsilon}, c_\alpha, \vec{E}) = \psi_{diff}(c_\alpha) + \psi_{el}(\vec{E}) + \psi_{mech}(\boldsymbol{\varepsilon}) \,. \tag{2.22}$$

The mass transport process is described by ψ_{diff}, adopting species concentrations c_α, as the state variables. The contribution $\psi_{el}(\vec{E})$ models the electro-quasistatic interactions, in terms of the electric field $\vec{E}$. Finally, ψ_{mech} is the mechanical energy density, function of the deformation only through the history of the local value of the small strain tensor. Materials that are modeled by (2.22) are classified as *simple materials*.

The electric displacement field is taken to be linearly related to the electric field

$$\psi_{el}(\vec{E}) = -\frac{1}{2}\pitchfork \vec{E} \cdot \vec{E}\,, \qquad (2.23)$$

where

$$\vec{D} = \pitchfork \vec{E} = -\pitchfork \nabla[\phi]\,. \qquad (2.24)$$

The permittivity $\pitchfork$ of a homogeneous material is usually given relative to that of vacuum $\pitchfork_0 = 8.85 \times 10^{-12}\ \text{CV}^{-1}\text{m}^{-1}$, as a relative permittivity $\pitchfork_r$, i.e. $\pitchfork = \pitchfork_r\,\pitchfork_0$.

The electrostatic potential ϕ is the result of idealized electric charges moving from one electrode to the other, modeled by Fickian-diffusion that linearly correlates the mass flux of species α to the gradient of its *electrochemical* potential

$$\vec{h}_\alpha = -\boldsymbol{M}_\alpha \nabla[\bar{\mu}_\alpha]\,, \qquad (2.25)$$

by means of a positive definite mobility tensor $\boldsymbol{M}_\alpha$. Identity (2.25) satisfies thermodynamic restrictions (2.21).

A classical specialization of mobility tensor $\boldsymbol{M}_\alpha$ for *dilute solutions accounting for saturation* is the isotropic non linear case [251]

$$\boldsymbol{M}_\alpha(c_{\text{Li}^+}, c_{\text{X}^-}) = \pitchfork_\alpha\, c_\alpha\,(1 - \theta_{\text{Li}^+} - \theta_{\text{X}^-})\, \mathbb{1}\,, \qquad \alpha = \text{Li}^+, \text{X}^-\,. \qquad (2.26)$$

The amount $\pitchfork_\alpha > 0$ is usually termed the *ion mobility* and represents the average velocity of species α in the solution when acted upon by a force of 1 N/mol independent of the origin of the force[4]; θ_α is defined as the ratio $\theta_\alpha = \frac{c_\alpha}{c^{max}}$, where c^{max} stands for the cumulative saturation limit for ions Li$^+$ and X$^-$ in the solution, in condition of electroneutrality. Equation (2.26) represents the physical requirement that both the pure ($c_\alpha = 0$) and the saturated ($\theta_{\text{Li}^+} + \theta_{\text{X}^-} = 1$) phases have vanishing mobilities in the electrolyte. It can be seen as a special case of the Maxwell-Stefan approach (see Appendix 2.B). Exploiting the electroneutrality condition

$$c_{\text{Li}^+} - c_{\text{X}^-} = 0\,, \qquad (2.27)$$

discussed in [55], the specialization for the mobility tensor simplifies to

$$\boldsymbol{M}_\alpha(c_\alpha) = \pitchfork_\alpha\, c_\alpha\,\left(1 - 2\frac{c_\alpha}{c^{max}}\right)\, \mathbb{1}\,. \qquad (2.28)$$

The free energy $\psi_{diff}(c_\alpha)$ in a mixture depends on the composition of the mixture itself[5]. Guided by the numerical analyses in [55, 63], where it was shown that concentration peaks amount to about 50% of the saturation limit, the modeling assumption is here taken that *concentrations are sufficiently far from saturation to disregard energetic interactions in the solution yet not small enough to neglect the saturation contribution*. The free energy thus reads:

$$\psi_{diff}(c_{\text{Li}^+}, c_{\text{X}^-}) = \mu_{\text{Li}^+}^0\, c_{\text{Li}^+}\ + \mu_{\text{X}^-}^0\, c_{\text{X}^-}\ + RT\, c^{max}\,(\theta_{\text{Li}^+}\,\ln[\theta_{\text{Li}^+}] + \theta_{\text{X}^-}\,\ln[\theta_{\text{X}^-}]) \\ + RT\, c^{max}\,(1 - \theta_{\text{Li}^+} - \theta_{\text{X}^-})\,\ln[(1 - \theta_{\text{Li}^+} - \theta_{\text{X}^-})]\,. \qquad (2.29)$$

In formula above, R is the universal gas constant; μ_α^0 is a reference value of the chemical potential of diffusing species $\alpha = \text{Li}^+, \text{X}^-$. By exploiting electroneutrality (2.27), the chemical potential results in the form

$$\mu_\alpha = \mu_\alpha^0\ + RT\,\ln[\frac{c_\alpha}{c^{max} - 2c_\alpha}]\,, \qquad (2.30)$$

---

[4]As the free energy density ψ has been selected as the thermodynamic potential, no source of confusion between the ion mobility $\pitchfork_\alpha$ and the internal energy density u will arise henceforth.

[5]The case of diluted (in the sense of [22]) solutions will be considered henceforth whereas other theories will be summarized in Appendices.

thus leading to the following expression for the mass flux

$$\vec{h}_\alpha = -\mathbb{D}_\alpha \, \nabla\, [\, c_\alpha\,] - z_\alpha \, F \, \natural_\alpha \, c_\alpha \, \left(1 - 2\frac{c_\alpha}{c^{max}}\right) \, \nabla\, [\,\phi\,] \,. \tag{2.31}$$

$\mathbb{D}_\alpha$ is defined by $\mathbb{D}_\alpha = \natural_\alpha \, R\,T$ (this equation is sometimes termed after Nernst-Einstein).

By comparing (2.31) with the mass flux formula for infinitely diluted solutions

$$\vec{h}_\alpha = -\mathbb{D}_\alpha \, \nabla\, [\, c_\alpha\,] - z_\alpha \, F \, \natural_\alpha \, c_\alpha \, \nabla\, [\,\phi\,] \,, \tag{2.32}$$

one concludes that saturation has no effect on the diffusivity: in fact, the impact of saturation on the mobility tensor (2.28) and on the chemical potential (2.30) counteract each other in the evaluation of diffusivity[6]. Saturation does affect the electric contribution in the mass flux (2.31) by changing the mobility, thus creating either a lower mass flux at a given potential gradient or a higher potential gradient at a given flux.

The mechanical behavior of the separator/electrolyte system is taken isotropic, linear elastic

$$\psi_{mech}(\boldsymbol{\varepsilon}) = \frac{1}{2}\,\boldsymbol{\varepsilon} \,:\, \mathbb{C} \,:\, \boldsymbol{\varepsilon} = \frac{1}{2}\,\left(K \operatorname{tr}[\,\boldsymbol{\varepsilon}\,]^2 + 2G \,||\operatorname{dev}[\,\boldsymbol{\varepsilon}\,]\,||^2\right) \,,, \tag{2.33}$$

K, G are the bulk and shear modulus respectively. Symbol $\operatorname{tr}[\,-\,]$ denotes the trace operator whereas $\operatorname{dev}[\,-\,]$ is the deviator operator.

Thermodynamics restrictions (2.21) imply

$$\sigma = K \operatorname{tr}[\,\boldsymbol{\varepsilon}\,] \, \mathbb{1} + 2G \operatorname{dev}[\,\boldsymbol{\varepsilon}\,] \,. \tag{2.34}$$

2.5 Governing equations and weak form

Governing equations can be derived by incorporating constitutive equations (2.24), (2.31), and (2.34) into balance equations. The unknown fields result from the thermodynamic choices made. They are here the concentrations $c_{\mathrm{Li^+}}$, $c_{\mathrm{X^-}}$, displacements $\vec{u}$, and the electric potential ϕ. Governing equations hold at all points $\vec{x} \in V$ in all instants of interval $[0, t_f]$

$$\frac{\partial c_{\mathrm{Li^+}}}{\partial t} + \operatorname{div}\left[-\mathbb{D}_{\mathrm{Li^+}} \, \nabla\, [\, c_{\mathrm{Li^+}}\,] - F \, \natural_{\mathrm{Li^+}} \, c_{\mathrm{Li^+}} \, \left(1 - 2\frac{c_{\mathrm{Li^+}}}{c^{max}}\right) \, \nabla\, [\,\phi\,]\right] = 0\,, \tag{2.35a}$$

$$\frac{\partial c_{\mathrm{X^-}}}{\partial t} + \operatorname{div}\left[-\mathbb{D}_{\mathrm{X^-}} \, \nabla\, [\, c_{\mathrm{X^-}}\,] + F \, \natural_{\mathrm{X^-}} \, c_{\mathrm{X^-}} \, \left(1 - 2\frac{c_{\mathrm{X^-}}}{c^{max}}\right) \, \nabla\, [\,\phi\,]\right] = 0\,, \tag{2.35b}$$

$$\operatorname{div}\left[-\natural \, \nabla\left[\frac{\partial \phi}{\partial t}\right] + F \, (\mathbb{D}_{\mathrm{X^-}} \, \nabla\, [\, c_{\mathrm{X^-}}\,] - \mathbb{D}_{\mathrm{Li^+}} \, \nabla\, [\, c_{\mathrm{Li^+}}\,])\right] +$$
$$-F^2 \operatorname{div}\left[\left(\natural_{\mathrm{Li^+}} \, c_{\mathrm{Li^+}} \, \left(1 - 2\frac{c_{\mathrm{Li^+}}}{c^{max}}\right) + \natural_{\mathrm{X^-}} \, c_{\mathrm{X^-}} \, \left(1 - 2\frac{c_{\mathrm{X^-}}}{c^{max}}\right)\right) \, \nabla\, [\,\phi\,]\right] = 0\,, \tag{2.35c}$$

$$\operatorname{div}\left[\mathbb{C} \,:\, \boldsymbol{\varepsilon}\right] = \vec{0}\,. \tag{2.35d}$$

The difference between equations (2.31) and (2.32) makes this set of governing equations different from the one used in [55]. Boundary conditions

$$\vec{h}_{\mathrm{Li^+}} \cdot \vec{n} = -h_{BV} \qquad \vec{x} \in \partial^N V \tag{2.36a}$$

---

[6]The role played by the non linear mobility tensor and by the free energy density at saturation in Fick's law (2.31) is further investigated in appendix 2.C.

$$\vec{h}_{\mathrm{X}^-} \cdot \vec{n} = 0 \qquad \vec{x} \in \partial^N V \tag{2.36b}$$

$$\mathrm{curl}\left[\vec{H}\right] \cdot \vec{n} = -F\,h_{BV} \qquad \vec{x} \in \partial^N V\,, \tag{2.36c}$$

$$\boldsymbol{\sigma} \cdot \vec{n} = \vec{p} \qquad \vec{x} \in \partial^N V\,, \tag{2.36d}$$

are imposed along Neumann boundaries[7] $\partial^N V$. It is typical in batteries to fully impose Neumann conditions (2.36a) for concentration, in terms of mass fluxes, during galvanostatic processes. To complete the problem, Dirichlet boundary conditions have to be enforced along part $\partial^D V$, ($\partial V = \partial^D V \cup \partial^N V$). Rigid body motion inhibition and zero electric potential have to be included through Dirichlet boundary conditions.

Initial conditions are required for the concentration of ions $c_{\mathrm{Li}^+}(\vec{x}, t = 0)$ and $c_{\mathrm{X}^-}(\vec{x}, t = 0)$ in the electrolyte solution. As at time $t = 0$ thermodynamic equilibrium holds, concentrations are uniform and obey the electroneutrality condition (2.27) in volume V. Consistently, a positive constant c_{bulk} will be defined as

$$c_{bulk} = c_{\mathrm{Li}^+}(\vec{x}, t = 0) = c_{\mathrm{X}^-}(\vec{x}, t = 0)\,. \tag{2.37}$$

This constant will further be used to scale concentrations.

Initial conditions for electric potential and displacements define a boundary value problem at $t = 0$. In view of the perfect electroneutrality, Gauss law and balance of momentum provide the necessary and sufficient equations to be solved for ϕ and $\vec{u}$ at $t = 0$:

$$\mathrm{div}\left[\natural\,\nabla\left[\phi\right]\right] = 0 \qquad \vec{x} \in V,\ t = 0\,, \tag{2.38a}$$

$$\mathrm{div}\left[\mathbb{C} : \boldsymbol{\varepsilon}\right] = \vec{0} \qquad \vec{x} \in V,\ t = 0\,, \tag{2.38b}$$

together with the usual given boundary conditions for displacements and tractions and homogeneous boundary conditions for potential and current, in view of thermodynamic equilibrium at initial time.

The evolution problem can be formulated in a weak form by multiplying the governing equations (2.35) by a suitable set of test functions and performing an integration over the domain, exploiting Green's formula to reduce the order of differentiation. Adopting a Galerkin approach, weak forms are built using variations (denoted henceforth with symbol $\hat{\cdot}$) of the same variables that rule the problem, namely concentrations $\hat{c}_{\mathrm{Li}^+}$, $\hat{c}_{\mathrm{X}^-}$, displacements $\vec{\hat{u}}$, and electric potential $\hat{\phi}$. The following identities are derived straightforwardly

$$\frac{RT}{c_{bulk}} \int_V \hat{c}_{\mathrm{Li}^+}\ \left\{ \frac{\partial c_{\mathrm{Li}^+}}{\partial t} + \mathrm{div}\left[\vec{h}_{\mathrm{Li}^+}\right]\right\} \mathrm{d}V = \tag{2.39a}$$
$$\frac{RT}{c_{bulk}} \int_V \hat{c}_{\mathrm{Li}^+}\ \frac{\partial c_{\mathrm{Li}^+}}{\partial t}\ + \mathbb{D}_{\mathrm{Li}^+}\ \nabla\left[\hat{c}_{\mathrm{Li}^+}\right] \cdot \nabla\left[c_{\mathrm{Li}^+}\right] + F\,\natural_{\mathrm{Li}^+}\,c_{\mathrm{Li}^+}\ \left(1 - 2\frac{c_{\mathrm{Li}^+}}{c^{max}}\right)\ \nabla\left[\hat{c}_{\mathrm{Li}^+}\right] \cdot \nabla\left[\phi\right]\,\mathrm{d}V +$$
$$-\frac{RT}{c_{bulk}} \int_{\partial^N V} \hat{c}_{\mathrm{Li}^+}\ h_{BV}\ \mathrm{d}\Gamma = 0\,,$$

$$\frac{RT}{c_{bulk}} \int_V \hat{c}_{\mathrm{X}^-}\ \left\{ \frac{\partial c_{\mathrm{X}^-}}{\partial t} + \mathrm{div}\left[\vec{h}_{\mathrm{X}^-}\right]\right\} \mathrm{d}V = \tag{2.39b}$$
$$\frac{RT}{c_{bulk}} \int_V \hat{c}_{\mathrm{X}^-}\ \frac{\partial c_{\mathrm{X}^-}}{\partial t}\ + \mathbb{D}_{\mathrm{X}^-}\ \nabla\left[\hat{c}_{\mathrm{X}^-}\right] \cdot \nabla\left[c_{\mathrm{X}^-}\right] - F\,\natural_{\mathrm{X}^-}\,c_{\mathrm{X}^-}\ \left(1 - 2\frac{c_{\mathrm{X}^-}}{c^{max}}\right)\ \nabla\left[\hat{c}_{\mathrm{X}^-}\right] \cdot \nabla\left[\phi\right]\,\mathrm{d}V = 0\,,$$

$$\int_V \hat{\phi}\ \mathrm{div}\left[\frac{\partial \vec{D}}{\partial t} + F\left(\vec{h}_{\mathrm{Li}^+} - \vec{h}_{\mathrm{X}^-}\right)\right] \mathrm{d}V = \tag{2.39c}$$

---

[7]Boundary conditions (2.36a), (2.36c) and (2.36d) have been derived in Section 3.3 of [55]. Extension of Neumann boundaries are defined for each field and differ from field to field. In order to enlighten the notation the field dependence has not been specified in writing $\partial^N V$ and has been omitted. Same arguments apply to Dirichlet boundaries.

$$\int_V \nabla\left[\,\hat\phi\,\right] \cdot \left\{ \not\in \nabla\left[\frac{\partial\phi}{\partial t}\right] + F^2 \left(\mathbb{h}_{\mathrm{Li^+}}\, c_{\mathrm{Li^+}}\, \left(1 - 2\frac{c_{\mathrm{Li^+}}}{c^{max}}\right) + \mathbb{h}_{\mathrm{X^-}}\, c_{\mathrm{X^-}}\, \left(1 - 2\frac{c_{\mathrm{X^-}}}{c^{max}}\right) \right) \nabla\left[\phi\right] \right\}\,\mathrm{d}V +$$

$$- F \int_V \nabla\left[\,\hat\phi\,\right] \cdot (\mathbb{D}_{\mathrm{X^-}} \nabla\left[\,c_{\mathrm{X^-}}\,\right] - \mathbb{D}_{\mathrm{Li^+}} \nabla\left[\,c_{\mathrm{Li^+}}\,\right])\,\mathrm{d}V - F \int_{\partial^N V} \hat\phi\, h_{BV}\,\mathrm{d}\Gamma = 0\,,$$

$$-\frac{1}{\tau}\int_V \vec{\hat u} \cdot\ \mathrm{div}\left[\,\boldsymbol\sigma\,\right] \mathrm{d}V = \frac{1}{\tau}\int_V \hat{\boldsymbol\varepsilon}\ :\ \mathbb{C}\ :\ \boldsymbol\varepsilon\,\mathrm{d}V - \frac{1}{\tau}\int_{\partial^N V} \vec{\hat u}\cdot\ \overline p\,\mathrm{d}\Gamma = 0\,. \qquad (2.39\mathrm{d})$$

Boundary conditions (2.36a), (2.36c) and (2.36d) have been used. The mass balance equations (2.39a) has been scaled by coefficient $\frac{RT}{c_{bulk}}$, deriving from constitutive equation (2.30), to give to the new weak form the physical dimension of a power expenditure. For the same reason the balance of momentum (2.39d) has been divided by a time scale[8] coefficient τ.

Fields that govern the problem are scaled to make them dimensionless and of order one:

$$c_\alpha^* = \frac{c_\alpha}{c_{bulk}}, \qquad \phi^* = \frac{F}{RT}\,\phi, \qquad \vec u^* = \frac{\vec u}{L}\,, \qquad (2.40)$$

L stands for a given characteristic length. A dimensionless weak form can finally be given in a time interval $[0, t_f]$ as

Find $y^*(\vec x, t) \in \mathcal{V}^{[0,t_f]}$ such that

$$\frac{\mathrm{d}}{\mathrm{d}t}b^*\left(\hat y^*(\vec x), y^*(\vec x, t)\right) + a^*\left(\hat y^*(\vec x), y^*(\vec x, t)\right) = f^*(\hat y(\vec x)) \qquad \forall \hat y(\vec x) \in \mathcal{V}\,, \ (2.41)$$

where

$$b^*\left(\hat y^*(\vec x), y^*(\vec x, t)\right) = RT\, c_{bulk}\ \int_V \hat c_{\mathrm{Li^+}}^*\, c_{\mathrm{Li^+}}^* + \hat c_{\mathrm{X^-}}^*\, c_{\mathrm{X^-}}^*\,\mathrm{d}V + \not\in \left(\frac{RT}{F}\right)^2 \int_V \nabla\left[\,\hat\phi^*\,\right]\cdot\nabla\left[\,\phi^*\,\right]\,\mathrm{d}V\,,$$

$$a^*\left(\hat y^*(\vec x), y^*(\vec x, t)\right) =$$

$$RT\, c_{bulk}\, \mathbb{D}_{\mathrm{Li^+}}\ \int_V \nabla\left[\,\hat c_{\mathrm{Li^+}}^*\,\right]\cdot\nabla\left[\,c_{\mathrm{Li^+}}^*\,\right] + c_{\mathrm{Li^+}}^*\, \left(1 - 2\frac{c_{\mathrm{Li^+}}^*}{c_{max}^*}\right) \nabla\left[\,\hat c_{\mathrm{Li^+}}^*\,\right]\cdot\nabla\left[\,\phi^*\,\right]\mathrm{d}V +$$

$$RT\, c_{bulk}\, \mathbb{D}_{\mathrm{X^-}}\ \int_V \nabla\left[\,\hat c_{\mathrm{X^-}}^*\,\right]\cdot\nabla\left[\,c_{\mathrm{X^-}}^*\,\right] - c_{\mathrm{X^-}}^*\, \left(1 - 2\frac{c_{\mathrm{X^-}}^*}{c_{max}^*}\right) \nabla\left[\,\hat c_{\mathrm{X^-}}^*\,\right]\cdot\nabla\left[\,\phi^*\,\right]\mathrm{d}V +$$

$$RT\, c_{bulk}\, \mathbb{D}_{\mathrm{Li^+}}\ \int_V \nabla\left[\,\hat\phi^*\,\right]\cdot\nabla\left[\,\phi^*\,\right] \left(1 - 2\frac{c_{\mathrm{Li^+}}^*}{c_{max}^*}\right) c_{\mathrm{Li^+}}^* + \nabla\left[\,\hat\phi^*\,\right]\cdot\nabla\left[\,c_{\mathrm{Li^+}}^*\,\right]\,\mathrm{d}V +$$

$$RT\, c_{bulk}\, \mathbb{D}_{\mathrm{X^-}}\ \int_V \nabla\left[\,\hat\phi^*\,\right]\cdot\nabla\left[\,\phi^*\,\right] \left(1 - 2\frac{c_{\mathrm{X^-}}^*}{c_{max}^*}\right) c_{\mathrm{X^-}}^* - \nabla\left[\,\hat\phi^*\,\right]\cdot\nabla\left[\,c_{\mathrm{X^-}}^*\,\right]\,\mathrm{d}V +$$

$$\frac{L^2}{\tau}\ \int_V \hat{\boldsymbol\varepsilon}^*\ :\ \mathbb{C}\ :\ \boldsymbol\varepsilon^*\,\mathrm{d}V\,,$$

$$f^*(\hat y^*(\vec x)) = RT\ \int_{\partial^N V} (\hat\phi^* + \hat c_{\mathrm{Li^+}}^*)\, h_{BV}\,\mathrm{d}\Gamma + \frac{L}{\Delta t}\ \int_{\partial^N V} \vec{\hat u}^*\cdot\ \overline p\,\mathrm{d}\Gamma\,,$$

with $y^*(\vec x, t) = \{c_{\mathrm{Li^+}}^*, c_{\mathrm{X^-}}^*, \phi^*, \vec u^*\,\}$.

2.6 One-dimensional modeling of ionic transport in a fluid electrolyte

2.6.1 Description

A battery with a storage capacity of 720mAh is dealt with, see [55]. It undergoes a galvanostatic process of charge at different C-rates $(0.25, 0.5, 1, 2, \text{and } 4)$. The electrolyte is supposed to have a saturation limit

---

[8]In the simulations the time scale coefficient τ has been taken to be coincident with the finite difference time increment Δt.
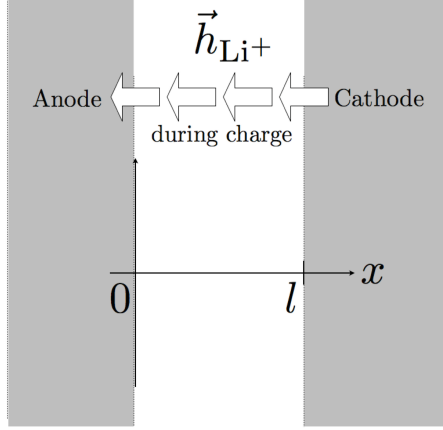
Figure 2.1: *A one-dimensional model of a Li-ion battery, with separator of size $l = 2.8 \times 10^{-4}$m. The flux of Li^+ ions during charge is indicated.*

for $LiPF_6$ of 5000mol m^{-3} (hence $c^{max} = 10^4 \text{mol m}^{-3}$). How saturation affects the battery performances is analyzed next. As in [63], mechanical effects are not taken into account. The charge/discharge process is assumed to be isothermal at $T = 25^o$C.

The current $I(t)$ (with t in seconds) is tuned in time as

$$I(t) = (1 - e^{-t}) I_{nC}, \tag{2.42}$$

I_{nC} stands for the steady current at a C-rate equal to n. The concentration of ions across the electrolyte is uniform at $t = 0$ and amounts to $c_{bulk} = 1500 \text{ mol m}^{-3}$. The flux of Lithium ions at the electrodes/separator interfaces (with net area $A = 2 \times 10^{-2} \text{m}^2$) is related to the given current $I(t)$ flowing through the battery.

A uniform ionic flow at the interfaces is considered, enabling a 1D description. Boundary conditions (2.36) thus read

$$h_{BV}|_{(x=0)}(t) = h_{BV}|_{(x=l)}(t) = -\frac{I(t)}{FA}, \tag{2.43a}$$

$$\vec{h}_{X^-} \cdot \vec{n}\Big|_{(x=0)}(t) = \vec{h}_{X^-} \cdot \vec{n}\Big|_{(x=l)}(t) = 0, \tag{2.43b}$$

- see also figure 2.1. From identity (2.42), the "steady" mass flux at $t \gg 0$ reads

$$h_{1C} = -\frac{I_{1C}}{FA},$$

Diffusivities are given by $\mathbb{D}_{Li^+} = 2 \times 10^{-11} \text{m}^2\text{s}^{-1}$, $\mathbb{D}_{PF_6^-} = 3 \times 10^{-11} \text{m}^2\text{s}^{-1}$.

The separator thickness is $l = 280 \mu$m. All data are taken from [63] except from the relative permittivity, taken equal to $\epsilon_r = 2.25$.

2.6.2 Discretization and time advancing by finite differences

Discretization is performed by separating variables, with spatial test $\varphi_i(x)$ and shape functions $\varphi_j(x)$ and nodal unknowns (collectively gathered in column y with component $y_j(t)$) that depend solely on time. The weak form (2.41) is then transformed in a first order Ordinary Differential Equation (ODE) in time[9], which reads:

$$\text{Find } y(t) \text{ s.t.} \qquad b_i^* \cdot \dot{y}(t) + a_i^* \cdot y(t) + {}^{sat}a_i^*[\, y(t) \,] = f_i^*(t) \qquad \text{for } i = 1, 2, ..., N \tag{2.44}$$

---

[9]As in Section 7 of [55] the star superscript is omitted from the definition of dimensionless quantities for the sake of readability: for example, in this section $c_j^{Li^+}$ stands for the j-th nodal unknown for Li-ions dimensionless concentration at time t. Furthermore, the usual Einstein summation convention is applied henceforth: when an index variable appears twice in a single term it implies summation of that term over all the values of the index.

Operators b_i^* and a_i^* are not influenced by the saturation of the electrolyte and coincide with those used in [55], given by

$$\frac{1}{RT\,c_{bulk}}\,b_i^*\cdot\frac{\partial y}{\partial t}(t) = \int_0^l \varphi_i^{\mathrm{Li}^+}\,\varphi_j^{\mathrm{Li}^+}\,\mathrm{d}x\,\frac{\partial c_j^{\mathrm{Li}^+}}{\partial t} + \int_0^l \varphi_i^{\mathrm{X}^-}\,\varphi_j^{\mathrm{X}^-}\,\mathrm{d}x\,\frac{\partial c_j^{\mathrm{X}^-}}{\partial t} + \frac{\oint}{c_{bulk}}\,\frac{RT}{F^2}\,\int_0^l \frac{\partial\varphi_i^\phi}{\partial x}\,\frac{\partial\varphi_j^\phi}{\partial x}\,\mathrm{d}x\,\frac{\partial\phi_j}{\partial t}\,,$$

$$\frac{a_i^*[\,y(t)\,]}{RT\,c_{bulk}} = \mathbb{D}_{\mathrm{Li}^+}\int_0^l \frac{\partial\varphi_i^{\mathrm{Li}^+}}{\partial x}\,\frac{\partial\varphi_j^{\mathrm{Li}^+}}{\partial x}\,\mathrm{d}x\,c_j^{\mathrm{Li}^+} + \mathbb{D}_{\mathrm{Li}^+}\int_0^l \varphi_j^{\mathrm{Li}^+}\,\frac{\partial\varphi_i^{\mathrm{Li}^+}}{\partial x}\,\frac{\partial\varphi_k^\phi}{\partial x}\,\mathrm{d}x\,c_j^{\mathrm{Li}^+}\,\phi_k +$$

$$\mathbb{D}_{\mathrm{X}^-}\int_0^l \frac{\partial\varphi_i^{\mathrm{X}^-}}{\partial x}\,\frac{\partial\varphi_j^{\mathrm{X}^-}}{\partial x}\,\mathrm{d}x\,c_j^{\mathrm{X}^-} - \mathbb{D}_{\mathrm{X}^-}\int_0^l \varphi_j^{\mathrm{X}^-}\,\frac{\partial\varphi_i^{\mathrm{X}^-}}{\partial x}\,\frac{\partial\varphi_k^\phi}{\partial x}\,\mathrm{d}x\,c_j^{\mathrm{X}^-}\,\phi_k +$$

$$\mathbb{D}_{\mathrm{Li}^+}\int_0^l \frac{\partial\varphi_i^\phi}{\partial x}\,\frac{\partial\varphi_k^\phi}{\partial x}\,\varphi_j^{\mathrm{Li}^+}\,\mathrm{d}x\,c_j^{\mathrm{Li}^+}\,\phi_k + \mathbb{D}_{\mathrm{Li}^+}\int_0^l \frac{\partial\varphi_i^\phi}{\partial x}\,\frac{\partial\varphi_j^{\mathrm{Li}^+}}{\partial x}\,\mathrm{d}x\,c_j^{\mathrm{Li}^+} +$$

$$\mathbb{D}_{\mathrm{X}^-}\int_0^l \frac{\partial\varphi_i^\phi}{\partial x}\,\frac{\partial\varphi_k^\phi}{\partial x}\,\varphi_j^{\mathrm{X}^-}\,\mathrm{d}x\,c_j^{\mathrm{X}^-}\,\phi_k - \mathbb{D}_{\mathrm{X}^-}\int_0^l \frac{\partial\varphi_i^\phi}{\partial x}\,\frac{\partial\varphi_j^{\mathrm{X}^-}}{\partial x}\,\mathrm{d}x\,c_j^{\mathrm{X}^-}\,,$$

$$\frac{f_i^*(t)}{RT\,c_{bulk}} = \frac{1}{c_{bulk}}\int_{\partial^N V}(\varphi_i^\phi + \varphi_i^{\mathrm{Li}^+})\,h_{BV}\,\mathrm{d}\Gamma\,,$$

The non linear form $^{sat}a_i^*[\,y(t)\,]$ on the contrary, contains the saturation contributions (not accounted for in [55]). It reads

$$\frac{^{sat}a_i^*[\,y(t)\,]}{RT\,c_{bulk}} = \mathbb{D}_{\mathrm{Li}^+}\int_0^l \varphi_j^{\mathrm{Li}^+}\,c_j^{\mathrm{Li}^+}\left(-\frac{2}{c_{max}}\,\varphi_n^{\mathrm{Li}^+}\,c_n^{\mathrm{Li}^+}\right)\frac{\partial\varphi_i^{\mathrm{Li}^+}}{\partial x}\,\frac{\partial\varphi_k^\phi}{\partial x}\,\phi_k\,\mathrm{d}x +$$

$$+\,\mathbb{D}_{\mathrm{Li}^+}\int_0^l \varphi_j^{\mathrm{Li}^+}\,c_j^{\mathrm{Li}^+}\left(-\frac{2}{c_{max}}\,\varphi_n^{\mathrm{Li}^+}\,c_n^{\mathrm{Li}^+}\right)\frac{\partial\varphi_i^\phi}{\partial x}\,\frac{\partial\varphi_k^\phi}{\partial x}\,\phi_k\,\mathrm{d}x +$$

$$-\,\mathbb{D}_{\mathrm{X}^-}\int_0^l \varphi_j^{\mathrm{X}^-}\,c_j^{\mathrm{X}^-}\left(-\frac{2}{c_{max}}\,\varphi_n^{\mathrm{X}^-}\,c_n^{\mathrm{X}^-}\right)\frac{\partial\varphi_i^{\mathrm{X}^-}}{\partial x}\,\frac{\partial\varphi_k^\phi}{\partial x}\,\phi_k\,\mathrm{d}x +$$

$$+\,\mathbb{D}_{\mathrm{X}^-}\int_0^l \varphi_j^{\mathrm{X}^-}\,c_j^{\mathrm{X}^-}\left(-\frac{2}{c_{max}}\,\varphi_n^{\mathrm{X}^-}\,c_n^{\mathrm{X}^-}\right)\frac{\partial\varphi_i^\phi}{\partial x}\,\frac{\partial\varphi_k^\phi}{\partial x}\,\phi_k\,\mathrm{d}x\,,$$

A family of time-advancing methods based on the so-called θ-scheme can be set up for the discrete problem (2.44). In the numerical simulations that follows, the backward Euler scheme ($\theta = 1$) has been selected, thus seeking for $y(t + \Delta t)$ such that

$$b_i^*\cdot\frac{y(t+\Delta t)}{\Delta t} + a_i^*\cdot y(t+\Delta t) + {}^{sat}a_i^*[\,y(t+\Delta t)\,] = f_i^*(t+\Delta t) + b_i^*\cdot\frac{y(t)}{\Delta t}\,, \qquad (2.45)$$

As in [55], a *Newton-Raphson* scheme has been implemented to solve the non-linear problem (2.45).

2.6.3 Simulations

Charge process simulations have been carried out with different C-rates. An anti-symmetric ionic concentration profile arises in the electrolyte, initiated at the bulk concentration c_{bulk} that reflects thermodynamic equilibrium at time $t = 0$. Such a feature, emerged in [55] at a unit C-rate, is clearly envisaged also at different charging speeds, as emphasized in Figure 2.2. Either when C-rates are high (say 2 or more), or when the charge duration allows to reach a steady-state configuration at moderate C-rates (say about 1), the concentration near the electrodes are close to the limit concentration $c_{\mathrm{Li}^+} = 0$ at one side and close to the symmetric concentration $c_{\mathrm{Li}^+} = 2c_{bulk}$ at the other electrode. The latter concentration is higher than half of the saturation limit of the Li salt in the electrolyte solvent.

a) C-rate = 0.25, $t_f = 1000$s

b) C-rate = 1, $t_f = 1000$s

c) C-rate = 4, $t_f = 54$s

d)

e)
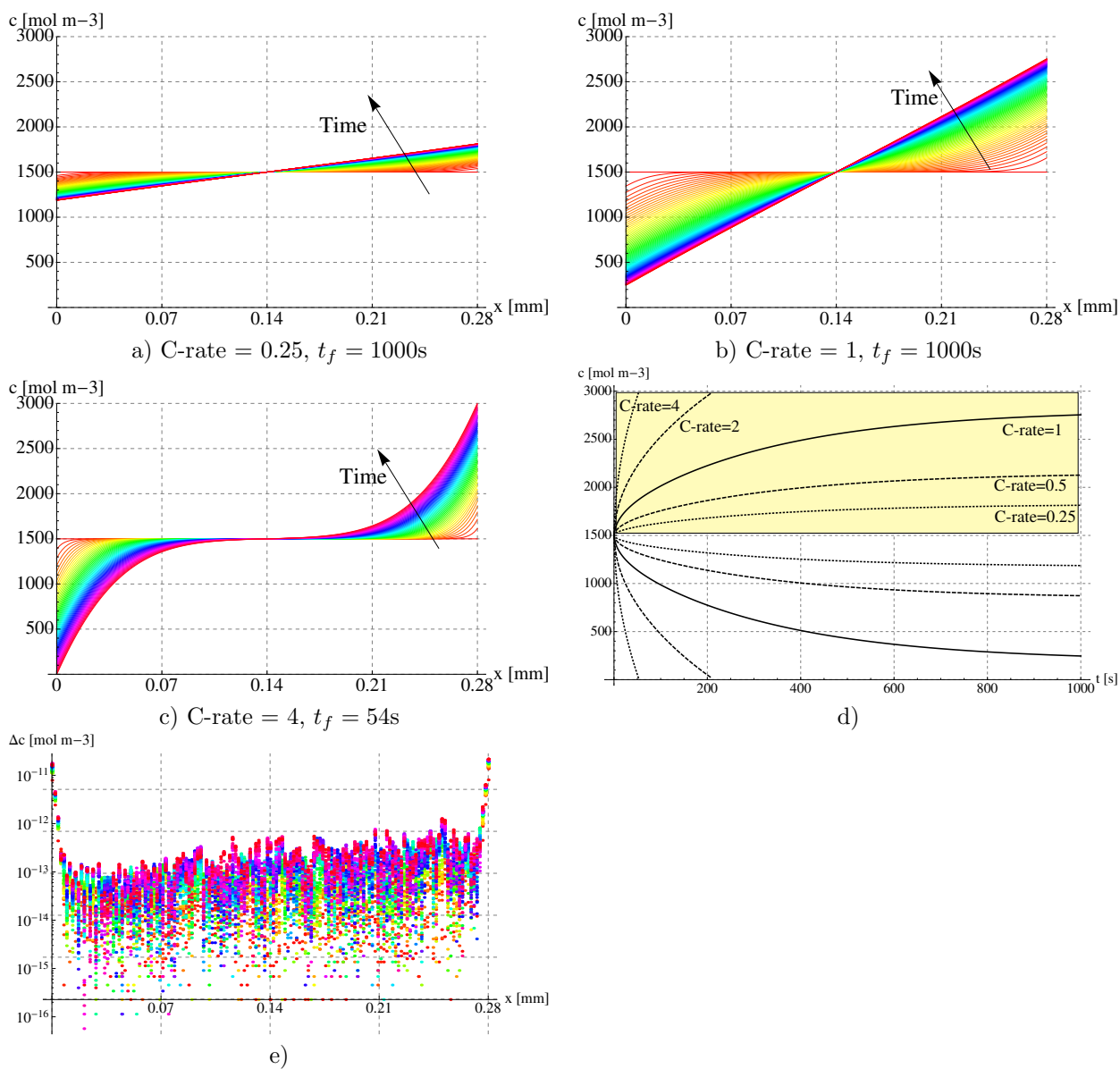
Figure 2.2: *Concentration plots. a-c) Lithium ions concentration profiles $c_{\mathrm{Li}^+}(x,t)$ at different C-rates. In all cases the concentration at the initial time equals c_{bulk}, thus satisfying thermodynamic equilibrium. For high C-rates, the steady state configuration cannot be attained, since the limit condition of vanishing concentration at an electrode is reached earlier. d) Concentration profiles with saturation for a galvanostatic process at different C-rates at Cathode (upper, shadowed area) and Anode. For C-rates greater or equal to 2 the limit condition of vanishing concentration at an electrode is reached and the steady state conditions cannot be attained. e) Scattering of the absolute value of the difference in concentration along the electrolyte between the solutions with and without saturation for a galvanostatic process at unit C-rate. Different colors indicate different times.*

Several numerical analyses were performed to investigate the influence of spatial and temporal discretization. The results for 150 equal finite elements and a constant time step of 1 second are here given. At the initial time the electric potential follows equations (2.38) and has to be homogeneous for thermodynamic equilibrium with no current nor mass flow.

$$\phi(\vec{x}, 0) = 0 \qquad \vec{x} \in V, \tag{2.46}$$

After a "sufficiently long" time, the steady state configuration has been approximated at C-rates less than 2. Analyses at higher C-rates end prematurely before achieving the steady state configuration, because the limit concentration $c_{\text{Li}^+} = 0$ was reached at the Anode. In particular, for C-rate=2 the final time was $t_f = 210$s, whereas for C-rate=4 the analyses have been terminated at $t_f = 54$s. Concentration profiles in the presence of saturation at different C-rates are represented in figure 2.2-d. The upper part of the figure, which is shadowed, refers to the Cathode, where concentration of Li$^+$ ions increase during charge processes. The lowest part refers to the Anode. The concentration profiles are symmetric with respect to the bulk concentration $c_{bulk} = 1500 \text{mol m}^{-3}$. As shown in [55] for a unit C-rate, the steady state asymptotic behavior is recovered well, but steady state concentrations have not been represented to the sake of readability.

Denote with $c_{\text{Li}^+}^{nosat}(x, t)$ the solution for the Li-ions concentration under the assumption far from saturation - i.e. assuming $c^{max} \to \infty$ in governing equations (2.35) - and with $c_{\text{Li}^+}(x, t)$ the solution for the Li-ions concentration of governing equations (2.35) with $c^{max} = 10^4 \text{mol m}^{-3}$. Figure 2.2-e depicts the absolute difference in concentration $\Delta c(x, t)$ between the solutions with and without saturation

$$\Delta c(x, t) = |c_{\text{Li}^+}(x, t) - c_{\text{Li}^+}^{nosat}(x, t)|,$$

along the electrolyte $0 \le x \le 0.28$mm for a galvanostatic process at a unit C-rate. Similar profiles result for other C-rates. The difference ranges between $10^{-15} < \Delta c(x, t) < 10^{-12}$ mol m^{-3} depending on time $0 \le t \le t_f = 1000$s. It can be assessed from figure 2.2 that ionic concentrations are in the order of 10^3mol m^{-3} along the electrolyte in the whole time frame. Accordingly, the influence of the saturation on concentrations is negligible. This effect is attributed to electroneutrality.

As the deviation from electroneutrality is small, see discussions in [55], the analysis that follows provides an acceptable rationale to the observed independence of ionic concentrations upon saturation. Consider mass balance equations (2.35a) and (2.35b), here rewritten when electroneutrality (2.27) applies[10]

$$\frac{\partial c}{\partial t} + \text{div}\left[-\mathbb{D}_{\text{Li}^+} \nabla[c] - F \mathbb{h}_{\text{Li}^+} c \left(1 - 2\frac{c}{c^{max}}\right) \nabla[\phi]\right] = 0, \tag{2.47a}$$

$$\frac{\partial c}{\partial t} + \text{div}\left[-\mathbb{D}_{\text{X}^-} \nabla[c] + F \mathbb{h}_{\text{X}^-} c \left(1 - 2\frac{c}{c^{max}}\right) \nabla[\phi]\right] = 0. \tag{2.47b}$$

By multiplying the Li$^+$ balance equation with the ion mobility $\mathbb{h}_{\text{X}^-}$ and the X$^-$ balance equation with the ion mobility $\mathbb{h}_{\text{Li}^+}$ the two equations (2.47) can be added, leading to

$$(\mathbb{h}_{\text{X}^-} + \mathbb{h}_{\text{Li}^+})\frac{\partial c}{\partial t} - 2RT(\mathbb{h}_{\text{X}^-} * \mathbb{h}_{\text{Li}^+}) \Delta[c] = 0. \tag{2.48}$$

Ionic concentrations in the assumption of electroneutrality are therefore independent upon c^{max}. Indeed, equation (2.48) can be derived without taking into account the saturation in Fick's law (2.31).

Denote with $\phi_{nosat}(x, t)$ the solution for the electric potential when concentrations are far from saturation - i.e. assuming $c^{max} \to \infty$ in governing equations (2.35) - and with $\phi(x, t)$ the solution for the electric potential of governing equations (2.35) with $c^{max} = 10000 \text{mol m}^{-3}$. Electric potential profiles at the Cathode in the presence of saturation or without saturation at different C-rates are represented in figure 2.3.

Figure 2.4 depicts the evolution in time of the difference

$$\Delta\phi(x, t) = \phi(x, t) - \phi_{nosat}(x, t),$$

---

[10]implying $c_{\text{Li}^+} = c_{\text{X}^-} = c$
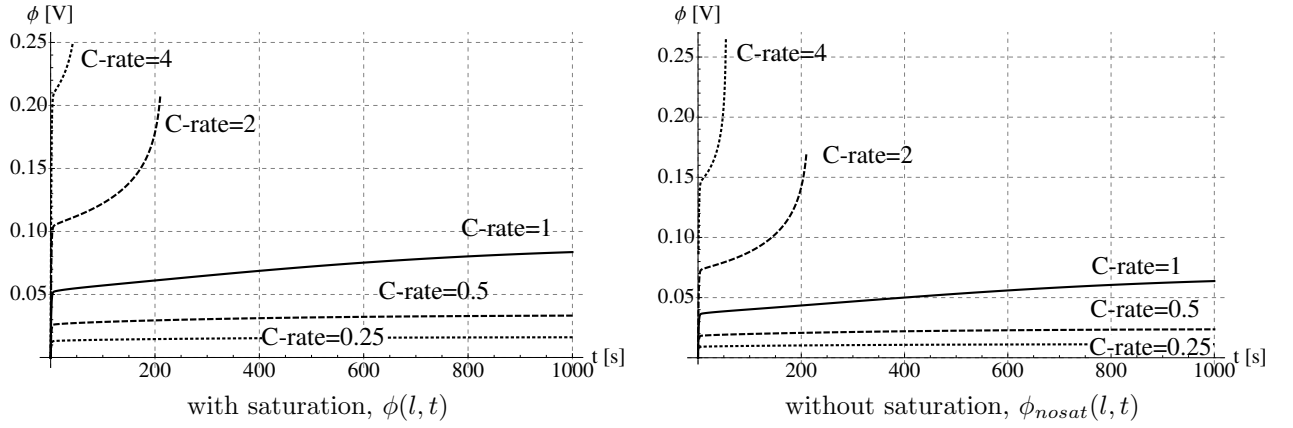
Figure 2.3: *Potential profile with and without saturation for a galvanostatic process at different C-rates at Cathode. The electric potential at the Anode is arbitrarily set to zero.*

in the electric potential $\phi(x)$. The picture clearly shows that saturation does influence the electric potential and that the difference increases with time for all C-rates. Having set the potential to be zero at the anode, this conclusion was theoretically predicted in Section 2.4, since saturation constitutively affects the electric contribution in the mass flux (2.31) by changing the mobility, thus creating a higher potential gradient in galvanostatic processes.

The relative difference

$$\Delta\phi(x,t) \times \phi_{nosat}^{-1}(x,t)\,,$$

is plotted in Figure 2.5. The latter shows that the saturation increases the electric potential by about 40% near the cathode for all C-rates. This effect appears to be more pronounced at small C-rates, when concentrations may not be as close to the saturation limit at the end of the analysis t_f as they are for high C-rates.

According to the Clausius-Planck inequality, the *Internal Entropy Production* (shortened in IEP) cannot be negative. Following the approach of rational thermodynamics of Coleman and Noll, it can be written as:

$$IEP(x,t) = -\frac{1}{T} \sum_{\alpha} \vec{h}_{\alpha} \cdot \nabla\left[\overline{\mu}_{\alpha}\right] \geq 0\,. \tag{2.49}$$

for isothermal processes with no inelastic mechanical effects. Substituting Fick's law (2.25) and the mobility (2.28) in (2.49), the total internal entropy production equals

$$\frac{1}{T} \sum_{\alpha} \int_0^{t_f} \int_0^L \frac{1}{\natural_{\alpha}\, c_{\alpha} \left(1 - 2\frac{c_{\alpha}}{c^{max}}\right)} \vec{h}_{\alpha} \cdot \vec{h}_{\alpha} \;\mathrm{d}x\mathrm{d}t\,, \tag{2.50}$$

with $\vec{h}_{\alpha}$ as in equation (2.31). Integration over time can be approximated in every time step by means of a trapezoidal rule. Furthermore, having used linear shape functions to approximate the concentration and potential fields, gradients are constant in each finite element. The scalar product $\vec{h}_{\alpha} \cdot \vec{h}_{\alpha}$ turns out to be a polynomial of degree four in the space variable x, which is trivially integrated. The integral

$$\frac{1}{T} \int_0^t \int_0^L \frac{1}{\natural_{\alpha}\, c_{\alpha} \left(1 - 2\frac{c_{\alpha}}{c^{max}}\right)} \vec{h}_{\alpha} \cdot \vec{h}_{\alpha} \;\mathrm{d}x\mathrm{d}\tau\,, \tag{2.51}$$

is plotted in Figure 2.6 as a function of time t. It represents the buildup of internally generated entropy for Li^+ (continuous curve) and for PF_6^- (dashed curve), respectively, at different C-rates in the presence of saturation. At low C-rates, the flux of ions PF_6^- abates with time (see Figure 5 in [55]) and the slope of the
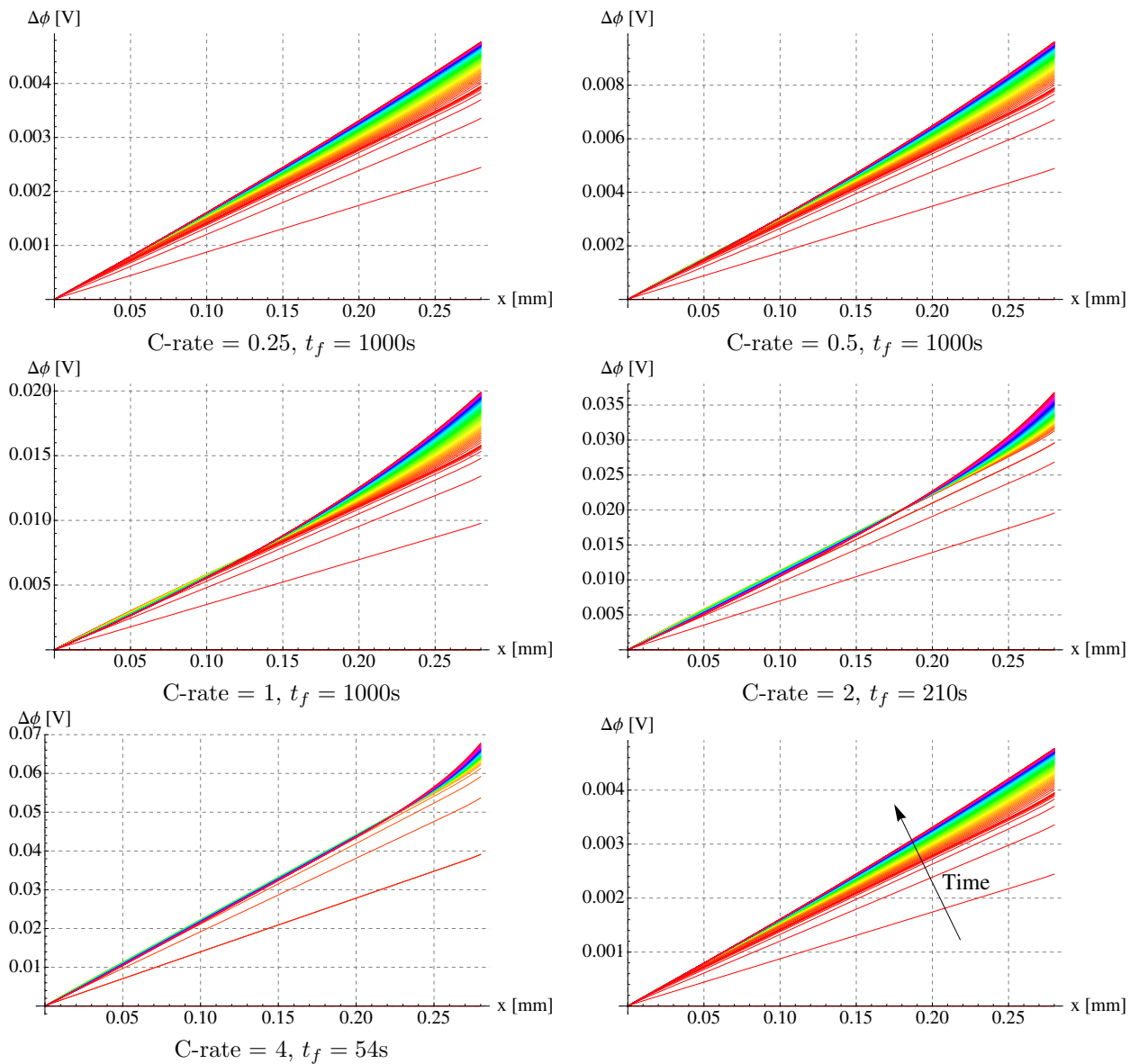
Figure 2.4: *Evolution in time of the difference* $\Delta\phi(x,t) = \phi(x,t) - \phi_{nosat}(x,t)$ *for several C-rates. The trend of the evolution in time is also depicted.*
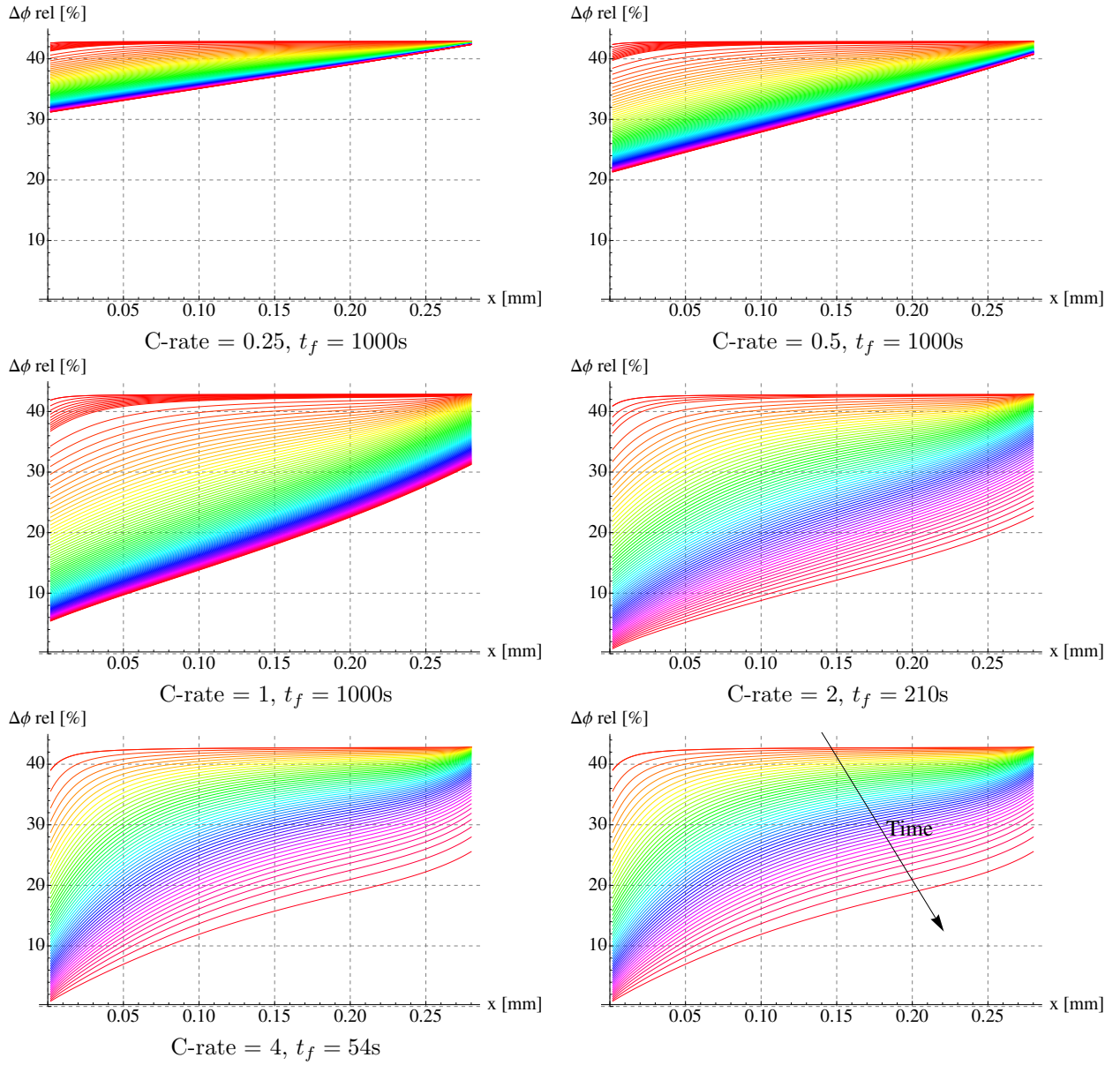
Figure 2.5: *Evolution in time of the ratio* $\Delta\phi(x,t) \times \phi_{nosat}^{-1}(x,t)$ *for several C-rates. The trend of the evolution in time is also depicted.*

IEP gets flatter and flatter with time[11]. Similarly, the flux of ions Li^+ tends to a constant while approaching the steady state conditions. The two effects combined induce a linear trend with time for the IEP at low C-rates. A similar behavior would be expected at higher C-rates, but the limit concentration is reached well before the steady state configuration.

Figure 2.7 compares the total IEP (2.50) with and without saturation. The increment of internally generated entropy due to the saturation is in the order of 40% of the unsaturated electrolyte IEP . The higher the C-rate the higher the rate of internally generated entropy. Nevertheless, as the limit concentration is reached at high charge rates, one cannot conclude that the total accumulation of IEP is larger at high C-rates.

---

[11]The flux near the electrode interfaces is dictated by the boundary conditions. The closer the regions to the electrodes the faster they reach the steady state - see Figure 5 in [55]). As discussed in [63] the Li^+ ionic current is mainly carried by migration at the beginning of the charging process, while under steady-state conditions diffusion and migrations contribute equally. The anionic mass flux reaches its peak rapidly, and once the steady state is approached, the flux of PF_6^- tends to vanish, and no contribution is provided further to the overall ionic conductivity.
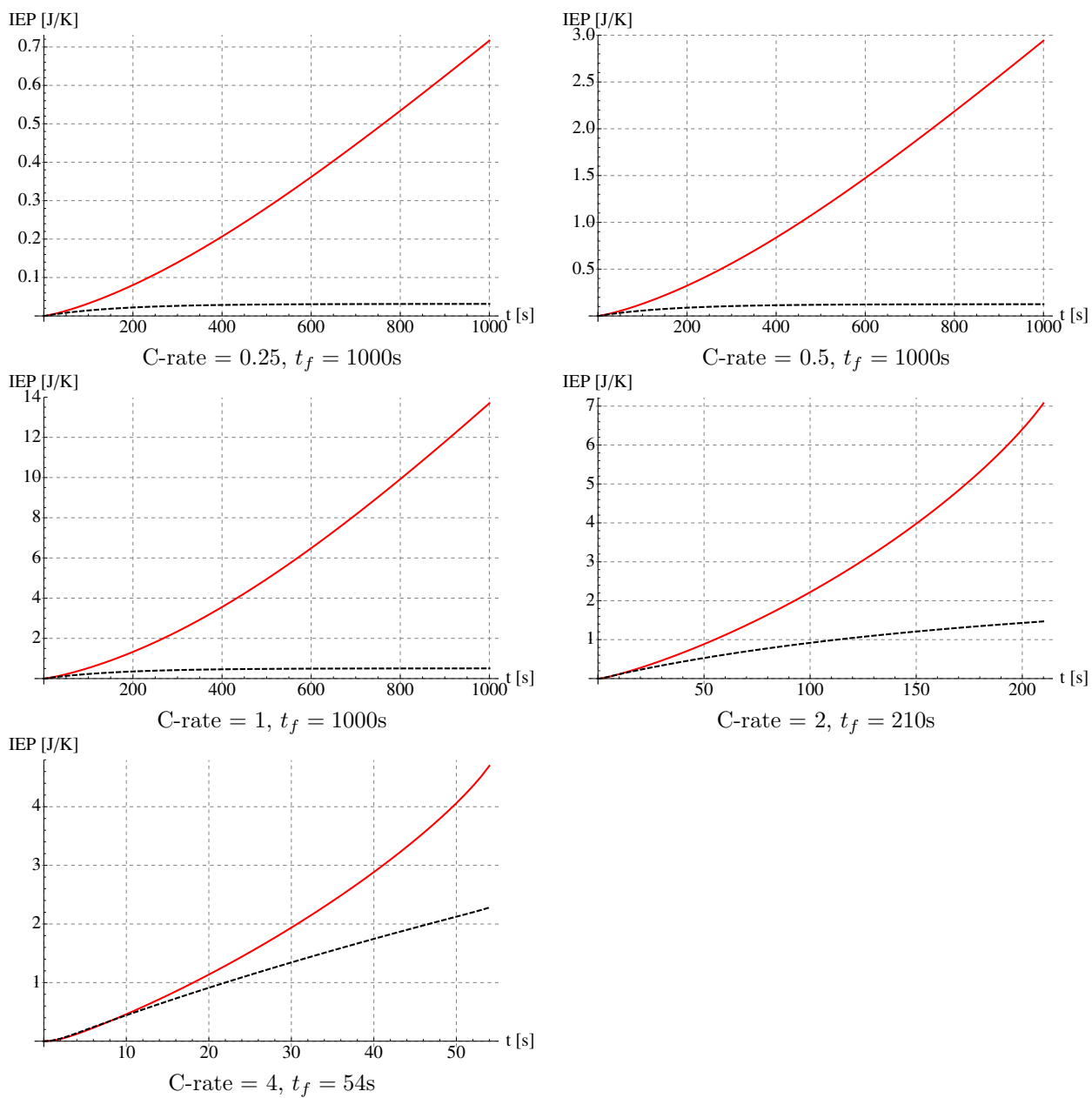
Figure 2.6: *Buildup of internally generated entropy for* Li^+ *(continuous curve) and for* PF_6^- *(dashed curve) at different C-rates in the presence of saturation.*
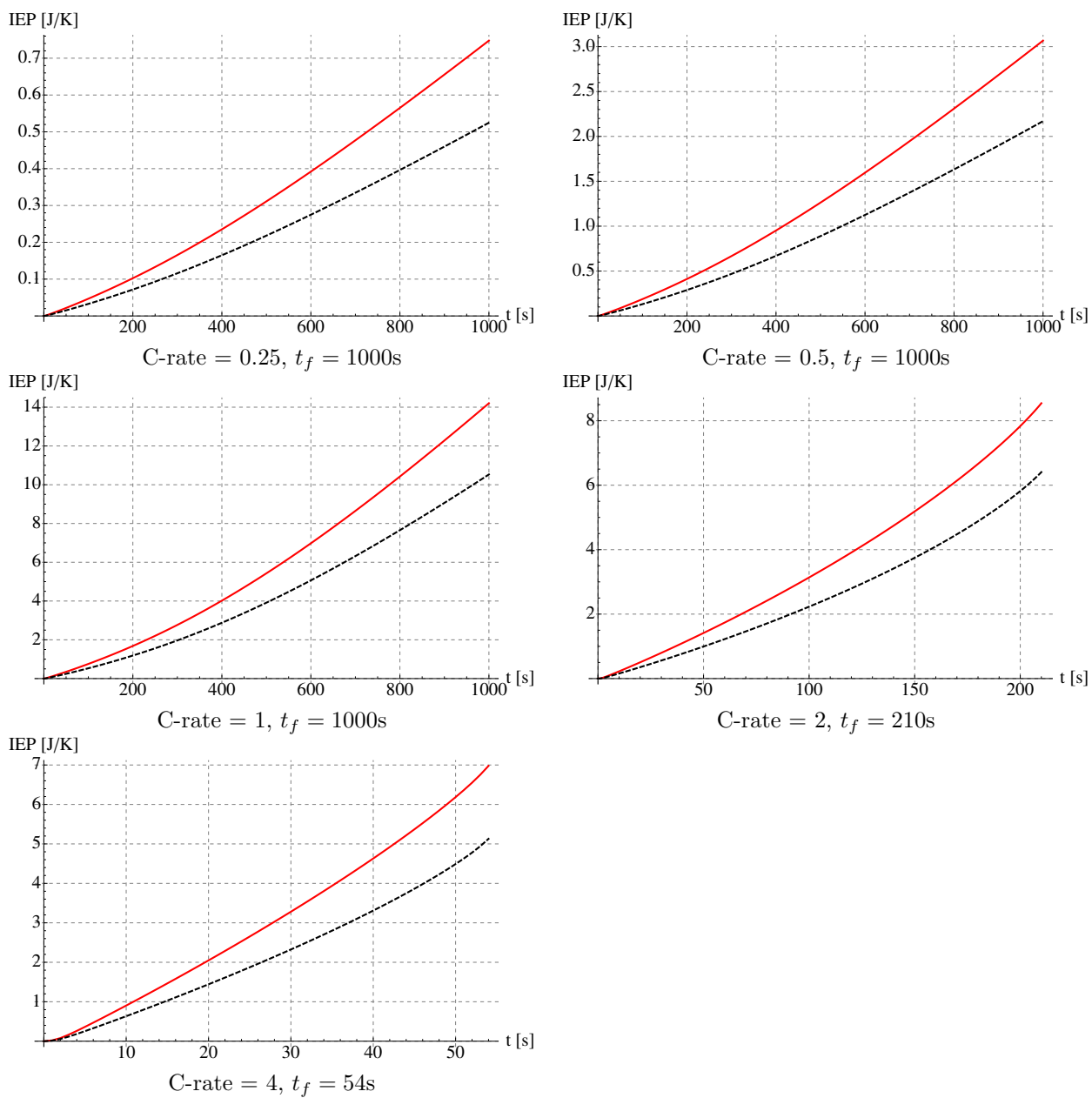
Figure 2.7: *Total internal entropy production (2.50) with (continuous curve) and without (dashed curve) saturation.*

2.7   Conclusions

In [55], ionic conductivity was modeled with the final aim of using computational simulations as a predictive tool in energy storage electrochemistry. A novel formulation was proposed, stemming from Maxwell's equations in their electro-quasi-static form instead of the classical condition of electroneutrality. From the thermodynamic standpoint, ideal solutions far from saturation were used underlying the constitutive theory for diffusion and migration processes. As shown in Section 2.6.3, ionic concentrations in real batteries can be higher than half of the saturation limit of the Li salt in the electrolyte solvent. Accordingly, the assumption of ideal solutions far from saturation can be questioned.

The present study investigated this assumption, for the case where concentrations are too high to neglect the role of saturation but still sufficiently low to exclude incomplete dissociation of the Li-salt. This conjecture is confirmed by the data and the numerical simulations on real batteries.

The adopted constitutive specifications (2.31) account for the saturation contribution. By comparing it with the mass flux constitutive equation adopted in [55], here reprinted in formula (2.32), one notices that saturation has no effect on the diffusivity. Under the assumption of electroneutrality, it can be assessed that saturation does not impact the concentration profiles either. In fact, the electroneutrality condition (2.27) is well approximated during the simulations and the influence of saturation on the concentration profiles is actually negligible - see Figure 2.2-e.

Saturation does however affect the electric potential in view of the mass flux equation (2.31) because it modifies the ionic mobility, inducing a higher potential gradient as shown in the simulations. Figures 2.4, 2.5 confirm that the saturation may increase the electric potential by about 40% near the cathode for all C-rates. Saturation influences the internal entropy production to a similar extent, as conveyed in Figures 2.6, 2.7.

In conclusion, saturation appears to be an essential ingredient in a multi scale and multi physics approach for battery modeling [68, 67]. Furthermore, the fully three-dimensional formulation that was proposed in [55] and the numerical algorithms that emanate from the weak form established therein have shown to be robust and capable of incorporating the new constitutive specifications, as required to account for the saturation.

Appendix

2.A   Electrochemical potential

The electromagnetic contribution (2.14) to the energy balance can be given a different expression in the framework of electro-quasi-statics, keeping in mind that charges are conveyed together with mass and thus the processes of migration and diffusion are coupled. The link between the two processes is Faraday's laws of electrolysis (2.3). Exploiting them and Gauss's law (2.4), (2.14) becomes

$$
\begin{aligned}
\mathcal{E}(\mathcal{P}) &= -\int_{\mathcal{P}} \frac{\partial \vec{D}}{\partial t} \cdot \nabla\,[\,\phi\,] + \vec{\imath} \cdot \nabla\,[\,\phi\,]\ \mathrm{d}\Omega \\[2mm]
&= -\int_{\mathcal{P}} \mathrm{div}\left[\,\phi\,\frac{\partial \vec{D}}{\partial t}\,\right] - \phi\,\mathrm{div}\left[\,\frac{\partial \vec{D}}{\partial t}\,\right] + F\sum_{\alpha} z_{\alpha}\,\vec{h}_{\alpha} \cdot \nabla\,[\,\phi\,]\ \mathrm{d}\Omega \\[2mm]
&= \int_{\mathcal{P}} \phi\,\frac{\partial \zeta}{\partial t} - \sum_{\alpha}\,(F\,z_{\alpha}\,\nabla\,[\,\phi\,])\cdot \vec{h}_{\alpha}\ \mathrm{d}\Omega - \int_{\partial\mathcal{P}} \phi\,\frac{\partial \vec{D}}{\partial t}\cdot \vec{n}\ \mathrm{d}\Gamma \\[2mm]
&= \sum_{\alpha}\int_{\mathcal{P}} (F\,z_{\alpha}\,\phi)\,\frac{\partial c_{\alpha}}{\partial t} - (F\,z_{\alpha}\,\nabla\,[\,\phi\,])\cdot \vec{h}_{\alpha}\ \mathrm{d}\Omega - \int_{\partial\mathcal{P}} \phi\,\frac{\partial \vec{D}}{\partial t}\cdot \vec{n}\ \mathrm{d}\Gamma\,.
\end{aligned}
\tag{2.52}
$$

From (2.14, 2.52), the power expenditure due to mass transfer and electromagnetic interactions specialize in the electrolyte as

$$
\mathcal{T}(\mathcal{P}) + \mathcal{E}(\mathcal{P}) = \sum_{\alpha}\int_{\mathcal{P}} (\mu_{\alpha} + F\,z_{\alpha}\,\phi)\,\frac{\partial c_{\alpha}}{\partial t} - \vec{h}_{\alpha}\,\cdot\,\nabla\,[\,\mu_{\alpha} + F\,z_{\alpha}\,\phi\,]\ \mathrm{d}\Omega - \int_{\partial\mathcal{P}} \phi\,\frac{\partial \vec{D}}{\partial t}\cdot \vec{n}\ \mathrm{d}\Gamma\,.
\tag{2.53}
$$

In the absence of charged species, only diffusion takes place; the relevant constitutive theory can be found in [24], section 66. In its dual way, in the absence of gradients of chemical potential, diffusion cannot proceed and current is thus driven by migration only. When diffusion is present, a current density appears due to Faraday's law and both processes contribute to the charge flux. It is therefore clear that concentration gradients and electric field act contemporarily to generate ion mobility. This is the intimate nature of the energy contribution (2.53) and of the electrochemical potential $\overline{\mu}_{\alpha}$ that in light of (2.53) will be *defined by the decomposition*

$$
\overline{\mu}_{\alpha} = \mu_{\alpha} + F\,z_{\alpha}\,\phi\,,
\tag{2.54}
$$

- see also [22], chapter XIII, section 3.4, formula (42). Accordingly, the local form of the first principle in terms of rates of the referential internal energy u reads also

$$
\frac{\partial u}{\partial t} = \boldsymbol{\sigma} : \frac{\partial \boldsymbol{\varepsilon}}{\partial t} + s_q - \mathrm{div}\,[\,\vec{q}\,] - \mathrm{div}\left[\,\phi\,\frac{\partial \vec{D}}{\partial t}\,\right] + \sum_{\alpha} \overline{\mu}_{\alpha}\,\frac{\partial c_{\alpha}}{\partial t} - \vec{h}_{\alpha}\cdot\nabla\,[\,\overline{\mu}\,._{\alpha}\,]\,.
\tag{2.55}
$$

2.B   Concentrated solutions

According to Ficks law (2.25) there is no influence of other phases on the flux of species α, i.e. cross-effects are ignored although they may appear in reality. To account for interactions between phases, the

standard approach [193] within the theory of Irreversible Thermodynamics replaces Fickian fluxes by linear combinations of the gradients of all involved electrochemical potentials. In the case of binary electrodes

$$\vec{h}_\alpha = -\sum_{\beta=1}^{2} \boldsymbol{M}_{\alpha\beta}(c_1, c_2)\, \nabla\left[\overline{\mu}_\beta\right] \qquad \alpha = 1,2\,. \tag{2.56}$$

Mobility tensors $\boldsymbol{M}_{\alpha\beta}(c_1, c_2)$ on turn depend on the concentration of all phases. A classical specialization of such mobility tensors is an isotropic choice

$$\boldsymbol{M}_{\alpha\beta}(c_1, c_2) = M_{\alpha\beta}(c_1, c_2)\, c_\alpha\, \mathbb{1}\,,$$

whereas linearity is not usually assumed for $M_{\alpha\beta}(c_1, c_2)$. The full matrix of mobility coefficients $M_{\alpha\beta}$ has to be positive semi-definite in order to be consistent with thermodynamic restriction (2.21) and symmetric due to the Onsager reciprocal relations. The approach that provides specifications for $M_{\alpha\beta}$ is usually known as the Maxwell-Stefan approach [192].

2.C   Steady state solutions

The porous electrode theory developed by Newman and coworkers [64] stems from the mass balance equation (2.2) and from electroneutrality condition

$$c_{\mathrm{Li}^+} = c_{\mathrm{X}^-} = c\,.$$

It is straightforward to derive equation (2.48) which is independent of the electric potential, even in the case of saturation as modeled via Fick's law (2.31). At steady state, the laplacian vanishes thus leading to a linear form $c_\infty(x) = ax + b$ for the concentration in 1D problems. The two parameters a and b can be determined by imposing the galvanostatic flux h_{1C} at $x = 0$ and by imposing the mass conservation through time, namely

$$\int_0^l c(x,t)\mathrm{d}x = \int_0^l c(x,0)\mathrm{d}x\ ,\,$$

which at steady state leads to

$$a\frac{l^2}{2} + b\,l = c_{bulk}\, l\,,$$

and finally to the steady state concentration

$$c_\infty(x) = c_{bulk} - \frac{h_{1C}}{2\mathbb{D}_{\mathrm{LI}^+}}\left(x - \frac{l}{2}\right). \tag{2.57}$$

The steady state solution is useful to envisage the role played by the non linear mobility tensor and by the free energy density at saturation in Fick's law (2.31). If one, for instance, takes the linear isotropic mobility tensor

$$\boldsymbol{M}_\alpha(c_\alpha) = \mathbb{m}_\alpha\, c_\alpha\, \mathbb{1}\,, \tag{2.58}$$

together with the ideal solution model (2.29), the mass balance equation (2.48) restated in 1D reads

$$(\mathbb{m}_{\mathrm{X}^-} + \mathbb{m}_{\mathrm{Li}^+})\frac{\partial c}{\partial t} - 2RT\, \mathbb{m}_{\mathrm{X}^-}\, \mathbb{m}_{\mathrm{Li}^+}\, \left\{f(c)\, \Delta\left[c\right] + f'(c)\,(c'(x))^2\right\} = 0\,, \tag{2.59}$$

having defined

$$f(c) = 1 + \frac{c}{c^{max}}\frac{2}{1 - 2\frac{c}{c^{max}}}\,.$$

At steady state, one is left with a non linear ordinary differential equation

$$f(c)\, \Delta\left[c\right] + f'(c)\,(c'(x))^2 = 0\,,$$

41
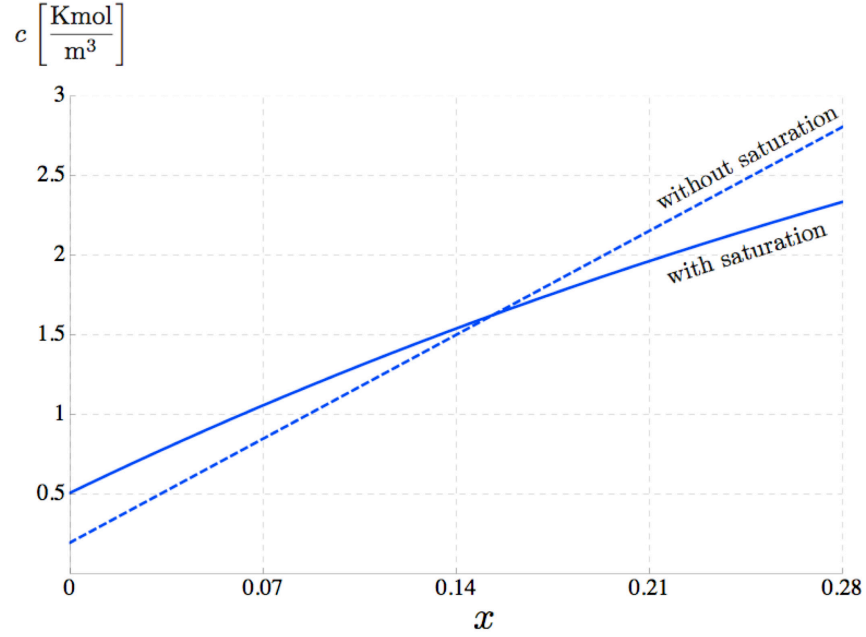
Figure 2.C.1: The effect of the saturation within the free energy density favors the diffusion into the electrolyte and reduces the concentration and the concentration gradient at the electrodes.

which admits the following solution

$$c_\infty(x) = \frac{e^{2a(b+x)} + a\ c^{max}}{2a} \ ,$$

with parameters a and b to be evaluated again by imposing the galvanostatic flux h_{1C} at $x = 0$ and by imposing the mass conservation through time. The effect of the saturation within the free energy density is clearly envisaged in figure 2.C.1. It corresponds to a higher diffusivity, in turn dependent upon the concentration, which favors the diffusion into the electrolyte and decreases both the concentration at the electrodes and the concentration gradient within the electrolyte. On the contrary, the non linear isotropic mobility tensor itself causes a decrease of the diffusivity, with opposite effects. Indeed, they cancel out in the final Fick's law (2.31).

Part II

Active Particles

Chapter 3

Modeling chemo-thermo-mechanical processes with trapping

3.1 Introduction

Several multi-disciplinary applications involve mass transport - driven by diffusion, migration or both - coupled with chemo-thermo-mechanics. In many cases, only a fraction of the total available mass of mobile species is effectively transported, whereas a significant counterpart remains immobilized by specific phenomena occuring concurrently with transport, i.e. trapping. Some examples clarify this concept.

One example is when metals are exposed to hydrogen gas, typically in storage tanks, and H atoms diffuse within the crystalline structure of the metal [282, 283, 284, 285, 286, 287, 288, 289]. H is found then not only in interstitial lattice sites, but also in defects such as vacancies, dislocations, grain boundaries, second-phase particle boundaries, and voids. Since such trapping of H in defects is energetically favorable, the mean residence time of diffusing hydrogen atoms is significantly longer in defects than in interstitial lattice sites. Furthermore, hydrogen free defects are filled very rapidly.

In electrochemical energy storage the fundamental mechanism of charge-discharge is the motion of ions between two electrodes. Particularly in Li-ion batteries, insertion of ions in active particles often alters the crystal structure of the particle itself, leading to a core-shell configuration with one segment, e.g. the shell in the case of insertion, rich in lithium with a sharp interface that separates it from a pristine inner core [243, 290, 259, 291, 292, 233]. Formation of chemical bonds between guest and host atoms allows alloying of lithium ions with the host matrix, transforming its initial crystal structure. Either fully reversible or not upon delithiation, those chemical reactions immobilize lithium ions, i.e. trap them, and make them unavailable for further diffusion in the storage particle.

We note that in addition to the examples described above, vacancies in metals, dendritic growth, solid propellant, bio-electrochemistry, solute solidification, and moisture diffusion in polymer nanocomposites provide additional examples of diffusion with trapping.

We do not model interface trap phenomena explicitly as was done by Torquato [264], as we use the *network* model of Larche and Cahn [227] instead. Thus it is assumed that the lattice sites of the hosting material form a network within which guest atoms can diffuse. In contrast, trap sites are taken to be isolated from one another and, hence, trapped atoms are immobilized within their specific trap.

Trapping of guest atoms is a kinetic process involving chemical and physical reactions described by the mass action law, set in a well-established thermodynamic framework [22, 23]. Deviation from stoichiometry in a solid composition can occur due to diffusion, and alloying reactions may cause large degrees of swelling that, when constrained, lead to mechanical stress. Such mechanical effects influence all other processes, since all chemo-transport-thermo-mechanical processes are coupled. These interactions are accounted for in this chapter, within a rigorous thermodynamic setting [24, 26] in the simple framework of small strains.

The chapter is organized as follows. Balance equations for conservation of mass, linear and angular momentum, energy, and entropy are introduced in Sections 3.2 and 3.3. Thermodynamic restrictions arise as

usual from the Curie symmetry principle and from the Coleman-Noll procedure. Subsequently in section 3.4 constitutive theory provides consistent phenomenological specifications for heat and mass fluxes, mechanical stress, as well as for the evolution of inelastic processes. Coupling of chemical kinetics to all other processes is analyzed in Section 3.5, pinpointing when phenomena can be categorized as not rate limiting and therefore modeled as infinitely fast. Governing Equations are finally summarized in Section 3.6.

3.2   Balance laws

Most species transport models consider the effect of hydrostatic stress and trapping on the species distribution in an inelastically deforming hosting material, assuming that species diffuse through lattice sites and that trap sites are filled via species diffusion. Only saturable and reversible traps are considered, such as dislocation cores. They are assumed to be isolated, in the sense that they do not form an extended network, and so do not present a continuous path for lattice diffusion. For this reason, some of the species flowing across the boundary $\partial \mathcal{P}$ of any subpart $\mathcal{P}$ of the body under investigation enters traps in the bulk and thus cease to contribute to species transport. The flux of species $\vec{h}$ is assumed to be purely interstitial lattice diffusion (and termed $\vec{h}_L$ from now on[1]), following Larchè and Cahn [227, 228].

3.2.1   Mass balance

The trapping process of a generic species, denoted henceforth with H, is described as a chemical reaction,

$$\text{H}_L \underset{k_L}{\overset{k_T}{\rightleftarrows}} \text{H}_T \ , \tag{3.1}$$

which portrays the conversion of mobile to trapped species and vice-versa by the rate of the reaction (3.1), denoted with $w^{(3.1)}$. Reaction (3.1) is unbalanced during species diffusion and interstitial species H_L is either made available or trapped. The mass balance equations yield

$$\frac{\partial c_L}{\partial t} + \text{div}\left[\vec{h}_L\right] + w^{(3.1)} = s_L \ , \tag{3.2a}$$

$$\frac{\partial c_T}{\partial t} - w^{(3.1)} = s_T \ . \tag{3.2b}$$

Symbols in equations (3.2) have the following meaning: c_β (with $\beta = L, T$) is the *molarity* (i.e. the number of moles per unit volume) of a generic species H_β; t is time; $\vec{h}_\beta$ is the mass flux in terms of moles, i.e. the number of moles of species H_β measured per unit area per unit time; s_L is the rate in moles per unit volume per unit time at which lattice species is generated by sources, and s_T is that for trapped species. Concentrations c_β are defined in space and time, i.e. $c_\beta = c_\beta(\vec{x}, t)$. The same holds for $\vec{h}_L$, $w^{(3.1)}$, s_β. Functional dependence however is specified when necessary only, to favor readability. It is assumed that trapped species are immobile since traps are isolated. Therefore, a mass flux term is absent in Eq. (3.2b).

3.2.2   Balance of momentum

The usual balance of forces

$$\text{div}\left[\,\boldsymbol{\sigma}\,\right] + \vec{b} = \vec{0} \tag{3.3}$$

holds, where $\boldsymbol{\sigma}$ is the stress tensor, $\vec{b}$ is the body force per unit volume, and we have assumed inertia forces to be negligible. The symmetry of the stress tensor follows from the balance of angular momentum [24].

3.2.3   Weak form and boundary conditions

The weak formulation of balance equations (3.2-3.3) results from multiplication by a suitable set of test functions - here denoted with a superposed carat - and from an integration upon the domain, exploiting

---

[1]Henceforth the subscript L refers to lattice (interstitial) sites and the subscript T to trap sites.

Green's formula to reduce the order of differentiation. Consider the mass balance Eq.(3.2-a)

$$\int_V \hat{\mu}_L \left\{ \frac{\partial c_L}{\partial t} + \text{div}\left[\vec{h}_L \right] + w^{(3.1)} - s_L \right\} dV =$$

(3.4)

$$= \int_V \hat{\mu}_L \frac{\partial c_L}{\partial t} dV + \int_V \text{div}\left[\hat{\mu}_L \vec{h}_L \right] - \nabla\left[\hat{\mu}_L \right] \cdot \vec{h}_L \, dV + \int_V \hat{\mu}_L \left(w^{(3.1)} - s_L \right) dV$$

$$= \int_V \hat{\mu}_L \frac{\partial c_L}{\partial t} dV - \int_V \nabla\left[\hat{\mu}_L \right] \cdot \vec{h}_L \, dV + \int_V \hat{\mu}_L \left(w^{(3.1)} - s_L \right) dV + \int_{\partial V} \hat{\mu}_L \vec{h}_L \cdot \vec{n} \, d\Gamma = 0 \ .$$

Within (3.4) a contribution is defined on the boundary ∂V, which has outward unit normal $\vec{n}$. It is unusual to know a priori the mass flux through the boundary. It is rather more natural to impose thermodynamic equilibrium between external and internal species at the domain boundary[2]. Nevertheless, for the sake of completeness, boundary conditions will be written as

$$\vec{h}_L \cdot \vec{n} = \overline{h} \qquad \vec{x} \in \partial^N V \ .$$

(3.5a)

The weak form of Eq. (3.2b) can be derived simply as

$$\int_V \hat{\mu}_T \left\{ \frac{\partial c_T}{\partial t} - w^{(3.1)} - s_T \right\} dV = 0 \ .$$

(3.6)

Finally, for the equilibrium equations (3.3) one writes the principle of virtual work as

$$\int_V -\hat{\boldsymbol{\varepsilon}} : \boldsymbol{\sigma} + \vec{\hat{u}} \cdot \vec{b} \, dV + \int_{\partial V} \vec{\hat{u}} \cdot \boldsymbol{\sigma} \cdot \vec{n} \, d\Gamma = 0 \ .$$

(3.7)

The given tractions along the Neumann part of the boundary $\partial^N V$ will be denoted with $\vec{p}$

$$\boldsymbol{\sigma} \cdot \vec{n} = \vec{p} \qquad \vec{x} \in \partial^N V \ .$$

(3.8)

A Dirichlet boundary condition (usually homogeneous) for the displacements is added along the Dirichlet part $\partial^D V$.

In conclusion, the weak form of the balance equations can be written in the time interval $[0, t_f]$ as

$$\text{Find } y \in \mathcal{V}^{[0,t_f]} \text{ such that} \qquad \frac{\partial}{\partial t} b\left(\hat{y}, z(t) \right) + a(\hat{y}, y(t)) = f(\hat{y}) \qquad \forall \hat{y} \in \mathcal{V}$$

(3.9)

where

$$b\left(\hat{y}, z \right) = \int_V \hat{\mu}_L c_L + \hat{\mu}_T c_T \, dV \ ,$$

$$a\left(\hat{y}, y \right) = -\int_V \nabla\left[\hat{\mu}_L \right] \cdot \vec{h}_L \, dV + \int_V \hat{\boldsymbol{\varepsilon}} : \boldsymbol{\sigma} \, dV + \int_V \left(\hat{\mu}_L - \hat{\mu}_T \right) w^{(3.1)} \, dV \ ,$$

$$f\left(\hat{y} \right) = -\int_{\partial^N V} \hat{\mu}_L \overline{h} \, d\Gamma + \int_{\partial^N V} \vec{\hat{u}} \cdot \vec{p} \, d\Gamma + \int_V \vec{\hat{u}} \cdot \vec{b} \, dV + \int_V \hat{\mu}_L s_L + \hat{\mu}_T s_T \, dV \ ,$$

with $z = \{ c_L, c_T \}$, $y = \{ \mu_L, \mu_T, \vec{u} \}$. Columns z and y collect the time-dependent unknown fields. Column $\hat{y}$ collects the steady-state test functions that correspond to the unknown fields in y.

To computationally solve the (either weak or strong) problem, constitutive equations must be specified, which is the subject of section 3.3. Ellipticity of the operators, functional and numerical properties of the solution and of its approximation depend on the constitutive assumptions and on the choice of the correct functional spaces $\mathcal{V}^{[0,t_f]}, \mathcal{V}$. However the identification of these spaces falls beyond the scope of the present work.

The weak form (3.9) acquires the usual physical meaning of power expenditure: for this reason the selection of the shape functions has been made in terms of chemical potentials $\hat{\mu}$ rather than concentrations.

---

[2]See also section 3.C to this aim. Note that the extent of Neumann boundaries are defined for each field and differ from field to field. In order to enlighten the notation however the field dependence has not been specified in writing $\partial^N V$ and has been left implicit. The same arguments apply to Dirichlet boundaries.

3.3 Thermodynamics

3.3.1 Energy balance

Denote with $\mathcal{B} \in \mathbb{R}^3$ the spatial domain of problem (3.2, 3.3). Consider an arbitrary material region $\mathcal{P} \subset \mathcal{B}$, which is taken as non-convecting. The first law of thermodynamics represents the balance of the interplay among the internal energy of $\mathcal{P}$, the power expended on $\mathcal{P}$, the heat transferred in $\mathcal{P}$, and the power due to mass exchanged on $\mathcal{P}$. The energy balance for the problem at hand, for *quasi-static interactions*, reads

$$\frac{\mathrm{d}\mathcal{U}}{\mathrm{d}t}(\mathcal{P}) = \mathcal{W}_u(\mathcal{P}) + \mathcal{Q}_u(\mathcal{P}) + \mathcal{T}_u(\mathcal{P}) \,, \tag{3.10}$$

with $\mathcal{U}$ the net internal energy of $\mathcal{P}$, $\mathcal{W}_u$ the mechanical external power, $\mathcal{Q}_u$ the power due to heat transfer, $\mathcal{T}_u$ the power due to mass transfer[3]. It is assumed that each of these processes is *energetically separable* in the balance. The individual contributions read

$$\mathcal{W}_u(\mathcal{P}) = \int_{\mathcal{P}} \vec{b} \cdot \vec{v} \, \mathrm{d}\Omega + \int_{\partial\mathcal{P}} \vec{t} \cdot \vec{v} \, \mathrm{d}\Gamma \,, \tag{3.11a}$$

$$\mathcal{Q}_u(\mathcal{P}) = \int_{\mathcal{P}} s_q \, \mathrm{d}\Omega - \int_{\partial\mathcal{P}} \vec{q} \cdot \vec{n} \, \mathrm{d}\Gamma \,, \tag{3.11b}$$

$$\mathcal{T}_u(\mathcal{P}) = \int_{\mathcal{P}} {}^u\mu_L \, s_L + {}^u\mu_T \, s_T \, \mathrm{d}\Omega - \int_{\partial\mathcal{P}} {}^u\mu_L \, \vec{h}_L \cdot \vec{n} \, \mathrm{d}\Gamma \,, \tag{3.11c}$$

where $\vec{t}$ is the surface traction, $\vec{v}$ is the velocity, s_q is the rate in energy per unit volume at which heat is generated by sources, and $\vec{q}$ is the flux of heat. Since they are defined over a finite sub-part $\mathcal{P}$, the four quantities $\mathcal{U}$, $\mathcal{W}_u$, $\mathcal{Q}_u$, and $\mathcal{T}_u$ are scalar functions of time.

The time variation of net internal energy $\mathcal{U}$ corresponds to the power expenditure of external agencies: a mechanical contribution $\mathcal{W}_u$ due to body forces $\vec{b}$ and surface tractions $\vec{t}$ that do work on velocities $\vec{v}$; a heat contribution $\mathcal{Q}_u$ where s_q is the heat supplied by external agencies and $\vec{q}$ is the heat flux vector; a mass contribution $\mathcal{T}_u$ in which the scalar ${}^u\mu_\beta$ denotes the change in specific energy provided by a unit supply of *moles* of species β.

As usual in the thermodynamics of continua, see e.g. [24], one can make use of the specific internal energy u per unit volume

$$\mathcal{U}(\mathcal{P}) = \int_{\mathcal{P}} u \, \mathrm{d}\Omega \,.$$

In small displacements one can define specific internal energy per unit mass or per unit volume, since both mass and volume do not change during the process. We choose to define it per unit volume. Standard application of the divergence theorem and of mass balances (3.2) leads from (3.11) to

$$\mathcal{W}_u(\mathcal{P}) = \int_{\mathcal{P}} \boldsymbol{\sigma} : \frac{\partial\boldsymbol{\varepsilon}}{\partial t} \, \mathrm{d}\Omega \,, \tag{3.12a}$$

$$\mathcal{Q}_u(\mathcal{P}) = \int_{\mathcal{P}} s_q - \mathrm{div}\,[\vec{q}] \, \mathrm{d}\Omega \,, \tag{3.12b}$$

$$\mathcal{T}_u(\mathcal{P}) = \int_{\mathcal{P}} {}^u\mu_L \, \frac{\partial c_L}{\partial t} + {}^u\mu_L \, w^{(3.1)} - \vec{h}_L \cdot \nabla\,[\,{}^u\mu_L\,] \, \mathrm{d}\Omega + \int_{\mathcal{P}} {}^u\mu_T \, \frac{\partial c_T}{\partial t} - {}^u\mu_T \, w^{(3.1)} \, \mathrm{d}\Omega \,. \tag{3.12c}$$

where $\boldsymbol{\varepsilon}$ is the strain tensor, i.e. $\frac{\partial\boldsymbol{\varepsilon}}{\partial t} = \mathrm{sym}\,[\,\nabla\,[\,\vec{v}\,]\,]$, The first law of thermodynamics is thus stated as follows

$$\int_{\mathcal{P}} \frac{\mathrm{d}u}{\mathrm{d}t} \, \mathrm{d}\Omega = \int_{\mathcal{P}} \boldsymbol{\sigma} : \frac{\partial\boldsymbol{\varepsilon}}{\partial t} + s_q - \mathrm{div}\,[\vec{q}] + {}^u\mu_L \, \frac{\partial c_L}{\partial t} + {}^u\mu_T \, \frac{\partial c_T}{\partial t} - \vec{h}_L \cdot \nabla\,[\,{}^u\mu_L\,] + ({}^u\mu_L - {}^u\mu_T)\, w^{(3.1)} \, \mathrm{d}\Omega \,.$$

It must hold for any region $\mathcal{P}$, since the latter is arbitrary. The local form of the first principle thus reads

$$\frac{\mathrm{d}u}{\mathrm{d}t} = \boldsymbol{\sigma} : \frac{\partial\boldsymbol{\varepsilon}}{\partial t} + s_q - \mathrm{div}\,[\vec{q}] + {}^u\mu_L \, \frac{\partial c_L}{\partial t} + {}^u\mu_T \, \frac{\partial c_T}{\partial t} - \vec{h}_L \cdot \nabla\,[\,{}^u\mu_L\,] + ({}^u\mu_L - {}^u\mu_T)\, w^{(3.1)} \,. \tag{3.13}$$

---

[3]Augmenting the energy balance with energy flows due to species transport is not always accomplished. Such a term is not included for instance in [22, 26] whereas it appears in [24].

3.3.2 Entropy imbalance

The second law of thermodynamics represents the balance of the interplay among the internal entropy of $\mathcal{P}$ and the entropy transferred in $\mathcal{P}$ due to mass exchange and heat transferred on $\mathcal{P}$. The entropy balance for the problem at hand, for *quasi-static interactions*, reads

$$\frac{\mathrm{d}\mathcal{S}}{\mathrm{d}t}(\mathcal{P}) - \frac{\mathrm{d}\mathcal{S}_i}{\mathrm{d}t}(\mathcal{P}) = \mathcal{Q}_\eta(\mathcal{P}) + \mathcal{T}_\eta(\mathcal{P}) \,, \tag{3.14}$$

where $\mathcal{S}$ is the net internal entropy of $\mathcal{P}$, $\mathcal{S}_i$ is the entropy produced inside $\mathcal{P}$, $\mathcal{Q}_\eta$ the entropy per unit time due to heat transfer, $\mathcal{T}_\eta$ the entropy per unit time due to mass transfer. The individual contributions read

$$\mathcal{Q}_\eta(\mathcal{P}) = \int_\mathcal{P} \frac{s_q}{T}\,\mathrm{d}\Omega - \int_{\partial\mathcal{P}} \frac{\vec{q}}{T}\cdot\vec{n}\,\mathrm{d}\Gamma \,, \tag{3.15a}$$

$$\mathcal{T}_\eta(\mathcal{P}) = \int_\mathcal{P} {}^\eta\mu_L\,s_L + {}^\eta\mu_T\,s_T\,\mathrm{d}\Omega - \int_{\partial\mathcal{P}} {}^\eta\mu_L\,\vec{h}_L\cdot\vec{n}\,\mathrm{d}\Gamma \,. \tag{3.15b}$$

Equation (3.14) stems from the non-trivial assumption that mechanics does not contribute directly to the total entropy flow in the entropy balance equation. This assumption is profoundly elaborated in [22, 293]. The scalar ${}^\eta\mu_\beta$ denotes the change in specific entropy provided by a unit supply of *moles*[4] of species $\beta = L, T$.

The second law of thermodynamics states that

$$\frac{\mathrm{d}\mathcal{S}_i}{\mathrm{d}t}(\mathcal{P}) \geq 0 \,.$$

One can make use of the specific internal entropy η per unit volume

$$\mathcal{S}(\mathcal{P}) = \int_\mathcal{P} \eta\,\mathrm{d}\Omega \,.$$

In small displacements one can define specific internal entropy per unit mass or per unit volume, since both mass and volume do not change during the process. We choose to define it per unit volume. Standard application of the divergence theorem and of mass balances (3.2) leads from (3.15) to

$$\frac{\mathrm{d}}{\mathrm{d}t}\int_\mathcal{P} \eta\,\mathrm{d}\Omega + \int_\mathcal{P} -\frac{s_q}{T} + \mathrm{div}\left[\frac{\vec{q}}{T}\right] - {}^\eta\mu_L\,s_L + \mathrm{div}\left[{}^\eta\mu_L\,\vec{h}_L\right] - {}^\eta\mu_T\,s_T\,\mathrm{d}\Omega \geq 0 \,. \tag{3.16}$$

By noting that

$$\mathrm{div}\left[\frac{\vec{q}}{T}\right] = \frac{1}{T}\,\mathrm{div}\left[\vec{q}\right] - \frac{1}{T^2}\,\vec{q}\cdot\nabla\left[T\right] \,,$$

taking advantage of identity (3.13) and of the sign definiteness of temperature, we can rephrase the entropy imbalance in terms of internal energy

$$\int_\mathcal{P} T\frac{\mathrm{d}\eta}{\mathrm{d}t} - \frac{1}{T}\,\vec{q}\cdot\nabla\left[T\right] - T\,{}^\eta\mu_L\,s_L + T\,\mathrm{div}\left[{}^\eta\mu_L\,\vec{h}_L\right] - T\,{}^\eta\mu_T\,s_T\,\mathrm{d}\Omega +$$

$$-\left\{\int_\mathcal{P} \frac{\mathrm{d}u}{\mathrm{d}t} - \boldsymbol{\sigma}:\frac{\partial\boldsymbol{\varepsilon}}{\partial t} - {}^u\mu_L\,\frac{\partial c_L}{\partial t} - {}^u\mu_T\,\frac{\partial c_T}{\partial t} + \vec{h}_L\cdot\nabla\left[{}^u\mu_L\right] - ({}^u\mu_L - {}^u\mu_T)\,w^{(3.1)}\,\mathrm{d}\Omega\right\} \geq 0 \,.$$

By exploiting the mass balance equations (3.2) the entropy imbalance becomes

$$\int_\mathcal{P} T\frac{\mathrm{d}\eta}{\mathrm{d}t} - \frac{\mathrm{d}u}{\mathrm{d}t}\,\mathrm{d}\Omega +$$

$$+\int_\mathcal{P} -\frac{1}{T}\,\vec{q}\cdot\nabla\left[T\right] - T\,{}^\eta\mu_L\,\frac{\partial c_L}{\partial t} - T\,{}^\eta\mu_T\,\frac{\partial c_T}{\partial t} + T\,\vec{h}_L\cdot\nabla\left[{}^\eta\mu_L\right] - T\,({}^\eta\mu_L - {}^\eta\mu_T)\,w^{(3.1)}\,\mathrm{d}\Omega +$$

---

[4]It is worth pointing out that [24] does not consider the contribution of mass to the flux of entropy in (3.14).

$$-\int_{\mathcal{P}} -\boldsymbol{\sigma} : \frac{\partial \boldsymbol{\varepsilon}}{\partial t} - {}^{u}\mu_L \frac{\partial c_L}{\partial t} - {}^{u}\mu_T \frac{\partial c_T}{\partial t} + \vec{h}_L \cdot \nabla \left[{}^{u}\mu_L \right] - \left({}^{u}\mu_L - {}^{u}\mu_T \right) w^{(3.1)} \, \mathrm{d}\Omega \geq 0 \, .$$

Denote with the symbol μ_β the quantity

$$\mu_\beta = {}^{u}\mu_\beta - T \, {}^{\eta}\mu_\beta \, , \tag{3.17}$$

and with the symbol $A^{(3.1)}$ the following

$$A^{(3.1)} = \mu_T - \mu_L \, , \tag{3.18}$$

in order to write the entropy imbalance as

$$\int_{\mathcal{P}} T \frac{\mathrm{d}\eta}{\mathrm{d}t} - \frac{\mathrm{d}u}{\mathrm{d}t} - \frac{1}{T} \vec{q} \cdot \nabla \left[T \right] + \mu_L \frac{\partial c_L}{\partial t} + \mu_T \frac{\partial c_T}{\partial t} +$$

$$-\vec{h}_L \cdot \nabla \left[\mu_L \right] - {}^{\eta}\mu_L \, \vec{h}_L \cdot \nabla \left[T \right] - w^{(3.1)} A^{(3.1)} + \boldsymbol{\sigma} : \frac{\partial \boldsymbol{\varepsilon}}{\partial t} \, \mathrm{d}\Omega \geq 0 \, .$$

Following [22] a new heat flux

$$\vec{\bar{q}} = \vec{q} + T \, {}^{\eta}\mu_L \, \vec{h}_L \, , \tag{3.19}$$

can be defined, whereby $T \, {}^{\eta}\mu_L \, \vec{h}_L$ represents the heat transfer due to diffusion of interstitial species in the lattice. $\vec{\bar{q}}$ is the thermodynamic response conjugate to the gradient of temperature, i.e.

$$\int_{\mathcal{P}} T \frac{\mathrm{d}\eta}{\mathrm{d}t} - \frac{\mathrm{d}u}{\mathrm{d}t} + \mu_L \frac{\partial c_L}{\partial t} + \mu_T \frac{\partial c_T}{\partial t} + \boldsymbol{\sigma} : \frac{\partial \boldsymbol{\varepsilon}}{\partial t} \, \mathrm{d}\Omega + \tag{3.20}$$

$$+\int_{\mathcal{P}} -\frac{1}{T} \vec{\bar{q}} \cdot \nabla \left[T \right] - \vec{h}_L \cdot \nabla \left[\mu_L \right] - w^{(3.1)} A^{(3.1)} \, \mathrm{d}\Omega \geq 0 \, .$$

3.3.3 Additive decompositions

It is customary in non-equilibrium thermodynamics [26, 294] to additively decompose the stress into the sum of two symmetric tensors, an elastic part $\boldsymbol{\sigma}^e$ and a viscous, dissipative part $\boldsymbol{\sigma}^d$

$$\boldsymbol{\sigma} = \boldsymbol{\sigma}^e + \boldsymbol{\sigma}^d \, . \tag{3.21}$$

The elastic part is assumed to be derivable from a potential.

The strain tensor $\boldsymbol{\varepsilon}$ can be also additively decomposed into a chemo-thermo-elastic tensor $\boldsymbol{\varepsilon}^{cte}$ and into an inelastic contribution $\boldsymbol{\varepsilon}^{in}$, following a rather classical decomposition of strains in standard dissipative systems [295]

$$\boldsymbol{\varepsilon} = \boldsymbol{\varepsilon}^{cte} + \boldsymbol{\varepsilon}^{in} \, . \tag{3.22}$$

The contribution $\boldsymbol{\sigma} : \frac{\partial \boldsymbol{\varepsilon}^{in}}{\partial t}$ has a dissipative nature, that will be discussed further in the paper. Tensor $\boldsymbol{\varepsilon}^{cte}$ will be subject to further additive decompositions, that will be introduced at a convenient time.

3.3.4 Helmholtz free energy

Different thermodynamic potentials can be considered rather than the internal energy u. The specific *Helmholtz free energy* is defined as

$$\psi = u - T \, \eta \, , \tag{3.23}$$

and will be used henceforth. It is taken as a function of temperature, concentrations, and the chemo-thermo-mechanical strain[5] and of some kinematic internal variables $\boldsymbol{\xi}$ that compare with the usual meaning in inelastic constitutive laws. It follows that

$$T \frac{\mathrm{d}\eta}{\mathrm{d}t} - \frac{\mathrm{d}u}{\mathrm{d}t} = -\frac{\mathrm{d}\psi}{\mathrm{d}t} - \eta \frac{\partial T}{\partial t} \, , \tag{3.24}$$

5

which can be inserted in (3.20) to derive the entropy imbalance in final form

$$\int_{\mathcal{P}} - \frac{\mathrm{d}\psi}{\mathrm{d}t} - \eta\,\frac{\partial T}{\partial t} + \mu_L\,\frac{\partial c_L}{\partial t} + \mu_T\,\frac{\partial c_T}{\partial t} + \boldsymbol{\sigma}^e : \frac{\partial \boldsymbol{\varepsilon}^{cte}}{\partial t} - \frac{1}{T}\vec{q}\cdot\nabla\,[\,T\,] + \tag{3.25}$$

$$-\vec{h}_L\cdot\nabla\,[\,\mu_L\,] - w^{(3.1)}\,A^{(3.1)} + \boldsymbol{\sigma}^d : \frac{\partial \boldsymbol{\varepsilon}^{cte}}{\partial t} + \boldsymbol{\sigma} : \frac{\partial \boldsymbol{\varepsilon}^{in}}{\partial t}\ \mathrm{d}\Omega \geq 0\,.$$

In view of the stated functional dependency of the free energy, its total derivative with respect to time reads

$$\frac{\mathrm{d}\psi}{\mathrm{d}t} = \frac{\partial\psi}{\partial T}\frac{\partial T}{\partial t} + \frac{\partial\psi}{\partial\boldsymbol{\varepsilon}^{cte}} : \frac{\partial\boldsymbol{\varepsilon}^{cte}}{\partial t} + \frac{\partial\psi}{\partial c_L}\frac{\partial c_L}{\partial t} + \frac{\partial\psi}{\partial c_T}\frac{\partial c_T}{\partial t} + \frac{\partial\psi}{\partial\boldsymbol{\xi}} : \frac{\partial\boldsymbol{\xi}}{\partial t}\,. \tag{3.26}$$

The internal force, conjugate to $\boldsymbol{\xi}$, will be denoted with the symbol $\boldsymbol{\chi}$, i.e.

$$\boldsymbol{\chi} = -\frac{\partial\psi}{\partial\boldsymbol{\xi}}\,. \tag{3.27}$$

3.3.5   Thermodynamic restrictions

Inequality (3.25) becomes

$$\int_{\mathcal{P}} -\frac{\partial\psi}{\partial T}\frac{\partial T}{\partial t} - \frac{\partial\psi}{\partial\boldsymbol{\varepsilon}^{cte}} : \frac{\partial\boldsymbol{\varepsilon}^{cte}}{\partial t} - \frac{\partial\psi}{\partial c_L}\frac{\partial c_L}{\partial t} - \frac{\partial\psi}{\partial c_T}\frac{\partial c_T}{\partial t} - \frac{\partial\psi}{\partial\boldsymbol{\xi}} : \frac{\partial\boldsymbol{\xi}}{\partial t} +$$

$$-\eta\,\frac{\partial T}{\partial t} + \mu_L\,\frac{\partial c_L}{\partial t} + \mu_T\,\frac{\partial c_T}{\partial t} + \boldsymbol{\sigma}^e : \frac{\partial\boldsymbol{\varepsilon}^{cte}}{\partial t} - \frac{1}{T}\vec{q}\cdot\nabla\,[\,T\,] +$$

$$-\vec{h}_L\cdot\nabla\,[\,\mu_L\,] - w^{(3.1)}\,A^{(3.1)} + \boldsymbol{\sigma}^d : \frac{\partial\boldsymbol{\varepsilon}^{cte}}{\partial t} + \boldsymbol{\sigma} : \frac{\partial\boldsymbol{\varepsilon}^{in}}{\partial t}\ \mathrm{d}\Omega \geq 0\,,$$

and must hold for any region $\mathcal{P}$, since the latter was arbitrarily taken. Therefore, the following *local* entropy imbalance, usually termed the Clausius-Duhem inequality, yields

$$\frac{\partial T}{\partial t}\left(-\eta - \frac{\partial\psi}{\partial T}\right) + \frac{\partial\boldsymbol{\varepsilon}^{cte}}{\partial t} : \left(\boldsymbol{\sigma}^e - \frac{\partial\psi}{\partial\boldsymbol{\varepsilon}^{cte}}\right) + \frac{\partial c_L}{\partial t}\left(\mu_L - \frac{\partial\psi}{\partial c_L}\right) + \frac{\partial c_T}{\partial t}\left(\mu_T - \frac{\partial\psi}{\partial c_T}\right) +$$

$$+\boldsymbol{\chi} : \frac{\partial\boldsymbol{\xi}}{\partial t} - \vec{h}_L\cdot\nabla\,[\,\mu_L\,] - w^{(3.1)}\,A^{(3.1)} - \frac{1}{T}\vec{q}\cdot\nabla\,[\,T\,] + \boldsymbol{\sigma}^d : \frac{\partial\boldsymbol{\varepsilon}^{cte}}{\partial t} + \boldsymbol{\sigma} : \frac{\partial\boldsymbol{\varepsilon}^{in}}{\partial t} \geq 0\,. \quad (3.28)$$

This inequality must hold for any value of the time derivative of the temperature T, the concentrations c_L and c_T, and the strain tensor $\boldsymbol{\varepsilon}^{cte}$. Since they appear linearly in the inequality, the factors multiplying them must be zero, as otherwise it would be possible to find a value for the time derivatives that violate the inequality. Therefore, the following restrictions apply

$$\boldsymbol{\sigma}^e = \frac{\partial\psi}{\partial\boldsymbol{\varepsilon}^{cte}}\,, \qquad \eta = -\frac{\partial\psi}{\partial T}\,, \qquad \mu_L = \frac{\partial\psi}{\partial c_L}\,, \qquad \mu_T = \frac{\partial\psi}{\partial c_T}\,, \tag{3.29}$$

thus yielding to the inequality

$$\underbrace{\boldsymbol{\sigma}^d : \frac{\partial\boldsymbol{\varepsilon}^{cte}}{\partial t} + \boldsymbol{\sigma} : \frac{\partial\boldsymbol{\varepsilon}^{in}}{\partial t} + \boldsymbol{\chi} : \frac{\partial\boldsymbol{\xi}}{\partial t}}_{\text{inelastic}} - \underbrace{\vec{h}_L\cdot\nabla\,[\,\mu_L\,]}_{\text{diffusive}} - \underbrace{\frac{1}{T}\vec{q}\cdot\nabla\,[\,T\,]}_{\text{thermal}} - \underbrace{w^{(3.1)}\,A^{(3.1)}}_{\text{chemical}} \geq 0\,, \tag{3.30}$$

This is not the only possible choice. Focusing on the functional dependence on the strain only, the Helmholtz free energy could be written as a function of the whole strain tensor and of its inelastic counterpart

$$\psi = \psi(\boldsymbol{\varepsilon}, \boldsymbol{\varepsilon}^{in}, ...)\,.$$

In the Coleman-Noll procedure, the stress is finally related to the derivative of the Helmholtz free energy wrt to the total strain

$$\boldsymbol{\sigma} = \frac{\partial\psi}{\partial\boldsymbol{\varepsilon}}\,.$$

In the realm of large strains, this approach has been taken for instance in [296, 297]. This approach models the dissipation as arising from the free energy.

50

which is the internal entropy production (multiplied with the temperature). Mechanical, diffusive, chemical, and thermal contributions are devised as shown. Inequality (3.30) has the usual dissipative structure [298]. Under the assumptions of Curie symmetry principle [22], fluxes and thermodynamic forces of different tensorial character do not couple. Inequality (3.30) thus can be written as

$$\boldsymbol{\sigma}^d : \frac{\partial \boldsymbol{\varepsilon}^{cte}}{\partial t} + \boldsymbol{\sigma} : \frac{\partial \boldsymbol{\varepsilon}^{in}}{\partial t} + \boldsymbol{\chi} : \frac{\partial \boldsymbol{\xi}}{\partial t} \geq 0 \,, \tag{3.31a}$$

$$-\vec{h}_L \cdot \nabla \left[\mu_L \right] - \frac{1}{T} \vec{q} \cdot \nabla \left[T \right] \geq 0 \,, \tag{3.31b}$$

$$-w^{(3.1)} A^{(3.1)} \geq 0 \,. \tag{3.31c}$$

Remark - In view of formula (3.29), the amount μ_β defined in eq. (3.17) acquires the meaning of *chemical potential* and therefore the term $A^{(3.1)}$ turns out to be the *affinity of the reaction* (3.1).

Remark - The Helmholtz free energy density has been derived with respect to time in Eq.(3.26). Exploiting the thermodynamic restriction (3.29) for entropy and for stress, the result in Eq. (3.24) leads to

$$-T \frac{\mathrm{d}}{\mathrm{d}t} \frac{\partial \psi}{\partial T} = \frac{\mathrm{d}u}{\mathrm{d}t} - \boldsymbol{\sigma}^e : \frac{\partial \boldsymbol{\varepsilon}^{cte}}{\partial t} - \mu_L \frac{\partial c_L}{\partial t} - \mu_T \frac{\partial c_T}{\partial t} + \boldsymbol{\chi} : \frac{\partial \boldsymbol{\xi}}{\partial t} \,. \tag{3.32}$$

This identity will be used in Appendix 3.B as the starting point to derive the generalized heat equation.

3.3.6 Specifications for $^u\mu_\beta$ and $^\eta\mu_\beta$

Identity (3.29b) allows expression of the entropy as a function of temperature, concentrations, chemo-thermo-mechanical strain, and internal variables. Since the specific energy u is a function of entropy, it also becomes a function of the same thermodynamic variables set. From the definition (3.23) of the Helmholtz free energy, it descends that

$$\frac{\mathrm{d}\psi}{\mathrm{d}c_\beta} = \frac{\mathrm{d}u}{\mathrm{d}c_\beta} + T \frac{\partial}{\partial c_\beta} \frac{\partial \psi}{\partial T} \,, \tag{3.33}$$

with $\beta = L, T$. In view of (3.29) the term on the left hand side is the chemical potential[6] of species β. We compute the entropy per mole, i.e. the partial molar entropy $^\eta\mu_\beta$, as

$$^\eta\mu_\beta = \frac{\partial \eta}{\partial c_\beta} = -\frac{\partial}{\partial c_\beta} \frac{\partial \psi}{\partial T} = -\frac{\partial}{\partial T} \frac{\partial \psi}{\partial c_\beta} = -\frac{\partial \mu_\beta}{\partial T} \,. \tag{3.34}$$

It thus descends from definition (3.17) that $^u\mu_\beta$ amounts to

$$^u\mu_L = \left. \frac{\mathrm{d}u}{\mathrm{d}c_L} \right|_{T,c_T,\boldsymbol{\varepsilon}^{cte},\boldsymbol{\xi}} \,, \qquad ^u\mu_T = \left. \frac{\mathrm{d}u}{\mathrm{d}c_T} \right|_{T,c_L,\boldsymbol{\varepsilon}^{cte},\boldsymbol{\xi}} \,. \tag{3.35}$$

This outcome is consistent with the local form of the first principle (3.13). It holds in fact:

$$\frac{\mathrm{d}\psi}{\mathrm{d}c_\beta} = \frac{\mathrm{d}u}{\mathrm{d}c_\beta} + T \frac{\partial}{\partial c_\beta} \frac{\partial \psi}{\partial T} = \frac{\partial u}{\partial c_\beta} + \frac{\partial u}{\partial \eta} \frac{\partial \eta}{\partial c_\beta} + T \frac{\partial}{\partial c_\beta} \frac{\partial \psi}{\partial T} = \frac{\partial u}{\partial c_\beta} = \mu_\beta \tag{3.36}$$

and

$$^u\mu_\beta = \frac{\mathrm{d}u}{\mathrm{d}c_\beta} = \frac{\partial u}{\partial c_\beta} + \frac{\partial u}{\partial \eta} \frac{\partial \eta}{\partial c_\beta} = \mu_\beta + T \, ^\eta\mu_\beta \,, \tag{3.37}$$

in agreement with definition (3.17). In summary therefore,

$$^\eta\mu_\beta = -\frac{\partial^2 \psi}{\partial c_\beta \partial T} \tag{3.38a}$$

---

[6]Note that $\frac{\mathrm{d}\psi}{\mathrm{d}c_\beta} = \frac{\partial \psi}{\partial c_\beta}$ in view of the notation on total and partial derivatives.

$$^u\mu_\beta \;\;=\;\; \frac{\partial \psi}{\partial c_\beta} - T\,\frac{\partial^2 \psi}{\partial c_\beta \partial T}\;. \tag{3.38b}$$

Remark - The identification (3.38) of the energetic and entropic contributions to the chemical potential provides a neat formulation for the entropy production inequality (3.31b). One writes in view of definition (3.19)

$$-\vec{h}_L \cdot \nabla\,[\,\mu_L\,] - \frac{1}{T}\,\vec{q}\;\cdot \nabla\,[\,T\,] = -\vec{h}_L \cdot (\nabla\,[\,\mu_L\,] + \,^\eta\mu_L\,\nabla\,[\,T\,]) - \frac{1}{T}\,\vec{q}\cdot\nabla\,[\,T\,]\;.$$

By means of Eq. (3.38), the vector $\nabla\,[\,\mu_L\,] + \,^\eta\mu_L\,\nabla\,[\,T\,]$ is independent upon the gradient of temperature, since it holds

$$\nabla\,[\,\mu_L\,] + \,^\eta\mu_L\,\nabla\,[\,T\,] = \frac{\partial^2\psi}{\partial c_L^2}\,\nabla\,[\,c_L\,] + \frac{\partial^2\psi}{\partial c_L \partial c_T}\,\nabla\,[\,c_T\,] + \frac{\partial^2\psi}{\partial c_L \partial \boldsymbol{\varepsilon}^{cte}}\;:\;\nabla\,[\,\boldsymbol{\varepsilon}^{cte}\,] + \frac{\partial^2\psi}{\partial c_L \partial \boldsymbol{\xi}}\;:\;\nabla\,[\,\boldsymbol{\xi}\,]\;. \tag{3.39}$$

3.4 Constitutive theory

There are several ways to satisfy the thermodynamic restriction (3.31b). A strategy that immediately descends from (3.31b) models the flux of interstitial species by Fickian-diffusion, and the "heat flux" $\vec{q}$ via Fourier's law, i.e.

$$\vec{h}_L = -\boldsymbol{M}_L(c_L)\,\nabla\,[\,\mu_L\,]\;, \qquad \vec{q} = -\boldsymbol{K}\,\nabla\,[\,T\,]\;, \tag{3.40}$$

by means of positive definite mobility and heat conductivity tensors $\boldsymbol{M}_L$ and $\boldsymbol{K}$, respectively. A cleaner and intuitive approach, which will be pursued from now on, relates the ordinary heat flux $\vec{q}$ to the gradient of temperature via Fourier's law, and relates the mass flux to the remaining gradients in view of Eq. (3.39) in a consistent way with the thermodynamic restriction (3.31b)

$$\vec{h}_L \;\;=\;\; -\boldsymbol{M}_L(c_L)\,(\nabla\,[\,\mu_L\,] + \,^\eta\mu_L\,\nabla\,[\,T\,])\;, \tag{3.41a}$$
$$\vec{q} \;\;=\;\; -\boldsymbol{K}\,\nabla\,[\,T\,]\;. \tag{3.41b}$$

More general approaches, which include the Soret effect of thermal diffusion and the Dufour effect of heat flow generated by concentration gradients, are obviously possible but will not be accounted for here.

The following isotropic non linear [251] specialization for the mobility tensor $\boldsymbol{M}_L$

$$\boldsymbol{M}_L(c_L) = \mathfrak{m}_L\,c_L^{max}\,\theta_L\,(1 - \theta_L)\,\mathbb{1}\;, \tag{3.42}$$

accounts for saturation. In formula (3.42): $\theta_L = c_L/c_L^{max}$; c_L^{max} is the saturation limit for interstitial species. The *mobility* $\mathfrak{m}_L > 0$ represents the average velocity of interstitial species when acted upon by a force of 1 N/mol independent of the origin of the force. Definition (3.42) represents the physical requirement that both the pure ($c_L = 0$) and the saturated ($c_L = c_L^{max}$) phases have vanishing mobilities. Assuming that the trapped species have vanishing mobility is an alternative view of modeling the absence of trapped species flux. Neither the mobility $\mathfrak{m}_L$ nor the saturation concentration c_L^{max} are assumed to change in time. Such a limitation can be removed without altering the conceptual picture if experimental data indicate an influence of temperature, stresses, or concentrations.

The Helmholtz free energy density ψ is modeled by decomposing it into separate parts: a diffusive contribution ψ_{diff}, a thermal contribution ψ_{th}, an elastic contribution ψ_{el}, and an inelastic (or *defect energy* [24]) counterpart ψ_{in}

$$\psi(c_L, c_T, T, \boldsymbol{\varepsilon}^{cte}, \boldsymbol{\xi}) = \psi_0 + \psi_{diff}(c_L, c_T, T, \boldsymbol{\xi}) + \psi_{th}(c_L, c_T, T) + \psi_{el}(\boldsymbol{\varepsilon}^{cte}, c_L, c_T, T) + \psi_{in}(c_L, c_T, T, \boldsymbol{\xi})\;. \tag{3.43}$$

This split is here taken for granted without motivation. A detailed analysis for the *microstructure term* ψ_{in} can be found in [299]. ψ_0 is a datum value.

The thermal contribution $\psi_{th}(c_L, c_T, T)$ is taken as

$$\psi_{th} = -c_H \,^\eta\mu_H^0 (T-T_0) - \frac{1}{2} \frac{c_{vH}^0 \, c_H}{T_0} (T-T_0)^2 - (c_L \,^\eta\mu_L^0 + c_T \,^\eta\mu_T^0)(T-T_0) - \frac{1}{2} \frac{c_{vL}^0 c_L + c_{vT}^0 c_T}{T_0} (T-T_0)^2 \ . \quad (3.44)$$

The subscript H designates the host material, which has concentration c_H in moles per unit volume. The specific heats c_{vH}^0, c_{vL}^0, and c_{vT}^0 are, by convention, energy per mole per degree Kelvin, and therefore we multiply it by concentration to convert the energy to energy per unit volume. Each species has its own specific heat, taken to be constant. We have included $^\eta\mu_H^0$, $^\eta\mu_L^0$, and $^\eta\mu_T^0$ to allow for entropy driven by thermal fluctuations[7].

Statistical mechanics provides a description of the entropy for isolated systems in terms of the density of states Ω , which in the case of two-state systems is the number of possible molecular configurations [25]. Making recourse to Stirling's approximation, one finds that the formula for combinations provides the following number of possible configurations of interstitial species atoms in an ideal crystalline lattice

$$\Omega_L = \left[\theta_L^{\theta_L} \, (1-\theta_L)^{(1-\theta_L)} \right]^{-N_A \, c_L^{max}} \ , \quad (3.45)$$

having denoted Avogadro's number with N_A. Inserting (3.45) into Boltzmann's equation

$$\eta_L^{diff} = k_B \, \ln \Omega_L \ , \quad (3.46)$$

one finds that the following well-known expression of the entropy arises, since the universal gas constant R is the product of Boltzmann constant k_B and Avogadro's number

$$\eta_L^{diff} = -R \, c_L^{max} \, (\theta_L \, \ln[\theta_L] + (1-\theta_L) \ln[1-\theta_L]) \ . \quad (3.47)$$

The η_T counterpart can be derived from the entropy Ω_T of the trapped species in terms of $\theta_T = c_T/c_T^{max}$ where the saturation limit for trapped species $c_T^{max}(\boldsymbol{\xi})$ may change in time due to inelastic deformations, accounted for by means of $\boldsymbol{\xi}$

$$\eta_T^{diff} = -R \, c_T^{max}(\boldsymbol{\xi}) \, (\theta_T(\boldsymbol{\xi}) \ln[\theta_T(\boldsymbol{\xi})] + (1-\theta_T(\boldsymbol{\xi})) \ln[1-\theta_T(\boldsymbol{\xi})]) \ . \quad (3.48)$$

The free energy density (per unit volume) of mobile guest atoms interacting with a host medium is described by a regular solution model [251, 23], which provides the following free energy density for the continuum approximation of mixing:

$$\psi_{diff}(c_L, c_T, T, \boldsymbol{\xi}) = \mu_L^0 \, c_L \ - \ T \eta_L^{diff} + \mu_T^0 \, c_T \ - \ T \eta_T^{diff} + \ RT \, c_L^{max} \, \chi \, \theta_L \, (1-\theta_L) \ . \quad (3.49)$$

The model of the Helmholtz free energy density in Eq. (3.49) represents the entropy of mixing plus energetic interactions. The terms μ_L^0 and μ_T^0 are reference values of chemical potentials that specify the free energy in the absence of interaction and entropic contributions, and specify the trap binding energy ΔE_τ (i.e. the negative of the Gibbs free energy change), and in turn are related to the *equilibrium constant* K_{eq} of reaction (3.1)

$$\Delta E_\tau \ = \ \mu_L^0 \ - \ \mu_T^0 \ = RT \, \ln[K_{eq}] \ . \quad (3.50)$$

The real valued constant χ in Eq. (3.49) - termed the *exchange parameter* [25] - characterizes the energy of interaction between mobile guest species and insertion sites. If all of the interactions between mobile species and sites are the same, then $\chi = 0$ and there is no energy of mixing: mixing is the ideal and purely entropic. The contribution $RT \, c_L^{max} \, \chi \, \theta_L \, (1-\theta_L)$, known as the excess Gibbs energy, endows the free energy density with a non convex behavior with respect to c_L for $\chi > 2$, which in turn may lead to phase segregation [252, 257, 300].

---

[7]Note that perfect gas theory suggests that there should also be a term containing the logarithm of density to fully characterize the entropy due to thermal fluctuations, but we omit this term as having negligible increments, and therefore its effect is lumped into ψ_0

The chemo-thermo-elastic strain $\boldsymbol{\varepsilon}^{cte}$ is considered to be made up of three separate contibutions: an elastic recoverable part after unloading $\boldsymbol{\varepsilon}^{el}$, a swelling contribution due to the insertion of species in the host material $\boldsymbol{\varepsilon}^{s}$, and a thermal distortion $\boldsymbol{\varepsilon}^{th}$:

$$\boldsymbol{\varepsilon}^{cte} = \boldsymbol{\varepsilon}^{el} + \boldsymbol{\varepsilon}^{s} + \boldsymbol{\varepsilon}^{th} \ . \tag{3.51}$$

The swelling contribution

$$\boldsymbol{\varepsilon}^{s} = \omega_L \left(c_L - c_L^0 \right) \, \mathbb{1} + \omega_T \left(c_T - c_T^0 \right) \, \mathbb{1} \, , \tag{3.52}$$

is assumed to be volumetric and proportional to the deviation $c_\beta - c_\beta^0$ from the reference concentration c_β^0 by means of the chemical expansion coefficients ω_β of species β. They equal one third of the partial molar volumes at a given temperature. Symbol $\mathbb{1}$ denotes the identity matrix. The thermal strain tensor, purely volumetric as for the swelling contribution, is assumed to be proportional to the difference with respect to a reference temperature T_0, by means of the factor α termed the thermal expansion coefficient

$$\boldsymbol{\varepsilon}^{th} = \alpha \, (T - T_0) \, \mathbb{1} \, , \, . \tag{3.53}$$

A possible choice for the elastic part of the free energy density $\psi_{el}(\boldsymbol{\varepsilon}^{cte}, c_L, c_T, T)$ in the small strain range is the usual quadratic form

$$\psi_{el}(\boldsymbol{\varepsilon}^{cte}, c_L, c_T, T) = \frac{1}{2} \, K(c_L, c_T, T) \, \mathrm{tr} \left[\boldsymbol{\varepsilon}^{cte} - \boldsymbol{\varepsilon}^{s} - \boldsymbol{\varepsilon}^{th} \right]^2 + G(c_L, c_T, T) \, || \, \mathrm{dev} \left[\boldsymbol{\varepsilon}^{cte} - \boldsymbol{\varepsilon}^{s} - \boldsymbol{\varepsilon}^{th} \right] \, ||^2 \, , \tag{3.54}$$

where K, G are the bulk and shear modulus respectively and they are made dependent on temperature and species concentrations. The stress tensor $\boldsymbol{\sigma}^e(\boldsymbol{\varepsilon}^{cte}, c_L, c_T, T)$ descends from the thermodynamic restriction (3.29a)

$$\boldsymbol{\sigma}^e = 2 \, G \, \mathrm{dev} \left[\boldsymbol{\varepsilon}^{cte} \right] + K \left\{ \mathrm{tr} \left[\boldsymbol{\varepsilon}^{cte} \right] - 3 \left[\omega_L \left(c_L - c_L^0 \right) + \omega_T \left(c_T - c_T^0 \right) + \alpha \, (T - T_0) \right] \right\} \mathbb{1} \, . \tag{3.55}$$

Note that the derivative $\partial \psi_{el} / \partial c_\beta$, with $\beta = L, T$, is the sum of two contributions

$$\frac{\partial \psi_{el}}{\partial c_\beta} = -\omega_\beta \, \mathrm{tr} \left[\boldsymbol{\sigma}^e \right] + \frac{1}{2} \frac{\partial K}{\partial c_\beta} \mathrm{tr} \left[\boldsymbol{\varepsilon}^{cte} - \boldsymbol{\varepsilon}^{s} - \boldsymbol{\varepsilon}^{th} \right]^2 + \frac{\partial G}{\partial c_\beta} || \, \mathrm{dev} \left[\boldsymbol{\varepsilon}^{cte} - \boldsymbol{\varepsilon}^{s} - \boldsymbol{\varepsilon}^{th} \right] ||^2 \, . \tag{3.56}$$

The first emanates from the swelling part of the strain, and is present even if the material properties are independent on concentration of species. Analogously,

$$\frac{\partial \psi_{el}}{\partial T} = -\alpha \, \mathrm{tr} \left[\boldsymbol{\sigma}^e \right] + \frac{1}{2} \frac{\partial K}{\partial T} \mathrm{tr} \left[\boldsymbol{\varepsilon}^{cte} - \boldsymbol{\varepsilon}^{s} - \boldsymbol{\varepsilon}^{th} \right]^2 + \frac{\partial G}{\partial T} || \, \mathrm{dev} \left[\boldsymbol{\varepsilon}^{cte} - \boldsymbol{\varepsilon}^{s} - \boldsymbol{\varepsilon}^{th} \right] ||^2 \, . \tag{3.57}$$

Inelastic internal entropy production (3.30) was described by the internal flux variables $\boldsymbol{\varepsilon}^{in}, \boldsymbol{\xi}$ and by their energy-conjugate forces $\boldsymbol{\sigma}, \boldsymbol{\chi}$. The existence of a convex dissipation potential is often assumed as a function of the flux variables, being non-negative and zero at the origin. Internal forces that drive the irreversible processes are linked to the flux variables via normality rules after enforcement of the principle of maximum dissipation [301, 302]. Complementarity laws are more often expressed after a Legendre transformation, in the form of evolution laws of flux variables as a function of the internal forces

$$\frac{\partial \boldsymbol{\varepsilon}^{in}}{\partial t} = \frac{\partial \varphi^{in}}{\partial \boldsymbol{\sigma}} \, , \qquad \frac{\partial \boldsymbol{\xi}}{\partial t} = \frac{\partial \varphi^{in}}{\partial \boldsymbol{\chi}} \, . \tag{3.58}$$

Standard J_2 flow theory with isotropic hardening and visco-plasticity of Perzyna type are considered in the numerical examples in section 3.C.

From Eq. (3.29) we derive the chemical potential of species $\beta = L, T$ as

$$\mu_\beta = \mu_\beta^0 - {}^\eta\mu_\beta^0 \, (T - T_0) - \frac{1}{2} \frac{c_{v\beta}^0}{T_0} (T - T_0)^2 + RT \ln \left[\frac{\theta_\beta}{1 - \theta_\beta} \right] + RT \, \chi(1 - 2\theta_\beta) + \frac{\partial \psi_{el}}{\partial c_\beta} + \frac{\partial \psi_{in}}{\partial c_\beta} \, . \tag{3.59}$$

From Eq. (3.38a), the entropic contribution of the chemical potential reads

$$^{\eta}\mu_\beta = -\,^{\eta}\mu_\beta^0 \,-\, \frac{c_{v\beta}^0}{T_0}(T-T_0) + R\ln\left[\frac{\theta_\beta}{1-\theta_\beta}\right] + R\,\chi(1-2\theta_\beta) + \frac{\partial^2\psi_{el}}{\partial T\partial c_\beta} + \frac{\partial^2\psi_{in}}{\partial T\partial c_\beta} \; . \tag{3.60}$$

By defining as usual the *interstitial diffusivity* by $\mathbb{D}_L = \mathbb{k}_L\,RT$, Fick's law (3.41a) becomes

$$\vec{h}_L(c_L, c_T, T, \boldsymbol{\varepsilon}^{cte}, \boldsymbol{\xi}) = -\,\mathbb{D}_L\,[1-2\chi\,\theta_L\,(1-\theta_L)]\,\nabla\,[\,c_L\,] +$$
$$-\,\boldsymbol{M}(c_L)\,\left[\frac{\partial^2\psi_{el}}{\partial c_L^2}\,\nabla\,[\,c_L\,] + \frac{\partial^2\psi_{el}}{\partial c_L\partial c_T}\,\nabla\,[\,c_T\,] + \frac{\partial^2\psi_{el}}{\partial c_L\partial\boldsymbol{\varepsilon}^{cte}}\,:\,\nabla\,[\,\boldsymbol{\varepsilon}^{cte}\,]\right] +$$
$$-\,\boldsymbol{M}(c_L)\,\left[\frac{\partial^2\psi_{in}}{\partial c_L^2}\,\nabla\,[\,c_L\,] + \frac{\partial^2\psi_{in}}{\partial c_L\partial c_T}\,\nabla\,[\,c_T\,] + \frac{\partial^2\psi_{in}}{\partial c_L\partial\boldsymbol{\varepsilon}^{cte}}\,:\,\nabla\,[\,\boldsymbol{\varepsilon}^{cte}\,] + \frac{\partial^2\psi_{in}}{\partial c_L\partial\boldsymbol{\xi}}\,:\,\nabla\,[\,\boldsymbol{\xi}\,]\right] \; . \tag{3.61}$$

By comparing (3.61) with the mass flux formula for infinitely diluted solutions, that can be easily derived by taking $c_L^{max} \to \infty$, one concludes that saturation has no effect on the diffusivity $\mathbb{D}_L$: in fact, the impact of saturation on the mobility tensor and on the chemical potential act one against the other and the effects cancel out in the evaluation of diffusivity. Saturation does affect mass transport by mechanical and thermal effects, even under the simple assumption that material parameters are not influenced by the interstitial concentration of species. In the simple case of $\psi_{in} = 0$ with constant K and G, the mass flux becomes

$$\vec{h}_L = -\,\mathbb{D}_L\,[1-2\chi\,\theta_L\,(1-\theta_L)]\,\nabla\,[\,c_L\,] - 3\,\boldsymbol{M}(c_L)\,K\omega_L\,\left[3\,\omega_L\,\nabla\,[\,c_L\,] + 3\,\omega_T\,\nabla\,[\,c_T\,] - \nabla\,[\,\mathrm{tr}\,[\,\boldsymbol{\varepsilon}^{cte}\,]\,]\right] \; .$$

3.5 Chemical kinetics

For ideal systems, in which the solvent (if any) does not take part in reactions and the chemical potentials have entropy and energy contributions only, the chemical kinetics of reaction (3.1) is often modeled via the law of mass action [22]

$$w^{(3.1)} = k_T\,\frac{\theta_L}{1-\theta_L} - k_L\,\frac{\theta_T}{1-\theta_T} \; , \tag{3.62a}$$

where k_T is the positive rate constant for the forward reaction (yielding trapped products T) and k_L the rate constant for the reverse reaction. Elastic and swelling contributions suggest some modifications to this form of the law of mass action. It is proposed here that factors k_L and k_T are no longer constant, but depend on the stress and on the concentrations (via elastic parameters) in the following way

$$k_L = \tilde{k}_L\,\exp\frac{\partial\psi_{el}/\partial c_T}{RT}\,\exp\frac{\partial\psi_{in}/\partial c_T}{RT}\,\exp\frac{-\,^{\eta}\mu_T^0(T-T_0)}{RT}\,\exp\frac{-c_{vT}^0(T-T_0)^2}{2RTT_0} \; , \tag{3.62b}$$

$$k_T = \tilde{k}_T\,\exp\frac{\partial\psi_{el}/\partial c_L}{RT}\,\exp\frac{\partial\psi_{in}/\partial c_L}{RT}\,\exp\frac{-\,^{\eta}\mu_L^0(T-T_0)}{RT}\,\exp\frac{-c_{vL}^0(T-T_0)^2}{2RTT_0}\,\exp\left[\chi(1-2\theta_L)\right] \; . \tag{3.62c}$$

with $\tilde{k}_T$ and $\tilde{k}_L$ constants and derivatives as in Eq. (3.56). This new formulation is consistent with the usual mass action law, which is recovered when elastic, swelling, and interaction contributions vanish.

The condition of null affinity $A^{(3.1)} = 0$ can be resolved for the Gibbs free energy change $\mu_L^0 - \mu_T^0$. From definition (3.18), formulae (3.50) and (3.59) the *equilibrium constant of reaction* (3.1) can be derived with simple algebra *at equilibrium conditions*

$$K_{eq} \;=\; \frac{\theta_T^{eq}}{1-\theta_T^{eq}}\,\frac{1-\theta_L^{eq}}{\theta_L^{eq}}\,\exp\frac{\left[\frac{\partial\psi_{el}}{\partial c_T} - \frac{\partial\psi_{el}}{\partial c_L}\right]^{eq}}{RT}\,\exp\frac{\left[\frac{\partial\psi_{in}}{\partial c_T} - \frac{\partial\psi_{in}}{\partial c_L}\right]^{eq}}{RT}\,\exp\left[-\chi(1-2\theta_L^{eq})\right]\times \tag{3.63}$$

$$\times \ \exp \frac{(^{\eta}\mu_L^0 - {}^{\eta}\mu_T^0)(T-T_0)}{RT} \ \exp \frac{(c_{vL}^0 - c_{vT}^0)(T-T_0)^2}{2RTT_0} \ .$$

Equilibrium concentrations of trapped and mobile species depend on temperature T and on the state of stress. The rates of the forward and backward reactions are equal at equilibrium, and the equilibrium constant, in the alternative form $K_{eq} = \tilde{k}_T / \tilde{k}_L$, can be derived from the mass action law (3.62a) by imposing $w^{(3.1)} = 0$. Identity (3.63) is recovered, consistently. Such an identity agrees well and extends *van't Hoff* relation that is often [25] used to model the temperature and pressure dependence of K_{eq}.

The thermodynamic restriction

$$w^{(3.1)} \, A^{(3.1)} \leq 0 \, ,$$

is satisfied using Eq.(3.62). To prove this statement, define with

$$
\aleph \ = \ \exp \frac{\frac{\partial \psi_{el}}{\partial c_L} - \frac{\partial \psi_{el}}{\partial c_T}}{RT} \ \exp \frac{\frac{\partial \psi_{in}}{\partial c_L} - \frac{\partial \psi_{in}}{\partial c_T}}{RT} \ \exp \frac{(^{\eta}\mu_T^0 - {}^{\eta}\mu_L^0)(T-T_0)}{RT} \ \times
$$
$$
\times \exp \frac{(c_{vT}^0 - c_{vL}^0)(T-T_0)^2}{2RTT_0} \ \exp \left[\chi \, (1 - 2\theta_L) \right] \ .
$$

The affinity and the reaction rate can be written as

$$
A^{(3.1)} \ = \ RT \ln \left[\frac{\theta_T}{1-\theta_T} \frac{1-\theta_L}{\theta_L} \frac{1}{\aleph} \frac{1}{K_{eq}} \right] \, ,
$$
$$
w^{(3.1)} \ = \ \tilde{k}_L \ \left\{ -\frac{\theta_T}{1-\theta_T} + \frac{\theta_L}{1-\theta_L} \, \aleph K_{eq} \right\} \ .
$$

If $w^{(3.1)} > 0$ then

$$\aleph > \frac{\theta_T}{1-\theta_T} \frac{1-\theta_L}{\theta_L} \frac{1}{K_{eq}} \, ,$$

and in turn $A^{(3.1)} < 0$. Viceversa if $w^{(3.1)} < 0$ then $A^{(3.1)} > 0$.

A classical way to enforce thermodynamic restrictions for the reaction (3.1) is to linearly relate the affinity and the reaction rate, by means of a phenomenological coefficient $L^{(3.1)} > 0$

$$w^{(3.1)} = -L^{(3.1)} \, A^{(3.1)} \, , \tag{3.64}$$

It was remarked in [22] that the linear phenomenological Eq.(3.64) is not *a priory* satisfactory for chemical reactions, although there is always a region close to equilibrium where it holds. From the equations (3.59) for the chemical potentials, the law of mass action in fact leads to

$$w^{(3.1)} = \tilde{k}_T \ \exp \left[\frac{\mu_L - \mu_L^0}{RT} \right] - \tilde{k}_L \ \exp \left[\frac{\mu_T - \mu_T^0}{RT} \right] \ .$$

With simple mathematical manipulations one derives

$$w^{(3.1)} = \tilde{k}_L \ \exp \left[\frac{\mu_T - \mu_T^0}{RT} \right] \ \left(\exp \left[-\frac{A^{(3.1)}}{RT} \right] - 1 \right) \, , \tag{3.65}$$

where $\mu_T - \mu_T^0$ can be expressed from Eq. (3.59) as a function of c_L, c_T, ε, T. Eq. (3.65) can be linearized for $A^{(3.1)}$ around the equilibrium configuration, in which the latter vanishes

$$w^{(3.1)} = -\tilde{k}_L \ \exp \left[\frac{\mu_T - \mu_T^0}{RT} \Big|^{eq} \right] \ \frac{A^{(3.1)}}{RT} + o(A^{(3.1)}) \, . \tag{3.66}$$

By direct comparison of (3.64) and (3.66), coefficient $L^{(3.1)}$ reads

$$L^{(3.1)} = \tilde{k}_L \ \exp \left[\frac{\mu_T - \mu_T^0}{RT} \Big|^{eq} \right] = \tilde{k}_T \ \exp \left[\frac{\mu_L - \mu_L^0}{RT} \Big|^{eq} \right] \, ,$$

and is always positive.

Species trapping was also pursued by *Thomas and Chopin* [303], who evaluated the rate of species exchange following the approach of *McNabb and Foster* [282]. The latter was used in place of the law of mass action. Such an approach falls beyond the scope of the present contribution.

3.5.1 Infinitely fast kinetics

In many circumstances, the rate limiting process in a multi-physics problem is, by far, often something other than the chemical reaction. For instance: i) the trapping and untrapping of hydrogen in dislocation cores is much faster than its diffusion in the host metal lattice [283, 288]; ii) the kinetics of transformation of high-affinity to low affinity integrins and vice versa in focal adhesions is much faster than the diffusion of the low-affinity integrin itself across the lipid bilayer membrane [304]. In such events it can be assumed that the reaction kinetics is infinitely fast, in the sense that the time required to reach chemical equilibrium is orders of magnitudes smaller than the time-scale of other processes. The concentrations of trapped and interstitial species is then governed by thermodynamic equilibrium at all times, and the trapped concentration c_T can be related to the interstitial one by the equation $A^{(3.1)} = 0$, i.e.

$$\mu_T = \mu_L \qquad \forall\, c_L, \boldsymbol{\varepsilon}, T \ , \tag{3.67}$$

with chemical potentials from Eq. (3.59).

3.6 Governing equations

Governing equations can be derived by incorporating the constitutive equations (3.41b), (3.55), (3.61), and the mass action law (3.62) into the balance equations (3.2), (3.3), and (3.32). Specifically, by using Eqs. (3.13), (3.38), (3.43), (3.44), (3.49), (3.54), and (3.62) the energy balance (3.32) can be written as in the Eq.(3.68d) below. The lengthy algebra that leads to the generalized heat equation is collected in Appendix 3.B. Governing equations are written in term of concentrations c_L and c_T, displacements $\vec{u}$, and temperature T as

$$\frac{\partial c_L}{\partial t} + \mathrm{div}\left[\,\vec{h}_L(c_L, c_T, T, \boldsymbol{\varepsilon}^{cte}, \boldsymbol{\xi})\,\right] + w^{(3.1)}(c_L, c_T, T, \boldsymbol{\varepsilon}^{cte}, \boldsymbol{\xi}) = s_L \ , \tag{3.68a}$$

$$\frac{\partial c_T}{\partial t} - w^{(3.1)}(c_L, c_T, T, \boldsymbol{\varepsilon}^{cte}, \boldsymbol{\xi}) = s_T \ , \tag{3.68b}$$

$$\mathrm{div}\left[\,\boldsymbol{\sigma}(\boldsymbol{\varepsilon}^{cte}, c_L, c_T, T)\,\right] + \vec{b} = \vec{0} \ , \tag{3.68c}$$

$$-T\frac{\partial^2 \psi}{\partial T^2}\frac{\partial T}{\partial t} - \mathrm{div}\left[\,\boldsymbol{K}\,\nabla\left[\,T\,\right]\,\right] = s_q + T\frac{\partial^2 \psi}{\partial T\partial\boldsymbol{\varepsilon}^{cte}} : \frac{\partial\boldsymbol{\varepsilon}^{cte}}{\partial t} + T\frac{\partial^2\psi}{\partial T\partial\boldsymbol{\xi}} : \frac{\partial\boldsymbol{\xi}}{\partial t} + \boldsymbol{\sigma}^d : \frac{\partial\boldsymbol{\varepsilon}^{cte}}{\partial t} +$$

$$+\,\boldsymbol{\sigma} : \frac{\partial\boldsymbol{\varepsilon}^{in}}{\partial t} - \vec{h}_L \cdot \nabla\left[\,{}^u\mu_L\,\right] + \left({}^u\mu_L - {}^u\mu_T\right)w^{(3.1)} \ . \tag{3.68d}$$

Equations (3.68) are accompanied by non linear evolution equations for the viscous stress $\boldsymbol{\sigma}^d$, the inelastic strain tensor $\boldsymbol{\varepsilon}^{in}$, and for $\boldsymbol{\xi}$. Boundary conditions

$$\vec{h}_L \cdot \vec{n} = \overline{h} \qquad \vec{x} \in \partial^N V \ , \tag{3.69a}$$

$$\vec{q} \cdot \vec{n} = \overline{q} \qquad \vec{x} \in \partial^N V \ , \tag{3.69b}$$

$$\boldsymbol{\sigma} \cdot \vec{n} = \vec{\overline{p}} \qquad \vec{x} \in \partial^N V \ , \tag{3.69c}$$

are imposed along Neumann boundaries $\partial^N V$. To ensure solvability of the problem, Dirichlet boundary conditions have to be enforced along $\partial^D V$, where $\partial V = \partial^D V \cup \partial^N V$ and $\partial^D V \cap \partial^N V = \emptyset$.

$$T = \overline{T} \qquad \vec{x} \in \partial^D V \ , \tag{3.70}$$

$$u = \overline{u} \qquad \vec{x} \in \partial^D V \ . \tag{3.71}$$

As assessed in [305], Dirichlet boundary conditions for concentration should not be imposed. The correct boundary condition that enforces equilibrium will be written as an equivalence of chemical potentials. An example will be discussed in section 3.C. Initial conditions are usually imposed for the concentration of interstitial species $c_L(\vec{x}, t = 0)$ as well as of trapped species $c_T(\vec{x}, t = 0)$ and temperature $T(\vec{x}, t = 0)$. To comply with equilibrium thermodynamics these conditions are uniform in volume V and equal to concentrations that are in equilibrium with external species. Balance of momentum, together with boundary conditions, provide the necessary and sufficient equations to solve for $\vec{u}$ at $t = 0$.

It is usual in plasticity to make use of the so-called *three-fields formulation*, in which the pressure is treated as an independent variable not characterized constitutively, whereas Eq.(3.29a) only applies in its deviatioric projection. Such a formulation develops from the Hu-Washizu functional, and the weak formulation of the problem derives from its stationarity with respect to its three fields [306]. It is advantageous to build a *three-field like* weak form for the governing equations (3.68), beause the higher order derivatives involving the trace of the stress tensor can be dealt with numerically in a more effective way.

3.7   Conclusions

A continuum coupled model of transport-reaction-thermo-mechanics with trapping has been dealt with in this chapter. It describes interstitial motion of guest species in a hosting material, with point-wise traps of generic type, their kinetics of filling and emptying, influenced by the mechanical stress state and by the temperature evolution.

The model is framed in a standard thermodynamic [22]. The energy and entropy contributions of the mass flux in the balance equations are accounted for. The selection of the Helmholtz free energy and of the dissipation potential leads to different constitutive characterizations, which apply well to several multi-physics problems. In this regard, this manuscript can be compared to other papers devoted to specific problems. For the important case of hydrogen flow in metal, for example, the present model extends the ones of Krom et al. [287] - which emanates from the previous work of Sofronis and McMeeking [286] - by removing Oriani's assumption of infinitely fast kinetics, Anand and co-workers [307, 305] as well as Toribio and Kharin [289] by extending van't Hoff equation for mass action and introducing mechanical effects. Depending upon the choice of constitutive specifications, the number of material parameters may be significant. In some cases their experimental estimation may be found to be basically impossible. The role of sensitivity analysis and uncertainty quantification, as well as the extension of the present effort to large strains, will be thus very important and carefully considered in further applications of this model to bio- and chemo-mechanics. Two case-studies are reported in order of complexity in Appendix 3.C showing the capability of the present model to reproduce intricated phenomena in different scientific areas. The insertion, diffusion, and trapping of ionic lithium in active particles within battery cells will be studied in Chapter 4.

Appendix

3.A J_2 flow theory with isotropic hardening

We assume that: i) the viscous stress is neglected and $\boldsymbol{\sigma}^e$ identifies with Cauchy's stress $\boldsymbol{\sigma}$; ii) only one scalar internal variable ξ is used and

$$\psi_{in}(\xi) = \frac{1}{2}K^{in}\xi^2 \,, \qquad K^{in} \geq 0 \,, \tag{3.72a}$$

together with a von Mises yield criterion

$$\varphi^{in}(\boldsymbol{\sigma}, \chi) = ||\operatorname{dev}[\boldsymbol{\sigma}]|| - \sqrt{\frac{2}{3}}\sigma_Y + \chi = 0 \,, \tag{3.72b}$$

and associated flow rule (3.58). The term σ_Y in Eq.(3.72b) denotes the yield stress while χ is a hardening parameter defined by Eq.(3.27). Kuhn-Tucker conditions

$$\frac{\partial\lambda}{\partial t} \geq 0 \,, \qquad \varphi^{in} \leq 0 \,, \qquad \frac{\partial\lambda}{\partial t}\varphi^{in} = 0 \,. \tag{3.72c}$$

complete the incremental form of the mechanical constitutive equations.

Owing to definitions (3.27), (3.48), and (3.49) the thermodynamic restriction (3.31a) is rephrased as follows

$$\boldsymbol{\sigma} : \frac{\partial\boldsymbol{\varepsilon}^{in}}{\partial t} + \chi\frac{\partial\xi}{\partial t} - RT\ln(1-\theta_T)\frac{\partial c_T^{max}}{\partial\xi}\frac{\partial\xi}{\partial t} \geq 0 \,. \tag{3.73}$$

In view of normal flow rules (3.58), the first two terms of (3.73) can be written as

$$\boldsymbol{\sigma} : \frac{\partial\boldsymbol{\varepsilon}^{in}}{\partial t} + \chi\frac{\partial\xi}{\partial t} \overset{\varphi^{in}=0}{=} (||\operatorname{dev}[\boldsymbol{\sigma}]|| + \chi)\frac{\partial\lambda}{\partial t} \overset{\varphi^{in}=0}{=} \sqrt{\frac{2}{3}}\sigma_Y\frac{\partial\lambda}{\partial t} \geq 0 \,. \tag{3.74}$$

Restriction (3.73) is left with

$$-\log(1-\theta_T)\frac{\partial c_T^{max}}{\partial\xi}\frac{\partial\lambda}{\partial t} \geq 0 \,. \tag{3.75}$$

The term $\log(1-\theta_T)$ is always negative since the trap concentration c_T cannot exceed the upper bound set by the saturation limit c_T^{max} and thus $0 \leq \theta_T \leq 1$. In view of experimental observations [285] showing that the number of trap sites increases with plastic deformation the positiveness of $\frac{\partial c_T^{max}}{\partial\xi}$ is guaranteed and therefore thermodynamic consistency (3.73) prevails.

3.B Energy balance

Making use of the time derivative of the internal energy (Eq. (3.13)) and of the thermodynamic prescriptions (3.29), the energy balance (3.32) can be written as

$$-T\frac{\mathrm{d}}{\mathrm{d}t}\frac{\partial\psi}{\partial T} = \boldsymbol{\sigma}^d : \frac{\partial\boldsymbol{\varepsilon}^{cte}}{\partial t} + \boldsymbol{\sigma} : \frac{\partial\boldsymbol{\varepsilon}^{in}}{\partial t} + s_q - \operatorname{div}[\vec{q}] + ({}^u\mu_L - \mu_L)\frac{\partial c_L}{\partial t} +$$

$$\left({}^{u}\mu_T - \mu_T\right) \frac{\partial c_T}{\partial t} - \vec{h}_L \cdot \nabla\left[{}^{u}\mu_L\right] + \left({}^{u}\mu_L - {}^{u}\mu_T\right) w^{(3.1)} \,. \tag{3.76}$$

The time derivative of the Helmholtz free energy has been derived in Eq.(3.26). It holds accordingly:

$$-T\frac{\mathrm{d}}{\mathrm{d}t}\frac{\partial \psi}{\partial T} = -T\frac{\partial^2 \psi}{\partial T^2}\frac{\partial T}{\partial t} - T\frac{\partial^2 \psi}{\partial T \partial \boldsymbol{\varepsilon}^{cte}} : \frac{\partial \boldsymbol{\varepsilon}^{cte}}{\partial t} - T\frac{\partial^2 \psi}{\partial T \partial c_L}\frac{\partial c_L}{\partial t} - T\frac{\partial^2 \psi}{\partial T \partial c_T}\frac{\partial c_T}{\partial t} - T\frac{\partial^2 \psi}{\partial T \partial \boldsymbol{\xi}} : \frac{\partial \boldsymbol{\xi}}{\partial t} \,. \tag{3.77}$$

If the latter is inserted in (3.76), the coefficient of $\frac{\partial c_L}{\partial t}$ turns out to be

$$\left(T\frac{\partial^2 \psi}{\partial T \partial c_L} + {}^{u}\mu_L - \mu_L\right) \,,$$

and vanishes in view of identity (3.38a) and of the definition (3.17) of μ_L. The same comes out for the coefficient of $\frac{\partial c_T}{\partial t}$. In summary, the generalized heat equation holds

$$-T\frac{\partial^2 \psi}{\partial T^2}\frac{\partial T}{\partial t} - \mathrm{div}\left[\,\boldsymbol{K}\,\nabla\left[T\right]\right] = s_q + T\frac{\partial^2 \psi}{\partial T \partial \boldsymbol{\varepsilon}^{cte}} : \frac{\partial \boldsymbol{\varepsilon}^{cte}}{\partial t} + T\frac{\partial^2 \psi}{\partial T \partial \boldsymbol{\xi}} : \frac{\partial \boldsymbol{\xi}}{\partial t} + \boldsymbol{\sigma}^d : \frac{\partial \boldsymbol{\varepsilon}^{cte}}{\partial t} +$$
$$+ \boldsymbol{\sigma} : \frac{\partial \boldsymbol{\varepsilon}^{in}}{\partial t} - \vec{h}_L \cdot \nabla\left[{}^{u}\mu_L\right] + \left({}^{u}\mu_L - {}^{u}\mu_T\right) w^{(3.1)} \,, \tag{3.78}$$

with ${}^{u}\mu_L$ and ${}^{u}\mu_T$ from Eq. (3.38b) and $w^{(3.1)}$ from Eq. (3.62).

3.C   Case-studies

Two case studies here dealt with. The first concerns the diffusion of vacancies in an aluminum lattice, induced by a stress field. The diffusion of vacancies is an isothermal process, which occurs without trapping and is thus a simple benchmark for the model described in the previous sections, which has been implemented within a user element (UEL) subroutine of Abaqus/Standard 2013. The outcomes have been compared with *Villani et al.* [308].

The general framework of thermo-chemo-mechanics with trapping applies well to the phenomena of hydrogen embrittlement in metals, which is considered as a second case-study. The transport model developed by Krom and co-workers [287, 288], which emanates from the work of Sofronis and McMeeking [286], fits perfectly the thermodynamic setting discussed in this paper. Both models investigate the effect of hydrostatic stress and trapping on the hydrogen distribution in a plastically deforming specimen steel, assuming that hydrogen atoms diffuse through the lattice, that trap sites are filled by lattice diffusion, and that additional traps are generated by plastic deformation.

3.C.1   Redistribution of vacancies in metals

The redistribution of vacancies in a crystal lattice induced by the stress due to a far-field load is studied on an ideally infinite aluminum plate with a central circular hole of radius $\overline{R} = 1$ μm, see Fig. 3.C.1.

The number of vacancies in moles per unit volume is denoted with c_L. Since the diffusion of vacancies occurs without trapping, neither c_T nor $w^{(3.1)}$ are defined. Furthermore, since the process takes place under thermal equilibrium conditions, there is no evolution of temperature. Finally, to compare with *Villani et al.* [308], energetic interactions have been discarded (i.e. $\chi = 0$). Material properties, K and G, have been taken as independent of vacancy concentration[8]. Following the assumption of elastic perfectly plastic (EPP) material response adopted by [308], no hardening is accounted for. Neither internally generated vacancies, $s_L = 0$, nor body forces have been considered, $\vec{b} = \vec{0}$.

The weak form can be transformed in a first order ordinary differential equation in time if discretization is performed via space-time separated variables, with spatial dependent test and shape functions, whereas nodal unknowns depend solely on time. A family of time-advancing methods based on the so-called θ-scheme can be set up assuming that solution $y(t)$ is given at time t, and that the algorithm is triggered by the initial

---

[8]To be compared against equations (12) and (33) in [308]. The chemical expansion coefficient ω_L replaces coefficient $\frac{\Delta v}{3}$ used in the reference, where Δv was defined as the relaxed lattice volume after one mole of atoms is removed from the lattice.
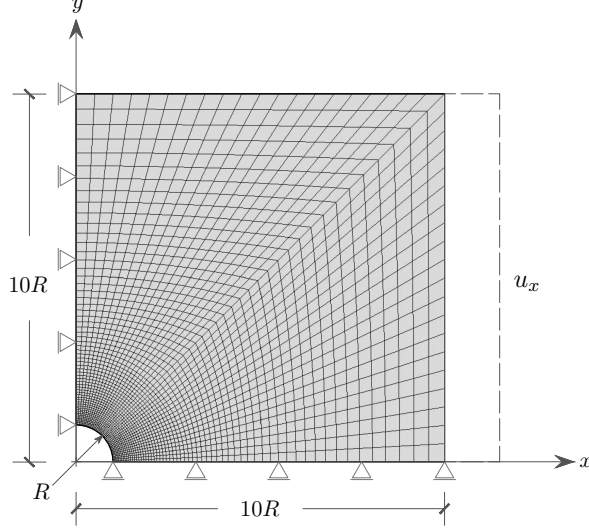
Figure 3.C.1: *Geometry and mechanical boundary conditions:* $\overline{R}$ *is the radius of the hole and* $10\,\overline{R}$ *the length of the edges. A tessellation of 2400 elements is displayed, too.*

conditions at time $t = 0$. The backward Euler scheme ($\theta = 1$) has been selected. A Newton-Raphson iterative algorithm has been implemented in an Abaqus User Element script to solve the non-linear problem. The fields that govern the problem as well as the time are scaled to dimension of unity with scaling factors emanating from constitutive equations.

At the initial time $t = 0$, the concentration of vacancies is taken to be uniform throughout the stress-free body

$$c_L(\vec{x}, 0) = c_L^0 \,, \tag{3.79}$$

with $c_L^0 = 10^{-2} \, \text{mol m}^{-3}$.

The vertical and horizontal displacements along the bottom and left edges have been constrained in view of symmetry, while the top edge and the boundary of the hole have been regarded as traction-free, as depicted in Fig. 3.C.1. A linearly increasing displacement has been enforced along the Dirichlet right edge $\partial^D V = \partial^r V$

$$u_x(\vec{x}, t)|_{\partial^D V} = 0.02\,\overline{R}\,\frac{t}{t_{end}} \,, \qquad \forall t \,\in [0, t_{end}] \,. \tag{3.80}$$

The concentration of vacancies has been prescribed along the top ($\partial^t V$) and right ($\partial^r V$) edges

$$c_L(\vec{x}, t)|_{\partial^t V} = c_L(\vec{x}, t)|_{\partial^r V} = c_L^0 \,, \qquad \forall t \in [0, t_{end}] \,. \tag{3.81}$$

The flux of vacancies across the boundary of the hole ($\partial^h V$) has been set to zero. The same applies to the bottom ($\partial^b V$) and left ($\partial^l V$) edges because of symmetry

$$\vec{h}_L(\vec{x}, t) \cdot \vec{n} = 0 \quad \vec{x} \in \partial^h V \cup \partial^b V \cup \partial^l V \,, \, \forall t \in [0, t_{end}] \,. \tag{3.82}$$

Several discretizations have been used in the numerical analyses. A mesh of 2400 elements is depicted in Fig. 3.C.1.

The hosting material, aluminum, is characterized by Young's modulus $E = 70\,\text{GPa}$, Poisson's ratio $\nu = 0.34$ and yield stress $\sigma_Y = 200\,\text{MPa}$. A negative value $\omega_L = -5 \times 10^{-7} \text{m}^3\,\text{mol}^{-1}$ has been taken for the chemical expansion coefficient, following [308]. From the same reference, it has been assumed a very high

61
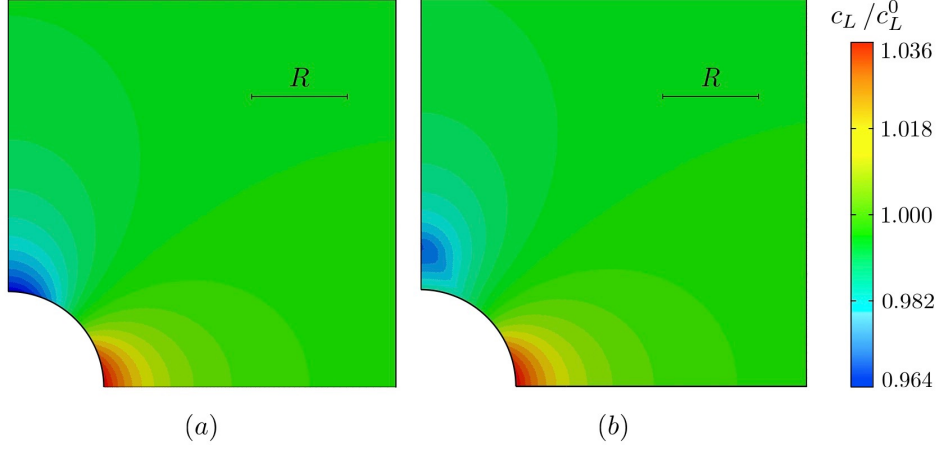
Figure 3.C.2: *Vacancies concentration at time $t = t_{end}$. a) Contour plot of the concentration distribution in an elastic material; b) steady state concentration distribution for elastic perfectly plastic material behavior.*

saturation limit for the vacancies $c_L^{max} = 10^5 \, \mathrm{mol \, m^{-3}}$ and that the process occurs at constant temperature $T = 700 \, \mathrm{K}$. The diffusivity is assumed $\mathbb{D}_L = 10^{-8} \, \mathrm{m^2 \, s^{-1}}$.

Fig. 3.C.2 plots the concentration of vacancies at $t = t_{end}$, normalized by c_L^0. Fig. 3.C.2a depicts the profile of concentration of vacancies in linear elastic materials. Red regions show an increase of concentration whereas the blue ones an opposite tendency. This distribution is consistent with Fig. 6 of [308]. The hydrostatic stress drives vacancy redistribution.

The role of the hydrostatic stress on vacancy distribution is analogous in EPP materials, yet differences arise in Fig. 3.C.2b. The decrease of concentration along the left edge is less pronounced and the location where the minimum is attained is shifted along the edge. The different concentration configurations follow from different stress distribution, see also Fig. 3.C.4a.
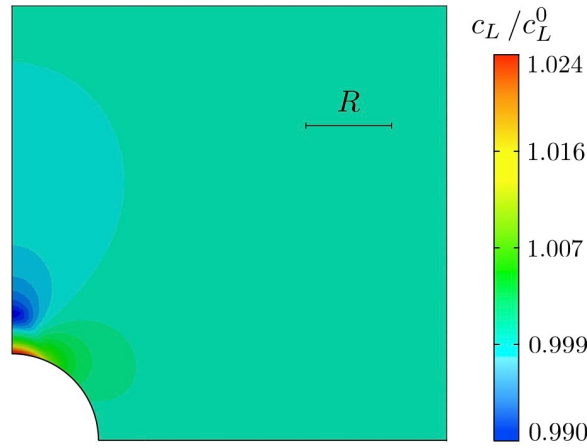
Figure 3.C.3: *Vacancies concentration. Contour plot of the steady state concentration distribution for elastic perfectly plastic material behavior after unloading.*

The effect of a loading-unloading cycle on the distribution of vacancies has been studied and plotted in Fig. 3.C.3. The loading process has been taken from Eq. (3.80) and then reversed until condition $u_x|_{\partial^D V} = 0$ was restored. Plastic deformations persisted after unloading, see Fig. 3.C.3. A non-uniform distribution of vacancies was induced by the corresponding stress field, in agreement with Fig. 9 of [308].

Analytical expressions for the stress and concentration fields at steady state in coupled diffusion-*elasticity* problems are available in [308]. They are depicted in Fig. 3.C.4, in terms of hydrostatic stress and concentration distribution along the perimeter of the hole (where angles $\delta = 0°$ and $\delta = 90°$ correspond to the bottom and left edges, respectively).
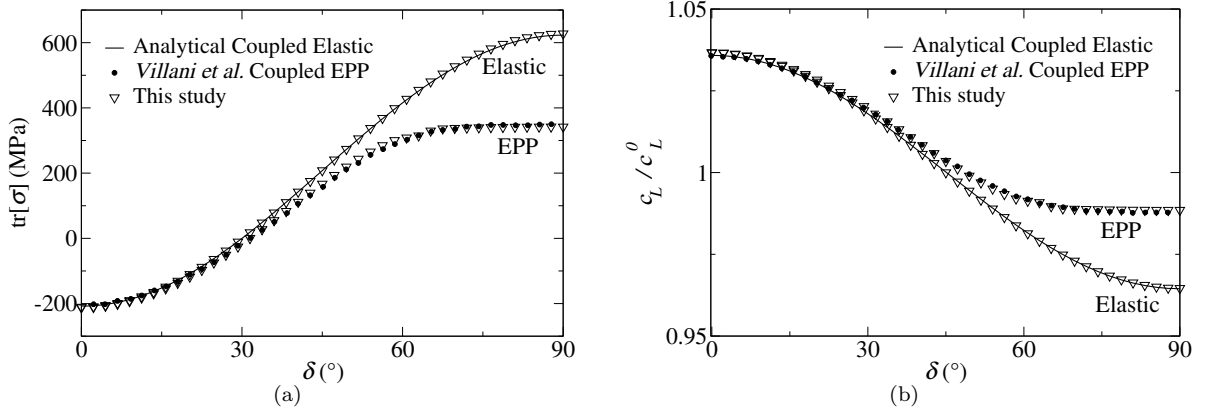
Figure 3.C.4: Distribution of the hydrostatic and of the concentration of vacancies along the hole of the plate. The latter has been normalized by the initial concentration c_L^0. The analytical solution for the coupled elastic-transport problem is plot with a continuous line and compared to the outcomes of the numerical analyses in Villani et al. (dots) and of this contribution (triangles) at time $t = t_{end}$. EPP identifies the elastic perfectly plastic material behavior.

The finite element approximation for the trace of the hydrostatic stress in elastic materials is excellent: it perfectly overlaps the analytical solution, see Fig. 3.C.4-a. For an elastic perfectly plastic (EPP) material a reduction of the stress gradient is visible for $\delta > 40°$, due to the Mises stress being limited by the yield stress σ_Y. The numerical approximation obtained with the present formulation is in perfect agreement with the numerical outcomes reported by *Villani et al.* [308], as depicted in Fig. 3.C.4-a.

Note that stresses do not seem to be influenced by vacancy concentrations, since the swelling contribution is very small compared to the mechanical deformations.

Figure 3.C.4-b shows the concentration profiles, predicted either analytically (Elastic) and numerically (Elastic and EPP), expressed in terms of the vacancy concentration normalized by c_L^0 along the surface of the hole. A good agreement has been found against the solution provided by [308]. Numerical results show deviations of the vacancy concentration from the initial value within a 5% range. As a consequence, $c_L \ll c_L^{max}$, which could be consistent with an infinitely dilute solution formulation.

3.C.2 H-embrittlement in metals

The model of Krom and coworkers assumes *thermal equilibrium* and *infinitely fast chemical kinetics* for trap filling. The latter hypothesis is usually attributed to Oriani [283], who postulated that within a continuum-level material point the microstructure affects the local distribution of hydrogen, keeping the hydrogen in trapping sites in thermodynamic equilibrium with lattice sites.

On the unsatisfactory basis that there is insufficient information either from experiments or detailed micro mechanical models, it is accepted that chemical expansion coefficients ω_L and ω_T are equal. Furthermore, since during hydrogen diffusion no significant phase changes seem to arise in steel, concentrations have little influence on its elastic properties.

The concentration of trapped hydrogen c_T is therefore related to the interstitial amount c_L by formula (3.67), that under the usually accepted assumption that $\theta_L \ll 1$ reads

$$\theta_T = \left(1 + \frac{1}{K_{eq}\,\theta_L}\right)^{-1} . \tag{3.83}$$

63

Equation (3.83) replaces the governing Eq.(3.68b).

Kumnick and Johnson [285] carried out permeation tests on pure iron with hydrogen gas charging and found that the trap density in iron increases sharply with deformations at low deformation levels and increases more gradually with further deformation. They also envisioned one single type of trap and estimated a trap binding energy $\Delta E_\tau = -60 \, \text{kJ} \, \text{mol}^{-1}$ independent of the deformation level within the range of $0 - 80\%$ cold work and independent on temperature within the range of $288 - 343$K. A fit of the number of trap sites vs equivalent plastic strain ε^p which is close to their experimental observations is

$$\log[c_T^{max} \, N_A] = 23.26 - 2.33 e^{-5.5\varepsilon^p} \,, \tag{3.84}$$

with N_A denoting Avogadro's number. After some manipulations, Eq.(3.68a) transforms into the following

$$\left[1 + \frac{c_T^{max}(\varepsilon^p)}{c_L^{max}} \frac{K_{eq}}{(1 + K_{eq}\theta_L)^2} \right] \frac{\partial c_L}{\partial t} + \theta_T \frac{\partial c_T^{max}}{\partial \varepsilon^p} \frac{\partial \varepsilon^p}{\partial t} - \text{div} \left[\mathbb{D}_L \, \nabla \left[c_L \right] - 3 \, \omega_L \, \boldsymbol{M}(c_L) \, \nabla \left[p \right] \right] = 0 \,. \tag{3.85}$$

A fit of data from [285] was adopted by *Sofronis and McMeeking* [286] to account for the dependence of the number of traps on plastic deformation $c_T^{max}(\varepsilon^p)$. The term $\theta_T \frac{\partial c_T^{max}}{\partial \varepsilon^p} \frac{\partial \varepsilon^p}{\partial t}$ was introduced later by *Krom et al.* [287], who adopted (3.84) to follow the history variation of traps.

The diffusivity $\mathbb{D}_L = 1.27 \times 10^{-8} \, \text{m}^2 \, \text{s}^{-1}$, the chemical expansion coefficient $\omega_L = 6,67 \times 10^{-7} \text{m}^3 \, \text{mol}^{-1}$, the saturation limit for lattice population $c_L^{max} = 8,43 \times 10^5 \text{mol} \, \text{m}^{-3}$, as well as the standard Gibbs free energy change for the reaction $\Delta E_\tau = -60 \, \text{kJ} \, \text{mol}^{-1}$ have been chosen according to [286]. The equilibrium constant was determined to be $K_{eq} = 2,8 \times 10^{10}$ by making use of Eq.(3.50).

The Young's modulus $E = 207$ GPa, Poisson's ratio $\nu = 0,3$ and initial Yield stress $\sigma_{Y0} = 250 \, \text{MPa}$ were taken. The power-law hardening relationship adopted in [286] for the host material has been piecewise linearized, see Fig. 3.C.5.
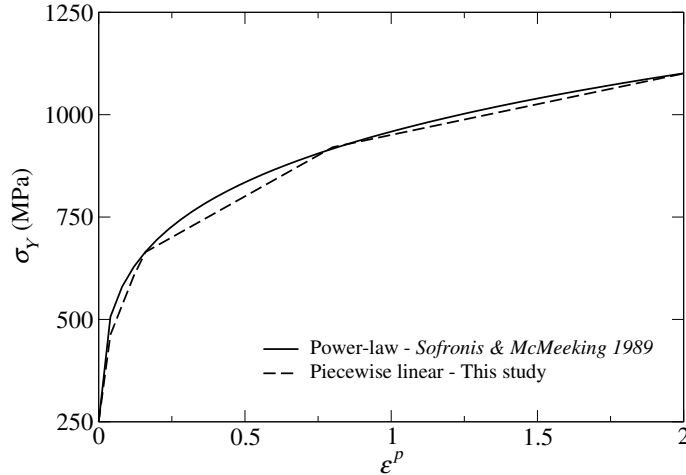
Figure 3.C.5: *Plot of the yield stress dependence on equivalent plastic strain. Comparison between the power law adopted in the literature [287, 286, 305] and the piecewise linear approximation adopted in the present contribution.*

3.C.2.1 Infinite plate with a circular hole

Consider the infinite plate with a circular hole analyzed in section 3.C.1 with a uniform concentration $c_L^0 = 3.46 \times 10^{-3} \text{mol} \, \text{m}^{-3}$ of hydrogen in the lattice which is in equilibrium with a trap population c_T^0 according to (3.83). The initially undeformed body is subject to a far field displacement, able to induce plastic deformations in the region nearby the hole, which generate new trap sites. The process leads to a

redistribution of hydrogen both in the lattice and in the newly generated traps. The hole is insulated and boundary condition (3.82) holds, i.e. the surface insertion/extraction of hydrogen between the body and the environment is very slow compared to the speed of the redistribution of internal hydrogen due to diffusion coupled to mechanical stresses. Thermal equilibrium is enforced at $T = 300\,\mathrm{K}$.

The imposed displacements along the right edge have been tuned according to (3.80), adopting

$$u_x(\vec{x}, t)|_{\partial^D V} = 0.02\,\frac{t}{t_{end}}\,, \qquad \forall t \in [0, t_{end}]\,, \tag{3.86}$$

and values of t_{end} ranging from $1\,\mathrm{s}$ to $100\,\mathrm{s}$ in order to investigate the effect of the strain rate. The surrounding part of the body is set to be a reservoir of hydrogen: the concentration is thus prescribed[9] according to (3.81). Boundary conditions (3.82) have been applied on the remaining edges.

Figure 3.C.6-a shows the behavior of the hydrostatic stress and the concentration divided by the initial value along the boundary of the hole ($\delta = 0°$ and $\delta = 90°$ respectively indicate bottom and left edges). It is worth noticing that the distribution of lattice concentration is reversed with respect to section 3.C.1 which is expected in view of the positiveness of ω_L. The non-symmetric profile of concentration agrees with the distribution of vacancies in aluminum when the elastic perfectly plastic material behavior was considered.

Figure 3.C.6-b shows the distribution of the equivalent plastic strain ε^p, trap concentration c_T and saturation limit c_T^{max} along the boundary of the hole. Concentrations have been normalized by c_L^0. The number of traps increases by 50% on the upper part of the hole, where plastic deformations occur, in agreement with Eq.(3.84). Traps sites are close to the saturation limit ($\theta_T \sim 0,99$), in agreement with constraint (3.83).

Numerical analyses have been carried out at different strain rates. No major differences in either c_L or c_T distributions have been observed (Fig. 3.C.6b refers to the outcomes obtained for $t_{end} = 100\,\mathrm{s}$), since the deformation induced by the boundary conditions is not sufficiently large to induce a depletion of the lattice sites in favor of traps.

3.C.2.2 Diffusion at a blunted crack tip

A specimen containing a small blunted crack tip is considered, as in Fig. 3.C.7. It is embedded in a gaseous hydrogen environment at pressure $p_{H_2} = 1\,\mathrm{atm}$ and temperature $T = 300\mathrm{K}$. The latter does not change during the whole process. The specimen has an initial uniform interstitial hydrogen content $c_L^0 = 3.46 \times 10^{-3}\,\mathrm{mol\,m^{-3}}$. A plane strain, local yielding configuration is enforced - as in [286] - by choosing a small crack tip radius, negligible if compared to the specimen characteristic length. In this way, the small scale yielding conditions are satisfied, i.e. the plastic zone is confined in an annular area about the crack tip whose size is negligible compared with any dimensions of the specimen. The boundary of the annulus is subjected to a given displacement field

$$u_x\left(\overline{R}, \delta\right) = \frac{K_I}{2\,\mu}\sqrt{\frac{\overline{R}}{2\,\pi}}\,\cos\left(\frac{\delta}{2}\right)\left[2 - 4\nu + 2\sin^2\left(\frac{\delta}{2}\right)\right]\,, \tag{3.90}$$

---

[9]Although concentrations are widely imposed as Dirichlet boundary conditions, the latter should rather enforce the equilibrium between H$_2$ in the the environment and the lattice hydrogen [305] as an equivalence of chemical potentials

$$\mu_L = \frac{1}{2}\,\mu_{H_2}\,. \tag{3.87}$$

According to [305], the chemical potential μ_{H_2} can be expressed in terms of the fugacity f_{H_2} of the gaseous species and a reference pressure p^0

$$\mu_{H_2} = \mu_{H_2}^0 + RT\,\ln\frac{f_{H_2}}{p^0}\,. \tag{3.88}$$

The standard chemical potential $\mu_{H_2}^0$ conventionally vanishes at a pressure of 0.101MPa and at a temperature of 298K. Equation (3.87) thus leads to a non linear boundary condition of type

$$RT\,\ln\frac{c_L}{c_L^{max} - c_L} - 3\,\omega_L\,p = \frac{\mu_{H_2}^0}{2} - \mu_L^0 + RT\,\ln\sqrt{\frac{f_{H_2}}{p^0}} \qquad \vec{x} \in \partial^D V\,, \tag{3.89}$$

.

65
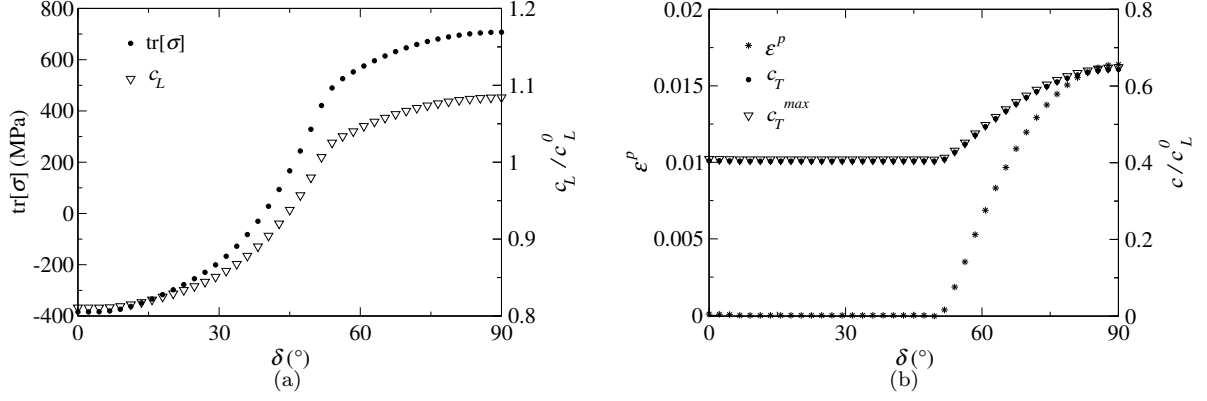
Figure 3.C.6: Two dimensional plots of a) hydrostatic stress and lattice concentration and b) equivalent plastic strain together with trap concentration and trap saturation limit along the hole of the plate. All the concentration distributions have been normalized by the initial lattice concentration c_L^0. The plots refer to the last step of increment of load, $t_{end} = 100\,\text{s}$

$$u_y\left(\overline{R}, \delta\right) = \frac{K_I}{2\,\mu} \sqrt{\frac{\overline{R}}{2\,\pi}} \sin\left(\frac{\delta}{2}\right) \left[4 - 4\nu - 2\cos^2\left(\frac{\delta}{2}\right)\right],$$

which induces a tensile Mode-I loading [286]. In Eq.(3.90) K_I is the stress intensity factor obtained from the linear elastic crack problem *at the specimen length-scale*. K_I is linearly increasing in time

$$K_I(t) = \tilde{K}_I \frac{t}{t_{end}} \quad t \in [0, t_{end}], \tag{3.91}$$

where $\tilde{K}_I = 89,2\,\text{MPa}\,\text{m}^{-1/2}$ and $t_{end} = 130\,\text{s}$. Displacements along the y direction have been constrained along the symmetry axis while the crack surface has been modeled as traction-free, see Fig. 3.C.7.

In order to compare our results with [287], the contributions of the pressure and of the saturation of c_L are neglected in boundary condition (3.89), while the fugacity equals the external pressure, exploiting the ideal gas model. In this way the lattice concentration at the external boundary coincides with the initial value inside the specimen. Its numerical value is computed from Sievert's law:

$$c_L = K_s \sqrt{p_{H_2}} \exp\left(\frac{-\overline{\Delta H}}{RT}\right), \tag{3.92}$$

where the experimentally measured constants K_s, $\overline{\Delta H}$ hold [286]:

$$K_s = 1040\frac{\text{mol}}{\sqrt{\text{MPa}}\,\text{m}^3} \qquad \overline{\Delta H} = \mu_L^0 = 28.6\frac{\text{KJ}}{\text{mol}}. \tag{3.93}$$

The initially uniform concentration $c_L^0 = 3.46 \times 10^{-3}\,\text{mol}\,\text{m}^{-3}$ is computed from (3.92) at $T = 300\,\text{K}$ and $p_{H_2} = 1\,\text{atm}$. A uniform initial concentration c_T^0 is established in view of equilibrium condition (3.83). Lattice concentration $c_L = c_L^0$ has been prescribed along the outer radius and the crack surface to simulate a process in which the reaction kinetics with the environment is fast compared to the diffusion rate of the hydrogen Along the symmetry axis the hydrogen flux has been set to zero.

The mesh consists of approximately 1200 elements (about 60 and 20 along the radial and tangential direction respectively) biased from the notch across the annulus.
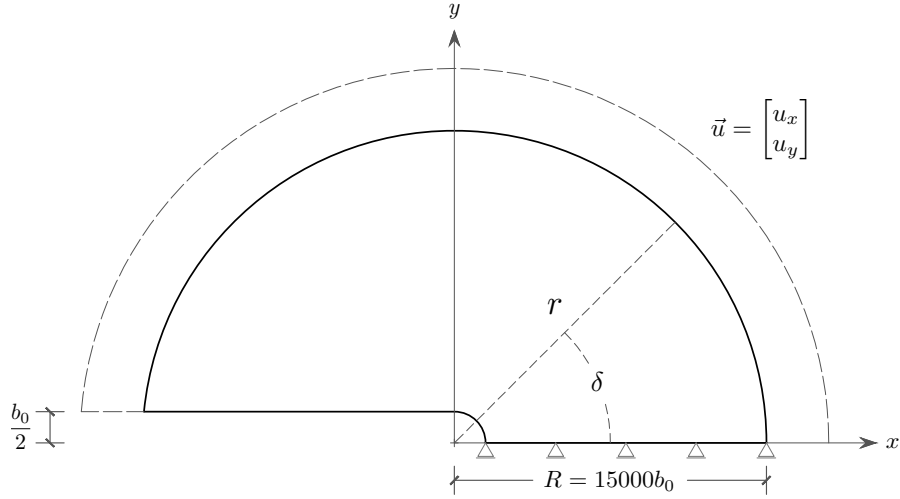
Figure 3.C.7: Schematic of the blunted crack geometry and boundary conditions. The initial crack tip opening displacement is b_0 and the external radius of the domain used in numerical analyses is R. Following [287, 286, 305], the diameter of the notch is $b_0 = 10 \, \mu m$ and the outer radius is $\overline{R} = 15000 \, b_0$.
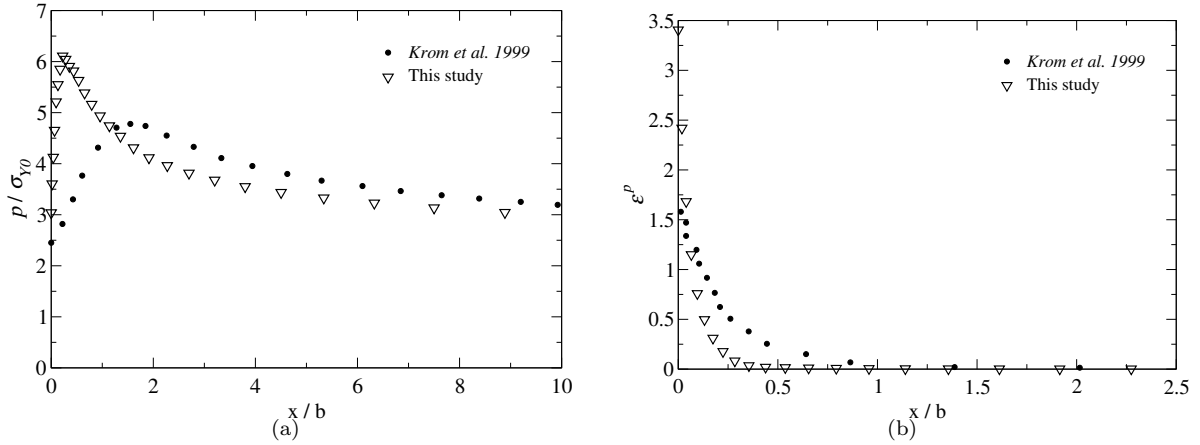
Figure 3.C.8: (a) Pressure divided by the initial yield stress σ_{Y0}; (b) Equivalent plastic strain in proximity of the crack tip along the symmetry axis (two different scales have been used for the x-axis). The plots show a comparison between numerical analyses carried out in this work and the results of Krom et al. [287] referring to the final step of load application, $t = 130 \, s$.

Figure 3.C.8 plots the pressure distribution as well as the equivalent plastic strain ε^p in proximity of the blunted crack tip along symmetry axis x. Coordinate x has been normalized to the *nominal crack-tip opening displacement* $b = 4.7 \, b_0$ following [287]. Plots refer to time $t = 130 \, s$.

A comparison with the results of *Krom et al.* [287] is made. An overestimation of the pressure and a shift of the peak is shown. The maximum predicted equivalent plastic strain roughly doubles the one predicted by *Krom et al.*. These differences are due to the hypothesis of small deformations, that severely influences the outcomes around the crack tip. The value of the equivalent plastic strain in Fig. 3.C.6-b and Fig. 3.C.8-b differ by two orders of magnitude, which shows the different impact on trap generation in the two examples.

Figure 3.C.9 shows the distribution of concentrations c_L and c_T along the symmetry axis at different
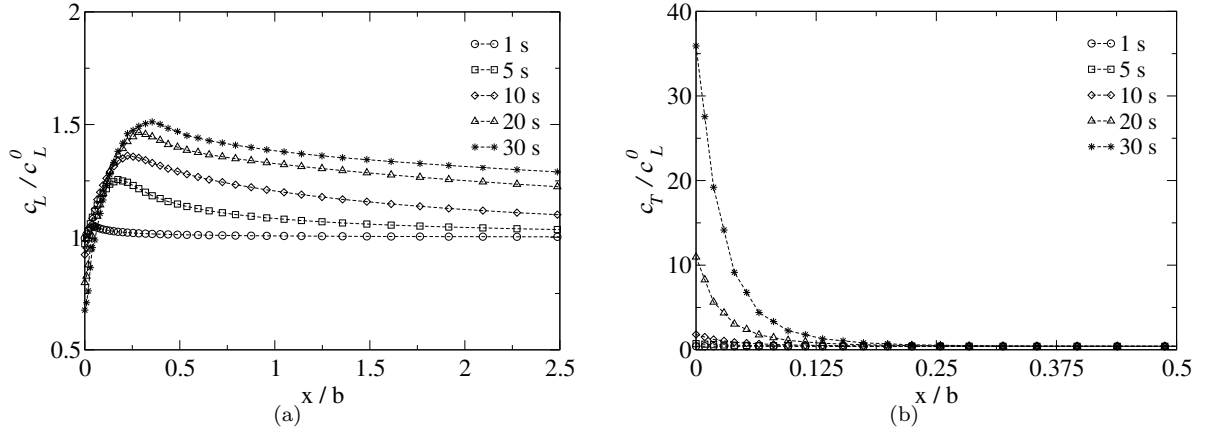
Figure 3.C.9: Plot of lattice (a) and traps (b) concentration normalized to the initial lattice concentration c_L^0 in proximity of the crack tip for different instants of time during the loading process (two different scale have been used for the x-axis).

times. An increase of trap concentration is limited to a narrow zone across the crack tip, in agreement with the development of plasticity predicted by the small strain theory, Fig. 3.C.8-b. A depletion of concentration in the lattice follows.

It can thus be concluded that the assumption of small strains should be questioned for the evaluation of strains and stresses in the vicinity of the crack tip (although blunted), since it may induce significant errors. This interesting conclusion strengthens the motivation for the extension of the present formulation to finite strains, which is in progress and will be the subject of further publications.

Chapter 4

On the response of active particles accounting for Li trapping

4.1 Introduction

The topic of insertion reaction electrodes is a major feature of battery systems. Intercalation and de-intercalation denote reactions involving insertion and extraction of guest species in host materials that have layer-type crystal structures [277]. When the hosting material has such a crystal structure there is space available for the presence of small ionic species as cations Li^+. Lithium Cobalt Oxide ($LiCoO_2$) is one of these materials. It has been studying for almost 40 years [309], showing excellent properties which make it widely used as cathode material for commercial applications.

Depending upon the lithium content, the mobile species in $LiCoO_2$ can randomly occupy sites between the layers (the so-called galleries) or may cause a modification of the host structure. In the former case, transient concentration gradients take place in the gallery space, whereas during phase-transitions the insertion process involves the motion of an interface that separates the Li-poor from the Li-rich regions. Thermodynamically, the voltage remains constant during the phase transition.

In this chapter the chemo-mechanical framework developed in Chapter 3 will be applied in order to investigate the response of a spherical particle accounting for trapping of Li ions. The material parameters that govern the chemical response will be tailored to simulate the experimental evidence of $LiCoO_2$ electrodes. To this end the electro-chemo-mechanical behavior of $LiCoO_2$ upon charge and discharge is reviewed in Section 4.2. Subsequently, in Section 4.3, the impact of Li trapping is investigated at thermodynamic level focusing on lithium free energy density. Governing equations are recalled from Chapter 3, in Section 4.4, for isothermal conditions, and then specialized in Section 4.5 for a spherical particle. The transient response of the particle upon both lithiation and delithiation is investigated through numerical examples in Section 4.6.

4.2 A review of experimental evidence and their modeling

$LiCoO_2$ provides good capacity, high energy density, good power rates, and excellent cycle life [309]. Such a favorable electrochemical behavior is associated with a sequence of phase transitions, which progressively change the crystal structure. Pristine lithium cobalt oxide possesses a layered structure, as reported in Figure 4.1a. The hexagonal unit cell consists of oxygen planes staked in an ABCABC sequence, with cobalt and lithium ions occupying alternative layers of octahedral sites. During battery charging, an external voltage forces the extraction of Li ions, perturbing the original crystal structure.

Reimers and Dahn [310] proposed a phase diagram for $LiCoO_2$ based on their experimental observation (Fig. 4.1b). It depicts the possibility of phase transitions as a function of temperature and lithium content (x in Li_xCoO_2). The phase change regions have been identified from the measured cell voltage profile for the first charge and discharge (Fig. 4.1c). The lattice parameters of the unit cell were also measured, pointing out the deformable behavior associated with Li insertion/removal.
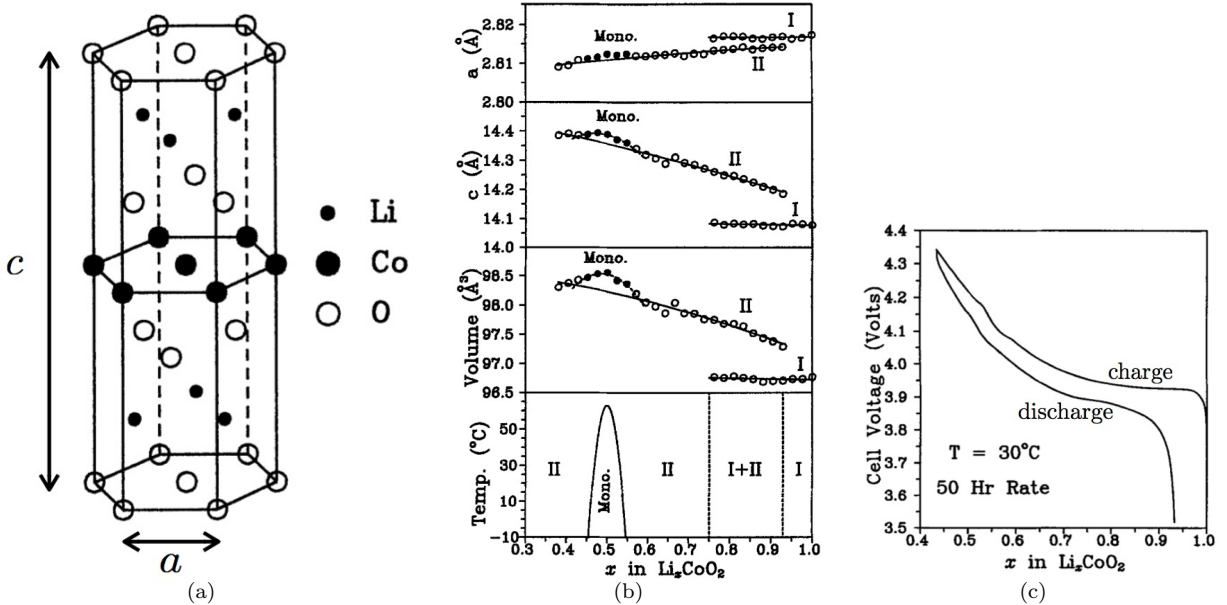
Figure 4.1: (a) Schematic diagram of the $LiCoO_2$ unit cell; (b) phase diagram and lattice parameters evolution as a function of lithium concentration x; (c) voltage profile for first charge and discharge as a function of lithium content x. Figures have been reprinted from [310].

A characteristic feature of $LiCoO_2$ electrodes is the voltage plateau observed between $x = 0.75$ and $x = 0.93$. Plateaus are distinctive of first-order phase transitions [277], where two different phases (as for I and II in Fig. 4.1b) coexist in the host. Those phases in $LiCoO_2$ consist of hexagonal unit cells, differing for lithium content and lattice parameters. The unit cell volume of Li rich phase I seems to be insensitive to the lithium content, while poor Li phase II contracts when Li increases.

Further lithium removal from $Li_{0.75}CoO_2$ leads to an order/disorder phase transition at $x \sim 0.5$, which also affects the geometry of the unit cell. When enough lithium is removed, the unit cell may undergo an ordering transition toward a monoclinic crystal structure. Such a transition is temperature dependent, as pointed out in the phase diagram in Fig. 4.1b, and involves considerable lattice deformations.

The extraction process may continue until the end member CoO_2, by application of greater voltages, as done in *Amatucci et al.* [311]. However, for $x < 0.5$ the hosting material highly degrades, affecting the reversibility of the intercalation process. The available Lithium for commercial application is thus considered to be about 50% of the pristine $LiCoO_2$, i.e. $0.5 \leq x \leq 1.0$.

The phase transformations taking place in lithium cobalt oxide have been investigated theoretically from first principles calculations [312]. This approach, in addition to predict the phase diagram, allow identifying the physical origin of the phase evolution. As discussed in [313], three mechanisms may lead to phase transition in metal oxides: *configurational*, *structural*, and *electronic transitions*.

Configurational transitions are driven by vacancies creation or annihilation. They involve ordering and disordering transitions, which modify the lithium-vacancies configuration. When the lithiation process involves also rearrangements of the host atoms (i.e. Co and O) we refer to *structural transitions*. *Electronic transitions* take place when change in the host are caused by changes in electronic properties driven by lithium content or temperature variations.

First principles calculations [312] confirmed the presence of order/disorder transition for $x \sim 0.5$, as measured experimentally. They assessed that the voltage plateau from $x = 0.75$ to $x = 0.93$ is a first-order electronic transition, since the host undergoes metal-insulator transition in addition to the structural change measured by *Reimers and Dahn*. It turns out that $LiCoO_2$ is metallic for $x < 0.75$ and semiconductor for

70

$x > 0.93$. The difference in lithium content also induces lattice mismatches. The phase-segregating behavior of LiCoO$_2$ has thus great impact on its electrochemical, thermal, and mechanical properties.

Due to the layered structure of the unit cell, Lithium diffuses through 2D pathways, which are dependent on crystal orientation. For this reason, accurate measurements have been carried out on thin films (rather than polycrystalline) LiCoO$_2$ electrodes [314, 315], in terms of diffusion coefficient D_{Li}. During phase change, the overall lithium diffusion in influenced by the phase boundary motion, which in turn is affected by the diffusion in each coexisting phase. Therefore application of Fick's law for the total lithium is inadequate in the phase change regime.

Mechanical properties of LiCoO$_2$ have been measured and predicted with molecular dynamics simulations as well [316, 317]. Elastic parameters, e.g. bulk (K) and shear (G) moduli, reflect the anisotropic behavior of lithium cobalt oxide crystals as well as their dependence on lithium content. In situ measurement of mechanical integrity of the electrode particle showed a degradation mechanism that is compatible with plastic deformations of LiCoO$_2$ [318].

As reviewed in [319], several intercalation models for phase-segregating electrodes have been recently proposed at the continuum scale. They aim at capturing the evolution of phase-interface that separates zones at different lithium content. Widespread approaches in this regard are the so called *sharp-interface* and *phase-fields models*.

The former approach splits the electrode particles in two distinct regions, with prescribed Lithium concentration jump at the interface, resembling two coexisting phases separated by a zero-thickness interface. The phase-boundary motion is controlled by the Lithium transport on each phase, as well as by the concentration gap at the interface. This model has been applied to spherical electrode particles, and also referred as *core-shell models*, often in conjunction with the porous electrode theory of Newman [241]. Mechanical effects can be incorporated in sharp-interface models, thus capturing the localization of severe stress states near the phase-boundary [32, 320].

The intercalation process in LiCoO$_2$ in spherical particles has been simulated with sharp-interface models accounting for the first-order phase transition from $x = 0.75$ and $x = 0.93$ [321, 243]. The insertion/removal process has been divided in three stages, to mimic the observed phase-diagram: two with a homogeneous host phase, I or II, and a third characterized by coexisting Li rich and poor phases.

Phase-fields models, usually stemming from Cahn-Hilliard theory, smears the phase boundary in a narrow region of finite thickness, thus avoiding localized discontinuities. The dynamics of phase-segregation is ruled by the free energy of the system. Differently from the Fickian description of diffusion, the Helmholtz free energy includes an interface energy, related to Li concentration gradients. Phase-segregation arises as a consequence of the thermodynamic evolution of the system. Such an approach has been used to simulate the spinodal decomposition in LiFePO$_4$ [250, 252] but are potentially applicable for intercalation in LiCoO$_2$ electrodes.

Alternative methods to recover lithium concentration profiles distinctive of phase-segregation have been proposed. In [300] the sequence of phase-segregations in graphite is modeled starting from a non-convex free energy profile, reflecting multiple equilibrium configurations, without resorting to interface energies. The driving force for lithium transport results to be proportional to hydrostatic stress gradients during phase transition, while in the single phases the lithium mass flux depends on concentration gradients as well. Li transport differs between single to multi-phases regimes, simulating the onset of sharper concentration fronts during phase-change.

A sharp-interface was even reproduced either creating a series of step-like concentration profiles [254] or by choosing concentration dependent parameters [255]. In [256, 257] the lithium within active particles is separated in mobile and alloyed by a kinetic process, which ultimately permits to recover a sharp interface. The present work follows this path of reasoning.

4.3   Free energy at chemical equilibrium

Following the theoretical framework developed in Chapter 3, lithium ions may reside in two distinct sites of the hosting material, namely *interstitial* and *trapping* sites. The *interstitial sites* are represented by specific sites among the host atoms where intercalated Li ions can easily move through. In addition, Li ions may

immobilize in specific *trapping sites* of the hosting structure, so that part of the intercalated lithium ceases to diffuse through the solid. The lithium diffusing interstitially will be denoted hereafter with Li_L and its molar concentration with c_L. On the other hand, trapped lithium will be denoted with Li_T and its concentration with c_T. The trapping process of lithium is then described by the following chemical reaction

$$\text{Li}_L \underset{k_L}{\overset{k_T}{\rightleftarrows}} \text{Li}_T \,, \tag{4.1}$$

which portrays the conversion of mobile to trapped species and vice versa by the rate of the reaction (4.1), denoted with $w^{(1)}$.

The energetic difference between Li ions occupying the interstitial and trapping sites, i.e. $\mu_L^0 - \mu_T^0$, is proportional to the *constant of chemical equilibrium* K^{eq} through the formula

$$\mu_L^0 - \mu_T^0 = R\,T \ln\left[K^{eq}\right] \,. \tag{4.2}$$

As derived in Chapter 3, the affinity $A^{(4.1)} = \mu_T - \mu_L$ (μ denotes the chemical potential) is the driving force for the chemical reaction (4.1). Positive values of $A^{(4.1)}$ promote trapping, whereas negative values induce lithium to escape traps. The condition $A^{(4.1)} = 0$ expresses chemical equilibrium, attained when the interstitial and trapped lithium are in such a proportion to infer a null reaction rate in the mass action equation. The latter condition is here adopted in order to assess the impact of the reaction (4.1) on lithium free energy.

Imposing a vanishing affinity, the trapped concentration can be related to the interstitial one by the following identity

$$\theta_T = \left\{ 1 + \frac{1 - \theta_L}{K^{eq}\,\theta_L}\,\alpha \right\}^{-1} \,, \tag{4.3}$$

which arises from Eq. (3.63) under the assumptions of no energetic interactions, i.e. $\chi = 0$, uniform temperature $T = T_0$, and

$$\alpha \;=\; \exp\frac{\left[\frac{\partial \psi_{el}}{\partial c_T} - \frac{\partial \psi_{el}}{\partial c_L}\right]^{eq}}{R\,T}\,\exp\frac{\left[\frac{\partial \psi_{in}}{\partial c_T} - \frac{\partial \psi_{in}}{\partial c_L}\right]^{eq}}{R\,T} \,. \tag{4.4}$$

This simplification allows investigating the evolution of the free energy, specifically its convexity, as a function of the molar fraction of *total* Lithium ions

$$\theta_{\text{Li}} = \frac{c_L + c_T}{c_{\text{Li}}^{max}} = \frac{\theta_L + \gamma\,\theta_T}{1 + \gamma} \,, \tag{4.5}$$

as the phase diagram in Fig. 4.1b advocates. In Eq. (4.5), $\gamma = c_T^{max}/c_L^{max}$ and $c_{\text{Li}}^{max} = c_L^{max} + c_T^{max}$ is the maximum storage capacity for the total lithium, at a point $\vec{x} \in \mathcal{B}$ and time t.

Under chemical equilibrium *at all times*, the diffusive part of the free energy, Eq. (3.49), can be rewritten in a dimensionless form as a function of θ_{Li}, making use of identities (4.3) and (4.5)

$$\hat{\psi}_{diff} \;=\; \hat{\mu}_L^0\,\hat{c}_L^{max}(\theta_{\text{Li}})\,\theta_L(\theta_{\text{Li}}) \,+\, \hat{\mu}_T^0\,\hat{c}_T^{max}(\theta_{\text{Li}})\,\theta_T(\theta_{\text{Li}}) \,+\, \hat{\psi}_\eta(\theta_{\text{Li}}) \,, \tag{4.6a}$$

$$\hat{\psi}_\eta(\theta_{\text{Li}}) \;=\; \hat{c}_L^{max}(\theta_{\text{Li}}) \left\{ \theta_L(\theta_{\text{Li}}) \ln\left[\theta_L(\theta_{\text{Li}})\right] + (1 - \theta_L(\theta_{\text{Li}})) \ln\left[1 - \theta_L(\theta_{\text{Li}})\right] \right\} +$$
$$+\, \hat{c}_T^{max}(\theta_{\text{Li}}) \left\{ \theta_T(\theta_{\text{Li}}) \ln\left[\theta_T(\theta_{\text{Li}})\right] + (1 - \theta_T(\theta_{\text{Li}})) \ln\left[1 - \theta_T(\theta_{\text{Li}})\right] \right\} \,, \tag{4.6b}$$

being $\hat{\psi}_\eta$ the entropic part of the diffusive free energy [322] and

$$\hat{\mu}_\beta^0 = \frac{\mu_\beta^0}{R\,T} \,, \qquad \hat{c}_\beta^{max} = \frac{c_\beta^{max}}{c_{\text{Li}}^{max}} \,. \tag{4.6c}$$

Eq. (4.6) is parametrized by the equilibrium constant K^{eq}, the parameter α, and constants γ and $\hat{\mu}_T^0$. Note that in view of the formula (4.2) $\hat{\mu}_L^0$ and $\hat{\mu}_T^0$ are not independent.

A study of the influence of α and K^{eq} on $\hat{\psi}_\eta(\theta_{Li})$ is shown in Fig. 4.1, where coefficient γ is taken as unit. Under this assumption, convexity of $\hat{\psi}_\eta(\theta_{Li})$ is lost when the ratio $K^{eq}/\alpha > 21.9071$.
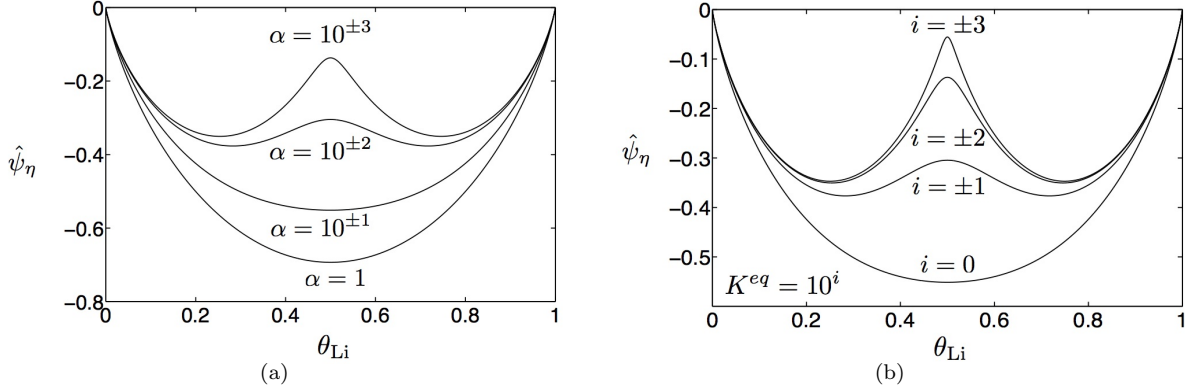
Figure 4.1: *Plot of the non-dimensional entropic free energy for $\gamma = 1$. a) for different values of α, assuming $K^{eq} = 1$: the free energy loses convexity at $\alpha = 21.9071$; b) for different values of K^{eq}, assuming $\alpha = 0.1$: the free energy loses convexity at $K^{eq} = 2.19071$.*

To further investigate the behavior of $\hat{\psi}_\eta$, the interstitial and trapping contributions have been split as

$$\hat{\psi}_\eta = \hat{\psi}_\eta^L + \hat{\psi}_\eta^T \,,$$

with obvious meaning of $\hat{\psi}_\eta^L$, $\hat{\psi}_\eta^T$ from Eq. (4.6b). Each contribution $\hat{\psi}_\eta^\beta$, $\beta = L, T$, is convex and exhibits a single minimum. Moreover $\hat{\psi}_\eta^\beta$ tends to zero either for $\theta_\beta \to 0$ and $\theta_\beta \to 1$. The role played by K^{eq} is evident in Fig. 4.2 where the individual contributions are plotted separately. It turns out that, for $K^{eq} = 10^3$ and $\gamma = 1$, $\hat{\psi}_\eta^L$ is nearly zero until $\theta_{Li} = 0.5$ while it evolves with a characteristic convex shape afterwards. On the other hand $\hat{\psi}_\eta^T$ evolves symmetrically to $\hat{\psi}_\eta^L$ with respect to $\theta_{Li} = 0.5$. This means that Li ions fill trap sites at first while interstitial sites start to fill when traps are almost saturated. The opposite happens for $K^{eq} = 10^{-3}$ because the interstitial sites are in turn energetically favored. For $\gamma \neq 1$ the individual contributions $\hat{\psi}_\eta^\beta$ are no longer symmetric as showed in Fig. 4.3. In particular γ determines the value of θ_{Li} where $\hat{\psi}_\eta^L$ and $\hat{\psi}_\eta^T$ intersect each others.

To summarize, for $|K^{eq}| \gg 1$ the individual contributions of the entropic free energy $\hat{\psi}_\eta^\beta$ evolve separately when plotted against θ_{Li}. Therefore the intercalation of Li ions can ideally divided in two stages: one dominated by Li insertion in interstitial sites and the other dominated by Li insertion in trapped sites. The coordinate θ_{Li} of the transition point between these two stages is tuned by γ independently from K^{eq}.

The interesting non-convex feature of the entropic free energy (see Fig. 4.1) may be wiped out in $\hat{\psi}_{diff}$ by the contribution

$$\hat{\mu}_L^0 \, \hat{c}_L^{max}(\theta_{Li}) \, \theta_L(\theta_{Li}) + \hat{\mu}_T^0 \, \hat{c}_T^{max}(\theta_{Li}) \, \theta_T(\theta_{Li}) \tag{4.7}$$

since the transformation (4.3) is non-linear. This does not happen, as shown in Fig. 4.4a. The influence of K^{eq} and of the linear terms (4.7) is quite evident, though: the first critical point moves toward zero concentration of total lithium, and the higher K^{eq} the less pronounced the change in the convexity for θ_{Li} becomes.

For some values of the parameters, the existence of two minimum energy states disappears, at least in the range $0 \leq \theta_{Li} \leq 1$. As clearly seen in Fig. 4.4b, this happens for $\alpha = 1$. Such a value of α arises when the chemical expansion coefficients of trapped and free species are equal and $\psi_{in} = 0$ (see Eq. (4.4)). These assumptions are generally taken, motivated but not justified by the lack of experimental quantifications [305, 252].
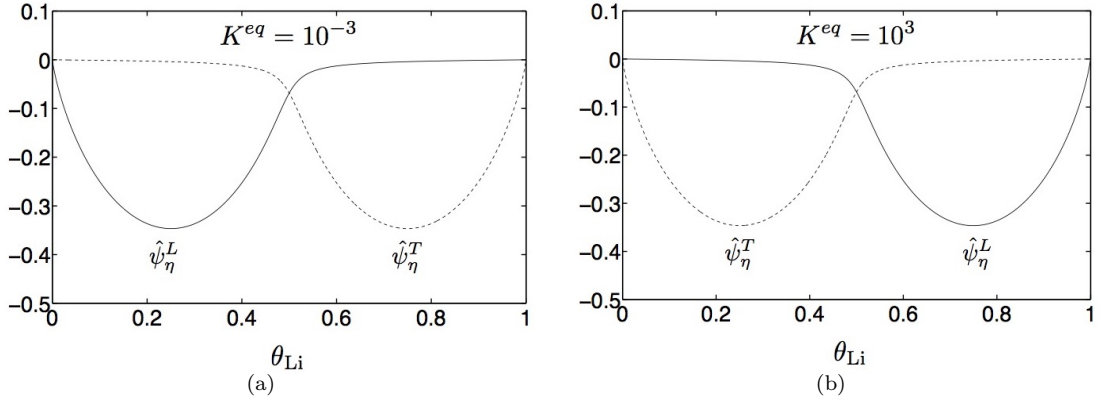
Figure 4.2: *Influence of K^{eq} on the separation between $\hat{\psi}_\eta^L$ and $\hat{\psi}_\eta^T$ for $\alpha = 1$ and $\gamma = 1$.*
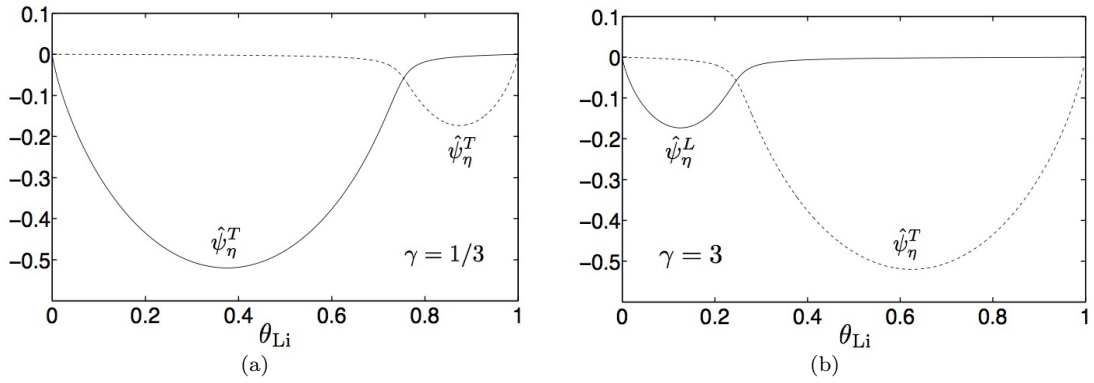
Figure 4.3: *Plot of $\hat{\psi}_\eta^L$ and $\hat{\psi}_\eta^T$ for $K^{eq} = 10^{-3}$ and $\gamma \neq 1$. For $\gamma = 1/3$ the two curves intersect at $\theta_{\mathrm{Li}} = 0.75$ while for $\gamma = 3$ the intersection point is located at $\theta_{\mathrm{Li}} = 0.25$.*
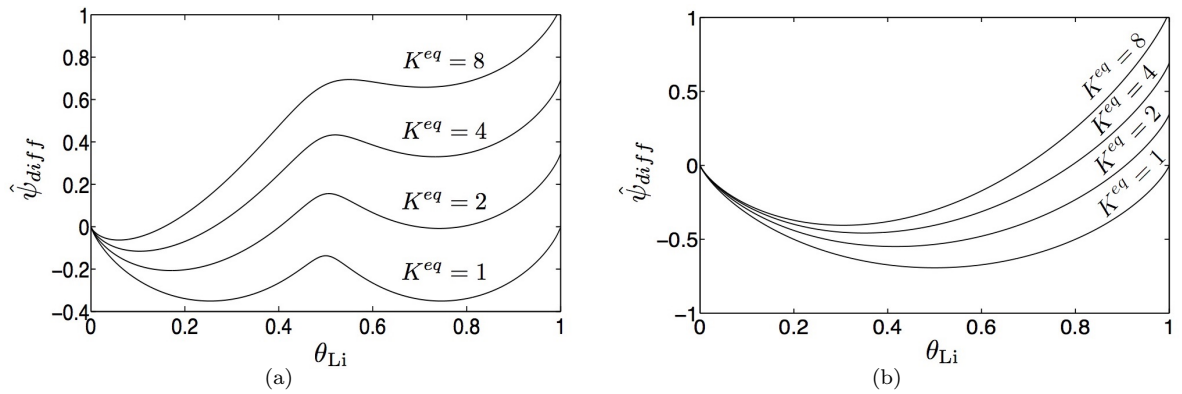
Figure 4.4: *Plot of the non-dimensional diffusive free energy $\hat{\psi}_{diff}$ for different values of K^{eq} for $\gamma = 1$ and $\hat{\mu}_T^0 = 0$. In (a) parameter $\alpha = 10^3$ while $\alpha = 1$ in (b).*

74

4.4 Governing equations for isothermal processes

The general set of governing equations developed in Chapter 3 is here taken in a simplified version in order to evaluate the chemo-mechanical response of a single electrode particle. Exploiting the conditions of thermal equilibrium, i.e. $T = T_0$ for all $\vec{x} \in \mathcal{B}$, governing equations (3.68) reduce to

$$\frac{\partial c_L}{\partial t} + \operatorname{div}\left[\vec{h}_L\right] + w^{(1)} = 0 \,, \tag{4.8a}$$

$$\frac{\partial c_L}{\partial t} - w^{(1)} = 0 \,, \tag{4.8b}$$

$$\operatorname{div}\left[\boldsymbol{\sigma}\right] = \vec{0} \,, \tag{4.8c}$$

for $\vec{x} \in \mathcal{B}$ and time $t \in \,]0\,,\,t_f]$.

The inelastic behavior of the hosting material is modeled without recurring to the internal variables $\boldsymbol{\xi}$ and by prescribing $\psi_{in} = 0$. Moreover we assume that the stress tensor does not include a viscous part so that $\boldsymbol{\sigma} = \boldsymbol{\sigma}^e$ holds hereafter. The evolution of the inelastic deformations is then modeled through the following visco-plastic law of Perzyna type

$$\frac{\partial \boldsymbol{\varepsilon}^{in}}{\partial t} = \frac{\operatorname{dev}\left[\boldsymbol{\sigma}\right]}{\|\operatorname{dev}\left[\boldsymbol{\sigma}\right]\|}\,\lambda \,, \qquad \lambda = \frac{\varphi\,\mathcal{H}(\varphi)}{g(\theta_T)} \,. \tag{4.9a}$$

In equation (4.9a) $\varphi = \|\operatorname{dev}\left[\boldsymbol{\sigma}\right]\| - \sqrt{2/3}\,\sigma_Y$ is the Mises yield function without hardening[1]; $\mathcal{H}$ is the Heaviside step function; $g(\theta_T)$ is the viscosity, assumed as a given function of the concentration of trapped species. A simple choice for $g(\theta_T)$ is the affine function

$$g(\theta_T) = g_0 + g_1\,\theta_T \,, \tag{4.9b}$$

with g_0, g_1 given positive parameters. Flow-rule (4.9a) is clearly associated, and satisfies Clausius-Planck inequality (3.28) in view of plastic incompressibility.

Eq. (4.9a) establishes that the rate of inelastic deformation is proportional to the ratio $\varphi/g(\theta_T)$ when the stress state is such that $\varphi \geq 1$. Accordingly either for $g(\theta_T) \to 0$ and $\partial \boldsymbol{\varepsilon}/\partial t \to \mathbf{0}$ the rate-independent plasticity is recovered. Moreover in the limit $g(\theta_T) \to \infty$ the material behaves like an elastic media regardless the value assumed by the yield function.

From definition (4.9a) $\boldsymbol{\varepsilon}^{in}$ is trace-less and the stress-strain relationship rewrites from (3.55) as

$$\boldsymbol{\sigma} = 2\,G\operatorname{dev}\left[\boldsymbol{\varepsilon} - \boldsymbol{\varepsilon}^{in}\right] + K\operatorname{tr}\left[\boldsymbol{\varepsilon} - \boldsymbol{\varepsilon}^s\right]\mathbb{1} \,, \tag{4.10}$$

with

$$\boldsymbol{\varepsilon} = \frac{1}{2}\left(\nabla\left[\vec{u}\right] + \nabla\left[\vec{u}\right]^T\right) \,, \tag{4.11}$$

and

$$\boldsymbol{\varepsilon}^s = \omega_L\left(c_L - c_L^0\right)\mathbb{1} + \omega_T\left(c_T - c_T^0\right)\mathbb{1} \,. \tag{4.12}$$

In the assumption of constant material parameters G and K, along with $\chi = 0$, chemical potentials derived in Chapter 3 Eq. (3.59) reduce to

---

[1] It is questionable that the concentration of trapped lithium does not influence the yield strength of the hosting material. To the best of our knowledge, there are no experimental data in this regard.

$$\mu_\beta = \mu_\beta^0 + R\,T \ln\left[\frac{\theta_\beta}{1-\theta_\beta}\right] - \omega_\beta \operatorname{tr}\left[\boldsymbol{\sigma}\right]\,, \qquad \beta = L,\,T\,. \tag{4.13}$$

Finally the constitutive relations for lithium flux and rate of chemical reaction yield

$$\vec{h}_L = -\mathbb{D}_L \nabla\left[c_L\right] + \frac{\mathbb{D}_L\,\omega_L}{R\,T}\,c_L \left(\frac{c_L^{max}-c_L}{c_L^{max}}\right)\nabla\left[\operatorname{tr}\left[\boldsymbol{\sigma}\right]\right]\,, \tag{4.14}$$

$$w^{(1)} = \tilde{k}_T\,\frac{c_L}{c_L^{max}-c_L} - \tilde{k}_L\,\frac{c_T}{c_T^{max}-c_T}\,, \tag{4.15}$$

with

$$\tilde{k}_T = k_T \exp\left[-\frac{\omega_L}{R\,T}\operatorname{tr}\left[\boldsymbol{\sigma}\right]\right]\,, \quad \tilde{k}_L = k_L \exp\left[-\frac{\omega_T}{R\,T}\operatorname{tr}\left[\boldsymbol{\sigma}\right]\right]\,. \tag{4.16}$$

4.5 Lithiation and delithiation of a LiCoO$_2$ spherical particle

In this section we particularize the set of governing equations (4.8) in order to simulate the lithium insertion and extraction processes of a spherical particle of domain Ω.

Boundary conditions for Eq. (4.8a) are modeled following [141], without recurring to the Butler-Volmer equations. For Li removal simulations, the particle is initially filled with lithium at uniform concentration $c_{\text{Li}}(\vec{x}, t=0) = c_{\text{Li}}^{0(\text{del})}$. Then lithium is extracted with an uniform and constant flux $\vec{h}_L \cdot \vec{n} = \overline{h}_L$ at particle boundary $\partial\Omega$ until the concentration c_{Li} on the external surface equals the limit $c_{\text{Li}}^{F(\text{del})}$. Then the extraction process proceeds holding fixed c_{Li} at $\partial\Omega$. The lithiation process is modeled in a similar way: an inward and constant flux $\overline{h}_L$ is imposed at the sphere boundary. The concentration of lithium increased from an initial uniform distribution $c_{\text{Li}}(\vec{x}, t=0) = c_{\text{Li}}^{0(\text{lit})}$. Once the lithium concentration reaches the limit $c_{\text{Li}}^{F(\text{lit})}$, this value is held fixed on the external boundary.

For the mechanical boundary conditions, the particle allows free expansion and contraction at its boundary. Rigid motions are restrained by imposing a null displacement at the center of the particle.

The selected particle geometry and boundary conditions allow taking advantage of conditions of spherical symmetry. Therefore governing equations (4.8) are restated in a spherical coordinate system $\{r, \theta, \phi\}$ with unit vectors $\{\vec{e}_r, \vec{e}_\theta, \vec{e}_\phi\}$ centered at the centroid of the sphere. In this way the functional dependence of interstitial and trapped concentrations reduces to

$$c_L = c_L\left(r, t\right)\,, \qquad c_T = c_T\left(r, t\right)\,,$$

and the displacement vector reads

$$\vec{u} = u\left(r, t\right)\vec{e}_r \otimes \vec{e}_r\,. \tag{4.17}$$

From formula (4.17) the *total* strain tensor writes

$$\boldsymbol{\varepsilon} = \varepsilon_r\,\vec{e}_r \otimes \vec{e}_r + \varepsilon_\theta\,\left(\vec{e}_\theta \otimes \vec{e}_\theta + \vec{e}_\phi \otimes \vec{e}_\phi\right)\,,$$

with components ε_r and ε_θ defined as

$$\varepsilon_r = \frac{\partial u}{\partial r}\,, \qquad \varepsilon_\theta = \frac{u}{r}\,.$$

The *inelastic* strain tensor assumes the form

$$\boldsymbol{\varepsilon}^{in} = \varepsilon_{in}\left[\vec{e}_r \otimes \vec{e}_r - \frac{1}{2}\left(\vec{e}_\theta \otimes \vec{e}_\theta + \vec{e}_\phi \otimes \vec{e}_\phi\right)\right]\,,$$

hence the flow rule (4.9a) can be represented only in terms of the scalar ε_{in}. Easy algebra calculations lead to rephrase formula (4.9a) with

$$\frac{\partial \varepsilon_{in}}{\partial t} = \sqrt{\frac{2}{3}}\, \lambda\, \text{sign}\,[\sigma_\tau]\,, \qquad \lambda = \frac{\varphi\,\mathcal{H}(\varphi)}{g(\theta_T)}\,, \qquad \varphi = \sqrt{\frac{2}{3}}\,(|\sigma_\tau| - \sigma_Y)\,, \tag{4.18}$$

having defined the stress tensor and its deviatoric part as follow

$$\boldsymbol{\sigma} = \sigma_r\,\vec{e}_r \otimes \vec{e}_r + \sigma_\theta\,(\vec{e}_\theta \otimes \vec{e}_\theta + \vec{e}_\phi \otimes \vec{e}_\phi)\,,$$

$$\text{dev}\,[\,\boldsymbol{\sigma}\,] = \frac{2}{3}\sigma_\tau \left[\vec{e}_r \otimes \vec{e}_r - \frac{1}{2}\,(\vec{e}_\theta \otimes \vec{e}_\theta + \vec{e}_\phi \otimes \vec{e}_\phi)\right]\,,$$

$$\sigma_\tau = \sigma_r - \sigma_\theta\,.$$

The constitutive equation (4.10) is then given in terms of scalar equations

$$\sigma_m = 3\,K\,(\varepsilon_m - 3\,\varepsilon_{sw})\,, \tag{4.20a}$$

$$\sigma_\tau = 2\,G\left(\varepsilon_\tau - \frac{3}{2}\,\varepsilon_{in}\right)\,, \tag{4.20b}$$

where

$$\sigma_m = \sigma_r + 2\,\sigma_\theta\,,$$

$$\varepsilon_m = \varepsilon_r + 2\,\varepsilon_\theta\,, \qquad \varepsilon_\tau = \varepsilon_r - \varepsilon_\theta\,,$$

$$\varepsilon_{sw} = \omega_L\,(c_L - c_L^0) + \omega_T\,(c_T - c_T^0)\,. \tag{4.21a}$$

The flux vector is now oriented only in radial direction

$$\vec{h}_L = h_r\,\vec{e}_r\,,$$

and it is constitutively defined as

$$h_r = -\mathbb{D}_L\,\frac{\partial c_L}{\partial r} + \frac{\mathbb{D}_L\,\omega_L}{R\,T}\,c_L\left(\frac{c_L^{max} - c_L}{c_L^{max}}\right)\frac{\partial \sigma_m}{\partial r}\,. \tag{4.22}$$

The rate of chemical reaction $w^{(1)}$ is still expressed by means of formulae (4.15) - (4.16).

Finally, governing equations (4.8) can be rewritten as follow

$$\frac{\partial c_L}{\partial t} + \frac{\partial h_r}{\partial r} + 2\frac{h_r}{r} + w^{(1)} = 0\,, \tag{4.23a}$$

$$\frac{\partial c_T}{\partial t} - w^{(1)} = 0\,, \tag{4.23b}$$

$$\frac{\partial \sigma_r}{\partial r} + 2\frac{\sigma_r - \sigma_\theta}{r} = 0\,, \tag{4.23c}$$

constituting a system of three scalar equations with unknowns c_L, c_T, u for $(r,t) \in [0, r_0] \times\,]0, t_f]$.

For the problem at hand Dirichlet boundary conditions are imposed in terms of radial displacement u at the particle center as follow

$$u(r = 0, t) = 0\,,$$

to prevent rigid body motions.

Neumann boundary conditions are prescribed both on particle surface and at particle center

$$h_r(r,t) = \bar{h}_L \qquad r = r_0 \,, \tag{4.24a}$$

$$\sigma_r(r,t) = 0 \qquad r = r_0 \,, \tag{4.24b}$$

$$h_r(r,t) = 0 \qquad r = 0 \,. \tag{4.24c}$$

Note that the constraint (4.24c) arises in view of the condition of spherical symmetry.

Initial conditions are imposed for concentration of interstitial species $c_L(r, t = 0)$ as well as of trapped species $c_T(r, t = 0)$. To comply with equilibrium thermodynamics these conditions are uniform in space. Balance of momentum, together with boundary conditions, provide the necessary and sufficient equations to define u at $t = 0$.

4.5.1   Material parameters and assumptions

Measurable material parameters of commercial $LiCoO_2$ cathode particles are taken from the literature and listed in Table 5.1. The pristine particle is here assumed of radius $r_0 = 10\,\mu m$.

Denoting with x the amount of Lithium ions of a Li_xCoO_2 electrode, in battery operations x ranges approximately between $x = 0.5$ and $x = 1.0$, as discussed in Section 4.2. Accordingly, the initial (0) and limit (F) concentrations for both lithiation (lit) and delithiation (del) processes are defined as

$$c_{Li}^{0\,(lit)} = c_{Li}^{F\,(del)} = c_{Li}^{max}/2 \,, \tag{4.25a}$$

$$c_{Li}^{F\,(lit)} = c_{Li}^{0\,(del)} = c_{Li}^{max} \,, \tag{4.25b}$$

in order to simulate the particle response upon fully battery charge/discharge[2].

In absence of further experiments, ω_L and ω_T have been taken identical and computed through Eq. (4.12), assuming the fully lithiated state as a reference state, i.e. by choosing $c_L^0 + c_T^0 = c_{Li}^{max}$. As reported in [107] the particle exhibits a volumetric expansion of 1.9% upon Li removal from $x = 1.0$ to $x = 0.5$. Accordingly the coefficients of chemical expansions are negative and result

$$\omega_L = \omega_T = \frac{1.9\%}{3\left(c_{Li}^{max}/2 - c_{Li}^{max}\right)} \,. \tag{4.26}$$

Chemical equilibrium is assumed at the beginning of both insertion and extraction. Thus the initial concentrations of interstitial and trapped species $c_L(r, t = 0)$ and $c_T(r, t = 0)$ can be computed from $c_{Li}^{0\,(lit)}$ or $c_{Li}^{0\,(del)}$ using Eqs. (4.3)-(4.5).

The imposed Li flux $\bar{h}_L$ corresponds to a charge/discharge current density $i_{ext} = 0.534\,A/m^2$, equivalent to a C rate of 0.5 according to formula [300]

$$C = \frac{3600\,i_{ext}\,A}{V\,F\,(c_{Li}^{max} - c_{Li}^{max}/2)} \,, \tag{4.27}$$

where A and V are respectively volume and surface area of the particle, F is Faraday's constant in Coulombs per moles. Charge and discharge operations have been simulated for a total time of 3 hours at constant temperature $T = 300\,K$.

As discussed in section 4.3, the thermodynamics of the trapping process is influenced by K^{eq} and γ. Numerical simulations for insertion and extraction will highlight the role of K^{eq} on the evolution of lithium concentration profiles. The ratio between maximum trapped and interstitial sites is assumed to be constant and equal to $\gamma = 1/3$. With this choice $\hat{\psi}_\eta^L$ and $\hat{\psi}_\eta^T$ intersects at $\theta_{Li} = 0.75$, as showed in Fig. 4.3a.

Trapping is modeled by the finite speed chemical kinetics equation (4.15). A parametric study of the evolution of the system at different values of the kinetic constants k_L and k_T is performed in the numerical examples that follow, in order to investigate the role played by the rate of chemical reaction.

---

[2]For numerical convenience the equation (4.25b) has been implemented as $c_{Li}^{F\,(lit)} = c_{Li}^{0\,(del)} = 0.99\,c_{Li}^{max}$

Material Parameters				Ref.
Maximum Lithium concentration	c_{Li}^{max}	2.390×10^4	mol/m^3	[152]
Lithium diffusivity	$\mathbb{D}_L$	5.387×10^{-15}	m^2/s	[152]
Coefficients of chemical expansion	$\omega_L = \omega_T$	-5.300×10^{-7}	m^3/mol	[107]
Young modulus	E	370	GPa	[152]
Poisson ratio	ν	0.2	-	[152]
Yield stress	σ_Y	1.0	GPa	[318]

Table 4.1: Material parameters taken from the literature.

The inelastic, rate-sensitive mechanical response - see Eq. (4.9) - allows studying the mechanical response as a function of the immobilized specie concentration. For the Perzyna-like model (4.9a) we define a lithium dependent *relaxation time* τ as follows

$$\tau = \frac{g_0 + g_1\,\theta_T}{E}\,, \tag{4.28}$$

with E denoting the Young's modulus as customary. Parameter g_1 modulates the lithium concentration dependence of τ which attains two extreme values, τ_0 and τ_1, respectively from $\theta_T = 0$ and $\theta_T = 1$. Mechanical degradation, compatible with plastic flow, has been experimentally observed [318]. A different mechanical response between phase I and II is expected, too, but evidence are not provided for the plastic regime. Nonetheless, to show the capability of the model we arbitrarily assume that trapped Li increases the viscosity of the host by choosing g_0 and g_1 such that $\tau_0 = 1\,\mathrm{s}$ and $\tau_1 = 60\,\mathrm{s}$.

4.6   Numerical simulations

The system of equations (4.23) has been solved numerically through the Finite Element Method. To this end the governing equations have been written in integral form and then discretized in space with 400 elements along the radius r, while the time evolution is resolved with a time increment $\Delta t = 3.6\,\mathrm{s}$. The resulting nonlinear algebraic problem has been solved with a Newton-Raphson scheme. This numerical procedure has been implemented in a MATLAB package script purposely written. The detailed procedure of the numerical approximation and resolution is postponed in Appendix 4.A.

4.6.1   Lithium extraction

The role of K^{eq} - Figures 4.1a and 4.2a compare the evolution of lithium profile for different values of K^{eq} at given k_T. The smaller the constant of chemical equilibrium, the higher the concentration gradients, clearly visible at high content of Lithium ions. In fact for $K^{eq} \ll 1$ and $\gamma = 1/3$ the un-trapping reaction dominates the initial phase of the extraction process as seen in Sec. 4.3. As the process moves forward and traps empty, the influence of un-trapping reaction on lithium transport becomes secondary.

For $K^{eq} = 0.01$ the un-trapping reaction dominates for lithium concentration grater than $c_{\mathrm{Li}}/c_{\mathrm{Li}}^{max} \sim 0.75$. For lower values of c_{Li}, traps are empty and lithium transport is not affect by the un-trapping process. This behavior resembles a phase transition of the hosting material. In fact Li distribution highlights two regions: the particle core where $c_{\mathrm{Li}}/c_{\mathrm{Li}}^{max} \sim 1$ and the particle shell where $c_{\mathrm{Li}}/c_{\mathrm{Li}}^{max} \leq 0.75$ separated by a sort of diffuse-interface of finite thickness.

The amplitude of concentration range in which the chemical kinetics timescale dominates is governed by parameter γ. In fact the availability of trap sites determines the amount of immobilized lithium at $t = 0$.
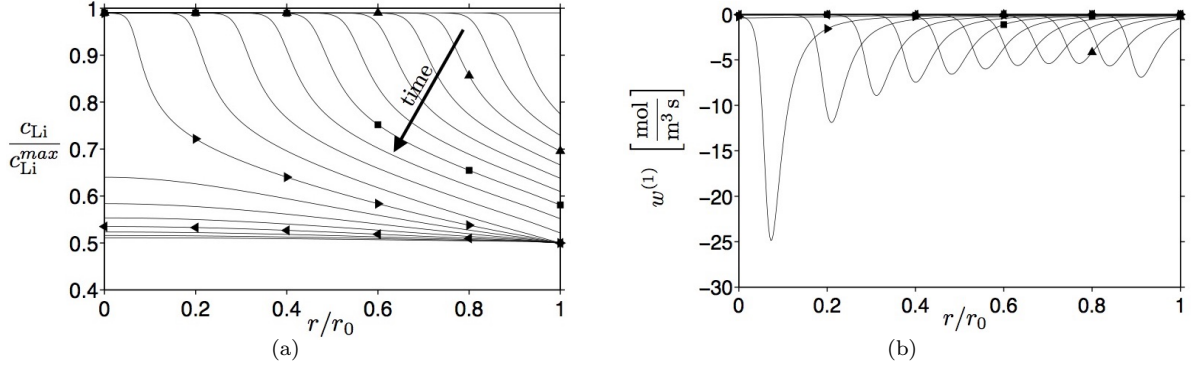
Figure 4.1: **Li extraction** - *Lithium concentration (a) and rate of chemical reaction (b) profiles as function of radial coordinate at intervals of 600 s for $K^{eq} = 0.01$ and $k_T = 1 \text{ mol}/(\text{m}^2\,\text{s})$.*

The spatial profile of $w^{(1)}$ for $K^{eq} = 0.01$ (Fig. 4.1b) shows that the reaction is constrained is a narrow zone (the smaller K^{eq}, the smaller the size of the reaction front, as shown comparing Fig. 4.2b with Fig. 4.1b). The latter travels from the external surface to the particle center, essentially with a constant velocity. Such a reaction front may identify a diffusive phase boundary, tracking the growth/consumption of two phases in the particle. The case $K^{eq} \gg 1$ is not considered here since the chemical reaction cause a negligible impact on the concentration profiles in the range $0.5 \leq \theta_{\text{Li}} \leq 1$ for $\gamma = 1/3$.
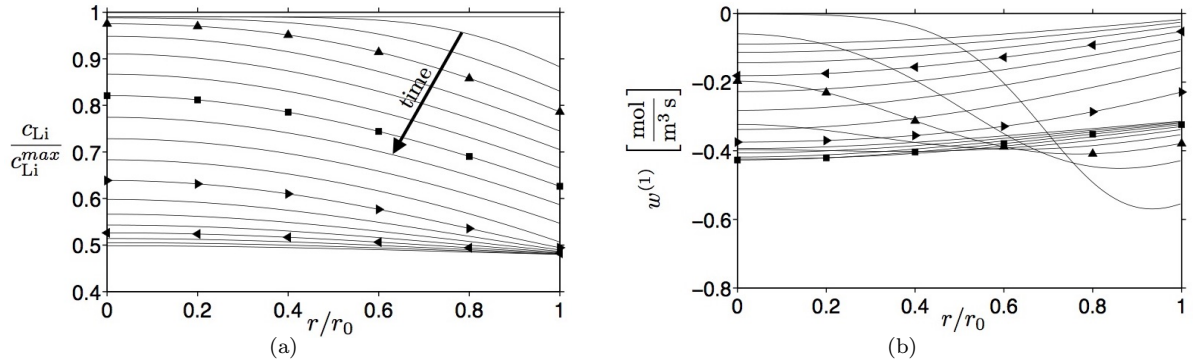
Figure 4.2: **Li extraction** - *Lithium concentration (a) and rate of chemical reaction (b) profiles as function of radial coordinate at intervals of 600 s for $K^{eq} = 1$ and $k_T = 1 \text{ mol}/(\text{m}^2\,\text{s})$.*

The role of the reaction velocity - The influence of the rate of chemical reaction is investigated for different values of k_T at given K^{eq} (see Figs. 4.1 and 4.3). Higher values of the chemical constants imply faster chemical reaction, i.e. trapped and interstitial species attain their chemical equilibrium configuration quicker. Since the concentration profiles do not show significant changes for $k_T > 1 \text{ mol}/(\text{m}^2\,\text{s})$, such a value resembles the *infinitely fast kinetics* condition, when the trapping reaction has its maximum impact on the concentration profiles.

Small values of k_T promote slow chemical kinetics, which reflect in small concentration gradients (Fig. 4.3a). In the limit case of *infinitely slow kinetics* ($k_T \to 0$) the trapped species cannot be extracted in the timescale of the process so that the chemical reaction has not effect at all.

The rate of chemical reaction (Figs. 4.1b and 4.3b) is influenced both in its magnitude and distribution: faster kinetics induce higher values of $w^{(1)}$ and concentrate the chemical reaction in narrower regions.

In conclusion, the numerical results for $K^{eq} \ll 1$ along with fast chemical kinetics, reproduce Li concentration profiles expected for phase-segregating electrodes. Indeed, the concentration profiles show steep
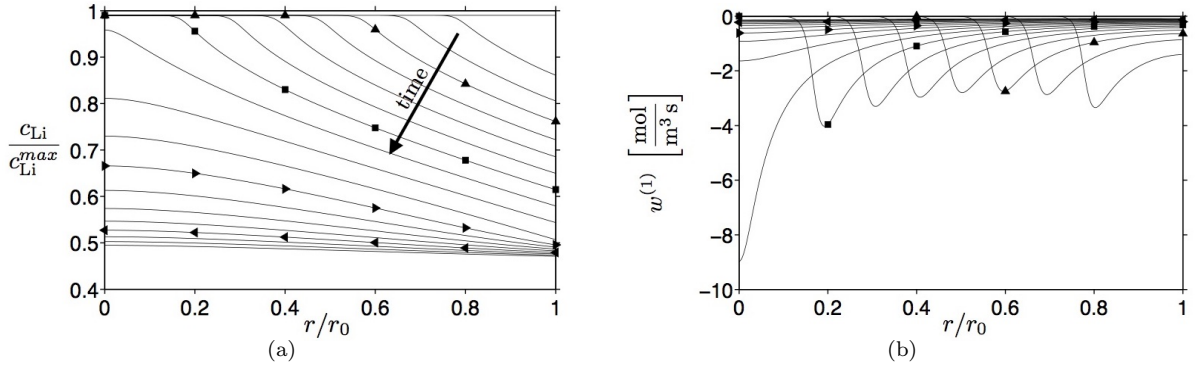
Figure 4.3: **Li extraction** - Lithium concentration (a) and rate of chemical reaction (b) profiles as function of radial coordinate at intervals of 600 s for $K^{eq} = 0.01$ and $k_T = 0.01 \ \mathrm{mol/(m^2\,s)}$.

gradients which separate regions with high (inner core) and low (particle shell) lithium content. This two regions may identify two coexisting phases separated by a diffusive interface where the trapping chemical reaction is localized.

4.6.2 Lithium insertion

The role of K^{eq} - Lithium concentration profiles show that K^{eq} influences the particle *state of charge* during the insertion process (see Figs. 4.4a and 4.5a). As the constant of chemical equilibrium becomes smaller the particle is capable to host less amount of lithium ions, especially in the particle core. The trapping reaction is not energetically favorite for $K^{eq} \ll 1$, therefore lithium ions accumulate at high concentrations in the interstitial sites before getting trapped. The process of trapping advances slowly toward the particle center, because the trapping reaction is the limiting process. The insertion is slower than the extraction process, whereby the un-trapping reaction was favorite by small values of K^{eq}.
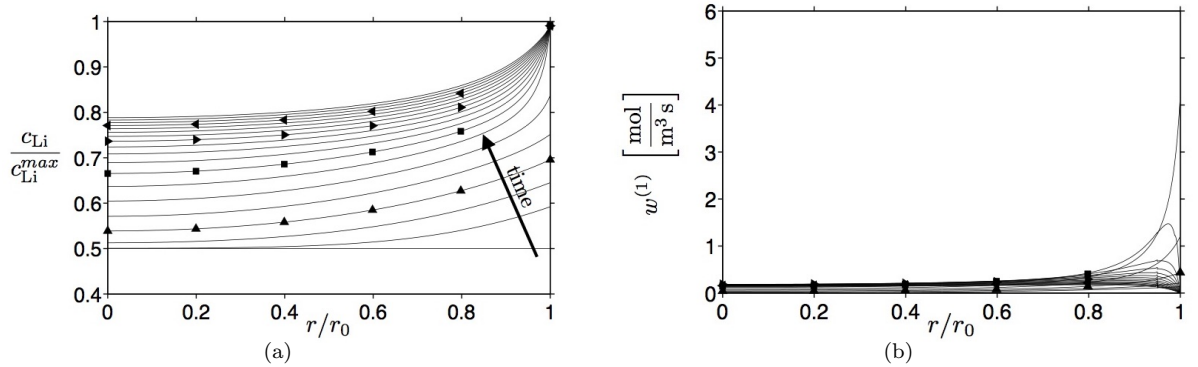
Figure 4.4: **Li insertion** - Lithium concentration (a) and rate of chemical reaction (b) profiles as function of radial coordinate at intervals of 600 s for $K^{eq} = 0.01$ and $k_T = 1 \ \mathrm{mol/(m^2\,s)}$.

As in the case of extraction, smaller values of chemical equilibrium give rise to more pronounced concentration gradients in space. Nevertheless, during the trapping process, the distribution of lithium ions does not resemble the core/shell distribution typical of a phase transition. In fact the steep concentration gradients which develop close to the external surface do not translate toward the particle center, rather they progressively relax as the lithium insertion advances.

81

Similar remarks apply to the chemical reaction. The trapping at low K^{eq} is in general quicker near the particle surface then at the interior (Fig. 4.4b). Differently from extraction, even for small values of K^{eq} the chemical reaction is not restricted into a narrow zone, except when lithium is initially trapped on the surface.
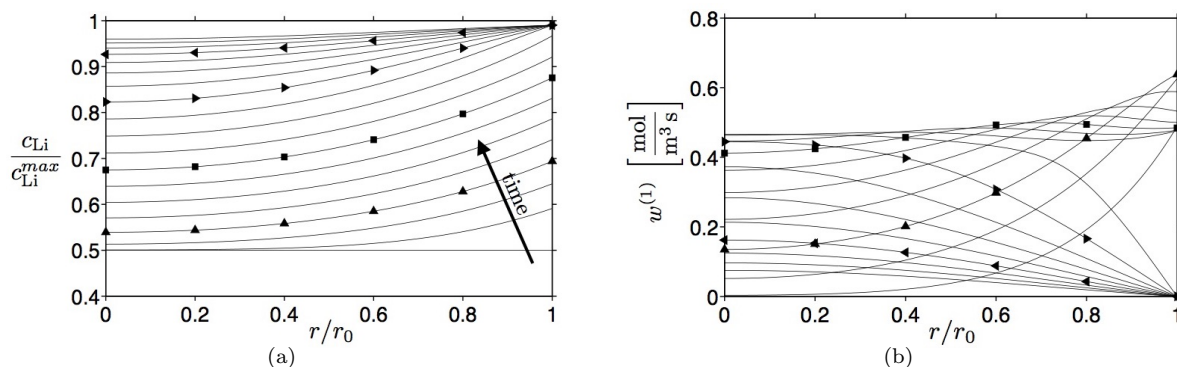
Figure 4.5: **Li insertion** - *Lithium concentration (a) and rate of chemical reaction (b) profiles as function of radial coordinate at intervals of 600 s for $K^{eq} = 1$ and $k_T = 1$ mol/(m^2 s).*

The role of the reaction velocity - Numerical analyses that have not been reported here for the sake of brevity show that the case $k_T = 1$ mol/(m^2 s) resembles the *infinitely fast kinetics*, as for the extraction process. Figures 4.4 and 4.6 compare different chemical kinetics for the same constant of chemical equilibrium. It shows, by comparison with Figure 4.1a, that the particle fills with lithium slower than it empties, for $K^{eq} \ll 1$, even though the chemical kinetics is not a limiting factor for the process. For slow chemical kinetics ($k_T = 0.01$) the trapping reaction is further delayed and the concentration distributions shows higher gradients in space then for fast kinetics on the external surface.
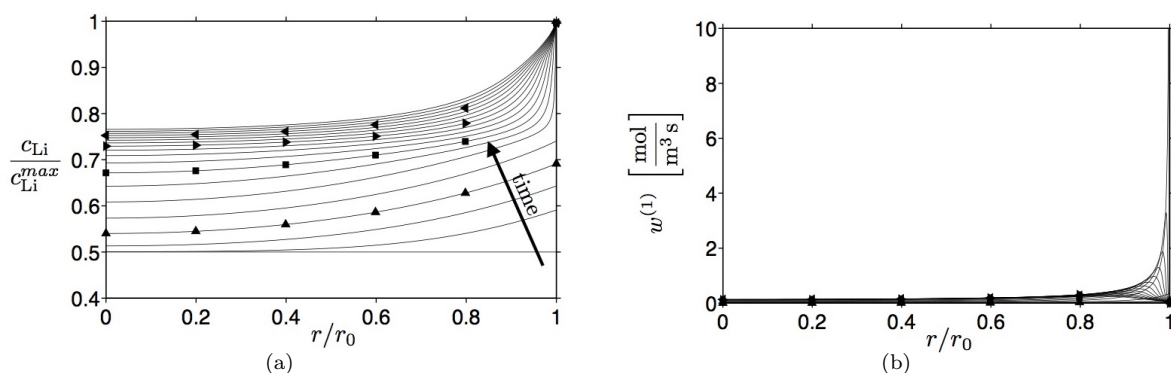
Figure 4.6: **Li insertion** - *Lithium concentration (a) and rate of chemical reaction (b) profiles as function of radial coordinate at intervals of 600 s for $K^{eq} = 0.01$ and $k_T = 0.01$ mol/(m^2 s).*

4.7 Conclusions

In this chapter the general framework developed in Chapter 3 has been applied in order to evaluate the response of a spherical LiCoO$_2$ particle upon lithiation and delithiation. This electrode material shows a

strong first-order phase transition characterized by the coexistence of Li-rich and Li-poor phases separated by a moving interface.

The present model assumes an electrode structure made of two distinct host sites for lithium intercalation, i.e. interstitial and trap sites, in which Li ions are mobile and immobile respectively. Lithium immobilization, also called trapping, is modeled as a chemical reaction.

At thermodynamic level, a chemical reaction may induce a non-convex free energy with multiple equilibrium configurations, as expected in phase segregating materials. However this feature is lost if the conditions of chemical equilibrium does not depends on thermo-mechanical effects, e.g. for $\omega_L = \omega_T$, $\psi_{in} = 0$, and uniform constant temperature. In these conditions the equilibrium between interstitial and trapped lithium depends only on parameters K^{eq} and γ that can be tuned in order to separate the intercalation process in two stages: one dominated by the insertion in the interstitial sites, and the other dominated by the insertion in the trap sites.

The transient response has been evaluated numerically by solving the resulting fully coupled problem of transport, mechanics and finite speed chemical kinetics. The evolution of Li concentration profiles and chemical kinetics have been analyzed for different values of K^{eq} and kinetics constant k_T at fixed $\gamma < 1$.

The numerical results have shown that the typical features of a phase segregation can be simulated for the extraction process in the case of $K^{eq} \ll 1$ along with a condition of infinitely-fast chemical kinetics. On the contrary such features cannot be recovered for the lithiation case by tuning parameters K^{eq} and k_T.

In conclusion controlling the lithium transient evolution by means of K^{eq}, γ, and k_T only is inappropriate, since it leads to severe differences in the overall behavior during insertion and extraction that are not observed experimentally. To meet the experimental evidence a slightly modification of the present model will be introduced in Chapter 5 by controlling the evolution of traps density c_T^{max}.

The mechanical response, which is basically induced by the distribution of the Li ions in the particle, will be analyzed in the next chapter for more realistic lithium profiles.

Appendix

4.A Finite element implementation

4.A.1 Non-dimensional governing equations and weak form

As customary the system of governing equations has been scaled with suitable coefficients in order to deal with a system of non-dimensional equations. In this way Eqs. (4.23) have been rephrased in term of adimensional variables

$$r^* = \frac{r}{\bar{l}}, \qquad t^* = \frac{t}{\bar{t}}, \qquad c_L^* = \frac{c_L}{\bar{c}}, \qquad c_T^* = \frac{c_T}{\bar{c}}, \qquad u^* = \frac{u}{\bar{l}}, \qquad \sigma_i^* = \frac{\sigma_i}{\bar{\sigma}}, \tag{4.29}$$

by introducing $\bar{l}$, $\bar{t}$, $\bar{c}$, $\bar{\sigma}$ as reference length, time, concentration, and stress respectively.

Taking advantage of definitions (4.29), governing equations (4.23) are equivalent to the following non-dimensional ones

$$\frac{\partial c_L^*}{\partial t^*} + \frac{\partial h_r^*}{\partial r^*} + 2\frac{h_r^*}{r^*} + w^{*\,(1)} = 0 \tag{4.30a}$$

$$\frac{\partial c_T^*}{\partial t^*} - w^{*\,(1)} = 0 \tag{4.30b}$$

$$\frac{\partial \sigma_r^*}{\partial r^*} + 2\frac{\sigma_r^* - \sigma_\theta^*}{r^*} = 0 \tag{4.30c}$$

for $(r^*, t^*) \in [0,\, r_0/\bar{r}] \times\,]0,\, t_f/\bar{t}]$.

Note that equations (4.30) have the same expression of (4.23) but are formulated in terms of non-dimensional variables. In the same way the non-dimensional constitutive laws mantain the same expression of (4.15) - (4.16) - (4.18) - (4.20) - (4.21a) - (4.22) as long as the original variables and parameters are replaced with (4.29) and the following non-dimensional constants

$$\mathbb{D}_L^* = \frac{\mathbb{D}_L\,\bar{t}}{\bar{l}^2}, \qquad \omega_L^* = \omega_L\,\bar{c}, \qquad \omega_T^* = \omega_T\,\bar{c}, \qquad (RT)^* = RT\,\frac{\bar{c}}{\bar{\sigma}},$$

$$(c_L^{max})^* = \frac{c_L^{max}}{\bar{c}}, \qquad (c_T^{max})^* = \frac{c_T^{max}}{\bar{c}}, \qquad k_L^* = \frac{k_L\,\bar{t}}{\bar{c}}, \qquad k_T^* = \frac{k_T\,\bar{t}}{\bar{c}},$$

$$K^* = \frac{K}{\bar{\sigma}}, \qquad G^* = \frac{G}{\bar{\sigma}}, \qquad g_0^* = \frac{g_0}{\bar{t}\,\bar{\sigma}}, \qquad g_1^* = \frac{g_1}{\bar{t}\,\bar{\sigma}}, \qquad \sigma_Y^* = \frac{\sigma_Y}{\bar{\sigma}}.$$

The weak formulation results from multiplying the strong form of governing equations (4.30) by a suitable set of tests functions and performing an integration upon the domain, exploiting the *integration by parts* formula with the aim of reducing the order of differentiation in space.

Even though the first order derivative of h_r can be reduced applying the integration by parts, its constitutive definition contains a second order derivative. In fact the Li flux is proportional to the stress gradient $\partial \sigma_m / \partial r$ (see Eq.(4.22)) which is in turn function of $\partial^2 u / \partial r^2$. The latter is undetermined in standard finite element since u is approximated with global $\mathcal{C}^0$ polynomials. To include the effect of stress gradient we follow the approach adopted in [127] by introducing a new variable $\Sigma(r, t)$ defined as

$$\Sigma - \sigma_m (c_L, c_T, u) = 0, \tag{4.32}$$

which will be approximate as an explicit degree of freedom. Eq. (4.32) is then added to the set of governing equations (4.30) for the numerical solution of the problem.

The overall weak form of the problem is derived starting from each governing equation separately. In what follow the asterisk is omitted for the sake of readability.

From the mass balance Eq. (4.30a) we obtain

$$4\pi \int_0^{r_0} \hat{c}_L \left\{ \frac{\partial c_L}{\partial t} + \frac{\partial h_r}{\partial r} + 2\frac{h_r}{r} + w^{(1)} \right\} r^2 \, \mathrm{d}r =$$

$$= 4\pi \int_0^{r_0} \hat{c}_L \left\{ \frac{\partial c_L}{\partial t} + w^{(1)} (c_L, c_T, \Sigma) \right\} r^2 \, \mathrm{d}r + 4\pi \int_0^{r_0} \frac{\partial \hat{c}_L}{\partial r} \left\{ \mathbb{D}_L \frac{\partial c_L}{\partial r} - \mathbb{D}_\Sigma (c_L) \frac{\partial \Sigma}{\partial r} \right\} r^2 \, \mathrm{d}r +$$

$$+ 4\pi \left[\hat{c}_L \, \bar{h}_L \, r^2 \right]\big|_{r=r_0} = 0,$$

where $\mathbb{D}_\Sigma$ stands for

$$\mathbb{D}_\Sigma = \frac{\mathbb{D}_L \, \omega_L}{R \, T} c_L \left(\frac{c_L^{max} - c_L}{c_L^{max}} \right).$$

The weak form of Eq. (4.30b) can be derived simply as

$$4\pi \int_0^{r_0} \hat{c}_T \left\{ \frac{\partial c_T}{\partial t} - w^{(1)} \right\} r^2 \, \mathrm{d}r =$$

$$= 4\pi \int_0^{r_0} \hat{c}_T \left\{ \frac{\partial c_T}{\partial t} - w^{(1)} (c_L, c_T, \Sigma) \right\} r^2 \, \mathrm{d}r = 0.$$

For the equilibrium equation (4.30c)

$$4\pi \int_0^{r_0} \hat{u} \left\{ \frac{\partial \sigma_r}{\partial r} + 2\frac{\sigma_r - \sigma_\theta}{r} \right\} r^2 \, \mathrm{d}r =$$

$$= -\frac{4}{3}\pi \int_0^{r_0} \frac{\partial \hat{u}}{\partial r} \left\{ 2\sigma_\tau (c_T, u) + \sigma_m (c_L, c_T, u) \right\} r^2 \, \mathrm{d}r - \frac{8}{3}\pi \int_0^{r_0} \hat{u} \left\{ \sigma_m (c_L, c_T, u) - \sigma_\tau (c_T, u) \right\} r \, \mathrm{d}r = 0.$$

Finally Eq. (4.32) returns

$$4\pi \int_0^{r_0} \hat{\Sigma} \left\{ \Sigma - \sigma_m (c_L, c_T, u) \right\} r^2 \, \mathrm{d}r = 0.$$

Notice that boundary conditions (4.24) have been applied and the test functions $\hat{c}_L$, $\hat{c}_T$, $\hat{u}$, $\hat{\Sigma}$ are null on the Dirichlet boundary. The latter condition arises since test functions represents admissible variations of the related degrees of freedom c_L, c_T, u, Σ.

In conclusion, the weak form of the balance equations can be written in the time interval $[0, t_f]$ as

Find $y(r, t) \in \mathcal{V}^{[0, t_f]}$ such that $\qquad \dfrac{\partial}{\partial t} b\left(\hat{y}(r), z(r, t)\right) + a\left(\hat{y}(r), y(r, t)\right) = f\left(\hat{y}(r)\right) \qquad \forall \hat{y}(r) \in \mathcal{V} \quad (4.33)$

where

$$b\left(\hat{y}(r),\,z(r,t)\right) \;=\; \int_0^{r_0} \left\{\hat{c}_L\,c_L + \hat{c}_T\,c_T\right\}\,r^2\,\mathrm{d}r\,,$$

$$a\left(\hat{y}(r),\,y(r,t)\right) \;=\; \int_0^{r_0} \frac{\partial \hat{c}_L}{\partial r}\left\{ \mathbb{D}_L\,\frac{\partial c_L}{\partial r} - \mathbb{D}_\Sigma\left(c_L\right)\frac{\partial \Sigma}{\partial r}\right\}\,r^2\,\mathrm{d}r + \int_0^{r_0}\left(\hat{c}_L - \hat{c}_T\right)w^{(1)}\left(c_L,c_T,\Sigma\right)r^2\,\mathrm{d}r +$$

$$+ \int_0^{r_0}\frac{\partial \hat{u}}{\partial r}\left\{2\,\sigma_\tau\left(c_T,u\right)+\sigma_m\left(c_L,c_T,u\right)\right\}r^2\,\mathrm{d}r + \int_0^{r_0}2\,\hat{u}\left\{\sigma_m\left(c_L,c_T,u\right)-\sigma_\tau\left(c_T,u\right)\right\}r\,\mathrm{d}r +$$

$$+ \int_0^{r_0}\hat{\Sigma}\left\{\Sigma - \sigma_m\left(c_L,c_T,u\right)\right\}r^2\,\mathrm{d}r\,,$$

$$f\left(\hat{y}(r)\right) \;=\; -\left.\left[\hat{c}_L\,\bar{h}_L\,r^2\right]\right|_{r=r_0}\,.$$

with $z = \{c_L,\,c_T\}$, $y = \{c_L,\,c_T,\,u,\,\Sigma\}$ collecting the time-dependent unknown fields. Column $\hat{y}$ collects the steady state test functions that correspond to the unknown fields in y, i.e. $\hat{y} = \{\hat{c}_L,\,\hat{c}_T,\,\hat{u},\,\hat{\Sigma}\}$. The identification of the functional space $\mathcal{V}$ falls beyond the scope of this work.

4.A.2   Numerical discretization

Following the standard finite element method, the spatial domain $\Omega = [0,\,r_0]$ is divided into N_h subdomains Ω^e, each one with nn nodes, such that

$$\Omega = \bigcup_{e=1}^{N_h}\Omega^e$$

Inside any subdomain any degree of freedom and its variation is approximated through the following interpolation

$$^h(\bullet)\,(r,t) = \sum_{i=1}^{nn} N^i(r)\,(\bullet)^i(t) = [N(r)]\,[(\bullet)(t)] \tag{4.34}$$

where the table $[N(r)]$ collects the time-independent local shape functions $N^i(r)$ as

$$[N(r)] = \left\{N^1(r),\,N^2(r),\,...,\,N^{nn}(r)\right\}$$

and $[(\bullet)(t)]$ collects the nodal values of variable $(\bullet)$ at time t as follow

$$[(\bullet)(t)] = \left\{(\bullet)^1(t),\,(\bullet)^2(t),\,...,\,(\bullet)^{nn}(t)\right\}^T$$

From Eq. (4.34) the differentiation in space result

$$\frac{\partial\,^h(\bullet)}{\partial r} = [B(r)]\,[(\bullet)(t)]$$

with

$$[B(r)] = \left\{\frac{\mathrm{d}N^1}{\mathrm{d}r},\,\frac{\mathrm{d}N^2}{\mathrm{d}r},\,...,\,\frac{\mathrm{d}N^{nn}}{\mathrm{d}r}\right\}$$

The discretization in time is performed applying the implicit backward Euler method. Accordingly we divide time interval $[0,\,t_f]$ into N_t temporal steps $\Delta t = t_f/N_t$. We define for convenience

$$\left.y(r)\right|_n = y(r,n\Delta t)\,,\qquad \left.\Delta y(r)\right|_{n+1} = \left.y(r)\right|_{n+1} - \left.y(r)\right|_n \qquad n = 1,\,2,\,...,\,N_t$$

The discretized weak form is finally obtained from (4.33) by applying the finite element interpolation (4.34) and the backward Euler scheme. It results in terms of approximate degrees of freedom $^h y = \{^h c_L, \, ^h c_T, \, ^h u, \, ^h \Sigma\}$ and variations $^h \hat{y} = \{^h \hat{c}_L, \, ^h \hat{c}_T, \, ^h \hat{u}, \, ^h \hat{\Sigma}\}$ as follow

Find $\left.^h y(r)\right|_{n+1} \in \, ^h \mathcal{V}$ such that

$$\frac{1}{\Delta t} \, ^h b \left(^h \hat{y}(r), \, \left.\Delta^h z(r)\right|_{n+1}\right) + \, ^h a \left(^h \hat{y}(r), \, \left.^h y(r)\right|_{n+1}\right) = f \left(^h \hat{y}(r)\right) \qquad \forall \, ^h \hat{y}(r) \in \, ^h \mathcal{V}, \quad n = 1, 2, \dots, N_t$$

(4.35)

where

$$^h b \left(^h \hat{y}(r), \, \left.\Delta^h z(r)\right|_{n+1}\right) = \overset{N_h}{\underset{e=1}{\mathbf{A}}} \left\{ [\hat{c}_L]^T \int_{\Omega^e} [N_L]^T [N_L] \left([c_L]_{n+1} - [c_L]_n\right) r^2 \, \mathrm{d}r + \right.$$
$$\left. + [\hat{c}_T]^T \int_{\Omega^e} [N_T]^T [N_T] \left([c_T]_{n+1} - [c_T]_n\right) r^2 \, \mathrm{d}r \right\},$$

$$^h a \left(^h \hat{y}(r), \, \left.^h y(r)\right|_{n+1}\right) = \overset{N_h}{\underset{e=1}{\mathbf{A}}} \left\{ [\hat{c}_L]^T \int_{\Omega^e} [B_L]^T [B_L] [c_L]_{n+1} \, \mathbb{D}_L \, r^2 \, \mathrm{d}r + \right.$$
$$- [\hat{c}_L]^T \int_{\Omega^e} [B_L]^T [B_\Sigma] [\Sigma]_{n+1} \, \left.\mathbb{D}_\Sigma(c_L)\right|_{n+1} \, r^2 \, \mathrm{d}r +$$
$$+ [\hat{c}_L]^L \int_{\Omega^e} [N_L]^T \, \left.w^{(1)} (c_L, c_T, \Sigma)\right|_{n+1} \, r^2 \, \mathrm{d}r +$$
$$- [\hat{c}_T]^T \int_{\Omega^e} [N_T]^T \, \left.w^{(1)} (c_L, c_T, \Sigma)\right|_{n+1} \, r^2 \, \mathrm{d}r +$$
$$+ [\hat{u}]^T \int_{\Omega^e} [B_u]^T \left(2 \, \left.\sigma_\tau (c_T, u)\right|_{n+1} + \left.\sigma_m (c_L, c_T, u)\right)\right|_{n+1} \, r^2 \, \mathrm{d}r +$$
$$+ [\hat{u}]^T \int_{\Omega^e} 2 [N_u]^T \left(\left.\sigma_m (c_L, c_T, u)\right|_{n+1} - \left.\sigma_\tau (c_T, u)\right)\right|_{n+1} \, r \, \mathrm{d}r +$$
$$\left. + [\hat{\Sigma}]^T \int_{\Omega^e} [N_\Sigma]^T \left([N_\Sigma] [\Sigma]_{n+1} - \left.\sigma_m (c_L, c_T, u)\right|_{n+1}\right) r^2 \, \mathrm{d}r \right\},$$

$$f \left(^h \hat{y}(r)\right) = - \left.\left([\hat{c}_L]^T [N_L]^T \bar{h}_L \, r^2\right)\right|_{r=r_0}.$$

Note that the integrals in (4.33) are now computed summating the contribution of any subdomain Ω^e by means of the assembly operator $\mathbf{A}$. Eq. (4.35) is equivalent to a system of non-linear equations for the unknowns $^h y$ which is solved here with a standard Newton-Raphson algorithm. Accordingly the solution is computed iteratively in terms of solution increments $\delta y^{(k+1)} = \{\delta c_L^{(k+1)}, \, \delta c_T^{(k+1)}, \, \delta u^{(k+1)}, \, \delta \Sigma^{(k)}\}$ at iteration $k+1$ for any time step (the superscript ^{h} have been removed for clarity). Without going through all details for convenience (see [323] for instance), the overall problem reduces to the following linear system

$$\underbrace{\begin{bmatrix} [K^{LL}] & [K^{LT}] & [\mathbf{0}] & [K^{L\Sigma}] \\ [K^{TL}] & [K^{TT}] & [\mathbf{0}] & [K^{T\Sigma}] \\ [K^{uL}] & [K^{uT}] & [K^{uu}] & [\mathbf{0}] \\ [K^{\Sigma L}] & [K^{\Sigma T}] & [K^{\Sigma u}] & [K^{\Sigma \Sigma}] \end{bmatrix}}_{[K^{(k)}_{n+1}]} \underbrace{\begin{bmatrix} [\delta c_L] \\ [\delta c_T] \\ [\delta u] \\ [\delta \Sigma] \end{bmatrix}}_{[\delta y^{(k+1)}_{n+1}]} = \underbrace{\begin{bmatrix} [R^L] \\ [R^T] \\ [R^u] \\ [R^\Sigma] \end{bmatrix}}_{[R^{(k)}_{n+1}]}$$

where the *consistent tangent matrix* $[K^{\alpha\,\beta}]$ and the *residual vector* components $[R^{\alpha}]$ are

$$
[K^{L\,L}] = \mathop{\mathbf{A}}_{e=1}^{N_h} \left\{ \frac{1}{\Delta t} \int_{\Omega^e} [N_L]^T [N_L] \, r^2 \, \mathrm{d}r + \int_{\Omega^e} [B_L]^T [B_L] \, \mathbb{D}_L \, r^2 \, \mathrm{d}r + \right.
$$
$$
\left. - \int_{\Omega^e} [B_L]^T \left([B_\Sigma] [\Sigma]^{(k)}_{n+1} \right) [N_L] \, \frac{\mathrm{d}\,\mathbb{D}_\Sigma}{\mathrm{d}\,c_L} \bigg|^{(k)}_{n+1} r^2 \, \mathrm{d}r + \int_{\Omega^e} [N_L]^T [N_L] \, \frac{\partial\,w^{(1)}}{\partial\,c_L} \bigg|^{(k)}_{n+1} r^2 \, \mathrm{d}r \right\} ,
$$

$$
[K^{L\,T}] = \mathop{\mathbf{A}}_{e=1}^{N_h} \left\{ \int_{\Omega^e} [N_L]^T [N_T] \, \frac{\partial\,w^{(1)}}{\partial\,c_T} \bigg|^{(k)}_{n+1} r^2 \, \mathrm{d}r \right\} ,
$$

$$
[K^{L\,\Sigma}] = \mathop{\mathbf{A}}_{e=1}^{N_h} \left\{ - \int_{\Omega^e} [B_L]^T [B_\Sigma] \, \mathbb{D}_\Sigma \big|^{(k)}_{n+1} r^2 \, \mathrm{d}r + \int_{\Omega^e} [N_L]^T [N_\Sigma] \, \frac{\partial\,w^{(1)}}{\partial\,\Sigma} \bigg|^{(k)}_{n+1} r^2 \, \mathrm{d}r \right\} ,
$$

$$
[K^{T\,L}] = \mathop{\mathbf{A}}_{e=1}^{N_h} \left\{ - \int_{\Omega^e} [N_T]^T [N_L] \, \frac{\partial\,w^{(1)}}{\partial\,c_L} \bigg|^{(k)}_{n+1} r^2 \, \mathrm{d}r \right\} ,
$$

$$
[K^{T\,T}] = \mathop{\mathbf{A}}_{e=1}^{N_h} \left\{ \frac{1}{\Delta t} \int_{\Omega^e} [N_T]^T [N_T] \, r^2 \, \mathrm{d}r - \int_{\Omega^e} [N_T]^T [N_T] \, \frac{\partial\,w^{(1)}}{\partial\,c_T} \bigg|^{(k)}_{n+1} r^2 \, \mathrm{d}r \right\} ,
$$

$$
[K^{T\,\Sigma}] = \mathop{\mathbf{A}}_{e=1}^{N_h} \left\{ - \int_{\Omega^e} [N_T]^T [N_\Sigma] \, \frac{\mathrm{d}\,w^{(1)}}{\mathrm{d}\,\Sigma} \bigg|^{(k)}_{n+1} r^2 \, \mathrm{d}r \right\} ,
$$

$$
[K^{u\,L}] = \mathop{\mathbf{A}}_{e=1}^{N_h} \left\{ \int_{\Omega^e} [B_u]^T [N_L] \, \frac{\partial\sigma_m}{\partial c_L} \bigg|^{(k)}_{n+1} r^2 \, \mathrm{d}r + 2 \int_{\Omega^e} [N_u]^T [N_L] \, \frac{\partial\sigma_m}{\partial c_L} \bigg|^{(k)}_{n+1} r \, \mathrm{d}r \right\} ,
$$

$$
[K^{u\,T}] = \mathop{\mathbf{A}}_{e=1}^{N_h} \left\{ \int_{\Omega^e} [B_u]^T [N_T] \left(2 \, \frac{\partial\sigma_\tau}{\partial c_T} \bigg|^{(k)}_{n+1} + \frac{\partial\sigma_m}{\partial c_T} \bigg|^{(k)}_{n+1} \right) r^2 \, \mathrm{d}r + \right.
$$
$$
\left. + 2 \int_{\Omega^e} [N_u]^T [N_T] \left(\frac{\partial\sigma_m}{\partial c_T} \bigg|^{(k)}_{n+1} - \frac{\partial\sigma_\tau}{\partial c_T} \bigg|^{(k)}_{n+1} \right) r \, \mathrm{d}r \right\} ,
$$

$$
[K^{u\,u}] = \mathop{\mathbf{A}}_{e=1}^{N_h} \left\{ \int_{\Omega^e} [B_u]^T [B_u] \left(2 \, \frac{\partial\sigma_\tau}{\partial\varepsilon_r} \bigg|^{(k)}_{n+1} + \frac{\partial\sigma_m}{\partial\varepsilon_r} \bigg|^{(k)}_{n+1} \right) r^2 \, \mathrm{d}r + \int_{\Omega^e} [B_u]^T [N_u] \left(2 \, \frac{\partial\sigma_\tau}{\partial\varepsilon_\theta} \bigg|^{(k)}_{n+1} + \frac{\partial\sigma_m}{\partial\varepsilon_\theta} \bigg|^{(k)}_{n+1} \right) r \, \mathrm{d}r + \right.
$$
$$
\left. + 2 \int_{\Omega^e} [N_u]^T [B_u] \left(\frac{\partial\sigma_m}{\partial\varepsilon_r} \bigg|^{(k)}_{n+1} - \frac{\partial\sigma_\tau}{\partial\varepsilon_r} \bigg|^{(k)}_{n+1} \right) r \, \mathrm{d}r + 2 \int_{\Omega^e} [N_u]^T [N_u] \left(\frac{\partial\sigma_m}{\partial\varepsilon_\theta} \bigg|^{(k)}_{n+1} - \frac{\partial\sigma_\tau}{\partial\varepsilon_\theta} \bigg|^{(k)}_{n+1} \right) \mathrm{d}r \right\} ,
$$

$$
[K^{\Sigma\,L}] = \mathop{\mathbf{A}}_{e=1}^{N_h} \left\{ - \int_{\Omega^e} [N_\Sigma]^T [N_L] \, \frac{\partial\sigma_m}{\partial c_L} \bigg|^{(k)}_{n+1} r^2 \, \mathrm{d}r \right\} ,
$$

$$
[K^{\Sigma\,T}] = \mathop{\mathbf{A}}_{e=1}^{N_h} \left\{ - \int_{\Omega^e} [N_\Sigma]^T [N_T] \, \frac{\partial\sigma_m}{\partial c_T} \bigg|^{(k)}_{n+1} r^2 \, \mathrm{d}r \right\} ,
$$

$$
[K^{\Sigma\,u}] = \mathop{\mathbf{A}}_{e=1}^{N_h} \left\{ - \int_{\Omega^e} [N_\Sigma]^T [B_u] \, \frac{\partial\sigma_m}{\partial\varepsilon_r} \bigg|^{(k)}_{n+1} r^2 \, \mathrm{d}r - \int_{\Omega^e} [N_\Sigma]^T [N_u] \, \frac{\partial\sigma_m}{\partial\varepsilon_\theta} \bigg|^{(k)}_{n+1} r \, \mathrm{d}r \right\} ,
$$

$$[K^{\Sigma\Sigma}] = \mathop{\mathbf{A}}_{e=1}^{N_h} \left\{ \int_{\Omega^e} [N_\Sigma]^T [N_\Sigma] \, r^2 \, \mathrm{d}r \right\} ,$$

$$[R^L] = - \mathop{\mathbf{A}}_{e=1}^{N_h} \left\{ \frac{1}{\Delta t} \int_{\Omega^e} [N_L]^T [N_L] \left([c_L]_{n+1}^{(k)} - [c_L]_n \right) r^2 \, \mathrm{d}r + \int_{\Omega^e} [B_L]^T [B_L] [c_L]_{n+1}^{(k)} \, \mathbb{D}_L \, r^2 \, \mathrm{d}r + \right.$$
$$\left. - \int_{\Omega^e} [B_L]^T [B_\Sigma] [\Sigma]_{n+1}^{(k)} \, \mathbb{D}_\Sigma\big|_{n+1}^{(k)} \, r^2 \, \mathrm{d}r + \int_{\Omega^e} [N_L]^T \, w^{(1)}\big|_{n+1}^{(k)} \, r^2 \, \mathrm{d}r \right\} + \left([N_L]^T \, \bar{h}_L \, r^2 \right)\Big|_{r=r_0} ,$$

$$[R^T] = - \mathop{\mathbf{A}}_{e=1}^{N_h} \left\{ \frac{1}{\Delta t} \int_{\Omega^e} [N_T]^T [N_T] \left([c_T]_{n+1}^{(k)} - [c_T]_n \right) r^2 \, \mathrm{d}r - \int_{\Omega^e} [N_T]^T \, w^{(1)}\big|_{n+1}^{(k)} \, r^2 \, \mathrm{d}r \right\} ,$$

$$[R^u] = - \mathop{\mathbf{A}}_{e=1}^{N_h} \left\{ \int_{\Omega^e} [B_u]^T \left(2 \, \sigma_\tau\big|_{n+1}^{(k)} + \sigma_m\big|_{n+1}^{(k)} \right) r^2 \, \mathrm{d}r + \int_{\Omega^e} 2 \, [N_u]^T \left(\sigma_m\big|_{n+1}^{(k)} - \sigma_\tau\big|_{n+1}^{(k)} \right) r \, \mathrm{d}r \right\} ,$$

$$[R^\Sigma] = - \mathop{\mathbf{A}}_{e=1}^{N_h} \left\{ \int_{\Omega^e} [N_\Sigma]^T \left([N_\Sigma] [\Sigma]_{n+1}^{(k)} - \sigma_m\big|_{n+1}^{(k)} \right) r^2 \, \mathrm{d}r \right\} .$$

The value assumed by the scalar functions and their derivatives appearing in $[K^{\alpha\beta}]$ and $[R^\alpha]$ can be easily computed from the respective definitions as long as they do not depend on the inelastic deformations. This applies to the rate of chemical reaction $w^{(1)}$, the stress component σ_m, as well as to $\mathbb{D}_\Sigma$.

Conversely the constitutive definition of σ_τ depends on ε_{in} and vice versa. In this case the flow rule (4.18) has to be integrated properly. This has been conducted here with a standard viscoplastic *Return-mapping Algorithm* [323]. The method is based on the definition of a *trial elastic state* as the state in which the evolution of ε_{in} is arbitrarily frozen from the previous time step. Accordingly the trial deviatoric stress is defined as

$$\sigma_\tau^{trial} = 2 \, G \left(\varepsilon_\tau\big|_{n+1}^{(k)} - \frac{3}{2} \, \varepsilon_{in}\big|_n \right) . \tag{4.36}$$

If the trial state does not cause the inelastic flow to occur, i.e. $\varphi(\sigma_\tau^{trial}) < 0$, the step is elastic which implies that

$$\sigma_\tau\big|_{n+1}^{(k)} = \sigma_\tau^{trial} ,$$

and the derivatives of σ_τ can be calculated merely from (4.36).

On the other hand, when $\varphi(\sigma_\tau^{trial}) \geq 0$ the solid undergoes viscoplastic flow. The increment of the inelastic deformation is computed by numerical integration of formula (4.18)

$$\varepsilon_{in}\big|_{n+1}^{(k)} - \varepsilon_{in}\big|_n = \sqrt{\frac{2}{3}} \, \Delta\lambda \, \mathrm{sign}[\sigma_\tau^{trial}] ,$$

which corrects the trial stress state as follow

$$\sigma_\tau\big|_{n+1}^{(k)} = \sigma_\tau^{trial} - 3 \sqrt{\frac{2}{3}} \, G \, \Delta\lambda \, \mathrm{sign}[\sigma_\tau^{trial}] . \tag{4.37}$$

The symbol $\Delta\lambda = \lambda \, \Delta t$ defines the increment of the plastic multiplier for the current iteration. The latter results by inserting Eq. (4.37) into Eq. (4.18) in the closed form expression

$$\Delta\lambda = \frac{|\sigma_\tau^{trial}| - \sigma_Y}{\sqrt{\frac{3}{2}} \, \frac{g(\theta_T)|_{n+1}^{(k)}}{\Delta t} + 3 \sqrt{\frac{2}{3}} \, G} . \tag{4.38}$$

The stress component is then computed by substituting (4.38) into (4.37) while the the corresponding derivatives are

$$\left.\frac{\partial \sigma_\tau}{\partial \varepsilon_r}\right|_{n+1}^{(k)} = 2\,G\,\left(1 - 3\,\sqrt{\frac{2}{3}}\,G\,\frac{\partial \Delta\lambda}{\partial \sigma_\tau^{trial}}\,\text{sign}[\sigma_\tau^{trial}]\right)\,,$$

$$\left.\frac{\partial \sigma_\tau}{\partial \varepsilon_\theta}\right|_{n+1}^{(k)} = -2\,G\,\left(1 - 3\,\sqrt{\frac{2}{3}}\,G\,\frac{\partial \Delta\lambda}{\partial \sigma_\tau^{trial}}\,\text{sign}[\sigma_\tau^{trial}]\right)\,,$$

$$\left.\frac{\partial \sigma_\tau}{\partial c_T}\right|_{n+1}^{(k)} = 3\,\sqrt{\frac{2}{3}}\,\frac{\partial \Delta\lambda}{\partial c_T}\,\text{sign}[\sigma_\tau^{trial}]\,.$$

consistently with the Return-Mapping Algorithm.

Chapter 5

A model for LiCoO$_2$ electrode particles

5.1   Introduction

Insertion and extraction of Li ions in LiCoO$_2$ particles involve a wide range of electro-chemo-mechanical phenomena as reviewed in Chapter 4. Among those, changes in lithium content involves a series of phase-transitions and mechanical deformation of the electrode.

The phase-segregating behavior of LiCoO$_2$ is depicted by the phase diagram reported in Fig. 5.1a. It identifies the stable host phases as a function of lithium content x and temperature T. Neglecting the formation of the *monoclinic* phase ("Mono." in Fig. 5.1a) in correspondence of $x \sim 0.5$ for convenience, the electrode exhibits a uniform single phase for $x < 0.75$ and $x > 0.93$. Phases I and II consist both of hexagonal unit cells, differing for lithium content and lattice parameters as reported in Figure 5.1b. The unit cell volume of Li-rich phase I seems to be insensitive to the lithium content, while poor Li phase II contracts when Li increases. The transition from phase I to phase II (and vice versa) takes place between $x = 0.75$ and $x = 0.93$ and has been recognized as a first-order phase transition. In this regime phases I and II coexist in the host separated by a phase-interface.
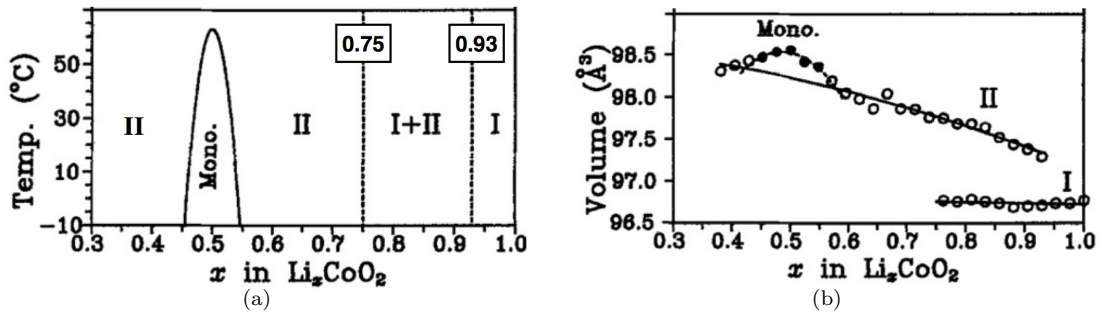
Figure 5.1: *Phase diagram (a) and unit cell volume (b) evolition as a function of lithium content x in $Li_x CoO_2$. Figures have been reprinted from [310].*

During phase-change, the overall lithium diffusion in the electrode is influenced by the phase boundary motion, which is in turn affected by the diffusion in each coexisting phase. The mechanical response of the electrode is influenced by the phase transition as well. Indeed a state of stress results from the lattice parameter mismatch at the interface between the two coexisting phases. Such a stress generation constitutes a so called *internal stress* since it is independent of any external stress as pointed out in [318]. Therefore, in the two-phase regime, the state of stress intensifies and might cause a mechanical degradation of LiCoO$_2$ compatible with plastic deformations.

The typical features of a phase-change can be simulated through trapping of Li ions in the hosting material as showed in Chapter 4. Despite some promising results has been achieved, this approach seems not to be completely appropriate as it leads to severe differences in the behavior during lithiation and delithiation. Moreover the phase-diagram of $LiCoO_2$ cannot be reproduced accurately.

In order to meet the experimental evidence, a slightly modification of the model analyzed in Chapter 4 is proposed here. In particular the trap density will be considered non-constant during the process as described in Section 5.2. The chemo-mechanical of a spherial $LiCoO_2$ particle will be simulated in Section 5.4 to evaluate the peculiarities of the model proposed. A three dimensional case will be analyzed in Section 5.5.

5.2 Modeling the evolution of c_T^{max}

The phase-transition occurring in Li_xCoO_2 between $x = 0.75$ and $x = 0.93$ is here modeled through a trapping reaction. By doing so we assume that the formation of Li-rich phase I is due to an immobilization of Li ions in the hosting material. On the other hand the electrode is assumed free of trapped lithium in the single phase II regime. Therefore phases I and II differ in the content of trapped lithium. The trapping process of lithium is described by the following chemical reaction

$$Li_L \overset{k_T}{\underset{k_L}{\rightleftharpoons}} Li_T \, , \tag{5.1}$$

which portrays the conversion of mobile Li_L to trapped Li_T species and vice versa by the rate of the reaction (5.1), denoted with $w^{(1)}$. The affinity $A^{(5.1)} = \mu_T - \mu_L$ (μ denotes the chemical potential) is the driving force for the chemical reaction (5.1). Positive values of $A^{(5.1)}$ promote trapping, whereas negative values induce lithium to escape traps. The condition $A^{(5.1)} = 0$ expresses chemical equilibrium.

Lithium cannot be trapped if there are no trap sites in the hosting material, as for $x < 0.75$ in the phase diagram of Fig. 5.1a. Furthermore, according to the same phase diagram the trapping process must be completed when $x > 0.93$.

It will be assumed henceforth that the molar density of trap sites c_T^{max} is not constant[1] (thus becoming a function of the location $\vec{x}$ and time t) and that it evolves with an internal variable ξ_T, which in turn is related to the concentration of interstitial lithium. It must be vanishing when $x < 0.75$: when lithium insertion takes place in the single Li-poor phase II no ions are immobilized. Once further lithium insertion takes place, i.e. $0.75 \leq x \leq 0.93$, the trapping reaction is triggered by the increase of available trap sites c_T^{max}. The lithium rich phase I is completely developed when traps are saturated with Li-ions and c_T^{max} reaches its ultimate value c_T^{MAX}. Further insertion is purely interstitial in the new material phase.

5.2.1 Helmholtz free energy and thermodynamic restrictions

We assume that an internal force χ_T allows c_T^{max} to evolve, in a similar manner as for the yield stress σ_y in isotropic plasticity. It thus holds

$$c_T^{max} = -\chi_T \, , \tag{5.2}$$

under the constraints $\chi_T = 0$ if $c_{Li} < c_{Li}^{II}$ and $\chi_T = -c_T^{MAX}$ if $c_{Li} \geq c_{Li}^{I}$.

$$\chi_T = \begin{cases} 0 & \text{if} \quad c_{Li} < c_{Li}^{II} \, , \\ \\ -c_T^{MAX} & \text{if} \quad c_{Li} > c_{Li}^{I} \, , \end{cases}$$

being c_{Li}^{II} and c_{Li}^{I} the concentration of total lithium correspondent to $x = 0.75$ and $x = 0.93$ in the phase diagram Fig. 5.1a. These constraints are approximated by means of an internal variable ξ_T and a *logistic function* $\mathcal{L}(\xi_T)$

$$\mathcal{L}(\xi_T) = -\frac{\chi_T}{c_T^{MAX}} = \frac{1}{1 + \exp\left[-B\,\xi_T\right]} \, . \tag{5.3}$$

---

[1]Non-constant trap densities do not constitute a novelty for trapping models. It customary for hydrogen transport models in metals to relate the density of trap sites to the equivalent plastic strains [286, 288, 287]. Here the trap sites are made dependent on the lithium molar content to mimic the pseudo-phase diagram of $LiCoO_2$.

The parameter B controls the sharpness of $\mathcal{L}(\xi_T)$ from 0 to 1, as depicted in Fig. 5.1a.
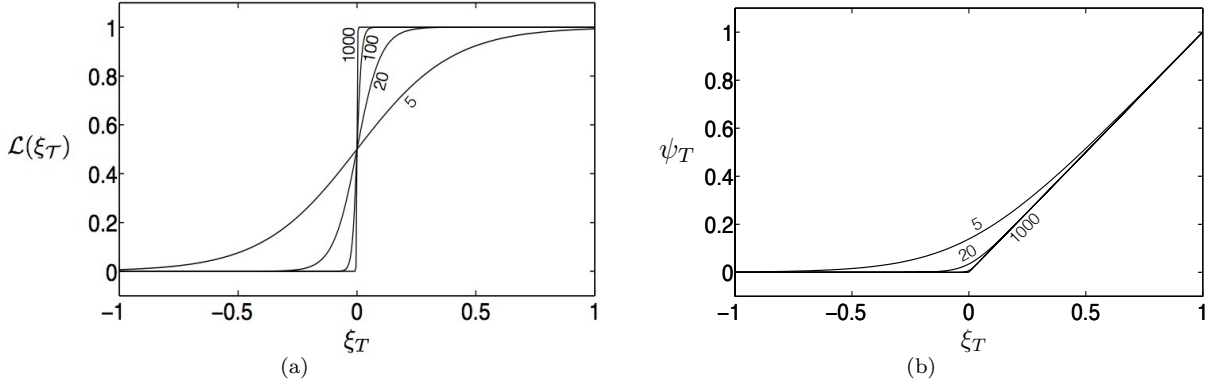
Figure 5.1: (a) Plot of the logistic function for $B = 5, 20, 100, 1000$. In the limit $B \to \infty$, the trap density changes sharply from 0 to c_T^{MAX} at $\xi_T = 0$. (b) Plot of the corresponding energy function for $B = 5, 20, 100, 1000$ and $c_T^{MAX} = 1$.

The internal force χ_T descends from an energetic contribution to the Helmholtz free energy, i.e.

$$\psi_T(\xi_T) = c_T^{MAX} \int \mathcal{L}(\xi_T) \, \mathrm{d}\xi_T = \frac{c_T^{MAX}}{B} \, \log\left[\exp\left[B \, \xi_T\right] + 1\right] \, , \tag{5.4}$$

which is plotted in Fig. 5.1b. The evolution of the internal variable (conceptually analogous to the flow rule in plasticity) is taken as non-associative, as follows

$$\frac{\partial \xi_T}{\partial t} = \frac{RT}{c_{\mathrm{Li}}^{MAX}} \, \frac{\partial c_L}{\partial t} \, , \tag{5.5}$$

with initial condition

$$\xi(0) = \frac{RT}{c_{\mathrm{Li}}^{MAX}} \, c_{\mathrm{Li}}^{II} \, .$$

denoting with c_{Li}^{MAX} the maximum possible total lithium concentration, given by $c_L^{max} + c_T^{MAX}$. It thus descends that

$$\xi_T(\vec{x}, t) = RT \, \frac{c_L(\vec{x}, t) - c_{\mathrm{Li}}^{II}}{c_{\mathrm{Li}}^{MAX}} \, , \tag{5.6}$$

dimensionally equivalent to a chemical potential.

The Clausius-Duhem inequality (3.28) is now enriched by the term $-\frac{\partial \psi_{diff}}{\partial \xi_T} \frac{\partial \xi_T}{\partial t} + \chi_T \frac{\partial \xi_T}{\partial t}$, and the restriction (3.31b) becomes

$$-\vec{h}_L \cdot \nabla\left[\mu_L\right] - \frac{\partial \psi_{diff}}{\partial \xi_T} \frac{\partial \xi_T}{\partial t} + \chi_T \frac{\partial \xi_T}{\partial t} \geq 0 \, . \tag{5.7}$$

5.2.2 Free energy at chemical equilibrium

As in Chapter 4, a vanishing affinity *at all times* is here considered to study the evolution of the free energy, specifically its convexity, as a function of the molar fraction of *total* Lithium ions. In view of the evolution of ξ_T

$$c_T^{max} = \frac{c_T^{MAX}}{1 + \exp\left[-B \, RT \, \frac{c_L - c_{\mathrm{Li}}^{II}}{c_{\mathrm{Li}}^{MAX}}\right]} \, , \tag{5.8}$$

93

and the trapped concentration c_T can be related to the interstitial lithium c_L by the following identity

$$c_T = \frac{1}{1 + \frac{1-\theta_L}{K_{eq}\,\theta_L}\,\alpha} \; \frac{c_T^{MAX}}{1 + \exp\left[-B\,RT\,\frac{c_L - c_{Li}^{II}}{c_{Li}^{MAX}}\right]} \tag{5.9}$$

that descends from Eq. (4.3) , with $\theta_L = c_L/c_L^{max}$ as usual. The dimensionless concentration θ_{Li} has been redefined with respect to (4.5), as follows

$$\theta_{Li} = \frac{c_L + c_T}{c_{Li}^{MAX}} \; . \tag{5.10}$$

The ratio c_T^{MAX}/c_L^{max} can be estimated following [243] for *sharp-interface* models. Phases I and II are in equilibrium at phase-interface respectively with their minimum and maximum Li solubilities, i.e. $\theta_{Li}^{I} = 0.93$ and $\theta_{Li}^{II} = 0.75$, as the phase diagram advocates. Assuming that the trapping reaction (5.1) is the sole responsible of segregation, phases I and II coexist at phase-boundaries with different content of immobile Li but equal interstitial population. Moreover the fully developed rich phase I is characterized by saturated traps ($c_T = c_T^{MAX}$), while poor phase II contain only interstitial host sites ($c_T^{max} = 0$). As a consequence, c_T^{MAX} in (5.3) can be quantified from the difference between between θ_{Li}^{I} and θ_{Li}^{II}

$$\frac{c_T^{MAX}}{c_{Li}^{MAX}} = \theta_{Li}^{I} - \theta_{Li}^{II} = 0.18 \; . \tag{5.11}$$

It follows that $c_T^{MAX}/c_L^{max} = 0.22$ and $c_L^{max}/c_{Li}^{MAX} = 0.82$.

The evolution of c_T^{max} is thus parametrized by K^{eq}, B, T, and α. The impact of these parameters is investigated in Figure 5.2 where c_T^{max} is plotted against θ_{Li}. In the case with $K^{eq} = 1000$ and $B = 1$ the evolution of c_T^{max} match well with the phase diagram. Traps does not change for either $\theta_{Li} < 0.75$ ($c_T^{max} = 0$) and $\theta_{Li} > 0.93$ ($c_T^{max} = c_T^{MAX}$). Between $\theta_{Li} = 0.75$ and 0.93 the trap density evolves essentially in a linear manner with respect the concentration of lithium. On the other hand for $K^{eq} = B = 1$ the trap density grows also for $\theta_{Li} > 0.93$ and reaches its maximum value for $\theta_{Li} = 1$.
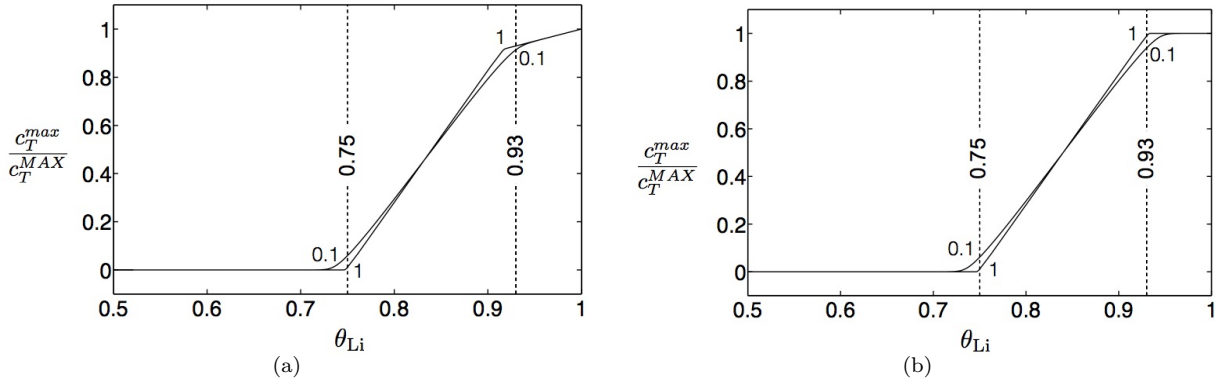
Figure 5.2: *Plot of the evolution of the trap density c_T^{max} as a function of the normalized content of lithium x. In (a) $K^{eq} = 1$ and $B = 0.1, 1$, while in (b) $K^{eq} = 1000$ and $B = 0.1, 1$. In both cases $T = 300\,K$ and $\alpha = 1$.*

In order to focus on the chemo-transport mechanisms, we neglect here the mechanical contribution. By doing so, the Helmholtz free energy density ψ is decomposed into two separate parts: the diffusive contribution ψ_{diff} and ψ_T

$$\psi(c_L, c_T, \xi_T) = \psi_{diff}(c_L, c_T, \xi_T) + \psi_T(\xi_T) \; . \tag{5.12}$$

The free energy density for the continuum approximation of mixing ψ_{diff} has been described in Chapter 4 in Eq. (4.6b). ψ_T is taken as in Eq. (5.4). For convenience the free energy is rewritten in dimensionless form as follow

$$\hat{\psi} = \hat{\psi}_{diff} + \hat{\psi}_T \,, \tag{5.13}$$

where

$$\hat{\psi}_{diff} = \hat{\mu}_L^0 \, \hat{c}_L^{max}(\theta_{\text{Li}}) \, \theta_L(\theta_{\text{Li}}) + \hat{\mu}_T^0 \, \hat{c}_T^{max}(\theta_{\text{Li}}) \, \theta_T(\theta_{\text{Li}}) + \hat{\psi}_\eta(\theta_{\text{Li}}) \,,$$

$$\hat{\psi}_\eta(\theta_{\text{Li}}) = \hat{c}_L^{max}(\theta_{\text{Li}}) \left\{ \theta_L(\theta_{\text{Li}}) \, \ln[\theta_L(\theta_{\text{Li}})] + (1 - \theta_L(\theta_{\text{Li}})) \, \ln[1 - \theta_L(\theta_{\text{Li}})] \right\} +$$
$$+ \hat{c}_T^{max}(\theta_{\text{Li}}) \left\{ \theta_T(\theta_{\text{Li}}) \, \ln[\theta_T(\theta_{\text{Li}})] + (1 - \theta_T(\theta_{\text{Li}})) \, \ln[1 - \theta_T(\theta_{\text{Li}})] \right\} \,,$$

being $\hat{\psi}_\eta$ the entropic part of the diffusive free energy and

$$\hat{\mu}_\beta^0 = \frac{\mu_\beta^0}{R\,T} \,, \qquad \hat{c}_\beta^{max} = \frac{c_\beta^{max}}{c_{\text{Li}}^{MAX}} \,, \qquad \hat{\psi}_T = \frac{\psi_T}{c_{\text{Li}}^{MAX} \, R\,T} \,.$$
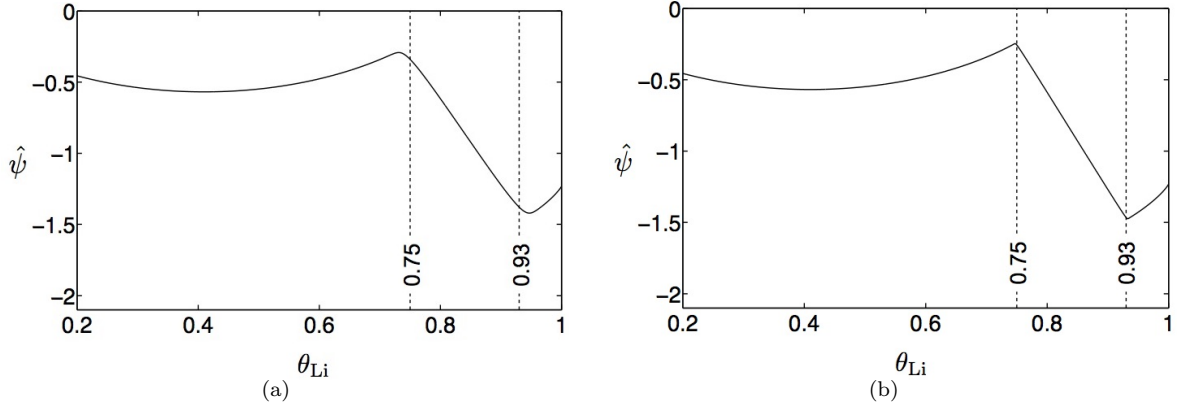
Figure 5.3: *Parametric plot of $\psi(c_L, c_T, \xi_T)$ as a function of θ_{Li} for $B = 0.1$ (a) and $B = 1$ (b). In these plots, $K_{eq} = 1000$, $\alpha = 1$, and $\hat{\mu}_L^0 = 0$, $T = 300\,K$, and $\alpha = 1$.*

In view of Eqs. (5.6), (5.9), and (5.10) the Helmholtz free energy $\hat{\psi}$ can be plot against θ_{Li}. Figure 5.3 depicts $\hat{\psi}$ for $K_{eq} = 1000$, $\alpha = 1$, and two different values of B. The plots show three distinctive behaviors in three different zones, namely for $\theta_{\text{Li}} < 0.75$, $\theta_{\text{Li}} > 0.93$ and the remaining interval. These three zones match well the phase domains in the diagram in Fig. 5.1a.

Because of the factor $RT = 2578.73$ within ξ_T, the graph of ψ_T is basically made by two straight lines. For for $\theta_{\text{Li}} < 0.75$ therefore, the Helmholtz free energy is essentially ψ_{diff}. Since however K_{eq} is very large and c_T^{max} close to zero, $\theta_T \sim 1$ and the main part of ψ_{diff} is in fact the entropic contibution for c_L

$$\psi_\eta^L = RT \, c_L^{max} \, (\theta_L \, \ln[\theta_L] + (1 - \theta_L) \, \ln[1 - \theta_L]) \,,$$

in view of the assumption made that $\mu_L^0 = 0$.

As $\theta_{\text{Li}} > 0.93$, the amount of trapped lithium is significant: indeed, because of the factor $RT = 2578.73$ within ξ_T the logistic function is close to 1 and $c_T^{max} \sim c_T^{MAX}$. Since K_{eq} is very large, traps tend to saturate soon, and $\theta_T \sim 1$ again. Therefore, in the region $\theta_{\text{Li}} > 0.93$ the Helmholtz free energy is dominated by the entropic contibution for θ_L and by ψ_T.

In the remaining region $0.75 < \theta_{\text{Li}} < 0.93$ the slope of the graph of $\hat{\psi}$ is almost constant. This behavior is dictated by the equilibrium constant, that is very high and favor the immediate saturation of traps under the

95

assumption of infinitely fast kinetics. In this region in fact, c_T^{max} evolves from a value close to zero to c_T^{MAX}. Since traps are instantaneously filled, $\theta_T \sim 1$ and the increment of ψ is essentially due to the factor $\mu_T^0 c_T$ and to ψ_T, which is linear in fact. In the simulations of Fig. 5.3 it was taken $K_{eq} = 1000$ that corresponds to $\hat{\mu}_T^0 = -6.9078$.

The smaller the value of B, the smoother the junction of the plot between the three regions described above. Small values of B in fact allow c_T^{max} to change before c_L reaches its maximum value. Figure 5.4 plots the Helmholtz free energy for $K_{eq} = 1$, $\alpha = 1$, and $\hat{\mu}_L^0 = \hat{\mu}_T^0 = 0$. Although the curves differ from 5.3, the qualitative description applies again.
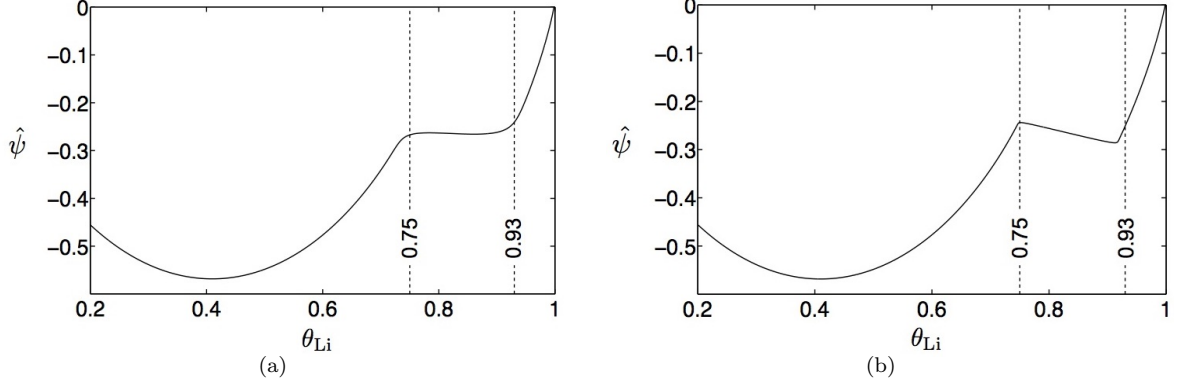
Figure 5.4: *Parametric plot of $\psi(c_L, c_T, \xi_T)$ as a function of θ_{Li} for $B = 0.1$ (a) and $B = 1$ (b). In these plots, $K_{eq} = 1$, $\alpha = 1$, $\psi_0 = 0$, and $\mu_L^0 = 0$.*

The Helmholtz free energy is clearly non convex and this feature is dictated by the description of trapping rather than by energetic interactions, that have not been accounted for here. One could then use this free energy within a core-shell model, to determine the equilibrium concentrations of lithium in a solid (a sphere, actually, in core-shell models) that contains two phases (Li-poor and Li-reach) separated by a sharp interface that moves under the assumption of thermodynamic equilibrium at all instants. The solution is provided by the so-called "tangent rule". We are not going to follow this path, and interested readers may refer to the large literature on the subject (see a review in [319] or [32]).

5.3 Governing equations with evolving c_T^{max}

Governing equations of the chemo-mechanical response of LiCoO$_2$ electrodes with evolving c_T^{max} are discussed in this section. As done in Chapter 4 we introduce several assumptions which simplify the general framework developed in Chapter 3. In particular, the process is assumed to be isothermal ($T = T_0$), the energetic interaction in the free energy are neglected ($\chi = 0$), and the stress tensor does not include a viscous part ($\boldsymbol{\sigma} = \boldsymbol{\sigma}^e$). In addition we consider the chemical reaction as an infinitely-fast process for simplicity. Therefore the the concentration of trapped lithium is no longer an independent variable, but is in turn function of the interstitial lithium and the stress tensor as follow

$$c_T(c_L, \boldsymbol{\sigma}) = \frac{K^{eq} c_L c_T^{max}(\xi_T)}{K^{eq} c_L + (c_L^{max} - c_L) \alpha(\mathrm{tr}\,[\boldsymbol{\sigma}])} \,, \tag{5.15a}$$

with

$$\alpha = \exp\left\{ \frac{\omega_L - \omega_T}{RT} \,\mathrm{tr}\,[\boldsymbol{\sigma}] \right\} , \tag{5.15b}$$

and

$$c_T^{max} = \frac{c_T^{MAX}}{1 + \exp\left[-B\,R\,T\,\frac{c_L - c_L^{II}}{c_{Li}^{MAX}}\right]} \,. \tag{5.15c}$$

96

The set of governing equations (3.68) thus reduces to

$$\frac{\partial c_L}{\partial t} + \frac{\partial c_T}{\partial t} + \text{div}\left[\vec{h}_L\right] = 0\,, \tag{5.16a}$$

$$\text{div}\left[\boldsymbol{\sigma}\right] = \vec{0}\,, \tag{5.16b}$$

for $\vec{x} \in \mathcal{B}$ and time $t \in \left]0\,,\,t_f\right]$.

Equation (5.16a) is the conservation of total lithium. Note that the conservation of lithium is not enforced here in terms of interstitial and trapped lithium separately. This fact relies on the assumption of infinitely-fast kinetics, accordingly the chemical kinetics is not explicitly modeled here.

The mechanical inelastic behavior is modeled as in Chapter 4 through the following Perzyna type visco-plastic law

$$\frac{\partial \boldsymbol{\varepsilon}^{in}}{\partial t} = \frac{\text{dev}\left[\boldsymbol{\sigma}\right]}{||\,\text{dev}\left[\boldsymbol{\sigma}\right]||}\,\lambda\,, \qquad \lambda = \frac{\varphi\,\mathcal{H}(\varphi)}{g(c_T)}\,. \tag{5.17a}$$

In equation (5.17a) $\varphi = ||\text{dev}\left[\boldsymbol{\sigma}\right]|| - \sqrt{2/3}\,\sigma_Y$ is the Mises yield function without hardening; $\mathcal{H}$ is the Heaviside step function; $g(c_T)$ is the viscosity, assumed as a given function of the concentration of trapped species. A simple choice for $g(c_T)$ is the affine function

$$g(c_T) = g_0 + g_1\,\frac{c_T}{c_T^{MAX}}\,, \tag{5.17b}$$

with g_0, g_1 given positive parameters.

From definition (5.17a) $\boldsymbol{\varepsilon}^{in}$ is trace-less and the stress-strain relationship rewrites from (3.55) as

$$\boldsymbol{\sigma} = 2\,G\,\text{dev}\left[\boldsymbol{\varepsilon} - \boldsymbol{\varepsilon}^{in}\right] + K\,\text{tr}\left[\boldsymbol{\varepsilon} - \boldsymbol{\varepsilon}^{s}\right]\mathbb{1}\,, \tag{5.18a}$$

with

$$\boldsymbol{\varepsilon} = \frac{1}{2}\left(\nabla\left[\vec{u}\right] + \nabla\left[\vec{u}\right]^{T}\right)\,, \tag{5.18b}$$

and

$$\boldsymbol{\varepsilon}^{s} = \omega_L\left(c_L - c_L^0\right)\mathbb{1} + \omega_T\left(c_T - c_T^0\right)\mathbb{1}\,. \tag{5.18c}$$

In the assumption of constant material parameters G and K, along with $\chi = 0$, the chemical potentials derived in Chapter 3 Eq. (3.59) reduce to

$$\mu_\beta = \mu_\beta^0 + R\,T\ln\left[\frac{\theta_\beta}{1 - \theta_\beta}\right] - \omega_\beta\,\text{tr}\left[\boldsymbol{\sigma}\right]\,, \qquad \beta = L, T\,. \tag{5.19}$$

Finally the constitutive definition of lithium flux yields

$$\vec{h}_L = -\mathbb{D}_L\,\nabla\left[c_L\right] + \frac{\mathbb{D}_L\,\omega_L}{R\,T}\,c_L\left(\frac{c_L^{max} - c_L}{c_L^{max}}\right)\nabla\left[\text{tr}\left[\boldsymbol{\sigma}\right]\right]\,. \tag{5.20}$$

Boundary conditions

$$\vec{h}_L \cdot \vec{n} = \bar{h} \tag{5.21a}$$

$$\boldsymbol{\sigma} \cdot \vec{n} = \vec{\bar{p}} \tag{5.21b}$$

are imposed along the Neumann boundaries $\partial^N V$. To ensure solvability of the problem, Dirichlet boundary conditions have to be enforced along $\partial^D V$ as follow

$$c_L = \bar{c_L}$$
$$\vec{u} = \bar{\vec{u}}$$

Initial conditions are usually imposed for concentration of interstitial species c_L. Balance of momentum, together with boundary conditions, provide the necessary and sufficient equations to define $\vec{u}$ at $t = 0$.

5.4   Lithiation and delithiation of a LiCoO$_2$ spherical particle

In this section the lithium insertion and extraction from LiCoO$_2$ particles will be simulated. The influence of parameters and model performance with evolving c_T^{max} will be analyzed with a series of one-dimensional studies on spherical particles, using radial-symmetry to enlighten the computational burden. The governing equations have been restated in a spherical coordinate system $\{r, \theta, \phi\}$ with unit vectors $\{\vec{e}_r, \vec{e}_\theta, \vec{e}_\phi\}$ centered at the centroid of the sphere[2]

$$\frac{\partial c_L}{\partial t} + \frac{\partial c_T}{\partial t} + \frac{\partial h_r}{\partial r} + 2\frac{h_r}{r} = 0, \tag{5.23a}$$

$$\frac{\partial \sigma_r}{\partial r} + 2\frac{\sigma_r - \sigma_\theta}{r} = 0, \tag{5.23b}$$

having defined

$$\vec{h}_L = h_r\,\vec{e}_r\,,$$
$$\boldsymbol{\sigma} = \sigma_r\,\vec{e}_r \otimes \vec{e}_r + \sigma_\theta\,(\vec{e}_\theta \otimes \vec{e}_\theta + \vec{e}_\phi \otimes \vec{e}_\phi)\,.$$

The particle, of radius $r_0 = 10\mu$m, allows free expansion and contraction at its boundary. Rigid motions (one-dimensional in nature) have been restrained by imposing a null displacement at the center of the particle. Boundary and initial conditions are modeled in the same manner as in Chapter 4. For Li removal simulations, the particle is initially filled with lithium at the uniform concentration $c_{\text{Li}}(r, t=0) = c_{\text{Li}}^{0(\text{del})}$. The Lithium is extracted with an uniform and constant flux $h_r = \overline{h}_L$, at the boundary $r = r_0$, until the concentration c_{Li} on the external surface equals the limit $c_{\text{Li}}^{F(del)}$. Then the extraction process proceeds holding fixed c_{Li} at $r = r_0$. The lithiation process is modeled in a similar way: an inward and constant flux $\overline{h}_L$ is imposed at the sphere boundary. The concentration of lithium increased from an initial uniform distribution $c_{\text{Li}}(r, t=0) = c_{\text{Li}}^{0(\text{lit})}$. Once the lithium concentration reaches the limit $c_{\text{Li}}^{F(\text{lit})}$, this value is held fixed on the external boundary. The initial (0) and limit (F) concentrations for lithiation (lit) and delithiation (F) processes are defined as

$$c_{\text{Li}}^{0\,(\text{lit})} = c_{\text{Li}}^{F\,(\text{del})} = c_{\text{Li}}^{MAX}/2\,, \tag{5.25a}$$
$$c_{\text{Li}}^{F\,(\text{lit})} = c_{\text{Li}}^{0\,(\text{del})} = c_{\text{Li}}^{MAX}\,, \tag{5.25b}$$

in order to simulate the particle response upon fully battery charge/discharge[3].

Chemical equilibrium is assumed throughout the process. Thus the initial concentration of interstitial lithium $c_L(r, t=0)$ can be computed from $c_{\text{Li}}^{0\,(\text{lit})}$ or $c_{\text{Li}}^{0\,(\text{del})}$ using Eqs. (5.9) - (5.10).

The prescribed Li flux on boundary $\overline{h}_L$ corresponds to a charge/discharge current density $i_{ext} = 0.534\,\text{A/m}^2$, equivalent to a C rate of 0.5 according to the formula [300]

$$C = \frac{3600\,i_{ext}\,A}{V\,F\,\left(c_{\text{Li}}^{MAX} - c_{\text{Li}}^{MAX}/2\right)}\,, \tag{5.26}$$

---

[2]The derivation of governing equations (5.23) is not reported here for convenience. The reader may refer to Section 4.5 for all the details.

[3]For numerical convenience the equation (5.25b) has been implemented as $c_{\text{Li}}^{F\,(\text{lit})} = c_{\text{Li}}^{0\,(\text{del})} = 0.99\,c_{\text{Li}}^{MAX}$

Material Parameters				Ref.
Maximum Lithium concentration	c_{Li}^{MAX}	2.390×10^4	mol/m^3	[152]
Lithium diffusivity	D_L	5.387×10^{-15}	m^2/s	[152]
Coefficients of chemical expansion	$\omega_L = \omega_T$	-5.300×10^{-7}	m^3/mol	[107]
Young modulus	E	370	GPa	[152]
Poisson ratio	ν	0.2	-	[152]
Yield stress	σ_Y	1.0	GPa	[318]
Maximum trap density	$c_T^{MAX}/c_{\text{Li}}^{MAX}$	0.18	-	this study
Relaxation time 0	g_0/E	1.0	s	this study
Relaxation time 1	$(g_0 + g_1)/E$	60	s	this study

Table 5.1: Material parameters adopted for the numerical simulations.

where A and V are respectively volume and surface area of the particle, F is Faraday's constant in Coulombs per moles. Charge and discharge operations have been simulated for a total time of 4 hours at temperature $T = 300\,\text{K}$.

Others material constants used for the numerical simulation that follow are listed in Table 5.1. Material parameters taken from the literature are representative of LiCoO$_2$ commercial particles. The role of constants B and K^{eq} will be investigated on the evolution of lithium concentration profiles.

The system of equations (5.23) have been solved numerically through the Finite Element Method as conducted in Chapter 4 (see Appendix 4.A for the details). Thus governing equations have been written in integral form and then discretized in space with 400 elements along the radius r, while the time evolution is resolved with a time increment $\Delta t = 3.6\,\text{s}$. The resulting nonlinear algebraic problem has been solved with a Newton-Raphson scheme. This numerical procedure has been implemented in a MATLAB package script purposely written. For completeness the explicit expressions for the residual vector and consistent tangent matrix of the Newton-Raphson algorithm is explicitly listed in Appendix 5.A.

5.4.1 Numerical simulations neglecting mechanical effects

The impact of evolving c_T^{max} on particle response is first evaluated by neglecting mechanical effects. Therefore, in this section we focus only on the chemo-diffusive problem described by governing equations (5.23). Mechanical influence on the chemical potentials μ_L and μ_T is neglected, hence the chemical potentials from Eq. (5.19) hold

$$\mu_\beta = \mu_\beta^0 + R\,T \ln\left[\frac{\theta_\beta}{1 - \theta_\beta}\right] \qquad \beta = \text{L, T}\,. \tag{5.27}$$

In this way the concentration of trapped species can be simplified from (5.15a) as follow

$$c_T(c_L) = \frac{K^{eq}\,c_L\,c_T^{max}(\xi_T)}{K^{eq}\,c_L + (c_L^{max} - c_L)}\,. \tag{5.28}$$

The governing equations for lithium transport in the particle thus reduce only to formula (5.23a), since the mechanics does not play any role. Moreover the lithium flux is now constitutively defined simply as

$$h_r = -\mathbb{D}_L \, \frac{\partial c_L}{\partial r} \; . \tag{5.29}$$

5.4.1.1 Lithium extraction

The role of B - Figures 5.1 and 5.2 show the evolution of lithium profile (a) and trap density (b) for different values of B at given $K^{eq} = 100$. For $B = 1\,\mathrm{mol/J}$ the lithium distribution resembles that typical of sharp-interface models (see [243] for comparison).

The extraction process can be divided in three different stages. For high content of lithium ($c_{\mathrm{Li}}/c_{\mathrm{Li}}^{MAX} > 0.93$ everywhere) the trap density is uniform and equal to c_T^{MAX}, hence the lithium distribution is governed by Fick's diffusion law in the entire particle. The initial regime is perturbed when $c_{\mathrm{Li}}/c_{\mathrm{Li}}^{MAX} \sim 0.93$ (i.e. $c_L/c_{\mathrm{Li}}^{MAX}$ approaches 0.75) because the trap density drops down to zero and the trapped lithium moves to the interstitial sites. The traps density is no longer uniform in space but evolves separating two regions where $c_T^{max} = 0$ (external shell) and $c_T^{max} = c_T^{MAX}$ (inner core). The Li ions distribute similarly in two regions with rich ($c_{\mathrm{Li}}/c_{\mathrm{Li}}^{MAX} > 0.93$) and poor ($c_{\mathrm{Li}}/c_{\mathrm{Li}}^{MAX} < 0.75$) concentration, separated by a diffuse-interface with small thickness (see Fig. 5.1a). Such an interface moves along the particle radius without significant change in its thickness. The particle thus enters in a two-phase coexistence with a formation of a phase-interface triggered by traps annihilation.

Once the trap density has been depleted everywhere the lithium distribution evolves with the same peculiarity of the first stage.
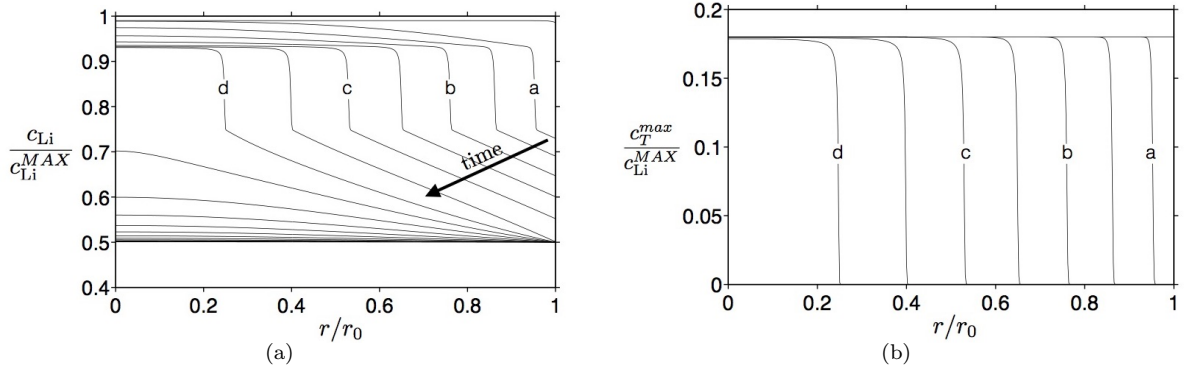
Figure 5.1: **Li extraction** - Lithium concentration (a) and trap density (b) profiles as function of radial coordinate at intervals of 900 s for $B = 1\,mol/J$ and $K^{eq} = 100$.

A sort of interface between Li rich and poor phases can be recognized for smaller values of B as well, as shown in Fig. 5.2a. Its width is neither negligible nor constant, since it grows in the particle core. The "smeariness" of the phase-interface that arises in Fig. 5.1a and 5.2a is thus essentially ruled by Eq. (5.15c) through parameter B.

The role of K^{eq} - The influence of the K^{eq} is evaluated in Figures 5.1 - 5.3 at given parameter $B = 1\,\mathrm{mol/J}$. The constant of chemical equilibrium has influence over the Li profile merely for $c_{\mathrm{Li}}/c_{\mathrm{Li}}^{MAX} \geq 0.75$, i.e. in the regime when traps are available for the chemical reaction.

High equilibrium constants promote the saturation of traps, when they are present, as discussed in Section 4.3 . Accordingly the trapped lithium remains basically untouched for high values of total lithium ($c_{\mathrm{Li}}/c_{\mathrm{Li}}^{MAX} > 0.93$) and the extraction process involves only the interstitial population (See Fig. 5.1a).

The scenario is different for $K^{eq} \ll 1$ because the un-trapping reaction is favorite in the regime when $c_T^{max} = c_T^{MAX}$. The chemical reaction thus dominates the first part of the extraction process and the Li concentration profiles develop with the same peculiarities described in Chapter 4. The effect of trap annihilation is recognizable in the change in slope for $c_{\mathrm{Li}}/c_{\mathrm{Li}}^{MAX} \sim 0.75$. However the latter is less evident than the one depicted in Fig. 5.1a for $K^{eq} \gg 1$ because the trap sites are almost empty when they vanish.
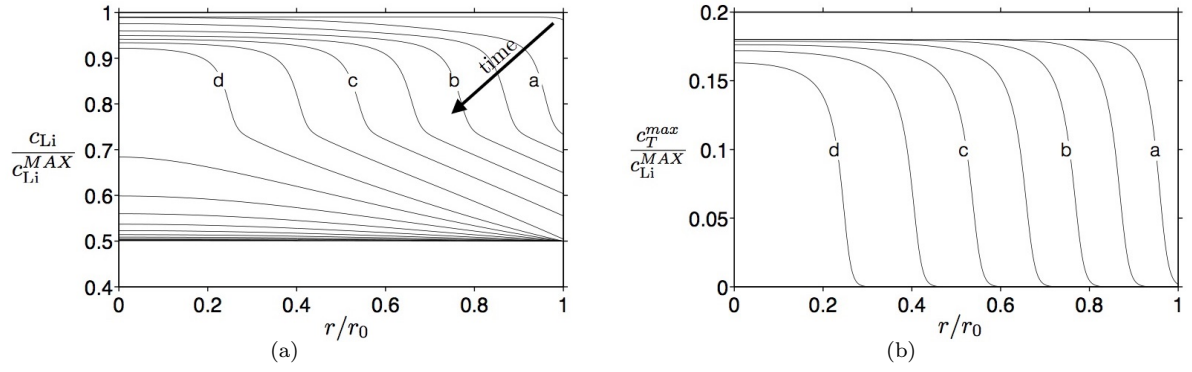
Figure 5.2: **Li extraction** - *Lithium concentration (a) and trap density (b) profiles as function of radial coordinate at intervals of* $900\,s$ *for* $B = 0.1\,mol/J$ *and* $K^{eq} = 100$.
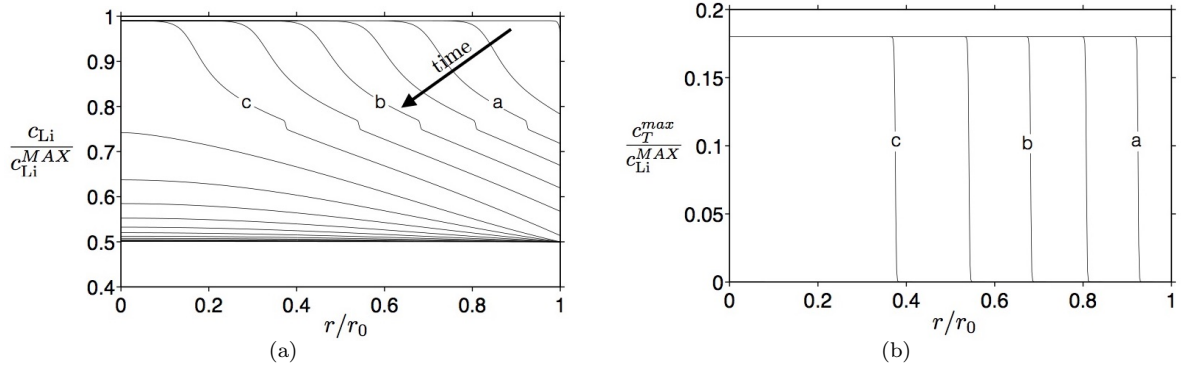
Figure 5.3: **Li extraction** - *Lithium concentration (a) and trap density (b) profiles as function of radial coordinate at intervals of* $900\,s$ *for* $B = 1\,mol/J$ *and* $K^{eq} = 0.01$.

5.4.1.2   Lithium insertion

The role of B - The development of lithium profiles and trap density are reported in Figures 5.4 - 5.5 for different values of B and $K^{eq} = 100$. The insertion process for both $B = 0.1$ and $B = 1\,mol/J$ can be partitioned in three stages as described for the extraction case. At first lithium fills the interstitial sites since no traps are present in the particle. When $c_{\mathrm{Li}}/c_{\mathrm{Li}}^{MAX}$ approaches 0.75 the traps density evolves as prescribed by formula (5.15c), causing the growth of a region with uniform $c_T^{max} = c_T^{MAX}$ (external shell) which progressively consumes the particle core where $c_T^{max} = 0$. Similarly the Li distribution evolves with the features of a phase-segregation with the presence of Li-rich and Li-poor phases in the particle. Once the traps density reaches the limit value c_T^{MAX} everywhere, the Li distribution evolves as in a single phase hosting material. As noticed for the extraction process, lithium profiles typical of sharp-interface models are well recovered for $B = 1\,mol/J$ and $K^{eq} = 100$.

The role of K^{eq} - The influence of K^{eq} can be evaluated by comparison between Fig. 5.4 and Fig. 5.6. As discussed for the extraction case, small values of K^{eq} do not appear to be appropriate. The onset of a phase-segregation is not visible in Fig. 5.6a because $K^{eq} \ll 1$ does not promote an immediate saturation of trap sites when they are created. Moreover, as noticed in Chapter 4, the particle is capable to host less amount of lithium ions, especially in the particle core at the final time.

5.4.1.3   Lithium distribution at steady-state

For any finite value of B, Li concentration profiles cannot be discontinuous at *steady-state* if interface energies are not accounted for. Phase-interfaces dissolve at steady state, reached when the Li flux at the boundary
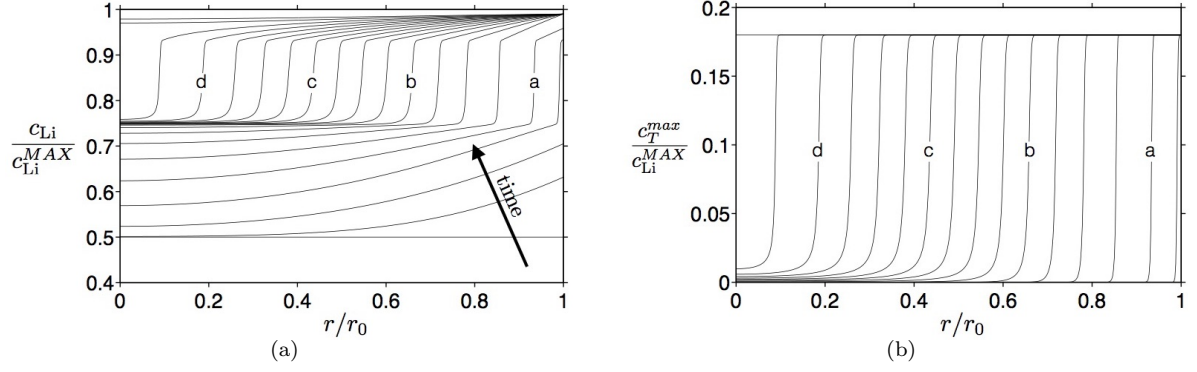
Figure 5.4: **Li insertion** - Lithium concentration (a) and trap density (b) profiles as function of radial coordinate at intervals of $900\,s$ for $B = 1\,mol/J$ and $K^{eq} = 100$.
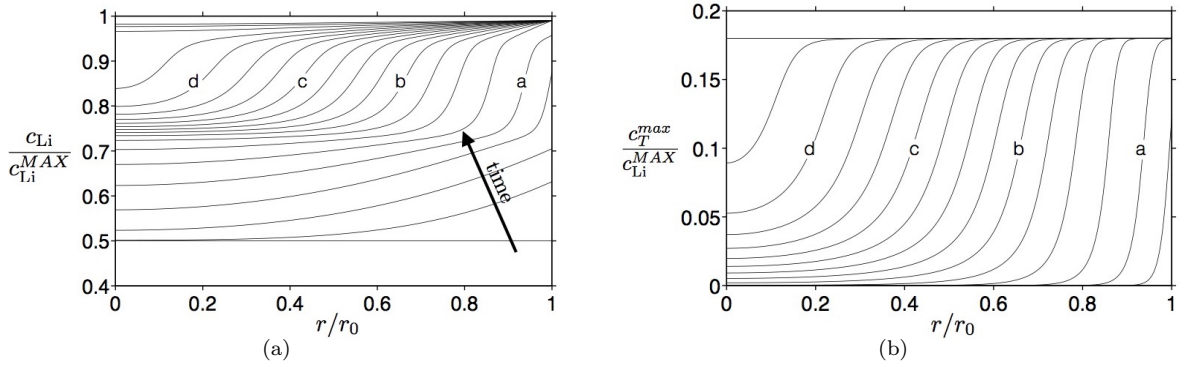
Figure 5.5: **Li insertion** - Lithium concentration (a) and trap density (b) profiles as function of radial coordinate at intervals of $900\,s$ for $B = 0.1\,mol/J$ and $K^{eq} = 100$.
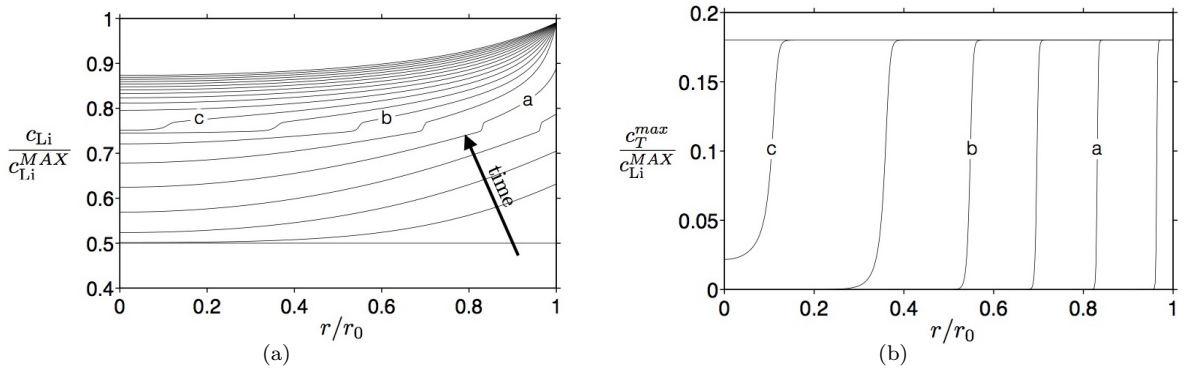
Figure 5.6: **Li insertion** - Lithium concentration (a) and trap density (b) profiles as function of radial coordinate at intervals of $900\,s$ for $B = 1\,mol/J$ and $K^{eq} = 0.01$.

vanishes and lithium internally redistributes. This feature relies on equations (5.23a) and (5.29) which at steady state are solved for a flat distribution of c_{Li}, as confirmed by the numerical results showed in Fig. 5.7.

5.4.2 Numerical simulations of the fully coupled chemo-mechanical problem

The role of the chemo-mechanical coupling - The evolution of lithium profiles accounting for mechanical effects is shown in Figure 5.8 assuming $B = 1\,\text{mol/J}$ and $K^{eq} = 100$. Parameters B and K^{eq} have been
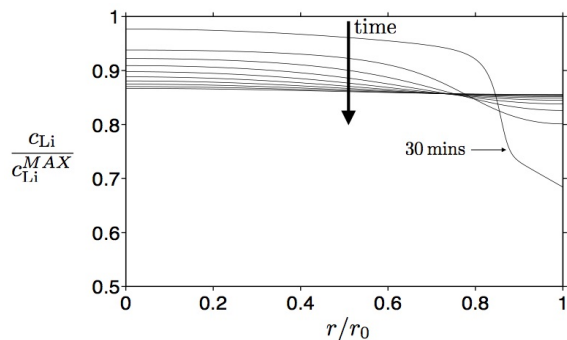
Figure 5.7: Time evolution of Li profiles for an isolated particles initially in a two-phase regime at time intervals of 1 hour. The initial Li distribution has been obtained by stopping the extraction process for $B = 0.1\,mol/J$ after 30 minutes (see Fig.5.2a). The concentration distribution progressively smoothes toward a uniform steady-state distributions in about 9 hours.

selected from the numerical analysis carried out in Section 5.4.1.

The impact of the mechanics on lithium distribution can be analyzed by comparison among Fig. 5.8 and Figs. 5.1a - 5.4a. The chemo-mechanical coupling causes a relaxation of Li concentration gradients attained during the evolution of c_T^{max}. Although the impact of mechanics is not negligible, the onset of a finite-with interface separating Li-rich and Li-poor phases is still recognizable. Numerical analyses, that have not been reported here for the sake of brevity, show that the lithium evolution does not change for $B > 1\,mol/J$.

The numerical analysis with $B \geq 1\,mol/J$ and $K^{eq} \gg 1$ is thus able to reproduce phase diagram of $LiCoO_2$ even though the mechanics is accounted for. For both charge and discharge processes, concentration profiles show steep gradients, which resemble a core/shell structure typical of a phase transformation. Gradients relax as the process advances, thus causing the phase boundary to progressively smear.
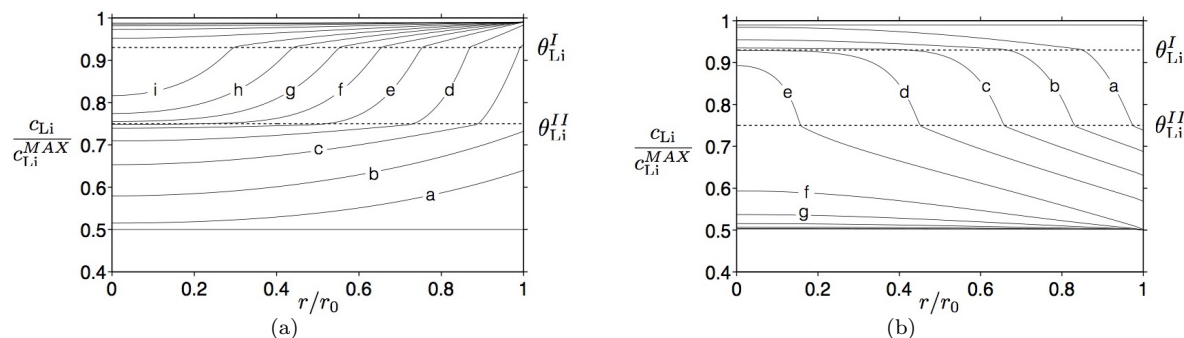
Figure 5.8: Lithium concentration profiles for $B = 1\,mol/J$ and $K^{eq} = 100$ at intervals of $1200\,s$ upon insertion (a) and extraction (b) processes.

The stress distribution - Figs. 5.9 and 5.10 plot the stress evolution during Li insertion and extraction, in terms of radial stress σ_r, hoop stress σ_θ, hydrostatic pressure p, and deviatoric stress σ_τ. Since the particle is mechanically free to expand and contract, the state of stress emanates merely from the lithium redistribution in the hosting lattice.

The hoop stress σ_θ (and the pressure p as well) is initially positive on the surface and compressive at the particle center during lithiation (see Fig. 5.9d), because of the negative value of the chemical expansion coefficients ω_L and ω_T. Vice versa during extraction. The radial stress is null on the particle surface, since it is imposed by the boundary conditions. It is compressive during insertion and positive during extraction (Figs. 5.9c and 5.10c).

The deviatoric part of the stress σ_τ exhibits peaks, which move in time in correspondence of the phase-boundary. Those peaks overcome the yield stress (because of the viscosity) close to the particle boundary, where concentration gradients are steeper. Plastic flow is thus experienced close to the particle surface during both insertion and extraction, causing a reversal of the hoop stress with time near the boundary (Figs. 5.9a and 5.10a). Plastic deformations are also responsible of residual stresses at steady state, when concentrations in the particle are uniform.

The pressure in the core shell is high (well above the yield stress upon Li removal), thus suggesting that the role of parameter α in equation (5.15) shall be considered carefully. Stress components σ_r, σ_θ as well as p exhibit stress quasi-plateaus during phase-transition as clearly visible in the extraction case. The extension of these plateaus is bounded by the smeared phase-interface, suggesting that lithium redistributes homogeneously in the particle core.

Although the insertion and extraction processes induces similar stress distributions (with opposite signs), their magnitude are considerably different during phase change.
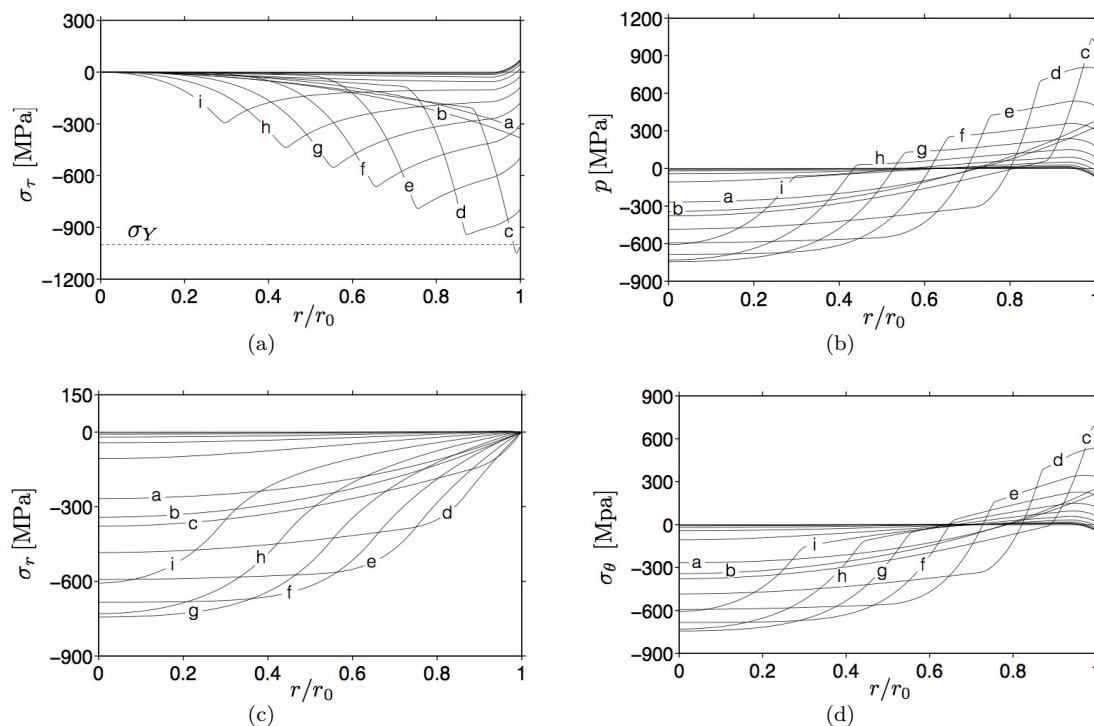
Figure 5.9: **Li insertion** - Stress state in terms of deviatoric part (a) and pressure (b), radial (c) and hoop (d) components as a function of radial coordinate at intervals of $1200\,s$ for $B = 1\,mol/J$ and $K^{eq} = 100$. The letters highlight the correspondence with the simultaneous lithium distributions as reported in Fig. 5.8a.
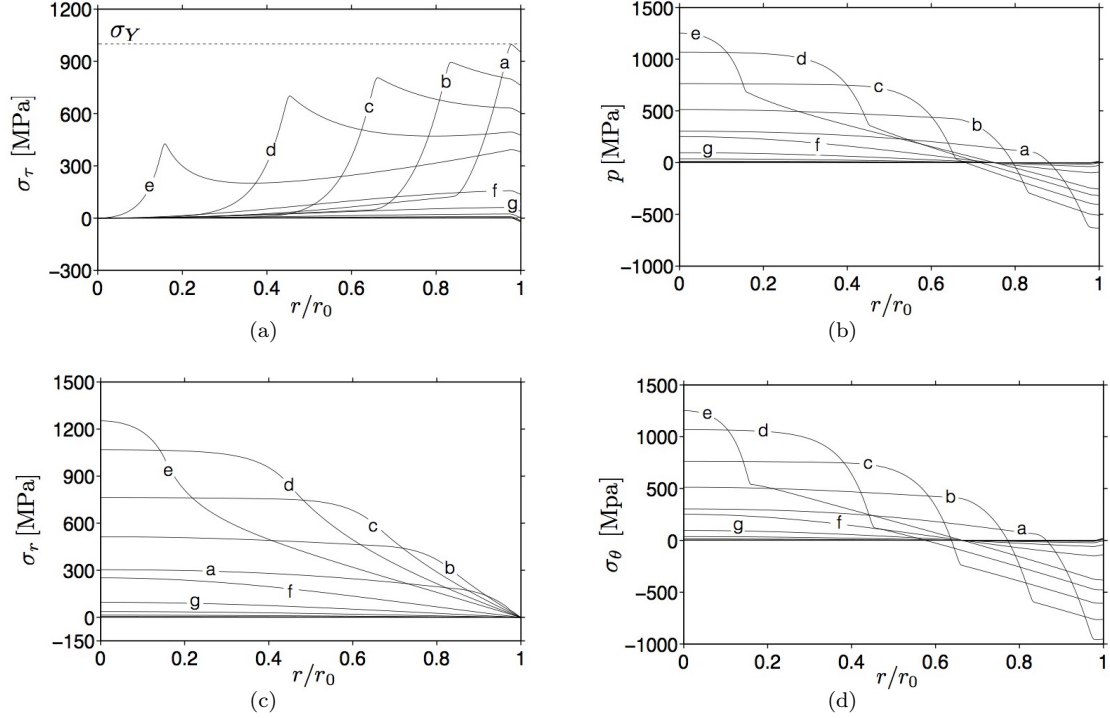
Figure 5.10: ***Li extraction*** - *Stress state in terms of deviatoric part (a) and pressure (b), radial (c) and hoop (d) components as a function of radial coordinate at intervals of $1200\,s$ for $B = 1\,mol/J$ and $K^{eq} = 100$. The letters highlight the correspondence with the simultaneous lithium distributions as reported in Fig. 5.8b.*

5.5 A 3D Example

A particle subjected to non-uniform boundary conditions is considered, specifically a sphere of radius $r_0 = 10\,\mu m$ free to expand and contract. The particle, with initial uniform Li concentration $c_{\text{Li}}(\vec{x}, t = 0) = 0.5\,c_{\text{Li}}^{MAX}$, is lithiated as described below.

Li insertion is prescribed only on a part of the particle surface, as shown in Figure 5.1a. The insertion area has been selected from the spherical cup with base radius $r_b = 1/5\,r_0$, representing $\sim 2\%$ of the whole particle surface. Lithium ions are initially inserted with uniform radial flux $\overline{h} = 5.556 \times 10^{-6}\,\text{mol}/(\text{m}^2\,\text{s})$ until Li concentration at point P ($x_2/r_0 = -1$) reaches the limit $\overline{c_{\text{Li}}} = 0.99\,c_{\text{Li}}^{MAX}$. The concentration is held fixed afterwards, at a uniform value $\overline{c_{\text{Li}}}$. Based on the outcomes for the 1D examples, $B = 1\,\text{mol/J}$ and $K^{eq} = 100$. Material parameters are summarized in Table 5.1.

The computational domain reduces to a quarter of sphere, since the problem is axisymmetric with respect to axis x_2. The Finite Element discretization ($28,623$ four-nodes tetrahedra for a total number of $151,176$ nodes) has been generated by means of ABAQUS CAE, biasing the mesh in correspondence to the Li insertion area (see Fig. 5.1b).

The load history is divided into two loading steps, to accomplish the Li insertion procedure, namely *Step1* for the Li-flux boundary condition and *Step2* for Li concentration one. The Backward Euler Algorithm allows time advancing, with time increments $\Delta t_1 = 0.36\,s$ and $\Delta t_2 = 36\,s$ respectively for *Step1* and *Step2*. To avoid volumetric locking, the mechanical governing equations have been implemented through B-BAR method [306]. The numerical algorithm has been implemented by means of an ABAQUS User Element Subroutine. Further details of the numerical resolution are postponed in Appendix 5.B.

Figure 5.2 plots the evolution of the lithium concentration along the x_2 axis for *Step1* (a) and *Step2* (b). In *Step1* lithium accumulates in a small region near the insertion area. The onset of the phase-segregation additionally lowers the effective Li diffusivity, causing saturation at point P after $120\,s$. The
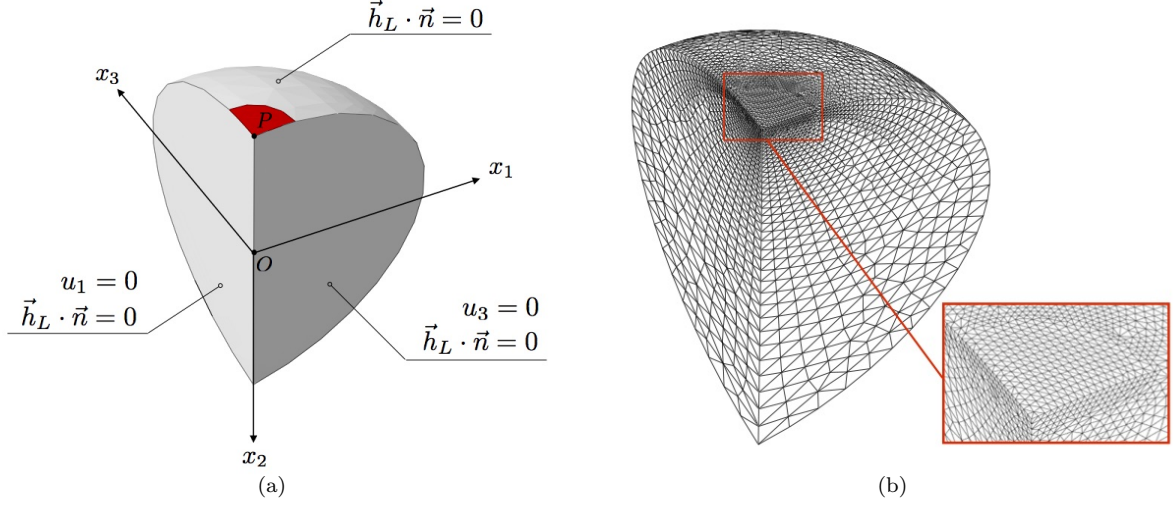
Figure 5.1: (a) Schematic representation of the geometry and boundary conditions used for the three-dimensional example. The surface where Li insertion takes place is highlighted in red. (b) Plot of the FE discretization generated with ABAQUS CAE.

analysis switches to *Step2* afterwards. As showed in Fig. 5.2b, steep gradients arise in the concentration gap between the solubility limits of phase I and phase II, resembling an interface with finite width. This "interface" progressively moves and relaxes along the x_2 axis as the particle fills.

The time scale of the processes in *Step2* is remarkably slower than that of *Step1*, because of a different Li flux between the two regimes at the particle surface. The inward flux that meets the Dirichlet boundary condition in *Step2* turns out to be much smaller than the assigned flux $\bar{h}$ at *Step1*.

Contour plots (see Fig. 5.3) also denotes the ability of the present model to recover a moving finite-width interface between Li-rich and Li-poor phases.
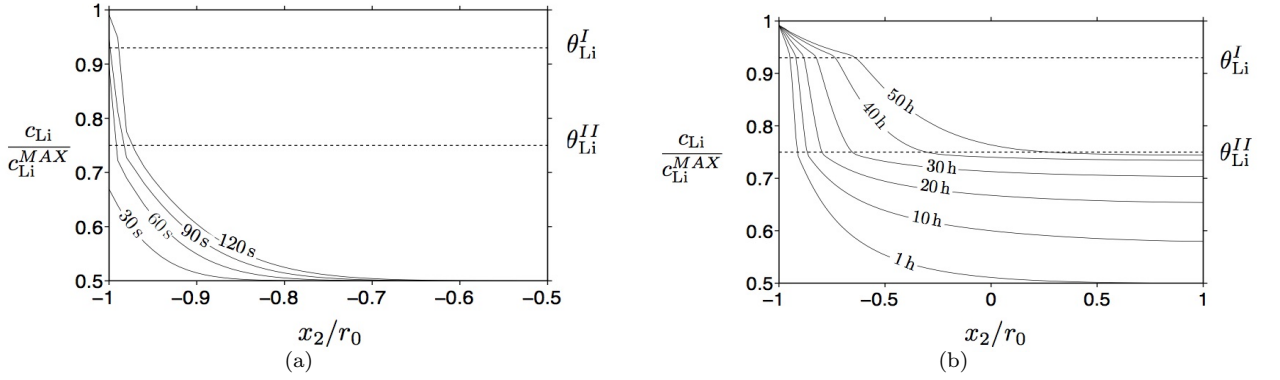
Figure 5.2: Lithium concentration profiles along the x_2 axis at different time instants during *Step*1 (a) and *Step*2. For the sake of readability the abscissa coordinate in (a) has been restricted to $-1 \leq x_2/r_0 \leq -1/2$.

The stress distribution along x_2 axis is plot in Fig. 5.4. Both pressure p and Mises stress $||\text{dev}[\boldsymbol{\sigma}]||$ show peaks in correspondence of the phase-interface. The thinner the interface thickness the higher the stress peak. This conclusion is corroborated by the 3D contour plots in Figure 5.5, which confirm that the stress components intensify near the phase-interface. The stress profile is quite complex: the Mises stress magnitude attains its maximum on the external surface, vice-versa for the hydrostatic pressure.

In this numerical simulation a plastic deformation field is observed only close to the Li insertion surface,
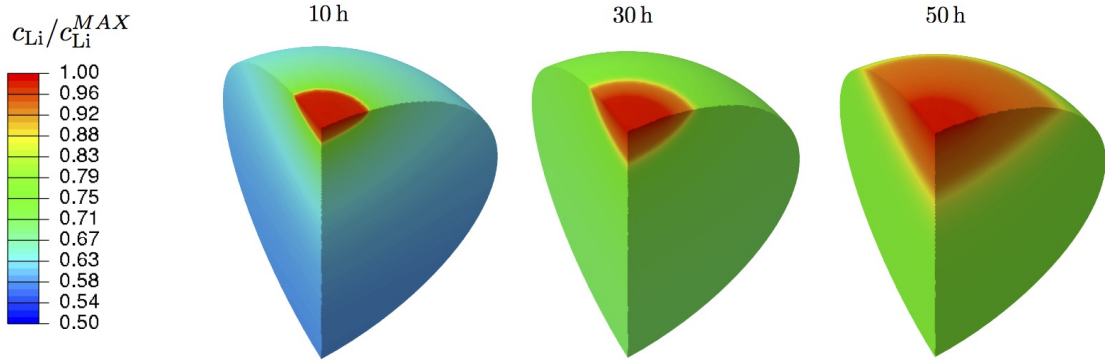
Figure 5.3: Contour plots of Li concentration at three different time instants.

as depicted in Figure 5.6. Such an inelastic deformation influences the stress distribution near to the insertion surface. For example the hydrostatic pressure inverts its sign from positive (tensile) to negative (compressive) in order to accomodate the residual plastic deformation.
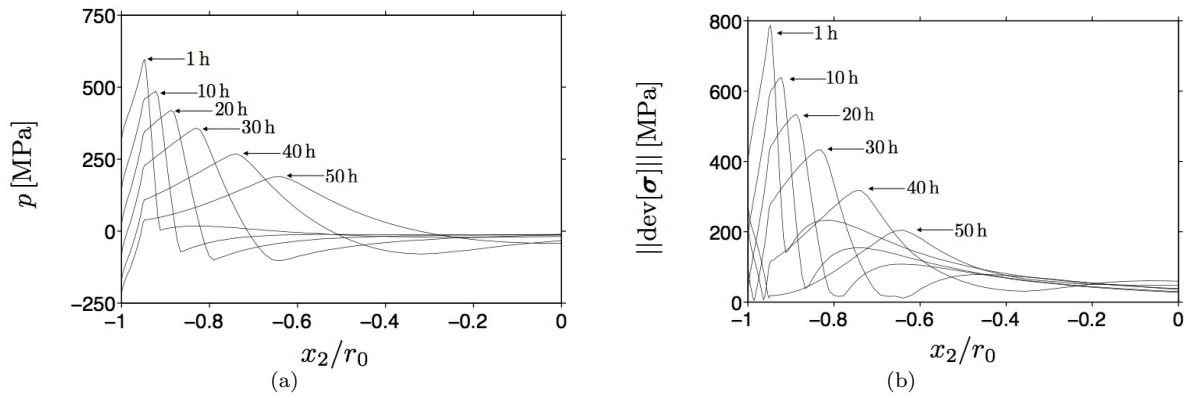
Figure 5.4: Hydrostatic pressure (a) and Mises stress (b) profiles along the x_2 axis at different time instants during Step2. For the sake of clarity the abscissa coordinate in has been restricted to $-1 \leq x_2/r_0 \leq 0$.
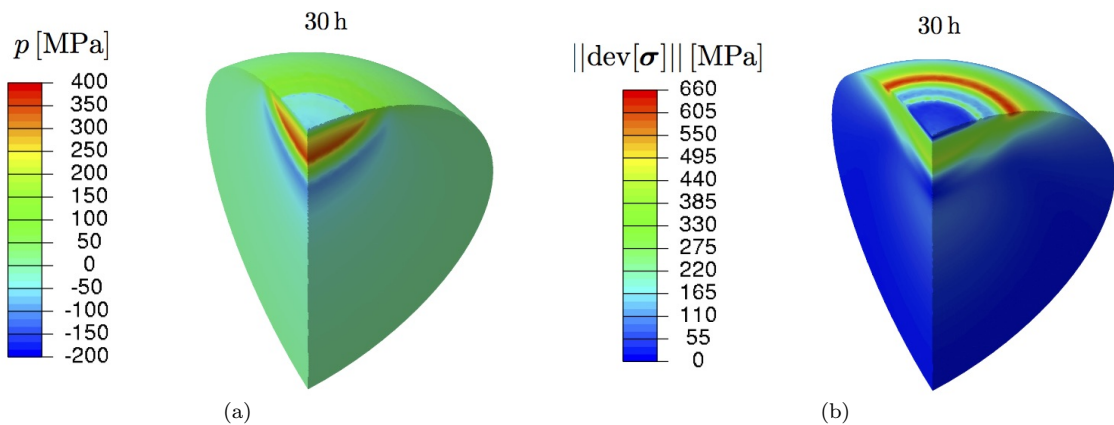
Figure 5.5: Contour plot of hydrostatic pressure (a) and Mises stress (b) at $t = 30\,h$.
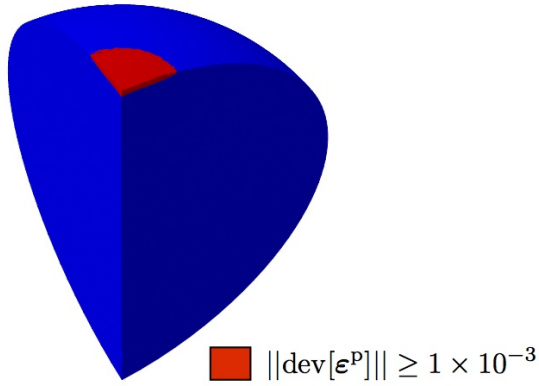
Figure 5.6: Three dimensional plot of the plasticized region at $t = 50\,h$.

$$\blacksquare \quad ||\mathrm{dev}[\boldsymbol{\varepsilon}^{\mathrm{p}}]|| \geq 1 \times 10^{-3}$$

5.6 Conclusions

In this Chapter a chemo-mechanical model of the response of $\mathrm{LiCoO_2}$ electrodes has been proposed based on experimental evidence. Phase-segregations and mechanical deformations are observed as lithium is inserted/extracted in the electrode. The first-order phase transition taking place between $x = 0.75$ and $x = 0.93$ in $\mathrm{Li}_x\mathrm{CoO_2}$ affects the diffusion of lithium in the electrode because of the coexistence of Li-rich and Li-poor phases. Moreover, the stress state intensifies during the phase-segregation leading to a stress evolution compatible with plastic flow in the electrode.

The phase-transition is here modeled through a trapping of Li ions in the hosting material. Accordingly the transition from the Li-poor phase to the Li-rich phase is triggered by lithium immobilization in the electrode and vice versa. In addition, the evolution of trap sites for Li immobilization has been prescribed in order to simulate the phase-diagram of $\mathrm{LiCoO_2}$. The inelastic mechanical response is modeled by means of a Perzyna-like visco plastic law introducing a viscosity dependent on the amount of trapped lithium. No interface energies are introduced here differently from other models for phase-segregation, e.g. sharp-interface and phase-field models.

Modeling the trapping reaction with evolving trap density leads to a non-convex Helmholtz free energy density as customary for phase-segregating materials. In particular three distinctive regimes arise as a function of lithium content in accordance to the phase diagram of $\mathrm{LiCoO_2}$.

The transient response of a spherical particle is analyzed through a series of numerical simulations. If the mechanics is neglected, a lithium evolution resembling that typical of sharp-interface models is recovered for both lithiation and delithiation. The numerical results slightly change if the mechanics is accounted for, since the chemo-mechanical governing equations are fully coupled. The simulated stress evolution in the particle shows an intensification of the stress state during the two-phase regime as observed experimentally.

Appendix

5.A 1D Finite Element Implementation

The consistent tangent matrix $[K_{n+1}^{(k)}]$ and residual vector $[R_{n+1}^{(k)}]$ for the Newton-Raphson algorithm can be easily derived following the same procedure described in Appendix 4.A. The approximated solution, at time step $n+1$, is computed iteratively (superscript k stands for the iteration counter) in terms of solution increments $\delta y^{(k+1)} = \{\delta c_L^{(k+1)}, \delta u^{(k+1)}, \delta \Sigma^{(k+1)}\}$ by solving the following linear problem

$$\underbrace{\begin{bmatrix} [K^{LL}] & [\mathbf{0}] & [K^{L\Sigma}] \\ [K^{uL}] & [K^{uu}] & [K^{u\Sigma}] \\ [K^{\Sigma L}] & [K^{\Sigma u}] & [K^{\Sigma\Sigma}] \end{bmatrix}}_{[K_{n+1}^{(k)}]} \underbrace{\begin{bmatrix} [\delta c_L] \\ [\delta u] \\ [\delta \Sigma] \end{bmatrix}}_{[\delta y_{n+1}^{(k+1)}]} = \underbrace{\begin{bmatrix} [R^L] \\ [R^u] \\ [R^\Sigma] \end{bmatrix}}_{[R_{n+1}^{(k)}]}$$

where the *consistent tangent matrix* $[K^{\alpha\beta}]$ and the *residual vector* components $[R^\alpha]$ are

$$[K^{LL}] = \underset{e=1}{\overset{N_h}{\mathbf{A}}} \left\{ \frac{1}{\Delta t} \int_{\Omega^e} [N_L]^T [N_L] \left(1 + \left.\frac{\partial c_T}{\partial c_L}\right|_{(n+1)}^{(k)} \right) r^2 \, \mathrm{d}r + \right.$$

$$+ \frac{1}{\Delta t} \int_{\Omega^e} [N_L]^T [N_L] \left(c_L|_{n+1}^{(k)} - c_L|_n \right) \left.\frac{\partial^2 c_T}{\partial c_L^2}\right|_{(n+1)}^{(k)} r^2 \, \mathrm{d}r +$$

$$+ \frac{1}{\Delta t} \int_{\Omega^e} [N_L]^T [N_L] \left(\Sigma|_{n+1}^{(k)} - \Sigma|_n \right) \left.\frac{\partial^2 c_T}{\partial \Sigma \, \partial c_L}\right|_{(n+1)}^{(k)} r^2 \, \mathrm{d}r +$$

$$\left. + \int_{\Omega^e} [B_L]^T [B_L] \, \mathbb{D}_L \, r^2 \, \mathrm{d}r - \int_{\Omega^e} [B_L]^T [N_L] \left([B_\Sigma] [\Sigma]_{n+1}^{(k)} \right) \left.\frac{\mathrm{d}\,\mathbb{D}_\Sigma}{\mathrm{d}\,c_L}\right|_{n+1}^{(k)} r^2 \, \mathrm{d}r \right\},$$

$$[K^{L\Sigma}] = \underset{e=1}{\overset{N_h}{\mathbf{A}}} \left\{ \frac{1}{\Delta t} \int_{\Omega^e} [N_L]^T [N_\Sigma] \left(c_L|_{n+1}^{(k)} - c_L|_n \right) \left.\frac{\partial^2 c_T}{\partial c_L \, \partial \Sigma}\right|_{(n+1)}^{(k)} r^2 \, \mathrm{d}r + \right.$$

$$+ \frac{1}{\Delta t} \int_{\Omega^e} [N_L]^T [N_\Sigma] \left.\frac{\partial c_T}{\partial \Sigma}\right|_{(n+1)}^{(k)} r^2 \, \mathrm{d}r +$$

$$+ \frac{1}{\Delta t} \int_{\Omega^e} [N_L]^T [N_\Sigma] \left([\Sigma]_{n+1}^{(k)} - [\Sigma]_n \right) \left.\frac{\partial^2 c_T}{\partial \Sigma^2}\right|_{(n+1)}^{(k)} r^2 \, \mathrm{d}r +$$

$$\left. - \int_{\Omega^e} [B_L]^T [B_\Sigma] \left.\mathbb{D}_\Sigma\right|_{n+1}^{(k)} r^2 \, \mathrm{d}r \right\},$$

109

$$[K^{u\,L}] = \mathop{\mathbf{A}}_{e=1}^{N_h} \left\{ \int_{\Omega^e} [B_u]^T\,[N_L] \left(2\,\left.\frac{\partial \sigma_\tau}{\partial c_L}\right|_{n+1}^{(k)} + \left.\frac{\partial \sigma_m}{\partial c_L}\right|_{n+1}^{(k)} \right) r^2\,\mathrm{d}r + \right.$$

$$\left. + 2\int_{\Omega^e} [N_u]^T\,[N_L] \left(\left.\frac{\partial \sigma_m}{\partial c_L}\right|_{n+1}^{(k)} - \left.\frac{\partial \sigma_\tau}{\partial c_L}\right|_{n+1}^{(k)} \right) r\,\mathrm{d}r \right\},$$

$$[K^{u\,u}] = \mathop{\mathbf{A}}_{e=1}^{N_h} \left\{ \int_{\Omega^e} [B_u]^T\,[B_u] \left(2\,\left.\frac{\partial \sigma_\tau}{\partial \varepsilon_r}\right|_{n+1}^{(k)} + \left.\frac{\partial \sigma_m}{\partial \varepsilon_r}\right|_{n+1}^{(k)} \right) r^2\,\mathrm{d}r + \int_{\Omega^e} [B_u]^T\,[N_u] \left(2\,\left.\frac{\partial \sigma_\tau}{\partial \varepsilon_\theta}\right|_{n+1}^{(k)} + \left.\frac{\partial \sigma_m}{\partial \varepsilon_\theta}\right|_{n+1}^{(k)} \right) r\,\mathrm{d}r + \right.$$

$$\left. + 2\int_{\Omega^e} [N_u]^T\,[B_u] \left(\left.\frac{\partial \sigma_m}{\partial \varepsilon_r}\right|_{n+1}^{(k)} - \left.\frac{\partial \sigma_\tau}{\partial \varepsilon_r}\right|_{n+1}^{(k)} \right) r\,\mathrm{d}r + 2\int_{\Omega^e} [N_u]^T\,[N_u] \left(\left.\frac{\partial \sigma_m}{\partial \varepsilon_\theta}\right|_{n+1}^{(k)} - \left.\frac{\partial \sigma_\tau}{\partial \varepsilon_\theta}\right|_{n+1}^{(k)} \right) \mathrm{d}r \right\},$$

$$[K^{u\,\Sigma}] = \mathop{\mathbf{A}}_{e=1}^{N_h} \left\{ \int_{\Omega^e} [B_u]^T\,[N_\Sigma] \left(2\,\left.\frac{\partial \sigma_\tau}{\partial \Sigma}\right|_{n+1}^{(k)} + \left.\frac{\partial \sigma_m}{\partial \Sigma}\right|_{n+1}^{(k)} \right) r^2\,\mathrm{d}r + \right.$$

$$\left. + 2\int_{\Omega^e} [N_u]^T\,[N_L] \left(\left.\frac{\partial \sigma_m}{\partial \Sigma}\right|_{n+1}^{(k)} - \left.\frac{\partial \sigma_\tau}{\partial \Sigma}\right|_{n+1}^{(k)} \right) r\,\mathrm{d}r \right\},$$

$$[K^{\Sigma\,L}] = \mathop{\mathbf{A}}_{e=1}^{N_h} \left\{ - \int_{\Omega^e} [N_\Sigma]^T\,[N_L] \left.\frac{\partial \sigma_m}{\partial c_L}\right|_{n+1}^{(k)} r^2\,\mathrm{d}r \right\},$$

$$[K^{\Sigma\,u}] = \mathop{\mathbf{A}}_{e=1}^{N_h} \left\{ - \int_{\Omega^e} [N_\Sigma]^T\,[B_u] \left.\frac{\partial \sigma_m}{\partial \varepsilon_r}\right|_{n+1}^{(k)} r^2\,\mathrm{d}r - \int_{\Omega^e} [N_\Sigma]^T\,[N_u] \left.\frac{\partial \sigma_m}{\partial \varepsilon_\theta}\right|_{n+1}^{(k)} r\,\mathrm{d}r \right\},$$

$$[K^{\Sigma\,\Sigma}] = \mathop{\mathbf{A}}_{e=1}^{N_h} \left\{ \int_{\Omega^e} [N_\Sigma]^T\,[N_\Sigma]\,r^2\,\mathrm{d}r - \int_{\Omega^e} [N_\Sigma]^T\,[N_\Sigma] \left.\frac{\partial \sigma_m}{\partial \Sigma}\right|_{n+1}^{(k)} r^2\,\mathrm{d}r \right\},$$

$$[R^L] = - \mathop{\mathbf{A}}_{e=1}^{N_h} \left\{ \frac{1}{\Delta t} \int_{\Omega^e} [N_L]^T\,[N_L] \left([c_L]_{n+1}^{(k)} - [c_L]_n \right) \left(1 + \left.\frac{\partial c_T}{\partial c_L}\right|_{(n+1)}^{(k)} \right) r^2\,\mathrm{d}r + \right.$$

$$+ \frac{1}{\Delta t} \int_{\Omega^e} [N_L]^T\,[N_\Sigma] \left([\Sigma]_{n+1}^{(k)} - [\Sigma]_n \right) \left.\frac{\partial c_T}{\partial \Sigma}\right|_{(n+1)}^{(k)} r^2\,\mathrm{d}r +$$

$$+ \int_{\Omega^e} [B_L]^T\,[B_L]\,[c_L]_{n+1}^{(k)}\,\mathbb{D}_L\,r^2\,\mathrm{d}r +$$

$$\left. - \int_{\Omega^e} [B_L]^T\,[B_\Sigma]\,[\Sigma]_{n+1}^{(k)}\,\left.\mathbb{D}_\Sigma\right|_{n+1}^{(k)}\,r^2\,\mathrm{d}r \right\} + \left. \left([N_L]^T\,\bar{h}_L\,r^2 \right)\right|_{r=r_0},$$

$$[R^u] = - \mathop{\mathbf{A}}_{e=1}^{N_h} \left\{ \int_{\Omega^e} [B_u]^T \left(2\,\left.\sigma_\tau\right|_{n+1}^{(k)} + \left.\sigma_m\right|_{n+1}^{(k)} \right) r^2\,\mathrm{d}r + \int_{\Omega^e} 2\,[N_u]^T \left(\left.\sigma_m\right|_{n+1}^{(k)} - \left.\sigma_\tau\right|_{n+1}^{(k)} \right) r\,\mathrm{d}r \right\},$$

$$[R^\Sigma] = - \mathop{\mathbf{A}}_{e=1}^{N_h} \left\{ \int_{\Omega^e} [N_\Sigma]^T \left([N_\Sigma]\,[\Sigma]_{n+1}^{(k)} - \left.\sigma_m\right|_{n+1}^{(k)} \right) r^2\,\mathrm{d}r \right\}.$$

The value assumed by the scalar functions and their derivatives appearing in $[K^{\alpha,\beta}]$ and $[R^\alpha]$ can be easily computed from the respective definitions for as long as they do not depend on inelastic deformations. This does not apply for σ_τ which constitutively depends on ε_{in} and vice versa. Therefore σ_τ and its derivatives are computed applying a viscoplastic *Retur-mapping Algorithm*, as described in Appendix 4.A.

5.B 3D Finite Element Implementation

5.B.1 Non-dimensional governing equations and weak form

The system of governing equations has been scaled with suitable coefficients in order to deal with a system of non-dimensional equations. In this way Eqs. (5.16) have been rephrased in term of the adimensional variables

$$x_i^* = \frac{x_i}{\bar{l}}, \qquad t^* = \frac{t}{\bar{t}}, \qquad c_L^* = \frac{c_L}{\bar{c}}, \qquad c_T^* = \frac{c_T}{\bar{c}}, \qquad u_i^* = \frac{u_i}{\bar{l}}, \qquad \sigma_{ij}^* = \frac{\sigma_{ij}}{\bar{\sigma}}, \tag{5.30}$$

by introducing $\bar{l}, \bar{t}, \bar{c}, \bar{\sigma}$ as reference length, time, concentration, and stress respectively.

Taking advantage of definitions (5.30), governing equations (5.16) are equivalent to the following non-dimensional ones

$$\frac{\partial c_L^*}{\partial t^*} + \frac{\partial c_T^*}{\partial t^*} + \text{div}^*[\vec{h}_L^*] = 0, \tag{5.31a}$$

$$\text{div}^*[\boldsymbol{\sigma}^*] = \vec{0}, \tag{5.31b}$$

where

$$\text{div}^*[\vec{h}_L^*] = \sum_{i=1}^{3} \frac{h_{Li}^*}{\partial x_i^*}, \qquad \text{div}^*[\boldsymbol{\sigma}^*] = \sum_{i=1}^{3} \sum_{j=1}^{3} \frac{\sigma_{ij}^*}{\partial x_j^*} \vec{e}_i, \qquad \vec{h}_L^* = \frac{\vec{h}_L \bar{t}}{\bar{c} \bar{l}}.$$

Note that equations (5.31) have the same expression of (5.16) but are formulated in terms of non-dimensional variables. In the same way the non-dimensional constitutive laws keep the same expression of (5.15) - (5.17) - (5.18) - (5.19) - (5.20) as long as the original variables and parameters are replaced with (5.30) and the following non-dimensional constants

$$\mathbb{D}_L^* = \frac{\mathbb{D}_L \bar{t}}{\bar{l}^2}, \qquad \omega_L^* = \omega_L \bar{c}, \qquad \omega_T^* = \omega_T \bar{c}, \qquad (RT)^* = RT \frac{\bar{c}}{\bar{\sigma}},$$

$$(c_L^{max})^* = \frac{c_L^{max}}{\bar{c}}, \qquad (c_T^{MAX})^* = \frac{c_T^{MAX}}{\bar{c}}, \qquad (K^{eq})^* = K^{eq}, \qquad B^* = B \frac{\bar{\sigma}}{\bar{c}},$$

$$K^* = \frac{K}{\bar{\sigma}}, \qquad G^* = \frac{G}{\bar{\sigma}}, \qquad g_0^* = \frac{g_0}{\bar{t} \bar{\sigma}}, \qquad g_1^* = \frac{g_1}{\bar{t} \bar{\sigma}}, \qquad \sigma_Y^* = \frac{\sigma_Y}{\bar{\sigma}}.$$

The weak formulation results from multiplying the strong form of governing equations (5.31) by a suitable set of tests functions and performing an integration upon the domain, exploiting the *integration by parts* formula with the aim of reducing the order of differentiation in space.

Even though the first order derivative of h_r can be reduced applying the integration by parts, its constitutive definition contains a second order derivative. To include the effect of stress gradient in equations (5.31a) we follow the approach adopted in Appendix 4.A by introducing a new variable $\Sigma(r,t)$ defined as

$$\Sigma - \text{tr}[\boldsymbol{\sigma}] = 0, \tag{5.33}$$

which will be approximate as an explicit degree of freedom. Eq. (5.33) is then added to the set of governing equations (5.31) for the numerical solution of the problem.

The overall weak form of the problem is derived starting from each governing equation separately. In what follow the asterisk is omitted for the sake of readability.

From the mass balance Eq. (5.31a) we obtain

$$\int_\Omega \hat{c}_L \left\{ \frac{\partial c_L}{\partial t} + \frac{\partial c_T}{\partial t} + \mathrm{div}\left[\,\vec{h}_L\,\right] \right\} \mathrm{d}V =$$

$$= \int_\Omega \hat{c}_L \left\{ \frac{\partial c_L}{\partial t} + \frac{\partial c_T(c_L, \Sigma)}{\partial t} \right\} \mathrm{d}V + \int_\Omega \nabla\left[\,\hat{c}_L\,\right] \cdot \left\{ \mathbb{D}_L \,\nabla\left[\,c_L\,\right] - \mathbb{D}_\Sigma\,(c_L)\,\nabla\left[\,\Sigma\,\right] \right\} \mathrm{d}V +$$

$$+ \int_{\partial^N\Omega} \hat{c}_L\,\bar{h}_L\,\mathrm{d}A = 0\,,$$

where $\mathbb{D}_\Sigma$ stands for

$$\mathbb{D}_\Sigma = \frac{\mathbb{D}_L\,\omega_L}{R\,T}\,c_L\,\left(\frac{c_L^{max} - c_L}{c_L^{max}} \right)\,.$$

For the equilibrium equation (5.31b)

$$\int_\Omega \vec{\hat{u}} \cdot \mathrm{div}\left[\,\boldsymbol{\sigma}\,\right] \mathrm{d}V = -\int_\Omega \nabla_S\left[\,\vec{\hat{u}}\,\right] : \boldsymbol{\sigma}(c_L, \Sigma, \vec{u})\,\mathrm{d}V + \int_{\partial^N\Omega} \vec{\hat{u}} \cdot \hat{\vec{p}}\,\mathrm{d}A = 0\,,$$

with ∇_S denoting the symmetric gradient operator.

Finally Eq. (5.33) returns

$$\int_\Omega \hat{\Sigma}\left\{ \Sigma - \mathrm{tr}\left[\,\boldsymbol{\sigma}(c_L, \Sigma, \vec{u})\,\right] \right\} \mathrm{d}V = 0\,.$$

Note that boundary conditions (5.21) have been applied and test functions $\hat{c}_L$, $\vec{\hat{u}}$, $\hat{\Sigma}$ are null on the Dirichlet boundary. The latter condition arises since test functions represents admissible variations of the related degrees of freedom, i.e. c_L, $\vec{u}$, Σ.

In conclusion, the weak form of the balance equations can be written in the time interval $[0,\,t_f]$ as

Find $y(\vec{x},t) \in \mathcal{V}^{[0,\,t_f]}$ such that $\quad \dfrac{\partial}{\partial t}\, b\,(\hat{y}(\vec{x}),\, c_L(\vec{x},t)) + a\,(\hat{y}(\vec{x}),\, y(\vec{x},t)) = f\,(\hat{y}(\vec{x})) \qquad \forall\,\hat{y}(\vec{x}) \in \mathcal{V}$ (5.34)

where

$$b\,(\hat{y}(\vec{x}),\, c_L(\vec{x},t)) = \int_\Omega \hat{c}_L\,c_L\,\mathrm{d}V\,,$$

$$a\,(\hat{y}(\vec{x}),\, y(\vec{x},t)) = \int_\Omega \hat{c}_L\,\frac{\partial c_T(c_L, \Sigma)}{\partial t}\,\mathrm{d}V + \int_\Omega \nabla\left[\,\hat{c}_L\,\right] \cdot \left\{ \mathbb{D}_L\,\nabla\left[\,c_L\,\right] - \mathbb{D}_\Sigma\,(c_L)\,\nabla\left[\,\Sigma\,\right] \right\} \mathrm{d}V +$$

$$+ \int_\Omega \nabla_S\left[\,\vec{\hat{u}}\,\right] : \boldsymbol{\sigma}(c_L, \Sigma, \vec{u})\,\mathrm{d}V + \int_\Omega \hat{\Sigma}\left\{ \Sigma - \mathrm{tr}\left[\,\boldsymbol{\sigma}(c_L, \Sigma, \vec{u})\,\right] \right\} \mathrm{d}V\,,$$

$$f\,(\hat{y}(\vec{x})) = -\int_{\partial^N\Omega} \hat{c}_L\,\bar{h}_L\,\mathrm{d}A + \int_{\partial^N\Omega} \vec{\hat{u}} \cdot \hat{\vec{p}}\,\mathrm{d}A\,.$$

with $y = \{c_L,\,\vec{u},\,\Sigma\}$ collecting the time-dependent unknown fields. Column $\hat{y}$ collects the steady state test functions that correspond to the unknown fields in y, i.e. $\hat{y} = \{\hat{c}_L,\,\vec{\hat{u}},\,\hat{\Sigma}\}$. The identification of the functional space $\mathcal{V}$ falls beyond the scope of this work.

5.B.2 Numerical discretization

Following the standard finite element method, the spatial domain Ω is divided into N_h subdomains Ω^e, each one with nn nodes, such that

$$\Omega = \bigcup_{e=1}^{N_h} \Omega^e$$

Inside any subdomain any degree of freedom (and its variation) is approximated through the following interpolation

$$^h c_L\,(\vec{x}, t) = [N_L(\vec{x})]\,[c_L(t)]\,, \qquad ^h \hat{c}_L\,(\vec{x}, t) = [N_L(\vec{x})]\,[\hat{c}_L(t)]\,, \tag{5.35a}$$

$$^h \vec{u}\,(\vec{x}, t) = [N_u(\vec{x})]\,[u(t)]\,, \qquad ^h \hat{\vec{u}}\,(\vec{x}, t) = [N_u(\vec{x})]\,[\hat{u}(t)]\,, \tag{5.35b}$$

$$^h \Sigma\,(\vec{x}, t) = [N_\Sigma(\vec{x})]\,[\Sigma(t)]\,, \qquad ^h \hat{\Sigma}\,(\vec{x}, t) = [N_\Sigma(\vec{x})]\,[\hat{\Sigma}(t)]\,, \tag{5.35c}$$

where the tables $[N(\vec{x})]$ collect the time-independent local shape functions $N^i(\vec{x})$ as

$$[N_L(\vec{x})] = [N_\Sigma(\vec{x})] = \left\{ N^1\,,\, N^2\,,\, ...,\, N^{nn} \right\},$$

$$[N_u(\vec{x})] = \begin{bmatrix} N^1 & 0 & 0 & N^2 & 0 & 0 & ... & N^{nn} & 0 & 0 \\ 0 & N^1 & 0 & 0 & N^2 & 0 & ... & 0 & N^{nn} & 0 \\ 0 & 0 & N^1 & 0 & 0 & N^2 & ... & 0 & 0 & N^{nn} \end{bmatrix},$$

and $[c_L(t)]\,,[u(t)]\,,[\Sigma(t)]$ collect the nodal values of variable $c_L, \vec{u}, \Sigma$ at time t as follow

$$[c_L(t)] = \left\{ c_L^1\,,\, c_L^2\,,\, ...,\, c_L^{nn} \right\}^T, \qquad [\hat{c}_L(t)] = \left\{ \hat{c}_L^1\,,\, \hat{c}_L^2\,,\, ...,\, \hat{c}_L^{nn} \right\}^T,$$

$$[u(t)] = \left\{ u_1^1\,,\, u_2^1\,,\, u_3^1\,,\, u_1^2\,,\, u_2^2\,,\, u_3^2\,,\, ...,\, u_1^{nn}\,,\, u_2^{nn}\,,\, u_3^{nn} \right\}^T,$$

$$[\hat{u}(t)] = \left\{ \hat{u}_1^1\,,\, \hat{u}_2^1\,,\, \hat{u}_3^1\,,\, \hat{u}_1^2\,,\, \hat{u}_2^2\,,\, \hat{u}_3^2\,,\, ...,\, \hat{u}_1^{nn}\,,\, \hat{u}_2^{nn}\,,\, \hat{u}_3^{nn} \right\}^T,$$

$$[\Sigma(t)] = \left\{ \Sigma^1\,,\, \Sigma^2\,,\, ...,\, \Sigma^{nn} \right\}^T \qquad [\hat{\Sigma}(t)] = \left\{ \hat{\Sigma}^1\,,\, \hat{\Sigma}^2\,,\, ...,\, \hat{\Sigma}^{nn} \right\}^T.$$

From Eq. (5.35) it results

$$\nabla\,[\,c_L\,] = [B_L(\vec{x})]\,[c_L(t)]\,,$$

$$\nabla_S[\,\hat{\vec{u}}\,]\,:\,\boldsymbol{\sigma} = [\hat{u}(t)]^T\,[B_u(\vec{x})]^T\,[\sigma(\vec{x}, t)\,],$$

$$\nabla\,[\,\Sigma\,] = [B_\Sigma(\vec{x})]\,[\Sigma(t)]\,,$$

with

$$[B_L(\vec{x})] = [B_\Sigma(\vec{x})] = \begin{bmatrix} N^{1,1} & N^{2,1} & ... & N^{nn,1} \\ N^{1,2} & N^{2,2} & ... & N^{nn,2} \\ N^{1,3} & N^{2,3} & ... & N^{nn,3} \end{bmatrix},$$

$$[B_u(\vec{x})] = \begin{bmatrix} N^{1,1} & 0 & 0 & N^{2,1} & 0 & 0 & \dots & N^{nn,1} & 0 & 0 \\ 0 & N^{1,2} & 0 & 0 & N^{2,2} & 0 & \dots & 0 & N^{nn,2} & 0 \\ 0 & 0 & N^{1,3} & 0 & 0 & N^{2,3} & \dots & 0 & 0 & N^{nn,3} \\ N^{1,2} & N^{1,1} & 0 & N^{2,2} & N^{2,1} & 0 & \dots & N^{nn,2} & N^{nn,1} & 0 \\ 0 & N^{1,3} & N^{1,2} & 0 & N^{2,3} & N^{2,2} & \dots & 0 & N^{nn,3} & N^{nn,2} \\ N^{1,3} & 0 & N^{1,1} & N^{2,3} & 0 & N^{2,1} & \dots & N^{nn,3} & 0 & N^{nn,1} \end{bmatrix} ,$$

and

$$[\sigma(\vec{x},t)] = \left\{ \sigma_{11} , \sigma_{22} , \sigma_{33} , \sigma_{12} , \sigma_{23} , \sigma_{13} \right\}^T$$

with

$$N^{i,j} = \frac{\partial N^i}{\partial x_j} \quad i = 1,2,3 \quad j = 1,2,3$$

The discretization in time is performed applying the implicit backward Euler method. Accordingly we divide time interval $[0, t_f]$ into N_t temporal steps $\Delta t = t_f/N_t$. We define for convenience

$$y(r)|_n = y(\vec{x}, n\Delta t), \qquad \Delta y(\vec{x})|_{n+1} = y(\vec{x})|_{n+1} - y(\vec{x})|_n \qquad n = 1, 2, ..., N_t$$

The discretized weak form is finally obtained from (5.34) by applying the finite element interpolation (5.35) and the backward Euler scheme. It results in terms of approximate degrees of freedom $^h y = \left\{ ^h c_L, \, ^h c_T, \, ^h \vec{u}, \, ^h \Sigma \right\}$ and variations $^h \hat{y} = \{ ^h \hat{c}_L, \, ^h \hat{c}_T, \, ^h \hat{\vec{u}}, \, ^h \hat{\Sigma} \}$ as follow

Find $^h y(\vec{x})|_{n+1} \in {}^h \mathcal{V}$ such that

$$\frac{1}{\Delta t} \, {}^h b \left({}^h \hat{y}(\vec{x}), \, \Delta^h c_L(\vec{x})|_{n+1} \right) + {}^h a \left({}^h \hat{y}(\vec{x}), \, {}^h y(\vec{x})|_{n+1} \right) = f \left({}^h \hat{y}(\vec{x}) \right) \qquad \forall \, {}^h \hat{y}(\vec{x}) \in {}^h \mathcal{V}, \quad n = 1, 2, ..., N_t$$

(5.40)

where

$$^h b \left({}^h \hat{y}(\vec{x}), \, \Delta^h z(\vec{x})|_{n+1} \right) = \underset{e=1}{\overset{N_h}{\mathbf{A}}} \left\{ [\hat{c}_L]^T \int_{\Omega^e} [N_L]^T [N_L] \left([c_L]_{n+1} - [c_L]_n \right) dV \right\} ,$$

$$^h a \left({}^h \hat{y}(\vec{x}), \, {}^h y(\vec{x})|_{n+1} \right) = \underset{e=1}{\overset{N_h}{\mathbf{A}}} \left\{ \frac{1}{\Delta t} [\hat{c}_L]^T \int_{\Omega^e} [N_L]^T [N_L] \left([c_L]_{n+1} - [c_L]_n \right) \left. \frac{\partial c_T(c_L, \Sigma)}{\partial c_L} \right|_{n+1} dV + \right.$$

$$+ \frac{1}{\Delta t} [\hat{c}_L]^T \int_{\Omega^e} [N_L]^T [N_\Sigma] \left([\Sigma]_{n+1} - [\Sigma]_n \right) \left. \frac{\partial c_T(c_L, \Sigma)}{\partial \Sigma} \right|_{n+1} dV +$$

$$+ [\hat{c}_L]^T \int_{\Omega^e} [B_L]^T [B_L] [c_L]_{n+1} \, \mathbb{D}_L|_{n+1} \, dV +$$

$$- [\hat{c}_L]^T \int_{\Omega^e} [B_L]^T [B_\Sigma] [\Sigma]_{n+1} \, \mathbb{D}_\Sigma(c_L)|_{n+1} \, dV +$$

$$+ [\hat{u}]^T \int_{\Omega^e} [B_u]^T [\sigma(c_L, \Sigma, u)]_{n+1} \, dV +$$

$$\left. + [\hat{\Sigma}]^T \int_{\Omega^e} [N_\Sigma]^T \left([N_\Sigma] [\Sigma]_{n+1} - \mathrm{tr} \left[\boldsymbol{\sigma}(c_L, \Sigma, \vec{u}) \right]|_{n+1} \right) dV \right\} ,$$

$$f\left({}^h\hat{y}(\vec{x})\right) = \overset{N_h}{\underset{e=1}{\mathbf{A}}}\left\{-[c_L]^T\int_{\partial^N\Omega^e}[N_L]^T\,\bar{h}_L\,\mathrm{d}A + [\hat{u}]^T\int_{\partial^N\Omega^e}[N_u]^T\cdot\hat{p}\,\mathrm{d}A\right\}.$$

Note that the integrals in (5.34) are now computed summating the contribution of any subdomain Ω^e by means of the assembly operator $\mathbf{A}$. Eq. (5.40) is equivalent to a system of non-linear equations for the unknowns ${}^h y$ which is solved with a standard Newton-Raphson algorithm. Accordingly the solution is computed iteratively in terms of solution increments $\delta y^{(k+1)} = \{\delta c_L^{(k+1)},\ \delta c_T^{(k+1)},\ \delta\vec{u}^{(k+1)},\ \delta\Sigma^{(k)}\}$ at iteration $k+1$ for any time step (the superscript ^{h} has been removed for clarity). Without going through all details for convenience (see [323] for instance), the overall problem reduces to the following linear system

$$\underbrace{\begin{bmatrix}[K^{LL}] & [\mathbf{0}] & [K^{L\Sigma}]\\[6pt] [K^{uL}] & [K^{uu}] & [K^{u\Sigma}]\\[6pt] [K^{\Sigma L}] & [K^{\Sigma u}] & [K^{\Sigma\Sigma}]\end{bmatrix}}_{[K_{n+1}^{(k)}]}\underbrace{\begin{bmatrix}[\delta c_L]\\[6pt] [\delta u]\\[6pt] [\delta\Sigma]\end{bmatrix}}_{[\delta y_{n+1}^{(k+1)}]} = \underbrace{\begin{bmatrix}[R^L]\\[6pt] [R^u]\\[6pt] [R^\Sigma]\end{bmatrix}}_{[R_{n+1}^{(k)}]}$$

where the *consistent tangent matrix* $[K^{\alpha\beta}]$ and the *residual vector* components $[R^\alpha]$ are

$$[K^{LL}] = \overset{N_h}{\underset{e=1}{\mathbf{A}}}\left\{\frac{1}{\Delta t}\int_{\Omega^e}[N_L]^T[N_L]\left(1+\left.\frac{\partial c_T}{\partial c_L}\right|_{(n+1)}^{(k)}\right)\mathrm{d}V +\right.$$
$$+\frac{1}{\Delta t}\int_{\Omega^e}[N_L]^T[N_L]\left(c_L|_{n+1}^{(k)}-c_L|_n\right)\left.\frac{\partial^2 c_T}{\partial c_L^2}\right|_{(n+1)}^{(k)}\mathrm{d}V +$$
$$+\frac{1}{\Delta t}\int_{\Omega^e}[N_L]^T[N_L]\left(\Sigma|_{n+1}^{(k)}-\Sigma|_n\right)\left.\frac{\partial^2 c_T}{\partial\Sigma\,\partial c_L}\right|_{(n+1)}^{(k)}\mathrm{d}V +$$
$$\left.+\int_{\Omega^e}[B_L]^T[B_L]\,\mathbb{D}_L\,\mathrm{d}V - \int_{\Omega^e}[B_L]^T[N_L]\left([B_\Sigma][\Sigma]_{n+1}^{(k)}\right)\left.\frac{\mathrm{d}\mathbb{D}_\Sigma}{\mathrm{d}c_L}\right|_{n+1}^{(k)}\mathrm{d}V\right\},$$

$$[K^{L\Sigma}] = \overset{N_h}{\underset{e=1}{\mathbf{A}}}\left\{\frac{1}{\Delta t}\int_{\Omega^e}[N_L]^T[N_\Sigma]\left(c_L|_{n+1}^{(k)}-c_L|_n\right)\left.\frac{\partial^2 c_T}{\partial c_L\,\partial\Sigma}\right|_{(n+1)}^{(k)}\mathrm{d}V +\right.$$
$$+\frac{1}{\Delta t}\int_{\Omega^e}[N_L]^T[N_\Sigma]\left.\frac{\partial c_T}{\partial\Sigma}\right|_{(n+1)}^{(k)}\mathrm{d}V +$$
$$+\frac{1}{\Delta t}\int_{\Omega^e}[N_L]^T[N_\Sigma]\left([\Sigma]_{n+1}^{(k)}-[\Sigma]_n\right)\left.\frac{\partial^2 c_T}{\partial\Sigma^2}\right|_{(n+1)}^{(k)}\mathrm{d}V +$$
$$\left.-\int_{\Omega^e}[B_L]^T[B_\Sigma]\left.\mathbb{D}_\Sigma\right|_{n+1}^{(k)}\mathrm{d}V\right\},$$

$$[K^{uL}] = \overset{N_h}{\underset{e=1}{\mathbf{A}}}\left\{\int_{\Omega^e}[B_u]^T\left[\frac{\partial\sigma}{\partial c_L}\right]_{n+1}^{(k)}[N_L]\,\mathrm{d}V\right\},$$

$$[K^{uu}] = \overset{N_h}{\underset{e=1}{\mathbf{A}}}\left\{\int_{\Omega^e}[B_u]^T\left[\frac{\partial\sigma}{\partial\varepsilon}\right]_{n+1}^{(k)}[B_u]\,\mathrm{d}V\right\},$$

$$[K^{u\,\Sigma}] = \mathop{\mathbf{A}}_{e=1}^{N_h} \left\{ \int_{\Omega^e} [B_u]^T \left[\frac{\partial\sigma}{\partial\Sigma}\right]_{n+1}^{(k)} [N_\Sigma]\,\mathrm{d}V \right\},$$

$$[K^{\Sigma\,L}] = \mathop{\mathbf{A}}_{e=1}^{N_h} \left\{ -\int_{\Omega^e} [N_\Sigma]^T [N_L] \left.\frac{\partial\mathrm{tr}\,[\boldsymbol{\sigma}]}{\partial c_L}\right|_{n+1}^{(k)} \mathrm{d}V \right\},$$

$$[K^{\Sigma\,u}] = \mathop{\mathbf{A}}_{e=1}^{N_h} \left\{ -\int_{\Omega^e} [N_\Sigma]^T \left[\frac{\partial\mathrm{tr}\,[\boldsymbol{\sigma}]}{\partial\varepsilon}\right]_{n+1}^{(k)} [B_u]\,\mathrm{d}V \right\},$$

$$[K^{\Sigma\,\Sigma}] = \mathop{\mathbf{A}}_{e=1}^{N_h} \left\{ \int_{\Omega^e} [N_\Sigma]^T [N_\Sigma]\,\mathrm{d}V - \int_{\Omega^e} [N_\Sigma]^T \left[\frac{\partial\mathrm{tr}\,[\boldsymbol{\sigma}]}{\partial\Sigma}\right]_{n+1}^{(k)} [N_\Sigma]\,\mathrm{d}V \right\},$$

$$[R^L] = -\mathop{\mathbf{A}}_{e=1}^{N_h} \left\{ \frac{1}{\Delta t} \int_{\Omega^e} [N_L]^T [N_L] \left([c_L]_{n+1}^{(k)} - [c_L]_n\right) \left(1 + \left.\frac{\partial c_T}{\partial c_L}\right|_{(n+1)}^{(k)}\right) \mathrm{d}V + \right.$$
$$+ \frac{1}{\Delta t} \int_{\Omega^e} [N_L]^T [N_\Sigma] \left([\Sigma]_{n+1}^{(k)} - [\Sigma]_n\right) \left.\frac{\partial c_T}{\partial\Sigma}\right|_{(n+1)}^{(k)} \mathrm{d}V +$$
$$+ \int_{\Omega^e} [B_L]^T [B_L] [c_L]_{n+1}^{(k)} \, \mathbb{D}_L \,\mathrm{d}V +$$
$$\left. - \int_{\Omega^e} [B_L]^T [B_\Sigma] [\Sigma]_{n+1}^{(k)} \left.\mathbb{D}_\Sigma\right|_{n+1}^{(k)} \mathrm{d}V + \int_{\partial^N\Omega^e} [N_L]^T \bar{h}_L\,\mathrm{d}A \right\},$$

$$[R^u] = -\mathop{\mathbf{A}}_{e=1}^{N_h} \left\{ \int_{\Omega^e} [B_u]^T [\sigma]_{n+1}^{(k)}\,\mathrm{d}V - \int_{\partial^N\Omega^e} [N_u]^T \cdot \hat{\bar{p}}\,\mathrm{d}A \right\},$$

$$[R^\Sigma] = -\mathop{\mathbf{A}}_{e=1}^{N_h} \left\{ \int_{\Omega^e} [N_\Sigma]^T \left([N_\Sigma] [\Sigma]_{n+1}^{(k)} - \mathrm{tr}\,[\boldsymbol{\sigma}]\Big|_{n+1}^{(k)}\right) \mathrm{d}V \right\}.$$

The value assumed by the scalar functions and their derivatives appearing in $[K^{\alpha\,\beta}]$ and $[R^\alpha]$ can be easily computed from the respective definitions as long as they do not depend on the inelastic deformations. This applies for the trapped concentration c_T, the volumetric part of the stress $\mathrm{tr}\,[\boldsymbol{\sigma}]$, as well as for $\mathbb{D}_\Sigma$.

Conversely the constitutive definition of $\mathrm{dev}\,[\boldsymbol{\sigma}]$ depends on ε^{in} and vice versa. In this case the flow rule (5.17a) has to be integrated properly. This has been conducted here with a standard viscoplastic *Return-mapping Algorithm* [323]. The method is based on the definition of a *trial elastic state* as a state in which the evolution of ε^{in} is arbitrarily frozen from the previous time step. Accordingly the trial deviatoric stress is defined as

$$\mathrm{dev}\,[\boldsymbol{\sigma}]\big|^{trial} = 2\,G \left(\varepsilon\big|_{n+1}^{(k)} - \varepsilon^{in}\big|_n\right). \tag{5.41}$$

116

If the trial state does not cause the inelastic flow to occur, i.e. $\varphi\left(\operatorname{dev}[\boldsymbol{\sigma}]\big|^{trial}\right) < 0$, the step is elastic which implies that

$$\operatorname{dev}[\boldsymbol{\sigma}]\big|_{n+1}^{(k)} = \operatorname{dev}[\boldsymbol{\sigma}]\big|^{trial} \, ,$$

and the derivatives of $\boldsymbol{\sigma}$ can be calculated merely from (5.41) and (5.18a) obtaining in matrix notation

$$\left[\frac{\partial \sigma}{\partial \varepsilon}\right]_{n+1}^{(k)} = \left(K - \frac{2}{3}\,G \right)[i]\,[i]^T + 2\,G\,[I] \, ,$$

$$\left[\frac{\partial \sigma}{\partial c_L}\right]_{n+1}^{(k)} = -3\,K\left(\omega_L + \omega_T\left.\frac{\partial c_T}{\partial c_L}\right|_{n+1}^{(k)} \right)[i] \, ,$$

$$\left[\frac{\partial \sigma}{\partial \Sigma}\right]_{n+1}^{(k)} = -3\,K\,\omega_T\left.\frac{\partial c_T}{\partial \Sigma}\right|_{n+1}^{(k)}[i] \, ,$$

with

$$[i] = \left\{ 1,\, 1,\, 1,\, 0,\, 0,\, 0 \right\}^T \, , \qquad [I] = \begin{bmatrix} 1 & 0 & 0 & 0 & 0 & 0 \\ 0 & 1 & 0 & 0 & 0 & 0 \\ 0 & 0 & 1 & 0 & 0 & 0 \\ 0 & 0 & 0 & \frac{1}{2} & 0 & 0 \\ 0 & 0 & 0 & 0 & \frac{1}{2} & 0 \\ 0 & 0 & 0 & 0 & 0 & \frac{1}{2} \end{bmatrix} \, .$$

On the other hand, when $\varphi\left(\operatorname{dev}[\boldsymbol{\sigma}]\big|^{trial}\right) \geq 0$ the solid undergoes viscoplastic flow. The increment of inelastic deformation is computed by numerical integration of formula (5.17a)

$$\boldsymbol{\varepsilon}^{in}\big|_{n+1}^{(k)} - \boldsymbol{\varepsilon}^{in}\big|_n = \Delta\lambda\,\boldsymbol{N}^{trial} \, , \tag{5.42a}$$

which corrects the trial stress state as follow

$$\operatorname{dev}[\boldsymbol{\sigma}]\big|_{n+1}^{(k)} = \operatorname{dev}[\boldsymbol{\sigma}]\big|^{trial} - 2\,G\,\Delta\lambda\,\boldsymbol{N}^{trial} \, , \tag{5.42b}$$

with

$$\boldsymbol{N}\big|^{trial} = \frac{\operatorname{dev}[\boldsymbol{\sigma}]\big|^{trial}}{\|\operatorname{dev}[\boldsymbol{\sigma}]\big|^{trial}\|} \tag{5.42c}$$

The symbol $\Delta\lambda = \lambda\,\Delta t$ defines the increment of the plastic multiplier for the current iteration. The latter is calculated by inserting Eq. (5.42b) into Eq. (5.17a) in the closed form expression

$$\Delta\lambda = \frac{\|\operatorname{dev}[\boldsymbol{\sigma}]\big|^{trial}\| - \sqrt{\frac{2}{3}}\,\sigma_Y}{\frac{g(c_T)\big|_{n+1}^{(k)}}{\Delta t} + 2\,G} \, . \tag{5.43}$$

The stress tensor is then computed by substituting (5.43) into (5.42b) and its derivatives read

$$\left[\frac{\partial\sigma}{\partial\varepsilon}\right]_{n+1}^{(k)} = \left(K - \frac{2}{3}\,G\,\theta_{n+1} \right) [\,i\,][\,i\,]^T + 2\,G\,\theta_{n+1}\,[I] - 2\,G\,\overline{\theta_{n+1}}\,[N_{n+1}][N_{n+1}]^T,$$

$$\left[\frac{\partial\sigma}{\partial c_L}\right]_{n+1}^{(k)} = -3\,K\,\left(\omega_L + \omega_T\,\left.\frac{\partial c_T}{\partial c_L}\right|_{n+1}^{(k)} \right)[\,i\,] - 2\,G\,\left.\frac{\partial\Delta\lambda}{\partial c_T}\right|_{n+1}^{(k)}\,\left.\frac{\partial c_T}{\partial c_L}\right|_{n+1}^{(k)}\,[N_{n+1}],$$

$$\left[\frac{\partial\sigma}{\partial\Sigma}\right]_{n+1}^{(k)} = -3\,K\,\omega_T\,\left.\frac{\partial c_T}{\partial c_L}\right|_{n+1}^{(k)}\,[\,i\,] - 2\,G\,\left.\frac{\partial\Delta\lambda}{\partial c_T}\right|_{n+1}^{(k)}\,\left.\frac{\partial c_T}{\partial\Sigma}\right|_{n+1}^{(k)}\,[N_{n+1}],$$

where

$$[N_{n+1}] = \left\{ N_{11}^{trial}\,,\,N_{22}^{trial}\,,\,N_{33}^{trial}\,,\,N_{12}^{trial}\,,\,N_{23}^{trial}\,,\,N_{13}^{trial} \right\}^T.$$

and

$$\theta_{n+1} = 1 - \frac{2\,G\,\Delta\gamma}{\|\,\mathrm{dev}\,[\,\boldsymbol{\sigma}\,]\|^{trial}\,\|}\,, \qquad \overline{\theta_{n+1}} = \frac{2\,G}{2\,G + \frac{g(c_T)|_{n+1}^{(k)}}{\Delta t}} + \theta_{n+1} - 1\,.$$

Finally the B-BAR method has been implemented in order to avoid volumetric locking. This numerical procedure reduces operatively in substituting the matrix $[B_u]$ with a matrix $[\overline{B_u}]$ defined conveniently. Details can be found in the broad literature on the argument (see [306] for example).

Part III

Porous Electrode

Chapter 6

Microscopic modeling of porous electrodes

6.1 Introduction

The behavior of battery cells is intrinsically multi-scale, as the multi-physics phenomena involving diffusion, migration, intercalation, and the accompanying mechanical effects take place at the characteristic length scale of the electrode compound, which is three orders of magnitudes smaller than the battery size [68].

In a recent contribution [67], a computational homogenization technique was tailored to Li-ion batteries by using a multiscale scheme with a complex multi-particle representative volume element (RVE). Such an approach allows modeling explicitly the electrochemical interactions that take place at the interface between particles, in which neutral lithium is stored, and the electrolyte, in which ionic lithium moves together with its salt counter-ions driven by diffusion and migration.

The mathematical modeling of porous-electrodes at microscopic scale is nowadays object of several studies that aim at coupling the involved complex multi-physics phenomena with realistic electrode microstructures [163, 151, 149, 150]. An accurate morphology reconstruction is crucial to model localized phenomena, like hot spot formation that causes thermal runway, as well as to identify averaged properties, which have been shown to be extremely sensitive to the size, shape, and particles distribution within the RVE.

(a)   (b)
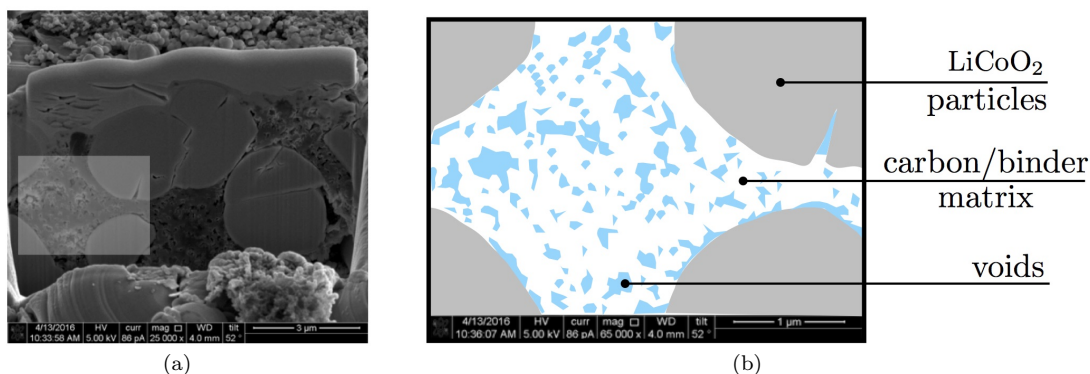
Figure 6.1: Cross-sectional image of a porous electrode microstructure obtained through FIB-SEM microscope (a). The phases involved are schematized in (b) in an enlarged portion.

Any porous electrode is a complex media made of different phases as showed in Fig. 6.1. It consists of particles of micrometric size (as $LiCoO_2$, $LiFePO_4$, and $LiMn_2O_4$) embedded in a porous matrix formed by the mixture of carbon nanoparticles and (polymeric) binder. The electrode particles are generally called *active*

or *storage* particles since Li ions are inserted/extracted from them during battery charging/discharging. The matrix increases the electrical conductivity of the electrode and provides structural integrity. The liquid electrolyte penetrates in the carbon/binder porosity up to the active particles surface allowing the electrochemical reaction to occur. For modeling perspectives, the electrode microstructure can be idealized as a three-phase media formed by active particles, conductive particles, and electrolyte as represented in Figure 6.2a.

For the sake of generality, the battery cell is supposed to have a single binary electrolyte which is a solution of a binary salt, say LiX, in a solvent, say a polymer. The electrolyte is then characterized by the presence of ionic species Li^+ and X^- after the complete dissociation of the binary salt LiX.

During battery discharging, Li ions intercalate in the active particles through the electrochemical reaction schematized in Fig. 6.2b. According to [86], Li^+ ions in active particles are screened by the mobile electrons, which accompany Li^+ when moves from one interstitial site to the other. Therefore the charge of Li cation after intercalation into active particles is instantaneously wiped out by the transport of electrons over the current collectors towards the particle surface. The active particles in the composite electrode are thus idealized as interstitial solid solution containing dissolved lithium Li and electrons e^- which are free to move.
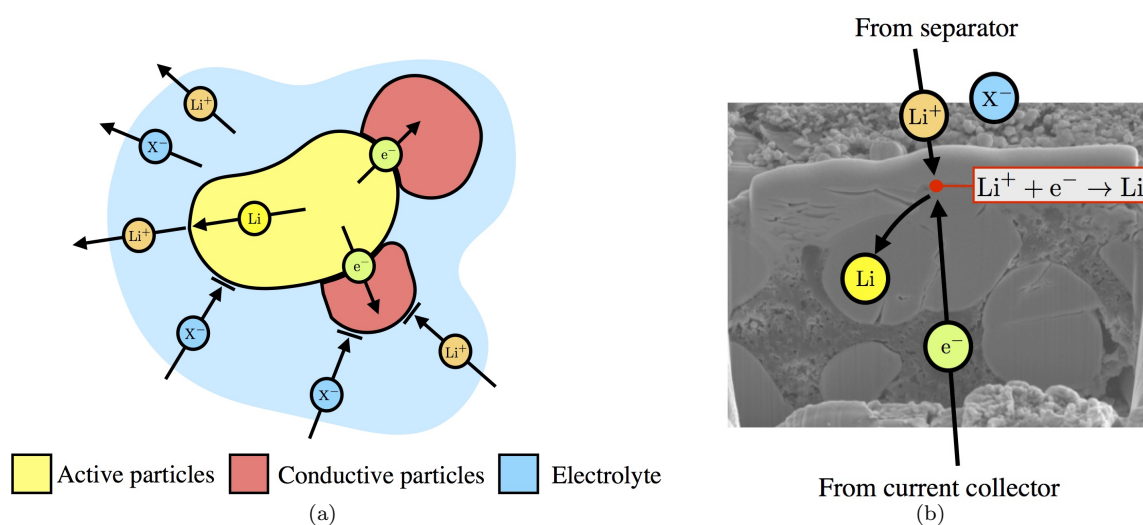
Figure 6.2: *Schematic illustration of the phases involved in the electrode modeling (a) and representation of the electrochemical reaction that take place at the active particle surface (b). In order to avoid confusion, Li ions dissolved in active particles are named Li rather than Li^+.*

The conductive particles are modeled in a similar way allowing only the transport of electrons since this phase does not admit the flow of any ionic species.

In this chapter the phenomena that take place in a porous electrode at micro-scale level are discussed. The fundamental balance laws for the electro-chemo-mechanical behavior of the phases involved are first introduced in a general form, then, specialized for active particles, conductive particles, and the electrolyte separately. Interface conditions among these phases are discussed in section 6.3.2. Subsequently, in section 6.4, constitutive laws are derived from thermodynamic principles for any phase. Governing equations and interface conditions are summarized in section 6.5. Finally numerical examples are shown in section 6.6.

6.2   Balance laws in abstract setting

Balance laws are here introduced in abstract setting. They will be particularized to the problem at hand in Section 6.3. As customary for multi-component systems, we consider an abstract entity embedded in the

solid or liquid, called network, which allows the definitions of displacements and strains [227]. The small displacement theory is considered sufficient for the scope of this contribution.

6.2.1 Conservation of moving species

The content of a moving species β inside a body is characterized by its molar concentration $c_\beta(\vec{x}, t)$ (i.e. number of moles per unit current volume). We assume here that the time variation of the species content, inside an arbitrary subregion $\mathcal{P}$ of a body $\mathcal{B}$, is both due to a flux across the boundary $\partial\mathcal{P}$ and a species generation inside $\mathcal{P}$. The first contribution is described by the projection of a flux vector $\vec{h}_\beta(\vec{x}, t)$ (i.e. the number of species moles per unit current area per unit time) along the outward normal vector $\vec{n}$, whereas the second one introduces a species supply rate $s_\beta(\vec{x}, t)$ (i.e. number of moles per unit current volume per unit time). Thus the global and local form of the species conservation laws are

$$\frac{\mathrm{d}}{\mathrm{d}t}\int_{\mathcal{P}} c_\beta \,\mathrm{d}V = -\int_{\partial\mathcal{P}} \vec{h}_\beta \cdot \vec{n}\,\mathrm{d}A + \int_{\mathcal{P}} s_\beta \,\mathrm{d}V \tag{6.1}$$

and

$$\frac{\partial c_\beta}{\partial t} + \mathrm{div}\left[\vec{h}_\beta\right] = s_\beta\,. \tag{6.2}$$

6.2.2 Maxwell's equations for electro quasistatic

The presence of charged species involve Maxwell's equations for the problem at hand. The *electro quasistatic* model - EQS henceforth - is here adopted rather then the full set of Maxwell's equations following [68]. This choice has the main advantage to replace the hyperbolic form og Maxwell's equations in favor of a simpler parabolic problem, as pointed out in [281]. The EQS model can be easily derived by neglecting the time derivative of the magnetic field $\vec{B}(\vec{x}, t)$ in Maxwell's equations, obtaining [281]

$$\mathrm{div}\left[\vec{D}\right] = \zeta\,, \tag{6.3a}$$

$$\mathrm{curl}\left[\vec{H}\right] = \frac{\partial\vec{D}}{\partial t} + \vec{i}\,, \tag{6.3b}$$

$$\mathrm{div}\left[\vec{B}\right] = 0\,, \tag{6.4a}$$

$$\mathrm{curl}\left[\vec{E}\right] = \vec{0}\,, \tag{6.4b}$$

where the (free) charge density $\zeta(\vec{x}, t)$, (free) current density $\vec{i}(\vec{x}, t)$, electric displacement $\vec{D}(\vec{x}, t)$, magnetizing $\vec{H}(\vec{x}, t)$ and the electric $\vec{E}(\vec{x}, t)$ vector fields have been introduced.

Equations (6.3) coincide with the first pair of Maxwell's equations [276], thus the local form of conservation of charge is still valid in the EQS model

$$\frac{\partial\zeta}{\partial t} = -\mathrm{div}\left[\vec{i}\right]\,. \tag{6.5}$$

Conversely, equations (6.4) differ from the Maxwell's equations since the *electromagnetic induction* is here ignored. Accordingly the magnetic field is still solenoidal while the electric field is now irrotational. The latter allow expressing the electromagnetic field in terms of an electric potential $\phi(\vec{x}, t)$, rather than both an electric and magnetic potentials $\vec{A}(\vec{x}, t)$ as in the authentic electromagnetic problem

$$\vec{E} = -\nabla\left[\phi\right]\,.$$

The connection between the first and second pairs of the EQS approximation is provided by the constitutive laws

$$\vec{D} = \epsilon_0 \vec{E} + \vec{P}, \tag{6.6a}$$

$$\vec{H} = \mu_0^{-1} \vec{B} - \vec{M}, \tag{6.6b}$$

where $\vec{P}(\vec{x}, t)$ and $\vec{M}(\vec{x}, t)$ are respectively the polarization and magnetization fields, while ϵ_0 and μ_0 are non negative universal constants [276]. In a general context $\vec{P}$ and $\vec{M}$ quantify the bounds charge and currents densities in media as constitutive response functions of both $\vec{E}$ and $\vec{B}$.

Owing to the Helmholtz decomposition theorem, the evolution of the electric field will be known once the evolution of its divergence is determined. The latter can be computed, in view of (6.6a), from the differential equation obtained by applying the divergence operator to (6.3b) as follow

$$\text{div}\left[\frac{\partial \vec{D}}{\partial t} + \vec{i} \right] = 0. \tag{6.7}$$

The magnetic contribution to the Lorentz is neglected in the EQS approximation, as discussed in [281]. Accordingly the Lorentz force per unit volume reads

$$\vec{b}_\zeta = \zeta \vec{E}. \tag{6.8}$$

In view of formulae (6.6a) - (6.7) - (6.8) the magnetic field does not affect both the evolution of the electric field and the Lorentz force, as long as $\vec{P}$ does not depend on $\vec{B}$. This is the case of isotropic, linear, homogeneous dielectrics for which $\vec{P}$ is usually expressed as

$$\vec{P} = \epsilon_0 \chi \vec{E}. \tag{6.9}$$

being χ a constant called *electric susceptibility*. In this way the constitutive definition of the electric displacement yields

$$\vec{D} = \epsilon_0 \epsilon_r \vec{E}, \tag{6.10}$$

where $\epsilon_r = (1 + \chi)$ is the *relative* permittivity. Eq. (6.10) will be used in Section 6.4 for the electrolyte solution. In this situation the magnetic field does exist but has not effect at all.

6.2.3 Faraday's Law

The concentration of charged species in solution (e.g. ions in the electrolyte phase) is coupled with the charge density through Faraday's law

$$\zeta = F \sum_\beta z_\beta c_\beta, \tag{6.11}$$

where F is Faraday's constant and z_β is the valency of β-th species[1]. By comparison between (6.2) and (6.5) in view of (6.11) we can write

$$\vec{i} = F \sum_\alpha z_\alpha \vec{h}_\alpha, \qquad s_\zeta = F \sum_\alpha z_\alpha s_\alpha. \tag{6.12}$$

Thus the current density $\vec{i}$ is related to the charged species flux $\vec{h}$, while the source term s in (6.2) entails a charge generation s_ζ as well.

---

[1]i.e. the number of electrons transferred per ion, typically +1 for Li^+ cations and -1 for X^- anions.

6.2.4 Balance of Momentum

The balance of linear and angular momentum are briefly summarized in its local form. As customary in the literature [133], the balance of linear momentum is considered in its quasistatic approximation, since the velocity of electro-diffusive processes is much slower than body deformation

$$\text{div}\left[\,\boldsymbol{\sigma}\,\right] + \vec{b} = \vec{0}, \qquad \boldsymbol{\sigma} = \boldsymbol{\sigma}^T, \tag{6.13}$$

where the Cauchy stress tensor $\boldsymbol{\sigma}\left(\vec{x}, t\right)$ and the body forces for unit current volume $\vec{b}\left(\vec{x}, t\right)$ account respectively for contact and *action-at-a-distance* forces (e.g. due to gravity and electromagnetic fields). However, as justified in [68], the Lorentz force $\vec{b}_\zeta$ is negligible compared to other mechanical effects since the charge separation in both active particles and electrolyte is irrelevant. The *electroneutrality approximation* therefore allows us to uncouple the mechanical and electric fields in the force balance equation (6.13), which in the absence of mechanical body forces becomes homogeneous.

6.3 Balance laws and interface conditions

The evolution of the electrochemical and mechanical fields at the finest scale is defined and monitored in an RVE of volume V and boundary ∂V. It is provided with the essential physical and geometrical information on the microstructural components, i.e. the active particles, the conductive particles, and the pore filling electrolyte. Two kinds of particles are modeled within the RVE: the active particles - collectively occupying domain V_a - and the conductive particles that define domain V_c. Accordingly, the *solid* phase will be occupy volume $V_s = V_a \cup V_c$. The electrolyte will fill the remaining volume V_e such that $V = V_s + V_e$.

6.3.1 Balance Equations

The conservation of moving species characterizes the species transport in two phases, namely the transport of lithium ions in the active particles and electrolyte as well as the transport of and X^- ions in the electrolyte[2]

$$\frac{\partial c_{\text{Li}}}{\partial t} + \text{div}\left[\,\vec{h}_{\text{Li}}\,\right] = 0 \qquad \vec{x} \in V_a\,, \tag{6.14a}$$

$$\frac{\partial c_{\text{Li}^+}}{\partial t} + \text{div}\left[\,\vec{h}_{\text{Li}^+}\,\right] = 0 \qquad \vec{x} \in V_e\,, \tag{6.14b}$$

$$\frac{\partial c_{\text{X}^-}}{\partial t} + \text{div}\left[\,\vec{h}_{\text{X}^-}\,\right] = 0 \qquad \vec{x} \in V_e\,. \tag{6.14c}$$

The concentration of lithium is identically zero in the conductive particles. There is no supply of species at the micro scale, as: (i) intercalation phenomena are analytically described as mass flux along proper interfaces; (ii) the degree of dissociation of the binary salt in the solution is complete.

Current density in active and conductive particles is due to electron transport so that the local form of electrons conservation

$$\frac{\partial c_{\text{e}^-}}{\partial t} + \text{div}\left[\,\vec{h}_{\text{e}^-}\,\right] = 0 \qquad \vec{x} \in \{V_a \cup V_c\}\,, \tag{6.15}$$

is equivalent to the local form of charge conservation in the assumption that the positively charged cores are steady. Following the same path of reasoning the conservation of charge in the electrolyte is guaranteed by equations (6.14b) - (6.14c).

As discussed in section 6.2.2 the electric displacement field (in the electrolyte denoted with $\vec{D}_e$, in the solid phase with $\vec{D}_s$) is governed by the following rate equations

---

[2]As said before, the lithium ions in the active particles will be denoted with Li rather than Li^+ for convenience.

$$\mathrm{div}\left[\frac{\partial \vec{D}_e}{\partial t} + F\left(\vec{h}_{\mathrm{Li}^+} - \vec{h}_{\mathrm{X}^-}\right)\right] = 0 \qquad \vec{x} \in V_e\,, \tag{6.16a}$$

$$\mathrm{div}\left[\frac{\partial \vec{D}_s}{\partial t} + \vec{i}_s\right] = 0 \qquad \vec{x} \in V_s\,. \tag{6.16b}$$

Inertia effects as well as non electrostatic bulk forces are neglected. In light of the electroneutrality assumption, electro-static forces are of secondary order. Therefore the balance of momentum (6.13) specializes as

$$\mathrm{div}\left[\,\boldsymbol{\sigma}\,\right] = \vec{0}\,, \qquad \boldsymbol{\sigma} = \boldsymbol{\sigma}^T\,, \qquad \vec{x} \in V\,. \tag{6.17}$$

6.3.2   Interface Conditions

We introduce the boundary values and the jump of a generic function $f\left(\vec{x}, t\right)$ at a generic interface $I = \partial V_\alpha \cap \partial V_\beta$ as

$$f|_I^\alpha = \lim_{\vec{x} \in V_\alpha \to I} f\left(\vec{x}, t\right)\,, \qquad f|_I^\beta = \lim_{\vec{x} \in V_\beta \to I} f\left(\vec{x}, t\right)\,,$$

and

$$[\![f]\!]_I = f|_I^\alpha - f|_I^\beta\,.$$

In the present framework, compatibility and traction continuity are imposed along all internal interfaces. These conditions along an interface $\partial V_a \cap \partial V_c$ between active particles and conductive particles read

$$[\![\,\vec{u}\,]\!] = \vec{0}\,,$$

$$[\![\boldsymbol{\sigma}]\!] \cdot \vec{n} = \vec{0}\,, \qquad \vec{n} = \vec{n_a} = -\vec{n_c}\,.$$

where $\vec{n}$ denotes the normal vector to a surface. Similar conditions can be stated for interfaces between active-active particles and conductive-conductive particles.

Interface between active particles and conductive particles $\partial V_a \cap \partial V_c$ - electrons are free to flow without causing discontinuities in the electric field, electric potential, and electrons chemical potential μ_{e^-}. Neutral lithium does not intercalate into conductive particles, thus

$$\vec{h}_{\mathrm{Li}} \cdot \vec{n}_a = 0 \qquad \vec{x} \in \partial V_a \cap \partial V_c\,. \tag{6.19}$$

Interface between electrolyte and conductive particles $\partial V_e \cap \partial V_c$ - there is no intercalation neither of Li ions nor of counterions. Electrons do not flow through the interface. The mass fluxes interfaces are thus homogeneous

$$\vec{h}_{\mathrm{Li}^+} \cdot \vec{n}_e = 0 \qquad \vec{x} \in \partial V_e \cap \partial V_c\,, \tag{6.20a}$$

$$\vec{h}_{\mathrm{X}^-} \cdot \vec{n}_e = 0 \qquad \vec{x} \in \partial V_e \cap \partial V_c\,, \tag{6.20b}$$

$$\vec{h}_{\mathrm{e}^-} \cdot \vec{n}_c = 0 \qquad \vec{x} \in \partial V_e \cap \partial V_c\,, \tag{6.20c}$$

and there is no current transport along those interfaces.

In order to devise the interface conditions for the electric potential, equation (6.3b) is invoked

$$\text{curl}\left[\vec{H}\right]\cdot\vec{n} = \left(\frac{\partial \vec{D}}{\partial t} + \vec{i}\right)\cdot\vec{n}. \tag{6.21}$$

It turns out that the evaluation of the magnetizing field $\vec{H}$ is required. In order to evaluate the latter across interfaces the differential problem (6.4a) must be deployed. In fact, interface conditions are the mere link between the magnetic and electric fields due to the electro quasistatic assumption. It will be assumed henceforth that the curl of the magnetizing field is continuous across all interfaces when projected in normal direction

$$\left(\frac{\partial \vec{D}_e}{\partial t} + F\left(\vec{h}_{\text{Li}^+} - \vec{h}_{\text{X}^-}\right)\right)\cdot\vec{n} = \left(\frac{\partial \vec{D}_s}{\partial t} + \vec{i}_s\right)\cdot\vec{n} \qquad \vec{x} \in \partial V_e \cap \partial V_s. \tag{6.22}$$

being $\vec{n} = \vec{n}_e = -\vec{n}_s$. Under this assumption the evaluation of $\vec{H}$ is not necessary.

Interface between electrolyte and active particles $\partial V_e \cap \partial V_a$ - The electrochemical reaction occurring at the active particle surface is here modeled through the standard Butler-Volmer equation. Therefore, instead of resolving explicitly the boundary layers between active particle and electrolyte, the involved phenomena are incorporated in a zero-thickness interface. Accordingly the electric potential can be discontinuous at the interface (see [324, 325] for a comprehensive treatment of the argument).

The electrochemical reaction at the active particles/electrolyte interfaces converts the oxidized Lithium to its neutral state before its diffusion into the active particles lattice (see Fig 6.2b). The surface current density i_{BV} is defined through the Butler-Volmer equation as

$$i_{BV} = i_0 \left\{ \exp\left[\frac{\alpha_A F \eta_S}{R T}\right] - \exp\left[-\frac{\alpha_C F \eta_S}{R T}\right] \right\}, \tag{6.23}$$

where i_0 is the exchange current density, α_A and α_B positive kinetic constants, and η_S is the surface overpotential.

The exchange current density is function of the concentration of lithium at the interface as follow [152]

$$i_0 = K_S F \left(c_{\text{Li}^+}|_{\partial V_e \cap \partial V_a}^e\right)^{\alpha_A} \left(c_{\text{Li}}^{max} - c_{\text{Li}}|_{\partial V_e \cap \partial V_a}^a\right)^{\alpha_A} \left(c_{\text{Li}}|_{\partial V_e \cap \partial V_a}^a\right)^{\alpha_C},$$

The surface overpotential is defined as

$$\eta_S = [\![\phi]\!] - U_S, \tag{6.24}$$

where U_S is the surface open circuit potential, while $[\![\phi]\!]$ refers to the electric potential jump at interface. According to [116], the surface open circuit potential U_S (also referred as surface OCP) is related to the ideal chemical potential, μ_{Li}, of lithium at the active particle surface through the following equation

$$F U_S(t) = \tilde{\mu}_{\text{Li}} - \mu_{\text{Li}}(t)|_{\partial V_e \cap \partial V_a}^a \tag{6.25}$$

where $\tilde{\mu}_{\text{Li}}$ is the chemical potential of lithium of a reference electrode.

Positive surface overpotential drives anodic currents, i.e. $i_{BV} > 0$, while negative η_S causes cathodic currents, i.e. $i_{BV} < 0$. The surface mass flux at particles surface in normal direction will be denoted with h_{BV}. It is related through Faraday's law to the surface current density in the same direction at the same location

$$i_{BV} = F h_{BV}. \tag{6.26}$$

On the other hand there is no intercalation of X^- ions into the active particles. In conclusions interface conditions can be summarized as follow

$$\vec{h}_{\mathrm{Li^+}} \cdot \vec{n}_e = -\vec{h}_{\mathrm{Li}} \cdot \vec{n}_a = -h_{BV} \qquad \vec{x} \in \partial V_e \cap \partial V_a \,, \tag{6.27a}$$

$$\vec{h}_{\mathrm{X^-}} \cdot \vec{n}_a = 0 \qquad \vec{x} \in \partial V_a \cap \partial V_e \,, \tag{6.27b}$$

$$\vec{h}_{e^-} \cdot \vec{n}_a = 0 \qquad \vec{x} \in \partial V_e \cap \partial V_a \,, \tag{6.27c}$$

$$\left(\frac{\partial \vec{D}_e}{\partial t} + F \left(\vec{h}_{\mathrm{Li^+}} - \vec{h}_{\mathrm{X^-}} \right) \right) \cdot \vec{n} = \left(\frac{\partial \vec{D}_s}{\partial t} + \vec{i}_s \right) \cdot \vec{n} \qquad \vec{x} \in \partial V_e \cap \partial V_a \,. \tag{6.27d}$$

with $\vec{n} = \vec{n}_e = -\vec{n}_a$.

6.4   Constitutive theory

Constitutive relations are derived from thermodynamic principles as showed in Chapter 2 for electrolyte solutions, and in Chapters 3 - 4 - 5 for active particles. For convenience we enforce isothermal conditions throughout the process.

6.4.1   Electrolyte

The local form of entropy imbalance derived in (2.19) reads

$$\begin{aligned}
&\frac{\partial \boldsymbol{\varepsilon}_e}{\partial t} : \left(\boldsymbol{\sigma}_e - \frac{\partial \psi_e}{\partial \boldsymbol{\varepsilon}_e} \right) + \frac{\partial \vec{E}_e}{\partial t} \cdot \left(\vec{D}_e - \frac{\partial \psi_e}{\partial \vec{E}_e} \right) + \frac{\partial c_{\mathrm{Li^+}}}{\partial t} \left(\mu_{\mathrm{Li^+}} - \frac{\partial \psi_e}{\partial c_{\mathrm{Li^+}}} \right) + \\
&\frac{\partial c_{\mathrm{X^-}}}{\partial t} \left(\mu_{\mathrm{X^-}} - \frac{\partial \psi_e}{\partial c_{\mathrm{X^-}}} \right) - \vec{h}_{\mathrm{Li^+}} \cdot \nabla \left[\bar{\mu}_{\mathrm{Li^+}} \right] - \vec{h}_{\mathrm{X^-}} \cdot \nabla \left[\bar{\mu}_{\mathrm{X^-}} \right] \geq 0 \,,
\end{aligned} \tag{6.28}$$

with $\bar{\mu}_\beta = \mu_\beta + z_\beta \, F \, \phi_e$ denoting the electrochemical potential.

The Helmholtz free energy density ψ_e is decomposed into separate parts: a diffusive contribution ψ_e^{diff}, an electric contribution ψ_e^{elect}, and an elastic contribution ψ_e^{el} [3]

$$\psi_e(\boldsymbol{\varepsilon}_e, c_{\mathrm{Li^+}}, c_{\mathrm{X^-}}, \vec{E}_e) = \psi_e^{diff}(c_{\mathrm{Li^+}}, c_{\mathrm{X^-}}) + \psi_e^{elect}(\vec{E}_e) + \psi_e^{el}(\boldsymbol{\varepsilon}_e) \,,$$

with

$$\begin{aligned}
\psi_e^{diff} &= \mu_{\mathrm{Li^+}}^0 \, c_{\mathrm{Li^+}} + R\,T\,c^{max} \Big\{ \theta_{\mathrm{Li^+}} \ln[\theta_{\mathrm{Li^+}}] + (1 - \theta_{\mathrm{Li^+}}) \ln[1 - \theta_{\mathrm{Li^+}}] \Big\} + \\
&+ \mu_{\mathrm{X^-}}^0 \, c_{\mathrm{Li^+}} + R\,T\,c^{max} \Big\{ \theta_{\mathrm{X^-}} \ln[\theta_{\mathrm{X^-}}] + (1 - \theta_{\mathrm{X^-}}) \ln[1 - \theta_{\mathrm{X^-}}] \Big\} \,,
\end{aligned} \tag{6.29a}$$

$$\psi_e^{elect} = \frac{1}{2} \, \mathcal{E}_e \, \vec{E}_e \cdot \vec{E}_e \,, \tag{6.29b}$$

$$\psi_e^{el} = \frac{1}{2} \, K_e \operatorname{tr} \left[\boldsymbol{\varepsilon}_e \right]^2 + G_e \left\| \operatorname{dev} \left[\boldsymbol{\varepsilon}_e \right] \right\|^2 \,. \tag{6.29c}$$

In equations (6.29a) μ_β^0 and c^{max} denote the reference chemical potential and the ions saturation limit, while $\theta_\alpha = c_\beta / c^{max}$ is the molar fraction of a generic species β. Symbol $\mathcal{E}_e = \mathcal{E}_0 \mathcal{E}_r$ is the permittivity of the

---

[3]For simplicity the electrolyte is modeled as an elastic media.

electrolyte solution. The mechanical behavior is here modeled assuming a linear-elastic response (K_e and G_e denote the bulk and shear modulus respectively) with the elastic strain tensor in formula (6.29c) defined as

$$\boldsymbol{\varepsilon}_e = \frac{1}{2}\left(\nabla\,[\,\vec{u_e}\,] + \nabla\,[\,\vec{u_e}\,]^T\right),$$

being $\vec{u}_e$ the displacement field in the electrolyte.

The definition of the stress tensor $\boldsymbol{\sigma}_e$, electric displacement $\vec{D}_e$, and chemical potentials μ_{Li^+}, μ_{X^-} follow from Eq. (6.28) using the Coleman-Noll procedure

$$\boldsymbol{\sigma}_e = \frac{\partial \psi^e}{\partial \boldsymbol{\varepsilon}_e} = K_e\,\text{tr}\,[\,\boldsymbol{\varepsilon}_e\,]\,\mathbb{1} + 2\,G_e\,\text{dev}\,[\,\boldsymbol{\varepsilon}_e\,]\,, \tag{6.30a}$$

$$\vec{D}_e = \frac{\partial \psi^e}{\partial \vec{E}_e} = \not\epsilon_e\,\vec{E}_e = -\not\epsilon_e\,\nabla\,[\,\phi_e\,]\,, \tag{6.30b}$$

$$\mu_{\text{Li}^+} = \frac{\partial \psi^e}{\partial c_{\text{Li}^+}} = \mu_{\text{Li}^+}^0 + R\,T\ln\left[\frac{c_{\text{Li}^+}}{c^{max} - 2\,c_{\text{Li}^+}}\right]\,, \tag{6.30c}$$

$$\mu_{\text{X}^-} = \frac{\partial \psi^e}{\partial c_{\text{X}^-}} = \mu_{\text{X}^-}^0 + R\,T\ln\left[\frac{c_{\text{X}^-}}{c^{max} - 2\,c_{\text{X}^-}}\right]\,. \tag{6.30d}$$

Finally the flux of Li$^+$ and X$^-$ ions is modeled through the Nernst-Plank equation (see Chapter 2 for the details)

$$\vec{h}_{\text{Li}^+} = -\mathbb{D}_{\text{Li}^+}\,\nabla\,[\,c_{\text{Li}^+}\,] - \frac{\mathbb{D}_{\text{Li}^+}\,F}{R\,T}\,c_{\text{Li}^+}\,\left(1 - 2\frac{c_{\text{Li}^+}}{c^{max}}\right)\,\nabla\,[\,\phi_e\,]\,, \tag{6.31a}$$

$$\vec{h}_{\text{X}^-} = -\mathbb{D}_{\text{X}^-}\,\nabla\,[\,c_{\text{X}^-}\,] + \frac{\mathbb{D}_{\text{X}^-}\,F}{R\,T}\,c_{\text{X}^-}\,\left(1 - 2\frac{c_{\text{X}^-}}{c^{max}}\right)\,\nabla\,[\,\phi_e\,]\,. \tag{6.31b}$$

6.4.2 Active particles

The flow of electrons in the solid part of the electrode is here modeled by Ohm's law as pursued in several publications [97, 116, 270]. Accordingly, the electromagnetic problem in the active and conductive particles will be considered in the electro static formulation. The time variation of the charge density $\frac{\partial c_{\text{e}^-}}{\partial t}$ and electric displacement $\frac{\partial \vec{D}_e}{\partial t}$ is thus neglected so that the local form of charge conservation (6.5) simplifies as

$$\text{div}\left[\vec{i}_a\right] = 0\,. \tag{6.32}$$

The chemo-mechanical response of the active particles is modeled following the framework developed in Chapters 3 - 4 - 5. We therefore assume that the particle host structure is made of two distinct sites for lithium insertion, namely interstitial L and trapped sites T. By doing so the concentration of neutral lithium reads

$$c_{\text{Li}} = c_L + c_T\,,$$

with c_L denoting interstitial (or lattice) lithium while c_T is trapped lithium. The latter cannot diffuse in the storage particles in the assumption that trap sites are isolated, thus the lithium flux yields

$$\vec{h}_{\text{Li}} = \vec{h}_L\,,$$

being $\vec{h}_L$ the flux of lattice lithium.

The Clausius-Duhem inequality for active particles accounts for the electro static energy added to the expression derived in Chapter 3 Eq. (3.28)

$$
\begin{aligned}
\frac{\partial \boldsymbol{\varepsilon}^{ce}}{\partial t} &: \left(\boldsymbol{\sigma}_a - \frac{\partial \psi_a}{\partial \boldsymbol{\varepsilon}^{ce}} \right) + \frac{\partial c_L}{\partial t} \left(\mu_L - \frac{\partial \psi_a}{\partial c_L} \right) + \frac{\partial c_T}{\partial t} \left(\mu_T - \frac{\partial \psi_a}{\partial c_{X^-}} \right) + \\
&- \vec{h}_L \cdot \nabla \left[\mu_L \right] - w^{(1)} A^{(1)} + \boldsymbol{\sigma}_a : \frac{\partial \boldsymbol{\varepsilon}^{in}}{\partial t} + \vec{i}_a \cdot \vec{E}_a \geq 0 \,.
\end{aligned}
\tag{6.33}
$$

Symbols $A^{(1)} = \mu_L - \mu_T$ and $w^{(1)}$ refer to the chemical affinity and rate of the trapping reaction respectively.

Note that the electrostatic term appearing in (6.33), i.e. the so called Joule effect $\vec{i}_a \cdot \vec{E}_a$, can be obtained following the same procedure adopted in Chapter 2 along with the electro static approximation, i.e. $\frac{\partial \vec{D}_a}{\partial t} = \vec{0}$.

The chemo-elastic strain $\boldsymbol{\varepsilon}^{ce}$ is considered to be made up of two separate contributions: an elastic recoverable part $\boldsymbol{\varepsilon}^{el}$, and a swelling (or chemical) contribution $\boldsymbol{\varepsilon}^s$

$$
\boldsymbol{\varepsilon}^{ce} = \boldsymbol{\varepsilon}^{el} + \boldsymbol{\varepsilon}^s \,.
$$

The chemical strain is assumed to be volumetric and proportional to the deviation $c_\beta - c_\beta^0$ from a reference concentration c_β^0 by means of a chemical expansion coefficient ω_β of species β

$$
\boldsymbol{\varepsilon}^s = \omega_L \left(c_L - c_L^0 \right) \mathbb{1} + \omega_T \left(c_T - c_T^0 \right) \mathbb{1} \,.
$$

Assuming also that the active particles can deform inelastically, the total strain tensor $\boldsymbol{\varepsilon}_a$ results in the sum of three contributions

$$
\boldsymbol{\varepsilon}_a = \boldsymbol{\varepsilon}^{el} + \boldsymbol{\varepsilon}^s + \boldsymbol{\varepsilon}^{in} \,,
$$

with

$$
\boldsymbol{\varepsilon}_a = \frac{1}{2} \left(\nabla \left[\vec{u_a} \right] + \nabla \left[\vec{u_a} \right]^T \right) \,,
$$

and $\vec{u}_a$ the displacement field in the active particles.

The evolution of the inelastic deformation $\boldsymbol{\varepsilon}^{in}$ must be consistent with the equation (6.33). A possible choice is the Perzyna like visco-plastic law adopted for the numerical simulations carried out in Chapters 4 and 5.

As customary the Helmholtz free energy emanates from the following additive decomposition

$$
\psi_a(\boldsymbol{\varepsilon}^{ce}, c_L, c_T) = \psi_a^{diff}(c_L, c_T) + \psi_a^{el}(\boldsymbol{\varepsilon}^{ce}) \,,
\tag{6.34}
$$

where

$$
\begin{aligned}
\psi_a^{diff} &= \mu_L^0 \, c_L + R\,T\,c_L^{max} \Big\{ \theta_L \ln[\theta_L] + (1 - \theta_L) \ln[1 - \theta_L] \Big\} + \\
&+ \mu_T^0 \, c_T + R\,T\,c_T^{max} \Big\{ \theta_T \ln[\theta_T] + (1 - \theta_T) \ln[1 - \theta_T] \Big\} \,,
\end{aligned}
\tag{6.35a}
$$

$$
\psi_a^{el} = \frac{1}{2} K_a \operatorname{tr} \left[\boldsymbol{\varepsilon}^{ce} - \boldsymbol{\varepsilon}^s \right]^2 + G_a \left\| \operatorname{dev} \left[\boldsymbol{\varepsilon}^{ce} - \boldsymbol{\varepsilon}^s \right] \right\|^2 \,.
\tag{6.35b}
$$

with obvious meaning of symbols μ_β^0, c_L^{max}, c_T^{max}, K_a, and G_a.

The constitutive definitions of the stress tensor $\boldsymbol{\sigma}_a$ and chemical potentials μ_L and μ_T are derived from Eq. (6.33) as follow

$$\boldsymbol{\sigma}_a = \frac{\partial \psi^a}{\partial \boldsymbol{\varepsilon}^{ce}} = K_a \operatorname{tr}\left[\, \boldsymbol{\varepsilon}^{ce} - \boldsymbol{\varepsilon}^s \,\right] \mathbb{1} + 2\,G_a \operatorname{dev}\left[\, \boldsymbol{\varepsilon}^{ce} - \boldsymbol{\varepsilon}^s \,\right] , \tag{6.36a}$$

$$\mu_L = \frac{\partial \psi^a}{\partial c_L} = \mu_L^0 + R\,T \ln\left[\frac{\theta_L}{1 - \theta_L}\right] - \omega_L \operatorname{tr}\left[\, \boldsymbol{\sigma}_a \,\right] , \tag{6.36b}$$

$$\mu_T = \frac{\partial \psi^a}{\partial c_T} = \mu_T^0 + R\,T \ln\left[\frac{\theta_T}{1 - \theta_T}\right] - \omega_T \operatorname{tr}\left[\, \boldsymbol{\sigma}_a \,\right] . \tag{6.36c}$$

Guided by the Joule effect in Clausius-Duhem inequality a linear law is set as usual for the electrons flow. The current density is made proportional to the gradient of the electric potential through the electrical conductivity $\kappa_a > 0$

$$\vec{i}_a = \kappa_a\,\vec{E}_a = -\kappa_a\,\nabla\left[\,\phi_a\,\right] . \tag{6.37}$$

The trapping reaction is assumed to be infinitely fast so that the condition of chemical equilibrium $A^{(1)} = 0$ holds throughout the process and the trapping reaction does not involve any energetic dissipation. Under this hypothesis the chemical potential of lithium dissolved in active particles yields

$$\mu_{\mathrm{Li}} = \mu_L = \mu_T .$$

Finally the expression of lithium flux is derived by applying the generalized Fick's law (see Chapter 3 for the details) obtaining

$$\vec{h}_{\mathrm{L}} = -\mathbb{D}_{\mathrm{L}}\,\nabla\left[\,c_L\,\right] + \frac{\mathbb{D}_{\mathrm{L}}\,\omega_L}{R\,T}\,c_L\,\left(\frac{c_L^{max} - c_L}{c_L^{max}}\right)\,\nabla\left[\,\operatorname{tr}\left[\,\boldsymbol{\sigma}_a\,\right]\,\right] . \tag{6.38}$$

In order to model phase-segregations in active particles as conducted in Chapter 5, an appropriate evolution law for c_T^{max} has to be defined.

6.4.3 Conductive particles

We assume the conductive particles made up of an electrical conductive medium with linear-elastic mechanical behavior. Following the same procedure detailed for the active particles, the constitutive definition of stress tensor and current density yield

$$\boldsymbol{\sigma}_c = K_c \operatorname{tr}\left[\,\boldsymbol{\varepsilon}_c\,\right] \mathbb{1} + 2\,G_c \operatorname{dev}\left[\,\boldsymbol{\varepsilon}_c\,\right] , \tag{6.39a}$$

$$\vec{i}_c = \kappa_c\,\vec{E}_c = -\kappa_c\,\nabla\left[\,\phi_c\,\right] \tag{6.39b}$$

with obvious meaning of material constants K_c, G_c, and κ_c.

6.5 Governing Equations

6.5.1 Electrolyte

Governing equations can be derived by incorporating the constitutive equations (6.30a), (6.30b), and (6.31) into balance equations (6.14b), (6.14c), (6.16a), and (6.17). The variable fields that rule the problem, resulting from the choice made for thermodynamic prescriptions, are ionic concentrations $c_{\mathrm{Li^+}}$ and $c_{\mathrm{X^-}}$, the electric potential ϕ_e, and the displacements $\vec{u}_e$. The governing equations hold at all points $\vec{x} \in V_e$ and time $t \in\,]0,\,t_f]$

$$
\begin{cases}
\dfrac{\partial c_{\mathrm{Li}^+}}{\partial t} + \mathrm{div}\left[\vec{h}_{\mathrm{Li}^+}\left(c_{\mathrm{Li}^+}, \phi_e\right)\right] = 0\,, \\[2.5ex]
\dfrac{\partial c_{\mathrm{X}^-}}{\partial t} + \mathrm{div}\left[\vec{h}_{\mathrm{X}^-}\left(c_{\mathrm{X}^-}, \phi_e\right)\right] = 0\,, \\[2.5ex]
\mathrm{div}\left[\dfrac{\partial \vec{D}_e(\phi_e)}{\partial t} + F\left(\vec{h}_{\mathrm{Li}^+}\left(c_{\mathrm{Li}^+}, \phi_e\right) - \vec{h}_{\mathrm{X}^-}\left(c_{\mathrm{X}^-}, \phi_e\right)\right)\right] = 0\,, \\[2.5ex]
\mathrm{div}\left[\boldsymbol{\sigma}_e\left(\vec{u}_e\right)\right] = \vec{0}\,.
\end{cases}
\tag{6.40}
$$

Interface conditions at the boundary between active particles and conductive particles follow the prescriptions given in Section 6.3.2. The boundary condition (6.22) must be rewritten since the electromagnetic problem in the solid part has been considered in the electro static approximation. Accordingly the term $\frac{\partial \vec{D}_s}{\partial t}$ vanishes for the solid phase so that the interface condition (6.22) reduces to

$$
\left(\frac{\partial \vec{D}_e}{\partial t} + F\left(\vec{h}_{\mathrm{Li}^+} - \vec{h}_{\mathrm{X}^-}\right)\right) \cdot \vec{n}_e + \vec{i}_s \cdot \vec{n}_s = 0 \qquad \vec{x} \in \partial V_e \cap \partial V_s\,.
\tag{6.41}
$$

The current density and Li$^+$ ions flux at the interface between electrolyte and active particles is prescribed by the Butler-Volmer equation (6.23). The latter establishes the discontinuity of the electric potential at the interface $[\![\phi]\!] = \phi_a - \phi_e$ as a result of the surface electrochemical reaction. The X$^-$ ions cannot intercalate neither into the active particles nor into the conductive particles. The continuity of the displacement field is prescribed for equation (6.40d) at all the interfaces. The interface conditions for the electrolyte phase can be summarized as follow

$$
\vec{h}_{\mathrm{Li}^+} \cdot \vec{n}_e =
\begin{cases}
-h_{BV} & \vec{x} \in \partial V_e \cap \partial V_a \\[2ex]
0 & \vec{x} \in \partial V_e \cap \partial V_c
\end{cases}
\tag{6.42a}
$$

$$
\vec{h}_{\mathrm{X}^-} \cdot \vec{n}_e = 0 \qquad \vec{x} \in \{\partial V_e \cap \partial V_a \cup \partial V_e \cap \partial V_c\}
\tag{6.42b}
$$

$$
\mathrm{curl}\left[\vec{H}_e\right] \cdot \vec{n}_e =
\begin{cases}
-i_{BV} & \vec{x} \in \partial V_e \cap \partial V_a \\[2ex]
0 & \vec{x} \in \partial V_e \cap \partial V_c
\end{cases}
\tag{6.42c}
$$

$$
\vec{u}_e =
\begin{cases}
\vec{u}_a & \vec{x} \in \partial V_e \cap \partial V_a \\[2ex]
\vec{u}_c & \vec{x} \in \partial V_e \cap \partial V_c
\end{cases}
\tag{6.42d}
$$

6.5.2 Active particles

Governing equations are derived incorporating the constitutive equations (6.36a), (6.37), and (6.38) into balance equations (6.14a), (6.17), and (6.32). The variable fields that rule the problem, resulting from the choice made for thermodynamic prescriptions, are the concentrations c_L, the electric potential ϕ_a, and the displacements $\vec{u}_a$. The governing equations hold at all points $\vec{x} \in V_a$ and time $t \in]0, t_f]$

$$
\begin{cases}
\dfrac{\partial c_L}{\partial t} + \dfrac{\partial c_T}{\partial t} + \mathrm{div}\left[\,\vec{h}_L\left(c_L,\,\boldsymbol{\sigma}_a\right)\right] = 0\,, \\[3ex]
\mathrm{div}\left[\,\vec{i}_a\left(\phi_a\right)\right] = 0\,, \\[3ex]
\mathrm{div}\left[\,\boldsymbol{\sigma}_a\left(c_L,\,\vec{u}_e\right)\right] = \vec{0}\,,
\end{cases}
\tag{6.43}
$$

Interface conditions at the boundary between the electrolyte and conductive particles follow the prescriptions given in Section 6.3.2. The electro-chemical interface conditions at the boundary between the electrolyte are explicitly modeled through the Butler-Volmer kinetic equation. On the other hand, at the boundary shared with conductive particles the neutral lithium cannot flow in normal direction. The continuity of the electric potential is enforced between the active and conductive particles. Displacements continuity is prescribed at the interfaces between both active and conductive particles. The interface conditions can be summarized as follow

$$
\vec{h}_{\mathrm{L}} \cdot \vec{n}_a =
\begin{cases}
h_{BV} & \vec{x} \in \partial V_a \cap \partial V_e \\[2ex]
0 & \vec{x} \in \partial V_a \cap \partial V_c
\end{cases}
\tag{6.44a}
$$

$$
\vec{i}_a \cdot \vec{n}_a = i_{BV} \qquad \vec{x} \in \partial V_a \cap \partial V_e
$$
$$
\phi_a = \phi_c \qquad\qquad \vec{x} \in \partial V_a \cap \partial V_c
\tag{6.44b}
$$

$$
\vec{u}_a =
\begin{cases}
\vec{u}_e & \vec{x} \in \partial V_a \cap \partial V_e \\[2ex]
\vec{u}_c & \vec{x} \in \partial V_a \cap \partial V_c
\end{cases}
\tag{6.44c}
$$

6.5.3 Conductive particles

Governing equations can be derived by incorporating the constitutive equations (6.39) into balance equations (6.17), and (6.32). The variable fields that rule the problem, resulting from the choice made for thermodynamic prescriptions, are the electric potential ϕ_c, and the displacements $\vec{u}_c$. The governing equations hold at all points $\vec{x} \in V_c$ and time $t \in]0,\,t_f]$

$$
\begin{cases}
\mathrm{div}\left[\,\vec{i}_c\left(\phi_c\right)\right] = 0\,, \\[3ex]
\mathrm{div}\left[\,\boldsymbol{\sigma}_c\left(\vec{u}_c\right)\right] = \vec{0}\,,
\end{cases}
\tag{6.45}
$$

Following the same path of reasoning of Sections 6.5.1 - 6.5.2, the interface conditions for conductive particles can be summarized as follow

$$
\vec{i}_c \cdot \vec{n}_c = 0 \qquad \vec{x} \in \partial V_c \cap \partial V_e
$$
$$
\phi_c = \phi_a \qquad\qquad \vec{x} \in \partial V_c \cap \partial V_a
\tag{6.46a}
$$

$$\vec{u}_c = \begin{cases} \vec{u}_e & \vec{x} \in \partial V_c \cap \partial V_e \\ \\ \vec{u}_a & \vec{x} \in \partial V_c \cap \partial V_a \end{cases} \tag{6.46b}$$

6.6 Numerical Example

The case study reported in the article by Danilov et al. [86] is reproduced for model validation. It considers a $10\,\mu$Ah all-solid state battery made up of three different layers as shown in Fig. 6.1a. The electrodes consist of a $320\,$nm thick polycrystalline LiCoO$_2$ cathode and a metallic Li anode separated by $1.5\,\mu$m solid-state electrolyte. The battery was charged and discharged according to the following regime: constant current/constant voltage (CCCV) charging with a 1.6 C-rate till the maximum voltage level of 4.2 V was reached, followed by 30 min relaxation period and a current constant discharge. Fig. 6.1b depicts the experimentally measured voltage profiles for the following applied discharge rates: 3.2, 6.4, 12.8, 25.6, and 51.2 C. In line with the cell morphology, the battery response was also simulated in [86] through a one-dimensional model. Material parameters difficult to measure experimentally, i.e. the kinetic constants of the Butler-Volmer equation, were estimated by comparing the experimental and numerical results.

(a)   (b)
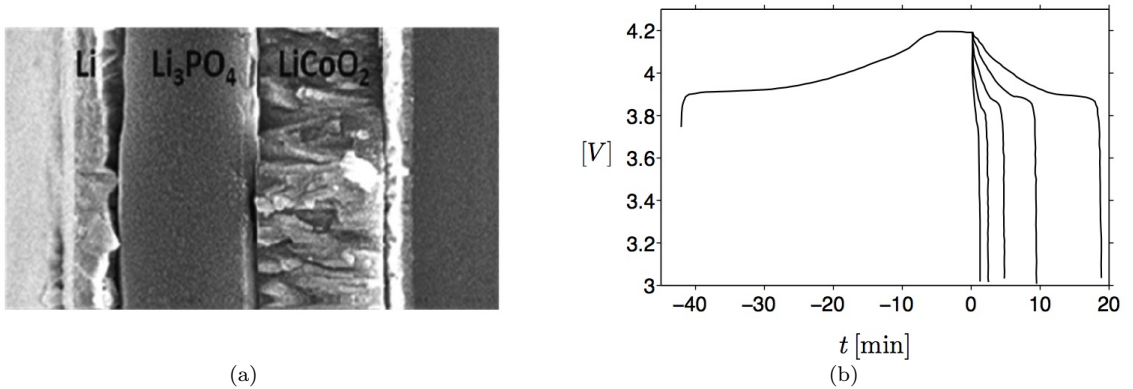
Figure 6.1: *SEM images of the all-solid-state battery tested in [86] (a), and experimentally measured voltage profiles during 1.6 C-rate charging and discharging at various C-rates (3.2, 6.4, 12.8, 25.6, and 51.2 C-rate) (b). Time t=0 corresponds to the start of each discharge rate.*

6.6.1 Modeling assumptions and material parameters

Although the battery morphology and boundary conditions are suitable for a one-dimensional description, governing equations have been implemented in a 2D plane-strain formulation. A schematic representation of the simulated battery geometry is depicted in Fig. 6.2.

Since the model proposed in [86] does not consider the mechanics in any battery components, the relevant material constants are taken from other references here, i.e [152, 107, 112, 326, 116].

Electrodes - The subscripts $_{an}$ and $_{ca}$ will identify anode and cathode from now to on. The electrodes are both modeled by means of governing equations of active particles (6.43). For simplicity trapping of lithium as well as the effect of inelastic deformations are not accounted for. In this way $c_T^{max} = 0$ and $\frac{\partial \varepsilon^{in}}{\partial t} = \vec{0}$ in the electrodes.

We also assume the metallic lithium as an unlimited reservoir of Li ions so that it is unaffected by the lithiation/delithiation processes. Therefore the concentration of lithium in the anode is uniform and constant throughout the process. All the material parameters of the electrodes are listed in Table 6.1.

Electrolyte - The solid-electrolyte response is described by governing equations (6.40) assuming a complete dissociation in Li$^+$ and X$^-$ ions. In the absence of experimental evidence, we model the electrolyte as

133
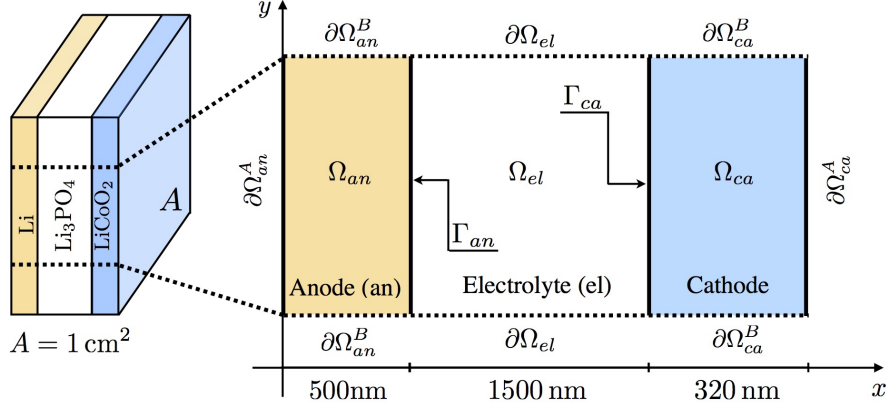
Figure 6.2: Schematic representation of the planar all-solid-state Li-ion battery simulated in the numerical example. Conductive particles are not present in this case.

rigid compared to the electrodes. This has been implemented by choosing a Young's modulus two orders of magnitude larger than for the cathode.

Differently from governing equations (6.40), the electrolyte model in [86] does not include the effects of saturation. Therefore parameter c^{max} is not provided. Here we take c^{max} much larger than the initial concentrations of the moving ions, in order to simulate the case of diluite solutions. A discussion on the role of saturation can be found in Chapter 2. The material parameters of the electrolyte are reported in Table 6.2.

Interfaces - The anode/electrolyte Γ_{an} and cathode/electrolyte Γ_{ca} interfaces follow the prescriptions of the interfaces between active particles and electrolyte.

Although the surface open circuit potential U_S is given in terms of the ideal chemical potential μ_{Li} at interface (see. Eq. (6.25)), here we take U_S of LiCoO$_2$ from [86] for reasons of consistency.

A relation between the battery OCP potential and extracted charge, Q_{ext}, has been experimentally determined by Danilov et al. [86]. The outcomes of those experimental fitting are depicted in Fig. 6.3 and have been used in their numerical computations. In equilibrium conditions, the concentration of lithium is uniform in the cathode, so that the extracted charge can written as

$$Q_{ext} = F \left(c_{Li} - c_{Li}^{init} \right) V_{ca} \,, \tag{6.47}$$

where c_{Li}^{init} is the concentration of lithium at the beginning of discharging, while V_{ca} is the volume of the cathode. According to Eq. (6.47), the battery OCP is function of the concentration of lithium in the cathode. During battery charging/discharging the concentration of lithium is no longer uniform in the cathode. In this regime the surface open circuit potential U_S at the Γ_{ca} interface is taken from Fig. 6.3 by computing Q_{ext} through formula (6.47) with c_{Li} measured at Γ_{ca}.

The other material parameters appearing in equation (6.23) for the interface Γ_{ca} are taken from [86] and read

$$\alpha_A = 0.6 \,, \qquad \alpha_C = 0.4 \,, \qquad K_S = 5.1 \times 10^{-6} \, \mathrm{m^{2.8} \, mol^{-0.6} \, s^{-1}} \qquad \text{on } \Gamma_{ca}.$$

For the interface between anode and electrolyte, it has been reported in [86] that the exchange current density for the metallic lithium electrode is much larger than for LiCoO$_2$

$$i_0^{an} \gg i_0^{ca}$$

hence the potential jump occurring at Γ_{an} is negligible compared to that at Γ_{ca}. In addition the open circuit potential of the metallic lithium is zero since it has been taken as the reference electrode.

134

Material Parameters Electrodes				Ref.
Maximum concentration of lithium in the cathode	c_L^{max}	2.33×10^4	mol/m^3	[86]
Diffusivity of Li ions in the cathode	$\mathbb{D}_L$	1.76×10^{-15}	m^2/s	[86]
Coefficient of chemical expansion of LiCoO$_2$ cathode	ω_L	-5.300×10^{-7}	m^3/mol	[107]
Young modulus of LiCoO$_2$ cathode	E_{ca}	370	GPa	[152]
Poisson ratio of LiCoO$_2$ cathode	ν_{ca}	0.2	-	[152]
Electrical conductivity of LiCoO$_2$ cathode	κ_{ca}	10	S/m	[112]
Young modulus of lithium anode	E_{an}	4.9	GPa	[326]
Poisson ratio of lithium anode	ν_{an}	0.36	-	[326]
Electrical conductivity of lithium anode	κ_{an}	1.08×10^7	S/m	[116]

Table 6.1: *Material parameters of electrodes used in the numerical simulations. The mechanical parameters are given in term of Young's modulus E and Poisson ratio ν.*

Material Parameters Electrolyte				Ref.
Saturation limit of the electrolyte	c^{max}	1.0×10^6	mol/m^3	this study
Diffusivity of Li$^+$ ions in the electrolyte	$\mathbb{D}_{Li^+}$	1.0×10^{-16}	m^2/s	[86]
Diffusivity of X$^-$ ions in the electrolyte	$\mathbb{D}_{X^-}$	5.1×10^{-15}	m^2/s	[86]
Young modulus of electrolyte	E_{el}	1.0×10^4	GPa	this study
Poisson ratio of electrolyte	ν_{el}	0.3	-	this study
Relative permittivity of electrolyte	ϵ_r	2.25	-	this study

Table 6.2: *Material parameters of the electrolyte used in the numerical simulations. The mechanical parameters are given in term of Young's modulus E and Poisson ratio ν.*
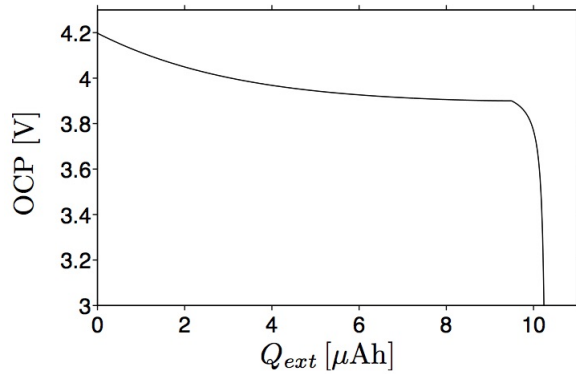
Figure 6.3: *Plot of the equilibrium voltage against the amount of extracted charge Q_{ext} determined from regression extrapolation [86]. The equilibrium voltage of the battery is equal to that of the positive electrode as the metallic Li is taken as reference electrode.*

Boundary conditions - The boundary conditions are imposed on the boundary of both the electrodes, $\partial\Omega_{an}$ and $\partial\Omega_{ca}$, and electrolyte $\partial\Omega_e$. For the sake of clarity the electrodes boundary is split in two parts as follow (see Fig. 6.2)

$$\partial\Omega_{an} = \partial\Omega_{an}^A \cup \partial\Omega_{an}^B, \qquad \text{and} \qquad \partial\Omega_{ca} = \partial\Omega_{ca}^A \cup \partial\Omega_{ca}^B.$$

An uniform charging current is prescribed on the boundary $\partial\Omega_{ca}^A$, while a null reference potential ϕ is imposed on $\partial\Omega_{an}^A$

$$\vec{i}_{ca} \cdot \vec{n}_{ca} = \frac{I(t)}{A} \qquad \text{on } \partial\Omega_{ca}^A, \qquad \phi_{an} = 0 \qquad \text{on } \partial\Omega_{an}^A,$$

where $A = 1\,\text{cm}^2$ is the battery cross-sectional area and $I(t)$ refers to the current flowing through the battery. In order to make initial and boundary conditions compatible with thermodynamic equilibrium at $t = 0$, I is tuned in time as

$$I(t) = \left(1 - \mathrm{e}^{-t}\right) I_{1.0}\, C_r, \tag{6.49}$$

where $I_{1.0} = 1 \times 10^{-1}\,\text{A/m}^2$ is the electric current corresponding to 1 C-rate discharge, while C_r is the discharge rate.

On the other hand the flux of current is zero on the remaining part of the boundary for reasons of symmetry, thus the following boundary conditions arise

$$\vec{i}_{an} \cdot \vec{n}_{an} = 0 \qquad \text{on } \partial\Omega_{an}^B, \qquad \vec{i}_{ca} \cdot \vec{n}_{ca} = 0 \qquad \text{on } \partial\Omega_{ca}^B, \qquad \vec{i}_{el} \cdot \vec{n}_{el} = 0 \qquad \text{on } \partial\Omega_{el},$$

Neither neutral lithium nor ionic species Li^+ and X^- can flow through the external boundary so that

$$\vec{h}_L \cdot \vec{n}_{an} = 0 \qquad \text{on } \partial\Omega_{an}, \qquad \vec{h}_L \cdot \vec{n}_{ca} = 0 \qquad \text{on } \partial\Omega_{ca}, \qquad \vec{h}_{\text{Li}^+} \cdot \vec{n}_{el} = \vec{h}_{\text{X}^-} \cdot \vec{n}_{el} = 0 \qquad \text{on } \partial\Omega_{el}.$$

Battery cell expansion/contraction is prevented by applying the following mechanical boundary conditions

$$u_x = 0 \qquad \text{on } \left\{\partial\Omega_{an}^A \cup \partial\Omega_{ca}^A\right\}, \qquad u_y = 0 \qquad \text{on } \left\{\partial\Omega_{el} \cup \partial\Omega_{an}^B \cup \partial\Omega_{ca}^B\right\}.$$

Initial conditions - Initial conditions at $t = 0$ are imposed for species concentration in both the cathode and electrolyte. Following [86] the distribution of moving species is uniform in each component at initial time

$$c_L\Big|_{t=0} = 1.2 \times 10^4 \text{mol/m}^3 \qquad \text{in } \Omega_{ca},$$

$$c_{\text{Li}^+}\Big|_{t=0} = c_{\text{X}^+}\Big|_{t=0} = 1.1 \times 10^4 \text{mol/m}^3 \qquad \text{in } \Omega_{el}.$$

Balance of momentum and Maxwell equations, together with boundary conditions, provide the necessary and sufficient equations to define $\vec{u}$ and ϕ at $t = 0$.

Numerical implementation - The governing equations have been solved numerically through the Finite Element Method. To this end the cell geometry has been discretized in space with 520 elements along the x coordinate (50 elements for anode, 150 elements or the electrolyte, 320 elements for the cathode), while the time evolution is resolved with a time increment $\Delta t = 0.1\,\text{s}$ throughout the simulations. The numerical method has been implemented in a MATLAB package script purposely written. The detailed procedure of the numerical approximation and resolution is postponed to Appendix 6.A for convenience.

6.6.2 Numerical outcomes and discussion

6.6.2.1 Electro-chemo-mechanical response at high discharge rate

The response of the battery at high C-rates is here investigated for Cr=51.2.

The evolution of lithium concentration - Figure 6.4a plots the evolution in time of Li$^+$ ions in the electrolyte and in the electrodes. The lithium ions intercalate inside the cathode, at Γ_{ca}, while the lithium cannot flow through the boundary $\partial\Omega_{ca}^A$. In this way the lithium content progressively increases in the cathode accumulating at the electrolyte interface. The simulation ends after 49.8 seconds, when lithium in the cathode reaches its saturation limit in correspondence of Γ_{ca} ($c_L^{max} = 2.33 \times 10^4$ mol/m^3). Indeed further current flow, in the prescribed regime, is prevented by saturation of lithium in the cathode. The latter is thus the limiting factor for the performance of this Li-ion battery.

(a)   (b)
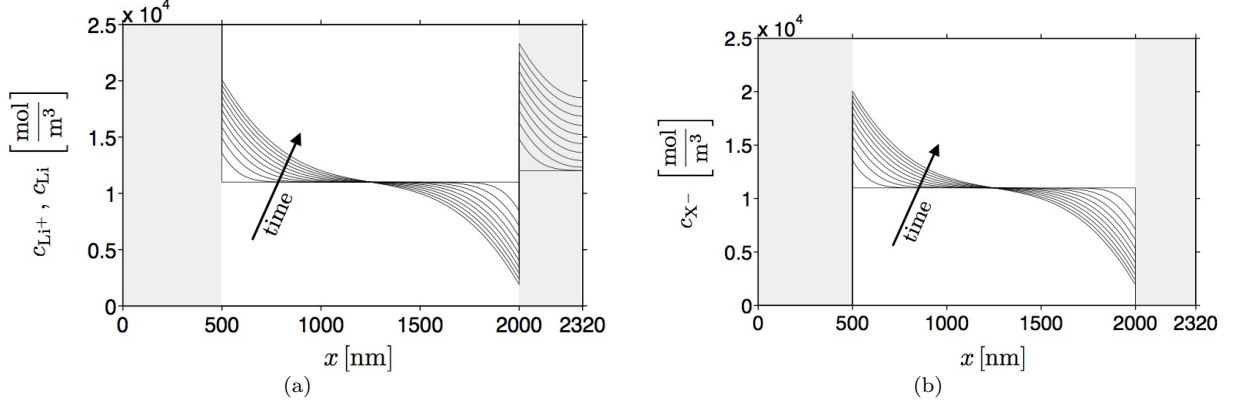
Figure 6.4: *Lithium concentration (a) and concentration of* X$^-$ *ions (b) as function of x coordinate at intervals of 5 s for Cr=51.2. For clarity the domain occupied by the electrodes is highlighted in gray.*

The concentration of Li$^+$ ions in the electrolyte, uniform at initial time, increases rapidly near Γ_{an} triggered by anode oxidation during battery discharge. On the contrary, near the interface Γ_{ca} the content of Li$^+$ ions depletes since lithium intercalates inside the cathode. Note that the overall amount of Li$^+$ ions dissolved in the electrolyte is conserved since lithium is consumed at Γ_{ca} with the same velocity as it is inserted at Γ_{an}, and charge remains balanced.

The distribution of X$^-$ (see Fig. 6.4b), evolves similarly to Li$^+$ even though X$^-$ can be neither inserted nor consumed at the electrolyte boundaries. This behavior relies on equations (6.40) whithout imposing the electroneutrality condition as pursued in [86]. The reader may refer to Chapter 2 for a detailed discussion on the argument.

The battery voltage - The evolution in time and space of the electric potential is shown in Fig. 6.5a. Since metallic Li has taken as the reference electrode, $\phi = 0$ V has been imposed at $x = 0$ throughout the process. At initial time ϕ is uniform in electrodes and electrolyte in view of thermodynamic equilibrium. Moreover the electric potential is continuous at the interface Γ_{an} while presents a a discontinuity on Γ_{ca}. The latter is prescribed at $t = 0$ based on the measured battery OCP at full charge state, i.e. $[\![\phi]\!]_{t=0} = 4.2$ V (see Fig. 6.3).

During battery discharge, the profile of ϕ develops according to Ohm's law in the electrodes. Therefore, the electric potential evolves linearly against the x coordinate, with negative slope. This feature is difficult to appreciate in Fig. 6.4b because the potential change in the electrodes is much smaller than the potential jump at $x = 2000$ nm.

The total battery voltage, which is the difference between the electric potential at the positive and negative electrodes, decreases in time during battery discharge. Assuming that the variation of ϕ in the electrodes is minor, the change in battery voltage is mainly due to the variations of ϕ inside the electrolyte and at the interface Γ_{ca}.
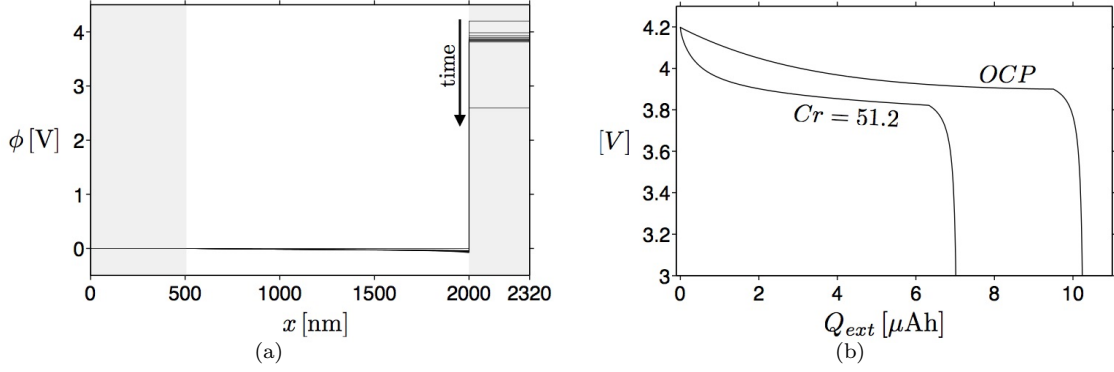
Figure 6.5: (a) Evolution of the electric potential as a function of the x coordinate at intervals of 5 s for Cr=51.2. (b) Comparison between the battery voltage, simulated at discharge rate Cr=51.2, and the battery open circuit potential OCP.

The battery voltage is plotted against the extracted charge Q_{ext} and compared with the equilibrium voltage in Fig. 6.5b. Note that not all the charge available in the battery is extracted when the discharge process is stopped. Moreover the simulated battery voltage is always below than the battery OCP. The difference between the OCP and the simulated potential is called battery overpotential η^{batt}.

The mechanical response - Figure 6.6 depicts the simulated mechanical response in terms of horizontal displacement u_x and stress component σ_{xx}. Since both anode and electrolyte do not account for any chemical strain, the stress evolution is induced only by a volume change in the cathode due to the lithiation process. The anode and electrolyte act passively by contrasting the volume change in the cathode with their mechanical stiffness.
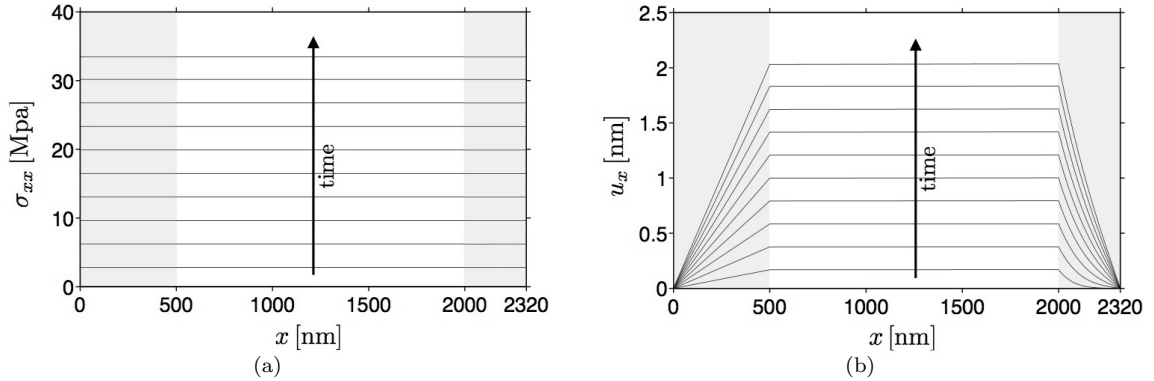
Figure 6.6: Stress component σ_{xx} (a) and horizontal displacement u_x (b) and profiles as function of x coordinate at intervals of 5 s for Cr=51.2. For clarity the domain occupied by the electrodes is highlighted in gray.

As shown in Figure 6.6a, the stress component σ_{xx} is constant inside the battery as a consequence of the one-dimensional nature of the problem at hand. In this conditions the state of stress does not influence the flux of lithium in the cathode (see Eq. 6.38). Since the coefficient of chemical expansion of $LiCoO_2$ is negative (see Chapter 4 for details) σ_{xx} is positive (tensile). The stress magnitude, zero at initial time, increases in time up to a maximum value value, at the end of the discharge process, comprised between 30 and 40 MPa.

The displacement profile develops linearly, with respect to the x coordinate, in both the anode and electrolyte (see Fig. 6.6b). On the other hand u_x does not evolve linearly inside the cathode because of the non linear distribution of neutral lithium. Note that the gradient of u_x in the electrolyte is essentially

138

zero compared to those simulated in the electrodes. This because the electrolyte has been modeled as rigid compared to the electrodes.

6.6.2.2 The influence of the discharge rate

The battery has been simulated upon discharging for various C-rates (3.2, 6.4, 12.8, 25.6, and 51.2) and charging with a 1.6 C-rate. Fig. 6.7 depicts a comparison between experiments and model predictions. Good agreement is obtained for all the curves.
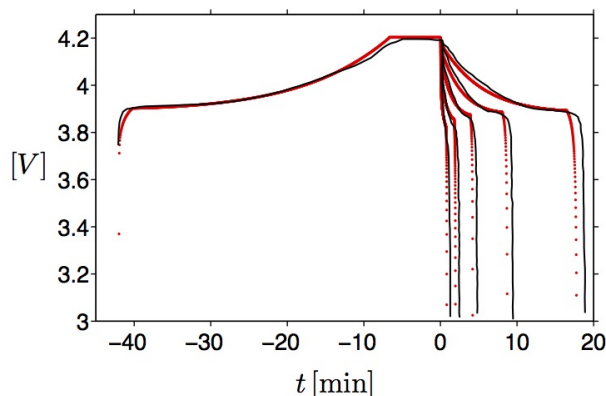
Figure 6.7: *Plot of the measured and simulated battery voltage during discharges with various C-rates, and charge at Cr=1.6. The black lines are the measurements, while the red dots are the model predictions.*

The simulated battery voltage are also plotted as function of the extracted charge in Fig. 6.8a. The rate of battery discharge influences the amount of extracted charge at the end of discharging. The higher the discharge rates, the less the extracted charge. In fact lower discharge rates implies a lower rate of lithium insertion in the cathode, and a more uniform Li distribution in the positive electrode. The total battery overpotential varies with the discharge rate as well. As expected, higher discharge rates cause higher battery overpotentials.

The influence of the discharge rate on the mechanical response is investigated in Figure 6.8b. It gathers the evolution of stress component σ_{xx} in time for the simulated discharge rates. It turns out that the stress rate is higher for higher C-rates. In fact, for the problem at hand, the stress magnitude is merely proportional to the amount of the intercalate ions in the cathode, i.e. proportional to the current flowing through the battery.
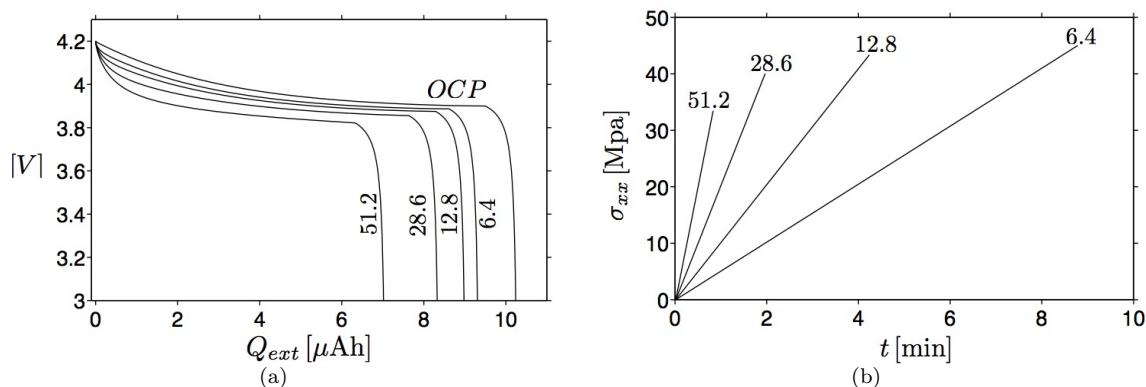
Figure 6.8: *Influence of the discharge rate on the evolution of the battery voltage (a) and stress component σ_{xx} (b).*

6.7   Conclusions

This chapter focuses on the microscopic modeling of a porous electrode compound. Any porous electrode is a heterogeneous media made of different phases. It consists of active (or storage) particles embedded in a porous matrix, and a liquid electrolyte that flows in the electrode porosity.

The fundamental electro-chemo-mechanical processes that characterize the overall battery response take place at the length scale of the electrode compound. Therefore a multiscale modeling is suitable for batteries that implement porous electrodes. A two-scale modeling has been proposed for example in [68] in the spirit of a computational homogenization approach.

Focusing on the microscopic scale, the electrode has been idealized as a three-phase media formed by active particles, conductive particles, and electrolyte. Balance laws and interface conditions among these phases are formulated starting from the fundamental laws of continuum mechanics. Constitutive equations are derived from rigorous thermodynamic principles. The electro-chemical reaction that take place at active particles surfaces in contact with the electrolyte has been modeled using the standard Butler-Volmer equation.

The model proposed has been validated by simulating the response of an all-solid-state battery. To this end, the governing equations has been resolved numerically through the finite element method. Good agreement between the simulated and the measured response of the battery is obtained for different discharge rates. The evolution of the involved electro-chemo-mechanical fields inside any battery components has been discussed as well.

Appendix

6.A   2D Finite Element Implementation

6.A.1   Non-dimensional governing equations and weak form

Electrodes - It is customary to scale the system of governing equations with suitable coefficients in order to deal with a system of non-dimensional equations. In this way Eqs. (6.43) have been rephrased in term adimensional variables[4]

$$ x_i^* = \frac{x_i}{\bar{l}}, \qquad t^* = \frac{t}{\bar{t}}, \qquad c_L^* = \frac{c_L}{\bar{c}}, \qquad \phi^* = \frac{\phi F}{RT}, \qquad u_i^* = \frac{u_i}{\bar{l}}, \qquad \sigma_{ij}^* = \frac{\sigma_{ij}}{\bar{\sigma}}, \tag{6.54} $$

by introducing $\bar{l}$, $\bar{t}$, $\bar{c}$, $\bar{\sigma}$ as reference length, time, concentration, and stress respectively.

Taking advantage of definitions (6.54), the governing equations (6.43) are equivalent to the following non-dimensional ones

$$ \frac{\partial c_L^*}{\partial t^*} + \text{div}^*[\vec{h}_L^*] = 0, \tag{6.55a} $$

$$ \text{div}^*[\vec{i}_a^*] = 0, \tag{6.55b} $$

$$ \text{div}^*[\boldsymbol{\sigma}_a^*] = \vec{0}, \tag{6.55c} $$

where

$$ \text{div}^*[\vec{h}_L^*] = \sum_{i=1}^{2} \frac{h_{Li}^*}{\partial x_i^*}, \qquad \text{div}^*[\boldsymbol{\sigma}_a^*] = \sum_{i=1}^{2} \sum_{j=1}^{2} \frac{\sigma_{ij}^*}{\partial x_j^*} \, \vec{e}_i, \qquad \vec{h}_L^* = \frac{\vec{h}_L \, \bar{t}}{\bar{c} \, \bar{l}}, \qquad \vec{i}_a^* = \frac{\vec{i}_a \, \bar{t}}{\bar{c} \, \bar{l} \, F}. $$

Note that equations (6.55) have the same expression of (6.43) but are formulated in terms of non-dimensional variables. In the same way the non-dimensional constitutive laws keep the same expression of (6.36a) - (6.37) - (6.38) as long as the original variables and parameters are replaced with (6.54) and the following non-dimensional constants

$$ \mathbb{D}_L^* = \frac{\mathbb{D}_L \, \bar{t}}{\bar{l}^2}, \qquad \omega_L^* = \omega_L \, \bar{c}, \qquad (RT)^* = RT \, \frac{\bar{c}}{\bar{\sigma}}, \qquad (c_L^{max})^* = \frac{c_L^{max}}{\bar{c}}, $$

$$ \kappa_a^* = \frac{\kappa_a \, \bar{t} \, RT}{\bar{c} \, \bar{l}^2 \, F^2}, \qquad K_a^* = \frac{K_a}{\bar{\sigma}}, \qquad G_a^* = \frac{G_a}{\bar{\sigma}}. $$

---

[4]The trapping of neutral Li is not considered in this example, accordingly c_T has been removed from governing equations (6.43).

The weak formulation results from multiplying the strong form of governing equations (6.55) by a suitable set of tests functions and performing an integration upon the domain, exploiting the *integration by parts* formula with the aim of reducing the order of differentiation in space.

Even though the first order derivative of h_r can be reduced applying the integration by parts, its constitutive definition contains a second order derivative. To include the effect of stress gradient in equations (6.55a) we follow the approach adopted in Appendix 4.A by introducing a new variable $\Sigma(r,t)$ defined as

$$\Sigma - \mathrm{tr}\left[\boldsymbol{\sigma}\right] = 0\,, \tag{6.57}$$

which will be approximate as an explicit degree of freedom. Eq. (6.57) is then added to the set of governing equations (6.55) for the numerical solution of the problem.

The weak form of each governing equation is derived below. The asterisk is omitted for the sake of readability.

From the mass balance Eq. (6.55a) we obtain

$$\int_{\Omega_a} \hat{c_L} \left\{ \frac{\partial c_L}{\partial t} + \mathrm{div}\left[\vec{h}_L\right] \right\} \, \mathrm{d}A =$$

$$= \int_{\Omega_a} \hat{c_L} \frac{\partial c_L}{\partial t} \, \mathrm{d}A + \int_{\Omega_a} \nabla\left[\hat{c_L}\right] \cdot \left\{ \mathbb{D}_L \nabla\left[c_L\right] - \mathbb{D}_\Sigma \left(c_L\right) \nabla\left[\Sigma\right] \right\} \mathrm{d}A +$$

$$+ \int_{\partial^N \Omega_{an}} \hat{c_L} \left\{ \vec{h}_L \cdot \vec{n}_{an} \right\} \mathrm{d}s + \int_{\partial^N \Omega_{ca}} \hat{c_L} \left\{ \vec{h}_L \cdot \vec{n}_{ca} \right\} \mathrm{d}s +$$

$$+ \int_{\Gamma_{an}} \hat{c_L} \left\{ \vec{h}_L \cdot \vec{n}_{an} \right\} \mathrm{d}s + \int_{\Gamma_{ca}} \hat{c_L} \left\{ \vec{h}_L \cdot \vec{n}_{ca} \right\} \mathrm{d}s = 0\,,$$

where $\mathbb{D}_\Sigma$ stands for

$$\mathbb{D}_\Sigma = \frac{\mathbb{D}_L \, \omega_L}{R\,T} \, c_L \left(\frac{c_L^{max} - c_L}{c_L^{max}} \right)\,.$$

and $\Omega_a = \Omega_{an} \cup \Omega_{ca}$ is the domain occupied by the electrodes.

The weak form of Eq. (6.55b) is simply

$$\int_{\Omega_a} \hat{\phi}_a \, \mathrm{div}\left[\vec{i}_a\right] \, \mathrm{d}A =$$

$$= \int_{\Omega_a} \nabla\left[\hat{\phi}_a\right] \cdot \left\{ \kappa_a \nabla\left[\phi_a\right] \right\} \mathrm{d}A +$$

$$+ \int_{\partial^N \Omega_{an}} \hat{\phi}_{an} \left\{ \vec{i} \cdot \vec{n}_{an} \right\} \mathrm{d}s + \int_{\partial^N \Omega_{ca}} \hat{\phi}_{ca} \left\{ \vec{i} \cdot \vec{n}_{ca} \right\} \mathrm{d}s +$$

$$+ \int_{\Gamma_{an}} \hat{\phi}_{an} \left\{ \vec{i} \cdot \vec{n}_{an} \right\} \mathrm{d}s + \int_{\Gamma_{ca}} \hat{\phi}_{ca} \left\{ \vec{i} \cdot \vec{n}_{ca} \right\} \mathrm{d}s = 0\,.$$

For the equilibrium equation (6.55c) we have

$$\int_{\Omega_a} \vec{\hat{u}}_a \cdot \mathrm{div}\left[\boldsymbol{\sigma}_a\right] \mathrm{d}A =$$

$$= -\int_{\Omega_a} \nabla_S\left[\vec{\hat{u}}_a\right] : \boldsymbol{\sigma}_a(c_L, \Sigma, \vec{u}_a) \, \mathrm{d}A +$$

$$+ \int_{\partial^N \Omega_{an}} \vec{\hat{u}}_{an} \cdot \left(\boldsymbol{\sigma}_{an} \, \vec{n}_{an}\right) \mathrm{d}s + \int_{\partial^N \Omega_{ca}} \vec{\hat{u}}_{ca} \cdot \left(\boldsymbol{\sigma}_{ca} \, \vec{n}_{ca}\right) \mathrm{d}s +$$

$$+ \int_{\Gamma_{an}} \vec{\hat{u}}_{an} \cdot (\boldsymbol{\sigma}_{an} \, \vec{n}_{an}) \, \mathrm{d}s + \int_{\Gamma_{ca}} \vec{\hat{u}}_{ca} \cdot (\boldsymbol{\sigma}_{ca} \, \vec{n}_{ca}) \, \mathrm{d}s = 0 \,,$$

with ∇_S denoting the symmetric gradient operator.

Finally Eq. (6.57) returns

$$\int_{\Omega_a} \hat{\Sigma} \Big\{ \Sigma - \mathrm{tr} \left[\boldsymbol{\sigma}_a(c_L, \Sigma, \vec{u}_a) \right] \Big\} \, \mathrm{d}A = 0 \,.$$

Note that test functions $\hat{c}_L$, $\hat{\phi}_a$, $\vec{\hat{u}}_a$, $\hat{\Sigma}$ are null on the Dirichlet boundary since represent admissible variations of the related degrees of freedom c_L, ϕ_a, $\vec{u}_a$, Σ.

Electrolyte - Following the same procedure used for electrodes, the governing equations (6.40) are first made non-dimensional by introducing the following non dimensional variables

$$x_i^* = \frac{x_i}{\bar{l}} \,, \quad t^* = \frac{t}{\bar{t}} \,, \quad c_{\mathrm{Li}^+}^* = \frac{c_{\mathrm{Li}^+}}{\bar{c}} \,, \quad c_{\mathrm{X}^-}^* = \frac{c_{\mathrm{X}^-}}{\bar{c}} \,, \quad \phi^* = \frac{\phi F}{RT} \,, \quad u_i^* = \frac{u_i}{\bar{l}} \,, \quad \sigma_{ij}^* = \frac{\sigma_{ij}}{\bar{\sigma}} \,, \quad (6.58)$$

with $\bar{l}$, $\bar{t}$, $\bar{c}$, $\bar{\sigma}$ representing reference length, time, concentration, and stress respectively.

Taking advantage of the definitions (6.58), the governing equations (6.40) are equivalent to the following non-dimensional ones

$$\frac{\partial c_{\mathrm{Li}^+}^*}{\partial t^*} + \mathrm{div}^*[\vec{h}_{\mathrm{Li}^+}^*] = 0 \,, \tag{6.59a}$$

$$\frac{\partial c_{\mathrm{X}^-}^*}{\partial t^*} + \mathrm{div}^*[\vec{h}_{\mathrm{X}^-}^*] = 0 \,, \tag{6.59b}$$

$$\mathrm{div}^* \left[\frac{\partial \vec{D}_e^*}{\partial t^*} + \left(\vec{h}_{\mathrm{Li}^+}^* - \vec{h}_{\mathrm{X}^-}^* \right) \right] = 0 \,, \tag{6.59c}$$

$$\mathrm{div}^*[\boldsymbol{\sigma}_e^*] = \vec{0} \,, \tag{6.59d}$$

where

$$\mathrm{div}^*[\vec{h}_\beta^*] = \sum_{i=1}^{2} \frac{h_\beta^*}{\partial x_i^*} \,, \quad \mathrm{div}^*[\boldsymbol{\sigma}_e^*] = \sum_{i=1}^{2} \sum_{j=1}^{2} \frac{\sigma_{ij}^*}{\partial x_j^*} \, \vec{e}_i \,, \quad \vec{h}_\beta^* = \frac{\vec{h}_\beta \, \bar{t}}{\bar{c} \, \bar{l}} \,, \quad \vec{D}_e^* = \frac{\vec{D}_e}{\bar{c} \, \bar{l} \, F} \,, \qquad \beta = \mathrm{Li}^+, \mathrm{X}^- \,.$$

In the same way the non-dimensional constitutive laws mantain the same expression of (6.30a) - (6.30b) - (6.31) as long as the original variables and parameters are replaced with (6.58) and the following non-dimensional constants

$$\mathbb{D}_{\mathrm{Li}^+}^* = \frac{\mathbb{D}_{\mathrm{Li}^+} \, \bar{t}}{\bar{l}^2} \,, \qquad \mathbb{D}_{\mathrm{X}^-}^* = \frac{\mathbb{D}_{\mathrm{X}^-} \, \bar{t}}{\bar{l}^2} \,, \qquad \left(\frac{F}{RT} \right)^* = 1 \,, \qquad \left(c^{max} \right)^* = \frac{c^{max}}{\bar{c}} \,,$$

$$\Ddagger_e^* = \frac{\Ddagger_e \, R \, T}{\bar{c} \, \bar{l}^2 \, F^2} \,, \qquad K_e^* = \frac{K_e}{\bar{\sigma}} \,, \qquad G_e^* = \frac{G_e}{\bar{\sigma}} \,.$$

The weak formulation results from multiplying the strong form of governing equations (6.59) by a suitable set of tests functions and performing an integration upon the domain, exploiting the *integration by parts* formula with the aim of reducing the order of differentiation in space.

143

As done for electrodes the overall weak form of the problem is derived by analyzing each governing equation separately at first. In what follow the asterisk is omitted for the sake of readability.

From the mass balance Eq. (6.59a) we obtain

$$
\int_{\Omega_e} \hat{c}_{\mathrm{Li+}} \left\{ \frac{\partial c_{\mathrm{Li+}}}{\partial t} + \mathrm{div}\left[\vec{h}_{\mathrm{Li+}} \right] \right\} \, \mathrm{d}A =
$$

$$
= \int_{\Omega_e} \hat{c}_{\mathrm{Li+}} \, \frac{\partial c_{\mathrm{Li+}}}{\partial t} \, \mathrm{d}A + \int_{\Omega_e} \nabla\left[\hat{c}_{\mathrm{Li+}}\right] \cdot \left\{ \mathbb{D}_{\mathrm{Li+}} \nabla\left[c_{\mathrm{Li+}}\right] + \mathbb{D}_\phi^+ \left(c_{\mathrm{Li+}} \right) \nabla\left[\phi_e\right] \right\} \mathrm{d}A +
$$

$$
+ \int_{\Gamma_{an}} \hat{c}_{\mathrm{Li+}} \left\{ \vec{h}_{\mathrm{Li+}} \cdot \vec{n}_e \right\} \mathrm{d}s + \int_{\Gamma_{ca}} \hat{c}_{\mathrm{Li+}} \left\{ \vec{h}_{\mathrm{Li+}} \cdot \vec{n}_e \right\} \mathrm{d}s = 0 \,,
$$

where $\mathbb{D}_\phi^+$ stands for

$$
\mathbb{D}_\phi^+ = \frac{\mathbb{D}_{\mathrm{Li+}} \, F}{R\,T} \, c_{\mathrm{Li+}} \left(1 - 2\, \frac{c_{\mathrm{Li+}}}{c^{max}} \right) \,.
$$

Similarly the weak form of (6.59b) reads

$$
\int_{\Omega_e} \hat{c}_{\mathrm{X-}} \left\{ \frac{\partial c_{\mathrm{X-}}}{\partial t} + \mathrm{div}\left[\vec{h}_{\mathrm{X-}} \right] \right\} \, \mathrm{d}A =
$$

$$
= \int_{\Omega_e} \hat{c}_{\mathrm{X-}} \, \frac{\partial c_{\mathrm{X-}}}{\partial t} \, \mathrm{d}A + \int_{\Omega_e} \nabla\left[\hat{c}_{\mathrm{X-}}\right] \cdot \left\{ \mathbb{D}_{\mathrm{X-}} \nabla\left[c_{\mathrm{X-}}\right] - \mathbb{D}_\phi^- \left(c_{\mathrm{X-}} \right) \nabla\left[\phi_e\right] \right\} \mathrm{d}A +
$$

$$
+ \int_{\Gamma_{an}} \hat{c}_{\mathrm{X-}} \left\{ \vec{h}_{\mathrm{X-}} \cdot \vec{n}_e \right\} \mathrm{d}s + \int_{\Gamma_{ca}} \hat{c}_{\mathrm{X-}} \left\{ \vec{h}_{\mathrm{X-}} \cdot \vec{n}_e \right\} \mathrm{d}s = 0 \,,
$$

with

$$
\mathbb{D}_\phi^- = \frac{\mathbb{D}_{\mathrm{X-}} \, F}{R\,T} \, c_{\mathrm{X-}} \left(1 - 2\, \frac{c_{\mathrm{X-}}}{c^{max}} \right) \,.
$$

The weak form of Eq. (6.59c) is simply

$$
\int_{\Omega_e} \hat{\phi}_e \left\{ \mathrm{div}\left[\frac{\partial \vec{D}_e}{\partial t} + \left(\vec{h}_{\mathrm{Li+}} - \vec{h}_{\mathrm{X-}} \right) \right] \right\} \mathrm{d}A =
$$

$$
+ \int_{\Omega_e} \nabla\left[\hat{\phi}_e\right] \cdot \left\{ \oint_e \nabla\left[\frac{\partial \phi_e}{\partial t} \right] \right\} \mathrm{d}A +
$$

$$
+ \int_{\Omega_e} \nabla\left[\hat{\phi}_e\right] \cdot \left\{ \mathbb{D}_{\mathrm{Li+}} \nabla\left[c_{\mathrm{Li+}}\right] + \mathbb{D}_\phi^+ \left(c_{\mathrm{Li+}} \right) \nabla\left[\phi_e\right] - \mathbb{D}_{\mathrm{X-}} \nabla\left[c_{\mathrm{X-}}\right] + \mathbb{D}_\phi^- \left(c_{\mathrm{X-}} \right) \nabla\left[\phi_e\right] \right\} \mathrm{d}A +
$$

$$
+ \int_{\Gamma_{an}} \hat{\phi}_e \left\{ \mathrm{curl}\left[\vec{H}_e \right] \cdot \vec{n}_e \right\} \mathrm{d}s + \int_{\Gamma_{ca}} \hat{\phi}_e \left\{ \mathrm{curl}\left[\vec{H}_e \right] \cdot \vec{n}_e \right\} \mathrm{d}s = 0 \,.
$$

Finally equation (6.59d) returns

$$
\int_{\Omega_e} \vec{\hat{u}}_a \cdot \mathrm{div}\left[\boldsymbol{\sigma}_e \right] \mathrm{d}A =
$$

$$
= - \int_{\Omega_e} \nabla_S\left[\vec{\hat{u}}_e \right] : \boldsymbol{\sigma}_e(\vec{u}_e) \, \mathrm{d}A + \int_{\Gamma_{an}} \vec{\hat{u}}_e \cdot \left(\boldsymbol{\sigma}_e \, \vec{n}_e \right) \mathrm{d}s + \int_{\Gamma_{ca}} \vec{\hat{u}}_e \cdot \left(\boldsymbol{\sigma}_e \, \vec{n}_e \right) \mathrm{d}s = 0 \,,
$$

with ∇_S denoting the symmetric gradient operator.

Test functions $\hat{c}_{\mathrm{Li}^+}, \hat{c}_{\mathrm{X}^-}, \hat{\phi}_e, \vec{\hat{u}}_e$, are null on the Dirichlet boundary since represent admissible variations of the related degrees of freedom $c_{\mathrm{Li}^+}, c_{\mathrm{X}^-}, \phi_e, \vec{u}_e$.

Interface conditions - The interface conditions (6.42) - (6.44) apply for integrals defined on interfaces Γ_{ca} and Γ_{an} for both electrodes and electrolyte. It is convenient to gather together all the contributions as follow

$$\int_{\Gamma_{an}} \hat{\Delta} c_{\mathrm{Li}} \, h_{BV} \, (\Delta\phi) \, \mathrm{d}s + \int_{\Gamma_{an}} \hat{\Delta}\phi \, i_{BV} \, (\Delta\phi) \, \mathrm{d}s + \int_{\Gamma_{an}} \hat{\Delta}\vec{u} \cdot \vec{T}_\Gamma \, (\Delta\vec{u}) \, \mathrm{d}s \,, \tag{6.61}$$

and

$$\int_{\Gamma_{ca}} \hat{\Delta} c_{\mathrm{Li}} \, h_{BV} \, (\Delta\phi) \, \mathrm{d}s + \int_{\Gamma_{ca}} \hat{\Delta}\phi \, i_{BV} \, (\Delta\phi) \, \mathrm{d}s + \int_{\Gamma_{ca}} \hat{\Delta}\vec{u} \cdot \vec{T}_\Gamma \, (\Delta\vec{u}) \, \mathrm{d}s \,. \tag{6.62}$$

Symbol Δ defines the jump of a certain variable at the interfaces (a stands for an or ca depending on the interface Γ where integrals are computed)

$$\Delta c_{\mathrm{Li}} = c_L - c_{\mathrm{Li}^+} \,, \qquad \Delta\phi = \phi_a - \phi_e \,, \qquad \Delta\vec{u} = \vec{u}_a - \vec{u}_e \,, \tag{6.63}$$

while $\vec{T}_\Gamma$ is the traction normal to the interface

$$\vec{T}_\Gamma = \boldsymbol{\sigma}_a \, \vec{n}_a = -\boldsymbol{\sigma}_e \, \vec{n}_e \,. \tag{6.64}$$

The interface conditions (6.42d) - (6.44c) are imposed by means of a penalty method. Accordingly the traction $\vec{T}_\Gamma$ is assumed function of the displacement jump at interface through the following linear formula

$$\vec{T}_\Gamma = K_\Gamma \, \Delta\vec{u} \,, \tag{6.65}$$

with K_Γ denoting the penalty parameter.

Overall weak form - In conclusion, the overall weak form of battery governing equations can be written in the time interval $[0, t_f]$ as

$$\text{Find } y(\vec{x}, t) \in \mathcal{V}^{[0, t_f]} \text{ such that} \qquad \frac{\partial}{\partial t} \, b\left(\hat{y}(\vec{x}), c_L(\vec{x}, t)\right) + a\left(\hat{y}(\vec{x}), y(\vec{x}, t)\right) = f\left(\hat{y}(\vec{x})\right) \qquad \forall \hat{y}(\vec{x}) \in \mathcal{V} \tag{6.66}$$

where

$$b\left(\hat{y}(\vec{x}), c_L(\vec{x}, t)\right) = \int_{\Omega_a} \hat{c}_L \, c_L \, \mathrm{d}A + \int_{\Omega_e} \hat{c}_{\mathrm{Li}^+} \, c_{\mathrm{Li}^+} \, \mathrm{d}A + \int_{\Omega_e} \hat{c}_{\mathrm{X}^-} \, c_{\mathrm{X}^-} \, \mathrm{d}A + \int_{\Omega_e} \natural_e \, \nabla[\hat{\phi}_e] \cdot \nabla[\phi_e] \, \mathrm{d}A \,,$$

$$\begin{aligned}
a\left(\hat{y}(\vec{x}), y(\vec{x}, t)\right) = & \int_{\Omega_a} \nabla[\hat{c}_L] \cdot \left\{ \mathbb{D}_L \, \nabla[c_L] - \mathbb{D}_\Sigma \, (c_L) \, \nabla[\Sigma] \right\} \mathrm{d}A + \int_{\Omega_a} \kappa_a \, \nabla[\hat{\phi}_a] \cdot \nabla[\phi_a] \, \mathrm{d}A + \\
& + \int_{\Omega_a} \nabla_S[\vec{\hat{u}}_a] : \boldsymbol{\sigma}_a(c_L, \Sigma, \vec{u}_a) \, \mathrm{d}A + \int_{\Omega_a} \hat{\Sigma} \left\{ \Sigma - \mathrm{tr}\left[\boldsymbol{\sigma}_a(c_L, \Sigma, \vec{u}_a)\right] \right\} \mathrm{d}A + \\
& + \int_{\Omega_e} \nabla[\hat{c}_{\mathrm{Li}^+}] \cdot \left\{ \mathbb{D}_{\mathrm{Li}^+} \, \nabla[c_{\mathrm{Li}^+}] + \mathbb{D}_\phi^+ \, (c_{\mathrm{Li}^+}) \, \nabla[\phi_e] \right\} \mathrm{d}A + \\
& + \int_{\Omega_e} \nabla[\hat{c}_{\mathrm{X}^-}] \cdot \left\{ \mathbb{D}_{\mathrm{X}^-} \, \nabla[c_{\mathrm{X}^-}] - \mathbb{D}_\phi^- \, (c_{\mathrm{X}^-}) \, \nabla[\phi_e] \right\} \mathrm{d}A + \\
& + \int_{\Omega_e} \nabla[\hat{\phi}_e] \cdot \left\{ \mathbb{D}_{\mathrm{Li}^+} \nabla[c_{\mathrm{Li}^+}] + \mathbb{D}_\phi^+ \, (c_{\mathrm{Li}^+}) \, \nabla[\phi_e] - \mathbb{D}_{\mathrm{X}^-} \nabla[c_{\mathrm{X}^-}] + \mathbb{D}_\phi^- \, (c_{\mathrm{X}^-}) \, \nabla[\phi_e] \right\} \mathrm{d}A +
\end{aligned}$$

$$+ \int_{\Omega_e} \nabla_S \left[\, \vec{\hat{u}}_e \, \right] : \boldsymbol{\sigma}_e(\vec{u}_e) \, \mathrm{d}A \, +$$

$$+ \int_{\Gamma_{an}} \hat{\Delta} c_{\mathrm{Li}} \, h_{BV} \left(\Delta \phi \right) \, \mathrm{d}s + \int_{\Gamma_{an}} \hat{\Delta} \phi \, i_{BV} \left(\Delta \phi \right) \, \mathrm{d}s - \int_{\Gamma_{an}} \hat{\Delta} \vec{u} \cdot \vec{T}_\Gamma \left(\Delta \vec{u} \right) \, \mathrm{d}s \, +$$

$$+ \int_{\Gamma_{ca}} \hat{\Delta} c_{\mathrm{Li}} \, h_{BV} \left(\Delta \phi \right) \, \mathrm{d}s + \int_{\Gamma_{ca}} \hat{\Delta} \phi \, i_{BV} \left(\Delta \phi \right) \, \mathrm{d}s - \int_{\Gamma_{ca}} \hat{\Delta} \vec{u} \cdot \vec{T}_\Gamma \left(\Delta \vec{u} \right) \, \mathrm{d}s \, ,$$

$$f \left(\hat{y}(\vec{x}) \right) = - \int_{\partial^N \Omega_{an}} \hat{c}_L \left\{ \vec{h}_L \cdot \vec{n}_{an} \right\} \mathrm{d}s - \int_{\partial^N \Omega_{ca}} \hat{c}_L \left\{ \vec{h}_L \cdot \vec{n}_{ca} \right\} \mathrm{d}s \, +$$

$$- \int_{\partial^N \Omega_{an}} \hat{\phi}_{an} \left\{ \vec{i} \cdot \vec{n}_{an} \right\} \mathrm{d}s - \int_{\partial^N \Omega_{ca}} \hat{\phi}_{ca} \left\{ \vec{i} \cdot \vec{n}_{ca} \right\} \mathrm{d}s \, +$$

$$+ \int_{\partial^N \Omega_{an}} \vec{\hat{u}}_{an} \cdot \left(\boldsymbol{\sigma}_{an} \, \vec{n}_{an} \right) \mathrm{d}s + \int_{\partial^N \Omega_{ca}} \vec{\hat{u}}_{ca} \cdot \left(\boldsymbol{\sigma}_{ca} \, \vec{n}_{ca} \right) \mathrm{d}s \, .$$

with $y = \{ c_L, \phi_a, \vec{u}_a, \Sigma, c_{\mathrm{Li}^+}, c_{\mathrm{X}^-}, \phi_e, \vec{u}_e \}$ collecting the time-dependent unknown fields. Column $\hat{y}$ collects the steady state test functions that correspond to the unknown fields in y, i.e. $\hat{y} = \{ \hat{c}_L, \hat{\phi}_a, \vec{\hat{u}}_a, \hat{\Sigma}, \hat{c}_{\mathrm{Li}^+}, \hat{c}_{\mathrm{X}^-}, \hat{\phi}_e, \vec{\hat{u}}_e \}$. The identification of the functional space $\mathcal{V}$ falls beyond the scope of this work.

6.A.2 Numerical discretization

Following the standard finite element method, any domain Ω_β is divided into N_β subdomains Ω_β^e, each one with nn nodes, such that

$$\Omega_a = \bigcup_{e=1}^{N_a} \Omega_a^e \, , \qquad \Omega_e = \bigcup_{e=1}^{N_e} \Omega_e^e \, .$$

Similarly the interfaces Γ_{an} and Γ_{ca} are divided into N_Γ zero-thickness finite elements as customary for cohesive fracture mechanics (see [327] for the details)

$$\Gamma_{an} \cup \Gamma_{ca} = \bigcup_{e=1}^{N_\Gamma} \Gamma^e \, .$$

Inside any subdomain any degree of freedom (and its variation) is approximated through the following interpolation

$$^h c_L \left(\vec{x}, t \right) = [N_L(\vec{x})] \, [c_L(t)] \, , \qquad ^h \hat{c}_L \left(\vec{x}, t \right) = [N_L(\vec{x})] \, [\hat{c}_L(t)] \, , \tag{6.67a}$$

$$^h \phi_\beta \left(\vec{x}, t \right) = [N_\phi(\vec{x})] \, [\phi_\beta(t)] \, , \qquad ^h \hat{\phi}_\beta \left(\vec{x}, t \right) = [N_\phi(\vec{x})] \, [\hat{\phi}_\beta(t)] \, , \tag{6.67b}$$

$$^h \vec{u}_\beta \left(\vec{x}, t \right) = [N_u(\vec{x})] \, [u_\beta(t)] \, , \qquad ^h \vec{\hat{u}}_\beta \left(\vec{x}, t \right) = [N_u(\vec{x})] \, [\hat{u}_\beta(t)] \, , \tag{6.67c}$$

$$^h \Sigma \left(\vec{x}, t \right) = [N_\Sigma(\vec{x})] \, [\Sigma(t)] \, , \qquad ^h \hat{\Sigma} \left(\vec{x}, t \right) = [N_\Sigma(\vec{x})] \, [\hat{\Sigma}(t)] \, , \tag{6.67d}$$

$$^h c_{\mathrm{Li}^+} \left(\vec{x}, t \right) = [N_{\mathrm{Li}}(\vec{x})] \, [c_{\mathrm{Li}^+}(t)] \, , \qquad ^h \hat{c}_{\mathrm{Li}^+} \left(\vec{x}, t \right) = [N_{\mathrm{Li}}(\vec{x})] \, [\hat{c}_{\mathrm{Li}^+}(t)] \, , \tag{6.67e}$$

$$^h c_{\mathrm{X}^-} \left(\vec{x}, t \right) = [N_{\mathrm{X}}(\vec{x})] \, [c_{\mathrm{X}^-}(t)] \, , \qquad ^h \hat{c}_{\mathrm{X}^-} \left(\vec{x}, t \right) = [N_{\mathrm{X}}(\vec{x})] \, [\hat{c}_{\mathrm{X}^-}(t)] \, , \tag{6.67f}$$

where tables $[N(\vec{x})]$ collect the time-independent local shape functions $N^i(\vec{x})$ as

146

$$[N_L(\vec{x})] = [N_\phi(\vec{x})] = [N_\Sigma(\vec{x})] = [N_{\mathrm{Li}}(\vec{x})] = [N_{\mathrm{X}}(\vec{x})] = \left\{ N^1 \,,\, N^2 \,,\, ... \,,\, N^{nn} \right\},$$

$$[N_u(\vec{x})] = \begin{bmatrix} N^1 & 0 & N^2 & 0 & ... & N^{nn} & 0 \\ 0 & N^1 & 0 & N^2 & ... & 0 & N^{nn} \end{bmatrix},$$

and $[c_L(t)]$, $[\phi_\beta(t)]$, $[u_\beta(t)]$, $[\Sigma(t)]$, $[c_{\mathrm{Li}^+}(t)]$, $[c_{\mathrm{X}^-}(t)]$ collecting the nodal values of variables c_L, ϕ_β, $\vec{u}_\beta$, Σ, c_{Li^+}, c_{X^-} at time t as follow

$$[c_L(t)] = \left\{ c_L^1 \,,\, c_L^2 \,,\, ... \,,\, c_L^{nn} \right\}^T, \qquad [\hat{c}_L(t)] = \left\{ \hat{c}_L^1 \,,\, \hat{c}_L^2 \,,\, ... \,,\, \hat{c}_L^{nn} \right\}^T,$$

$$[\phi_\beta(t)] = \left\{ \phi_\beta^1 \,,\, \phi_\beta^2 \,,\, ... \,,\, \phi_\beta^{nn} \right\}^T, \qquad [\hat{\phi}_\beta(t)] = \left\{ \hat{\phi}_\beta^1 \,,\, \hat{\phi}_\beta^2 \,,\, ... \,,\, \hat{\phi}_\beta^{nn} \right\}^T,$$

$$[u_\beta(t)] = \left\{ u_x^1 \,,\, u_y^1 \,,\, u_x^2 \,,\, u_y^2 \,,\, ... \,,\, u_x^{nn} \,,\, u_y^{nn} \right\}^T, \qquad [\hat{u}_\beta(t)] = \left\{ \hat{u}_x^1 \,,\, \hat{u}_y^1 \,,\, \hat{u}_x^2 \,,\, \hat{u}_y^2 \,,\, ... \,,\, \hat{u}_x^{nn} \,,\, \hat{u}_y^{nn} \right\}^T,$$

$$[\Sigma(t)] = \left\{ \Sigma^1 \,,\, \Sigma^2 \,,\, ... \,,\, \Sigma^{nn} \right\}^T, \qquad [\hat{\Sigma}(t)] = \left\{ \hat{\Sigma}^1 \,,\, \hat{\Sigma}^2 \,,\, ... \,,\, \hat{\Sigma}^{nn} \right\}^T,$$

$$[c_{\mathrm{Li}^+}(t)] = \left\{ c_{\mathrm{Li}^+}^1 \,,\, c_{\mathrm{Li}^+}^2 \,,\, ... \,,\, c_{\mathrm{Li}^+}^{nn} \right\}^T, \qquad [\hat{c}_{\mathrm{Li}^+}(t)] = \left\{ \hat{c}_{\mathrm{Li}^+}^1 \,,\, \hat{c}_{\mathrm{Li}^+}^2 \,,\, ... \,,\, \hat{c}_{\mathrm{Li}^+}^{nn} \right\}^T,$$

$$[c_{\mathrm{X}^-}(t)] = \left\{ c_{\mathrm{X}^-}^1 \,,\, c_{\mathrm{X}^-}^2 \,,\, ... \,,\, c_{\mathrm{X}^-}^{nn} \right\}^T, \qquad [\hat{c}_{\mathrm{X}^-}(t)] = \left\{ \hat{c}_{\mathrm{X}^-}^1 \,,\, \hat{c}_{\mathrm{X}^-}^2 \,,\, ... \,,\, \hat{c}_{\mathrm{X}^-}^{nn} \right\}^T,$$

Moreover from Eq. (6.67) it results

$$\nabla\,[\,c_L\,] = [B_L(\vec{x})]\,[c_L(t)]\,, \qquad \nabla\,[\,\phi_\beta\,] = [B_\phi(\vec{x})]\,[\phi_\beta(t)]\,, \qquad \nabla_S[\hat{\vec{u}}]\,:\,\boldsymbol{\sigma} = [\hat{u}(t)]^T\,[B_u(\vec{x})]^T\,[\sigma(\vec{x},t)]\,,$$

$$\nabla\,[\,\Sigma\,] = [B_\Sigma(\vec{x})]\,[\Sigma(t)]\,, \qquad \nabla\,[\,c_{\mathrm{Li}^+}\,] = [B_{\mathrm{Li}}(\vec{x})]\,[c_{\mathrm{Li}^+}(t)]\,, \qquad \nabla\,[\,c_{\mathrm{X}^-}\,] = [B_{\mathrm{X}}(\vec{x})]\,[c_{\mathrm{X}^-}(t)]\,,$$

with

$$[B_L(\vec{x})] = [B_\phi(\vec{x})] = [B_\Sigma(\vec{x})] = [B_{\mathrm{Li}}(\vec{x})] = [B_{\mathrm{X}}(\vec{x})] = \begin{bmatrix} N^{1,1} & N^{2,1} & ... & N^{nn,1} \\ N^{1,2} & N^{2,2} & ... & N^{nn,2} \end{bmatrix},$$

$$[B_u(\vec{x})] = \begin{bmatrix} N^{1,1} & 0 & N^{2,1} & 0 & ... & N^{nn,1} & 0 \\ 0 & N^{1,2} & 0 & N^{2,2} & ... & 0 & N^{nn,2} \\ N^{1,2} & N^{1,1} & N^{2,2} & N^{2,1} & ... & N^{nn,2} & N^{nn,1} \end{bmatrix},$$

and

$$[\sigma(\vec{x},t)] = \left\{ \sigma_{11} \,,\, \sigma_{22} \,,\, \sigma_{12} \right\}^T$$

with

$$N^{i,j} = \frac{\partial N^i}{\partial x_j} \quad i = 1,2 \quad j = 1,2$$

The discretization in time is performed applying the implicit backward Euler method. Accordingly we divide time interval $[0,\, t_f]$ into N_t temporal steps $\Delta t = t_f / N_t$. We define for convenience

$$y(r)|_n = y(\vec{x}, n\Delta t)\,, \qquad \Delta y(\vec{x})|_{n+1} = y(\vec{x})|_{n+1} - y(\vec{x})|_n \qquad n = 1, 2, ..., N_t$$

The discretized weak form is finally obtained from (6.66) by applying the finite element interpolation (6.67) and the backward Euler scheme. It results in terms of approximate degrees of freedom $^h y = \{\, ^h c_L,\, ^h \phi_a,\, ^h \vec{u}_a,\, ^h \Sigma,\, ^h c_{\mathrm{Li}^+},\, ^h c_{\mathrm{X}^-},\, ^h \phi_e,\, ^h \vec{u}_e \}$ and variations $^h \hat{y} = \{\, ^h \hat{c}_L,\, ^h \hat{\phi}_a,\, ^h \hat{\vec{u}}_a,\, ^h \hat{\Sigma},\, ^h \hat{c}_{\mathrm{Li}^+},\, ^h \hat{c}_{\mathrm{X}^-},\, ^h \hat{\phi}_e,\, ^h \hat{\vec{u}}_e \}$ as follow

Find $\left. ^h y(\vec{x}) \right|_{n+1} \in\, ^h \mathcal{V}$ such that

$$
\frac{1}{\Delta t}\, ^h b \left(^h \hat{y}(\vec{x}),\, \left. \Delta^h c_L(\vec{x}) \right|_{n+1} \right) + \, ^h a \left(^h \hat{y}(\vec{x}),\, \left. ^h y(\vec{x}) \right|_{n+1} \right) = f\left(^h \hat{y}(\vec{x}) \right) \qquad \forall\, ^h \hat{y}(\vec{x}) \in\, ^h \mathcal{V}, \quad n = 1, 2, \dots, N_t
$$
(6.71)

where

$$
\begin{aligned}
^h b \left(^h \hat{y}(\vec{x}),\, \left. \Delta^h z(\vec{x}) \right|_{n+1} \right) = &\, \mathop{\mathbf{A}}_{e=1}^{N_a} \left\{ [\hat{c}_L]^T \int_{\Omega_a^e} [N_L]^T [N_L] \left([c_L]_{n+1} - [c_L]_n \right) \mathrm{d}A + \right\} + \\
&+ \mathop{\mathbf{A}}_{e=1}^{N_e} \left\{ [\hat{c}_{\mathrm{Li}^+}]^T \int_{\Omega_e^e} [N_{\mathrm{Li}}]^T [N_{\mathrm{Li}}] \left([c_{\mathrm{Li}^+}]_{n+1} - [c_{\mathrm{Li}^+}]_n \right) \mathrm{d}A + \right. \\
&\quad + [\hat{c}_{\mathrm{X}^-}]^T \int_{\Omega_e^e} [N_{\mathrm{X}}]^T [N_{\mathrm{X}}] \left([c_{\mathrm{X}^-}]_{n+1} - [c_{\mathrm{X}^-}]_n \right) \mathrm{d}A + \\
&\quad \left. + [\hat{\phi}_e] \int_{\Omega_e^e} [B_\phi]^T [B_\phi] \left([\phi_e]_{n+1} - [\phi_e]_n \right) \mathrm{d}A \right\},
\end{aligned}
$$

$$
\begin{aligned}
^h a \left(^h \hat{y}(\vec{x}),\, \left. ^h y(\vec{x}) \right|_{n+1} \right) = &\, \mathop{\mathbf{A}}_{e=1}^{N_a} \left\{ [\hat{c}_L]^T \int_{\Omega_a^e} [B_L]^T [B_L] [c_L]_{n+1}\, \mathbb{D}_L\, \mathrm{d}A + \right. \\
&\quad - [\hat{c}_L]^T \int_{\Omega_a^e} [B_L]^T [B_\Sigma] [\Sigma]_{n+1}\, \left. \mathbb{D}_\Sigma(c_L) \right|_{n+1} \mathrm{d}A + \\
&\quad + [\hat{\phi}_a]^T \int_{\Omega_a^e} [B_\phi]^T [B_\phi] [\phi_a]_{n+1}\, \kappa_a\, \mathrm{d}A + \\
&\quad + [\hat{u}_e]^T \int_{\Omega_a^e} [B_u]^T [\sigma(c_L, \Sigma, \vec{u}_e)]_{n+1}\, \mathrm{d}A + \\
&\quad \left. + [\hat{\Sigma}]^T \int_{\Omega_a^e} [N_\Sigma]^T \left([N_\Sigma][\Sigma]_{n+1} - \mathrm{tr}\left[\boldsymbol{\sigma}(c_L, \Sigma, \vec{u}_a) \right]\big|_{n+1} \right) \mathrm{d}A \right\} + \\
&+ \mathop{\mathbf{A}}_{e=1}^{N_e} \left\{ [\hat{c}_{\mathrm{Li}^+}]^T \int_{\Omega_e^e} [B_{\mathrm{Li}}]^T [B_{\mathrm{Li}}] [c_{\mathrm{Li}^+}]_{n+1}\, \mathbb{D}_{\mathrm{Li}^+}\, \mathrm{d}A + \right. \\
&\quad + [\hat{c}_{\mathrm{Li}^+}]^T \int_{\Omega_e^e} [B_{\mathrm{Li}}]^T [B_\phi] [\phi_e]_{n+1}\, \mathbb{D}_\phi^+ (c_{\mathrm{Li}^+})\big|_{n+1}\, \mathrm{d}A + \\
&\quad + [\hat{c}_{\mathrm{X}^-}]^T \int_{\Omega_e^e} [B_{\mathrm{X}}]^T [B_{\mathrm{X}}] [c_{\mathrm{X}^-}]_{n+1}\, \mathbb{D}_{\mathrm{X}^-}\, \mathrm{d}A + \\
&\quad - [\hat{c}_{\mathrm{X}^-}]^T \int_{\Omega_e^e} [B_{\mathrm{X}}]^T [B_\phi] [\phi_e]_{n+1}\, \mathbb{D}_\phi^- (c_{\mathrm{X}^-})\big|_{n+1}\, \mathrm{d}A + \\
&\quad + [\hat{\phi}_e]^T \int_{\Omega_e^e} [B_\phi]^T [B_{\mathrm{Li}}] [c_{\mathrm{Li}^+}]_{n+1}\, \mathbb{D}_{\mathrm{Li}^+}\, \mathrm{d}A + \\
&\quad + [\hat{\phi}_e]^T \int_{\Omega_e^e} [B_\phi]^T [B_\phi] [\phi_e]_{n+1}\, \mathbb{D}_\phi^+ (c_{\mathrm{Li}^+})\big|_{n+1}\, \mathrm{d}A +
\end{aligned}
$$

$$
\begin{aligned}
&- [\hat{\phi}_e]^T \int_{\Omega_e^e} [B_\phi]^T [B_\mathrm{X}] [c_{\mathrm{X}-}]_{n+1}\, \mathbb{D}_{\mathrm{X}-}\, \mathrm{d}A + \\
&+ [\hat{\phi}_e]^T \int_{\Omega_e^e} [B_\phi]^T [B_\phi] [\phi_e]_{n+1}\, \mathbb{D}_\phi^- \left. (c_{\mathrm{X}-}) \right|_{n+1}\, \mathrm{d}A + \\
&+ [\hat{u}]^T \int_{\Omega_e^e} [B_u]^T [\sigma(u)]_{n+1}\, \mathrm{d}A \Bigg\} + \\
&+ \mathop{\mathbf{A}}_{e=1}^{N_\Gamma} \Bigg\{ [\hat{c}_L]^T \int_{\Gamma^e} [N_L]^T\, h_{BV} \left. (\Delta\phi) \right|_{n+1}\, \mathrm{d}s - [\hat{c}_{\mathrm{Li}+}]^T \int_{\Gamma^e} [N_{\mathrm{Li}}]^T\, h_{BV} \left. (\Delta\phi) \right|_{n+1}\, \mathrm{d}s + \\
&+ [\phi_a]^T \int_{\Gamma^e} [N_\phi]^T\, i_{BV} \left. (\Delta\phi) \right|_{n+1}\, \mathrm{d}s - [\phi_e]^T \int_{\Gamma^e} [N_\phi]^T\, i_{BV} \left. (\Delta\phi) \right|_{n+1}\, \mathrm{d}s + \\
&- [N_u^s]^T \int_{\Gamma^e} [N_u]^T \cdot \vec{T}_\Gamma \left. (\Delta u) \right|_{n+1}\, \mathrm{d}s + [N_u^s]^T \int_{\Gamma^e} [N_u]^T \cdot \vec{T}_\Gamma \left. (\Delta u) \right|_{n+1}\, \mathrm{d}s \Bigg\},
\end{aligned}
$$

$$
\begin{aligned}
f\left({}^h \hat{y}(\vec{x}) \right) = \mathop{\mathbf{A}}_{e=1}^{N_a} \Bigg\{ &- [c_L]^T \int_{\partial^N \Omega_{an}^e} [N_L]^T \left(\vec{h}_L \cdot \vec{n}_{an} \right) \Big|_{n+1}\, \mathrm{d}s - [c_L]^T \int_{\partial^N \Omega_{ca}^e} [N_L]^T \left(\vec{h}_L \cdot \vec{n}_{ca} \right) \Big|_{n+1}\, \mathrm{d}s + \\
&- [\phi_a]^T \int_{\partial^N \Omega_{an}^e} [N_\phi]^T \left(\vec{i} \cdot \vec{n}_{an} \right) \Big|_{n+1}\, \mathrm{d}s - [\phi_a]^T \int_{\partial^N \Omega_{ca}^e} [N_\phi]^T \left(\vec{i} \cdot \vec{n}_{ca} \right) \Big|_{n+1}\, \mathrm{d}s + \\
&+ [\hat{u}_a]^T \int_{\partial^N \Omega_{a}^e n} [N_u]^T \cdot (\boldsymbol{\sigma}_{ca}\, \vec{n}_{ca}) |_{n+1}\, \mathrm{d}s + [\hat{u}_a]^T \int_{\partial^N \Omega_c^e a} [N_u]^T \cdot (\boldsymbol{\sigma}_{ca}\, \vec{n}_{ca}) |_{n+1}\, \mathrm{d}s \Bigg\}.
\end{aligned}
$$

Note that the integrals in (6.71) are now computed summating the contribution of any subdomain Ω^e and Γ^e by means of the assembly operator $\mathbf{A}$. Eq. (6.71) is equivalent to a system of non-linear equations for the unknowns ${}^h y$ which is solved with a standard Newton-Raphson algorithm. Accordingly the solution is computed iteratively in terms of solution increments $\delta y^{(k+1)} = \{\, \delta c_L^{(k+1)},\, \delta\phi_a^{(k+1)},\, \delta\vec{u}_a^{(k+1)},\, \delta\Sigma^{(k)},\, \delta c_{\mathrm{Li}+}^{(k+1)},\, \delta c_{\mathrm{X}-}^{(k+1)},\, \delta\phi_e^{(k+1)},\, \delta\vec{u}_e^{(k+1)} \}$ at iteration $k+1$ for any time step (the superscript ^{h} has been removed for clarity). Without going through all details for convenience (see [323] for instance), the overall problem reduces to the following linear system

$$
\left([K_a]_{n+1}^{(k)} + [K_e]_{n+1}^{(k)} + [K_\Gamma]_{n+1}^{(k)} \right) [\delta y_{n+1}^{(k+1)}] = [R_{n+1}^{(k)}]
$$

where

$$
[K_a]_{n+1}^{(k)} = \begin{bmatrix} [K_a^{L\,L}] & [K_a^{L\,\Sigma}] & [0] & [0] \\ [K_a^{\Sigma\,L}] & [K^{\Sigma\,\Sigma}] & [0] & [K_a^{\Sigma\,u}] \\ [0] & [0] & [K_a^{\phi\,\phi}] & [0] \\ [K_a^{u\,L}] & [K^{u\,\Sigma}] & [0] & [K_a^{u\,u}] \end{bmatrix}, \quad
[K_e]_{n+1}^{(k)} = \begin{bmatrix} [K_e^{\mathrm{Li\,Li}}] & [0] & [K_e^{\mathrm{Li}\,\phi}] & [0] \\ [0] & [K_e^{\mathrm{X\,X}}] & [K_e^{\mathrm{X}\,\phi}] & [0] \\ [K_e^{\phi\,\mathrm{Li}}] & [K_e^{\phi\,\mathrm{X}}] & [K_e^{\phi\,\phi}] & [0] \\ [0] & [0] & [0] & [K_e^{u\,u}] \end{bmatrix},
$$

$$
[K_\Gamma]_{n+1}^{(k)} = \begin{bmatrix} [0] & [0] & [K_\Gamma^{\mathrm{Li}\,\phi}] & [0] \\ [0] & [0] & [0] & [0] \\ [0] & [0] & [K_\Gamma^{\phi\,\phi}] & [0] \\ [0] & [0] & [0] & [K_\Gamma^{u\,u}] \end{bmatrix}, \quad
[\delta y_{n+1}^{(k+1)}] = \begin{bmatrix} [\delta U^1] \\ [\delta U^2] \\ [\delta U^3] \\ [\delta U^4] \end{bmatrix}, \quad
[R_{n+1}^{(k)}] = \begin{bmatrix} [R^1] \\ [R^2] \\ [R^3] \\ [R^4] \end{bmatrix}.
$$

The *consistent tangent matrix* $[K_\beta^{\alpha\,\gamma}]$, *residual vector* components $[R^\alpha]$, and *solution vector* $[\delta U^\alpha]$ are

$$[K_a^{L\,L}] = \mathop{\mathbf{A}}_{e=1}^{N_a} \left\{ \frac{1}{\Delta t} \int_{\Omega_a^e} [N_L]^T\,[N_L]\,\mathrm{d}A + \int_{\Omega_a^e} [B_L]^T\,[B_L]\,\mathbb{D}_L\,\mathrm{d}A - \int_{\Omega_a^e} [B_L]^T\,[N_L]\,\left([B_\Sigma]\,[\Sigma]_{n+1}^{(k)}\right)\,\left.\frac{\mathrm{d}\,\mathbb{D}_\Sigma}{\mathrm{d}\,c_L}\right|_{n+1}^{(k)}\,\mathrm{d}A \right\},$$

$$[K_a^{L\,\Sigma}] = \mathop{\mathbf{A}}_{e=1}^{N_a} \left\{ -\int_{\Omega_a^e} [B_L]^T\,[B_\Sigma]\,\left.\mathbb{D}_\Sigma\right|_{n+1}^{(k)}\,\mathrm{d}A \right\},$$

$$[K_a^{\Sigma\,L}] = \mathop{\mathbf{A}}_{e=1}^{N_a} \left\{ -\int_{\Omega_a^e} [N_\Sigma]^T\,[N_L]\,\left.\frac{\partial \mathrm{tr}\,[\boldsymbol{\sigma}]}{\partial c_L}\right|_{n+1}^{(k)}\,\mathrm{d}A \right\},$$

$$[K_a^{\Sigma\,\Sigma}] = \mathop{\mathbf{A}}_{e=1}^{N_a} \left\{ \int_{\Omega_a^e} [N_\Sigma]^T\,[N_\Sigma]\,\mathrm{d}A - \int_{\Omega_a^e} [N_\Sigma]^T\,\left[\frac{\partial \mathrm{tr}\,[\boldsymbol{\sigma}]}{\partial \Sigma}\right]_{n+1}^{(k)}\,[N_\Sigma]\,\mathrm{d}A \right\},$$

$$[K_a^{\Sigma\,u}] = \mathop{\mathbf{A}}_{e=1}^{N_a} \left\{ -\int_{\Omega_a^e} [N_\Sigma]^T\,\left[\frac{\partial \mathrm{tr}\,[\boldsymbol{\sigma}]}{\partial \varepsilon}\right]_{n+1}^{(k)}\,[B_u]\,\mathrm{d}A \right\},$$

$$[K_a^{\phi\,\phi}] = \mathop{\mathbf{A}}_{e=1}^{N_a} \left\{ \int_{\Omega_a^e} [B_\phi]^T\,[B_\phi]\,\kappa_a\,\mathrm{d}A \right\},$$

$$[K_a^{u\,L}] = \mathop{\mathbf{A}}_{e=1}^{N_a} \left\{ \int_{\Omega_a^e} [B_u]^T\,\left[\frac{\partial \sigma}{\partial c_L}\right]_{n+1}^{(k)}\,[N_L]\,\mathrm{d}A \right\},$$

$$[K_a^{u\,u}] = \mathop{\mathbf{A}}_{e=1}^{N_a} \left\{ \int_{\Omega_a^e} [B_u]^T\,\left[\frac{\partial \sigma}{\partial \varepsilon}\right]_{n+1}^{(k)}\,[B_u]\,\mathrm{d}A \right\},$$

$$[K_a^{u\,\Sigma}] = \mathop{\mathbf{A}}_{e=1}^{N_a} \left\{ \int_{\Omega_a^e} [B_u]^T\,\left[\frac{\partial \sigma}{\partial \Sigma}\right]_{n+1}^{(k)}\,[N_\Sigma]\,\mathrm{d}A \right\},$$

$$[K_e^{\mathrm{Li}\,\mathrm{Li}}] = \mathop{\mathbf{A}}_{e=1}^{N_e} \left\{ \frac{1}{\Delta t} \int_{\Omega_e^e} [N_{\mathrm{Li}}]^T\,[N_{\mathrm{Li}}]\,\mathrm{d}A + \int_{\Omega_e^e} [B_{\mathrm{Li}}]^T\,[B_{\mathrm{Li}}]\,\mathbb{D}_{\mathrm{Li}+}\,\mathrm{d}A + \int_{\Omega_e^e} [B_{\mathrm{Li}}]^T\,[N_{\mathrm{Li}}]\,\left([B_\phi]\,[\phi_e]_{n+1}^{(k)}\right)\,\left.\frac{\mathrm{d}\,\mathbb{D}_\phi^+}{\mathrm{d}\,c_{\mathrm{Li}+}}\right|_{n+1}^{(k)}\,\mathrm{d}A \right\},$$

$$[K_e^{\mathrm{Li}\,\phi}] = \mathop{\mathbf{A}}_{e=1}^{N_e} \left\{ \int_{\Omega_e^e} [B_{\mathrm{Li}}]^T\,[B_\phi]\,\left.\mathbb{D}_\phi^+\right|_{n+1}^{(k)}\,\mathrm{d}A \right\},$$

$$[K_e^{\mathrm{X}\,\mathrm{X}}] = \mathop{\mathbf{A}}_{e=1}^{N_e} \left\{ \frac{1}{\Delta t} \int_{\Omega_e^e} [N_{\mathrm{X}}]^T\,[N_{\mathrm{X}}]\,\mathrm{d}A + \int_{\Omega_e^e} [B_{\mathrm{X}}]^T\,[B_{\mathrm{X}}]\,\mathbb{D}_{\mathrm{X}-}\,\mathrm{d}A - \int_{\Omega_e^e} [B_{\mathrm{X}}]^T\,[N_{\mathrm{X}}]\,\left([B_\phi]\,[\phi_e]_{n+1}^{(k)}\right)\,\left.\frac{\mathrm{d}\,\mathbb{D}_\phi^-}{\mathrm{d}\,c_{\mathrm{X}-}}\right|_{n+1}^{(k)}\,\mathrm{d}A \right\},$$

$$[K_e^{\mathrm{X}\,\phi}] = \mathop{\mathbf{A}}_{e=1}^{N_e} \left\{ \int_{\Omega_e^e} [B_{\mathrm{X}}]^T\,[B_\phi]\,\left.\mathbb{D}_\phi^-\right|_{n+1}^{(k)}\,\mathrm{d}A \right\},$$

$$[K_e^{\phi\,\mathrm{Li}}] = \mathop{\mathbf{A}}_{e=1}^{N_e} \left\{ \int_{\Omega_e^e} [B_\phi]^T [B_{\mathrm{Li}}]\, I\!\!D_{\mathrm{Li}+}\, \mathrm{d}A + \int_{\Omega_e^e} [B_\phi]^T [N_{\mathrm{Li}}] \left([B_\phi]\,[\phi_e]_{n+1}^{(k)}\right)\, \frac{\mathrm{d}\,I\!\!D_\phi^+}{\mathrm{d}\,c_{\mathrm{Li}+}}\bigg|_{n+1}^{(k)}\, \mathrm{d}A \right\},$$

$$[K_e^{\phi\,\mathrm{X}}] = \mathop{\mathbf{A}}_{e=1}^{N_e} \left\{ -\int_{\Omega_e^e} [B_\phi]^T [B_{\mathrm{X}}]\, I\!\!D_{\mathrm{X}-}\, \mathrm{d}A + \int_{\Omega_e^e} [B_\phi]^T [N_{\mathrm{X}}] \left([B_\phi]\,[\phi_e]_{n+1}^{(k)}\right)\, \frac{\mathrm{d}\,I\!\!D_\phi^-}{\mathrm{d}\,c_{\mathrm{X}-}}\bigg|_{n+1}^{(k)}\, \mathrm{d}A \right\},$$

$$[K_e^{\phi\,\phi}] = \mathop{\mathbf{A}}_{e=1}^{N_e} \left\{ \frac{1}{\Delta t} \int_{\Omega_e^e} [B_\phi]^T [B_\phi]\,\ddagger_e \mathrm{d}A + \int_{\Omega_e^e} [B_\phi]^T [B_\phi]\; I\!\!D_\phi^+\big|_{n+1}^{(k)}\, \mathrm{d}A - \int_{\Omega_e^e} [B_\phi]^T [B_\phi]\; I\!\!D_\phi^-\big|_{n+1}^{(k)}\, \mathrm{d}A \right\},$$

$$[K_e^{u\,u}] = \mathop{\mathbf{A}}_{e=1}^{N_e} \left\{ \int_{\Omega_e^e} [B_u]^T \left[\frac{\partial\sigma}{\partial\varepsilon}\right]_{n+1}^{(k)} [B_u]\, \mathrm{d}A \right\},$$

$$[K_\Gamma^{\mathrm{Li}\,\phi}] = \mathop{\mathbf{A}}_{e=1}^{N_\Gamma} \left\{ \int_{\Gamma^e} \left([N_L]^T - [N_{\mathrm{Li}}]^T\right)[N_\phi]\, \frac{\mathrm{d}\,h_{BV}}{\mathrm{d}\,\phi_a}\bigg|_{n+1}^{(k)}\, \mathrm{d}s + \int_{\Gamma^e} \left([N_L]^T - [N_{\mathrm{Li}}]^T\right)[N_\phi]\, \frac{\mathrm{d}\,h_{BV}}{\mathrm{d}\,\phi_e}\bigg|_{n+1}^{(k)}\, \mathrm{d}s \right\},$$

$$[K_\Gamma^{\phi\,\phi}] = \mathop{\mathbf{A}}_{e=1}^{N_\Gamma} \left\{ \int_{\Gamma^e} \left([N_\phi]^T - [N_\phi]^T\right)[N_\phi]\, \frac{\mathrm{d}\,i_{BV}}{\mathrm{d}\,\phi_a}\bigg|_{n+1}^{(k)}\, \mathrm{d}s + \int_{\Gamma^e} \left([N_\phi]^T - [N_\phi]^T\right)[N_\phi]\, \frac{\mathrm{d}\,i_{BV}}{\mathrm{d}\,\phi_e}\bigg|_{n+1}^{(k)}\, \mathrm{d}s, \right\},$$

$$[K_\Gamma^{u\,u}] = -\mathop{\mathbf{A}}_{e=1}^{N_\Gamma} \left\{ \int_{\Gamma^e} \left([N_u]^T - [N_u]^T\right)[N_u]\, \frac{\mathrm{d}\,\vec{T}_\Gamma}{\mathrm{d}\,\vec{u}_a}\bigg|_{n+1}^{(k)}\, \mathrm{d}s + \int_{\Gamma*e} \left([N_u]^T - [N_u]^T\right)[N_u]\, \frac{\mathrm{d}\,\vec{T}_\Gamma}{\mathrm{d}\,\vec{u}_e}\bigg|_{n+1}^{(k)}\, \mathrm{d}s \right\},$$

$$
\begin{aligned}
[R^1] = &-\mathop{\mathbf{A}}_{e=1}^{N_a} \left\{ \frac{1}{\Delta t} \int_{\Omega_a^e} [N_L]^T [N_L] \left([c_L]_{n+1}^{(k)} - [c_L]_n\right) \mathrm{d}A + \int_{\Omega_a^e} [B_L]^T [B_L]\,[c_L]_{n+1}^{(k)}\, I\!\!D_L\, \mathrm{d}A + \right. \\
&\quad -\int_{\Omega_a^e} [B_L]^T [B_\Sigma]\,[\Sigma]_{n+1}^{(k)}\; I\!\!D_\Sigma\big|_{n+1}^{(k)}\, \mathrm{d}A + \\
&\quad \left. +\int_{\partial^N\Omega_{an}^e} [N_L]^T \left(\vec{h}_L\cdot\vec{n}_{an}\right)\big|_{n+1}\, \mathrm{d}s + \int_{\partial^N\Omega_{ca}^e} [N_L]^T \left(\vec{h}_L\cdot\vec{n}_{an}\right)\big|_{n+1}\, \mathrm{d}s \right\} + \\
&-\mathop{\mathbf{A}}_{e=1}^{N_e} \left\{ \frac{1}{\Delta t} \int_{\Omega_e^e} [N_{\mathrm{Li}}]^T [N_{\mathrm{Li}}] \left([c_{\mathrm{Li}+}]_{n+1}^{(k)} - [c_{\mathrm{Li}+}]_n\right) \mathrm{d}A + \int_{\Omega_a^e} [B_{\mathrm{Li}}]^T [B_{\mathrm{Li}}]\,[c_{\mathrm{Li}+}]_{n+1}^{(k)}\, I\!\!D_{\mathrm{Li}+}\, \mathrm{d}A + \right. \\
&\quad \left. +\int_{\Omega_e^e} [B_{\mathrm{Li}}]^T [B_\phi]\,[\phi_e]_{n+1}^{(k)}\; I\!\!D_\phi^+\big|_{n+1}^{(k)}\, \mathrm{d}A \right\} + \\
&-\mathop{\mathbf{A}}_{e=1}^{N_\Gamma} \left\{ \int_{\Gamma^e} [N_L]^T\; h_{BV}\big|_{n+1}^{(k)}\, \mathrm{d}s - \int_{\Gamma^e} [N_{\mathrm{Li}}]^T\; h_{BV}\big|_{n+1}^{(k)}\, \mathrm{d}s \right\}.
\end{aligned}
$$

$$
\begin{aligned}
[R^2] = &-\mathop{\mathbf{A}}_{e=1}^{N_a} \left\{ \int_{\Omega_a^e} [N_\Sigma]^T \left([N_\Sigma]\,[\Sigma]_{n+1}^{(k)} - \mathrm{tr}\,[\boldsymbol{\sigma}]\big|_{n+1}^{(k)}\right) \mathrm{d}V \right\} + \\
&-\mathop{\mathbf{A}}_{e=1}^{N_e} \left\{ \frac{1}{\Delta t} \int_{\Omega_e^e} [N_{\mathrm{X}}]^T [N_{\mathrm{X}}] \left([c_{\mathrm{X}-}]_{n+1}^{(k)} - [c_{\mathrm{X}-}]_n\right) \mathrm{d}A + \int_{\Omega_e^e} [B_{\mathrm{X}}]^T [B_{\mathrm{X}}]\,[c_{\mathrm{X}-}]_{n+1}^{(k)}\, I\!\!D_{\mathrm{X}\cdot}\, \mathrm{d}A + \right. \\
&\quad \left. -\int_{\Omega_e^e} [B_{\mathrm{X}}]^T [B_\phi]\,[\phi]_{n+1}^{(k)}\; I\!\!D_\phi^-\big|_{n+1}^{(k)}\, \mathrm{d}A \right\},
\end{aligned}
$$

$$[R^3] = - \mathop{\mathbf{A}}_{e=1}^{N_a} \left\{ \int_{\Omega_a^e} [B_\phi]^T [B_\phi] [\phi_a]_{n+1}^{(k)} \kappa_a \, \mathrm{d}A \right. +$$

$$+ \int_{\partial^N \Omega_{an}^e} [N_\phi]^T \left(\vec{i} \cdot \vec{n}_{an} \right)\Big|_{n+1} \mathrm{d}s + \int_{\partial^N \Omega_{ca}^e} [N_\phi]^T \left(\vec{i} \cdot \vec{n}_{an} \right)\Big|_{n+1} \mathrm{d}s \Bigg\} +$$

$$- \mathop{\mathbf{A}}_{e=1}^{N_e} \left\{ \frac{1}{\Delta t} \int_{\Omega_e^e} [B_\phi]^T [B_\phi] \left([\phi_e]_{n+1}^{(k)} - [\phi_e]_n \right) \mathrm{d}A + \int_{\Omega_e^e} [B_\phi]^T [B_{\mathrm{Li}}] [c_{\mathrm{Li}^+}]_{n+1}^{(k)} \, \mathbb{D}_{\mathrm{Li}^+} \, \mathrm{d}A + \right.$$

$$+ \int_{\Omega_e^e} [B_\phi]^T [B_\phi] [\phi_e]_{n+1}^{(k)} \, \mathbb{D}_\phi^+\Big|_{n+1}^{(k)} \mathrm{d}A - \int_{\Omega_a^e} [B_\phi]^T [B_{\mathrm{X}}] [c_{\mathrm{X}^-}]_{n+1}^{(k)} \, \mathbb{D}_{\mathrm{X}^-} \, \mathrm{d}A +$$

$$+ \int_{\Omega_e^e} [B_\phi]^T [B_\phi] [\phi_e]_{n+1}^{(k)} \, \mathbb{D}_\phi^-\Big|_{n+1}^{(k)} \mathrm{d}A \Bigg\} +$$

$$- \mathop{\mathbf{A}}_{e=1}^{N_\Gamma} \left\{ \int_{\Gamma^e} [N_\phi]^T \; i_{BV}|_{n+1}^{(k)} \, \mathrm{d}s - \int_{\Gamma^e} [N_\phi]^T \; i_{BV}|_{n+1}^{(k)} \, \mathrm{d}s \right\},$$

$$[R^4] = - \mathop{\mathbf{A}}_{e=1}^{N_a} \left\{ \int_{\Omega_a^e} [B_u]^T [\sigma]_{n+1}^{(k)} \, \mathrm{d}V - \int_{\partial^N \Omega_{a\,n}^e} [N_u^s]^T \cdot (\boldsymbol{\sigma}_{ca}\, \vec{n}_{ca})|_{n+1} \, \mathrm{d}s - \int_{\partial^N \Omega_{ca}^e} [N_u^s]^T \cdot (\boldsymbol{\sigma}_{ca}\, \vec{n}_{ca})|_{n+1} \, \mathrm{d}s \right\} +$$

$$- \mathop{\mathbf{A}}_{e=1}^{N_e} \left\{ \int_{\Omega_e^e} [B_u]^T [\sigma]_{n+1}^{(k)} \, \mathrm{d}V \right\} +$$

$$+ \mathop{\mathbf{A}}_{e=1}^{N_\Gamma} \left\{ \int_{\Gamma^e} [N_u]^T \; \vec{T}_\Gamma\Big|_{n+1}^{(k)} \, \mathrm{d}s - \int_{\Gamma^e} [N_u]^T \; \vec{T}_\Gamma\Big|_{n+1}^{(k)} \, \mathrm{d}s \right\},$$

$$[\delta U^1] = \mathop{\mathbf{A}}_{e=1}^{N_a} [\, c_L \,] + \mathop{\mathbf{A}}_{e=1}^{N_e} [\, c_{\mathrm{Li}^+} \,] \qquad , \qquad [\delta U^2] = \mathop{\mathbf{A}}_{e=1}^{N_a} [\, \Sigma \,] + \mathop{\mathbf{A}}_{e=1}^{N_e} [\, c_{\mathrm{X}^-} \,],$$

$$[\delta U^3] = \mathop{\mathbf{A}}_{e=1}^{N_a} [\, \phi_a \,] + \mathop{\mathbf{A}}_{e=1}^{N_e} [\, \phi_e \,] \qquad , \qquad [\delta U^4] = \mathop{\mathbf{A}}_{e=1}^{N_a} [\, u_a \,] + \mathop{\mathbf{A}}_{e=1}^{N_e} [\, u_e \,].$$

The value assumed by the scalar functions and their derivatives appearing in $[K^{\alpha\,\beta}]$ and $[R^\alpha]$ can be easily computed from the respective definitions.

Bibliography

[1] B. Scrosati and J. Garche. Lithium batteries: status, prospects and future. *J POWER SOURCES*, 195:2419–2430, 2010.

[2] J.M. Tarascon and M. Armand. Issues and challenges facing rechargeable Lithium batteries. *NATURE*, 414:359–367, 2001.

[3] A. Danzer, V. Liebau, and F. Maglia. Aging of Lithium-ion batteries for electric vehicles. In B. Scrosati, J. Garche, and W. Tillmetz, editors, *Advances in battery technologies for electric vehicles*, pages 359–387. Woodhead Publishing, 2015.

[4] A. Salvadori and D. Grazioli. Computer simulation for battery design and lifetime prediction. In B. Scrosati, J. Garche, and W. Tillmetz, editors, *Advances in battery technologies for electric vehicles*, pages 417–442. Woodhead Publishing, 2015.

[5] L. Lu, X. Han, J. Li, J. Hua, and M. Ouyang. A review on the key issues for Lithium-ion battery management in electric vehicles. *J POWER SOURCES*, 226(0):272 – 288, 2013.

[6] J. Zhang and J. Lee. A review on prognostics and health monitoring of Li-ion battery. *J POWER SOURCES*, 196(15):6007 – 6014, 2011.

[7] A. Barre, B. Deguilhem, S. Grolleau, M. Gerard, F. Suard, and D. Riu. A review on Lithium-ion battery ageing mechanisms and estimations. *J POWER SOURCES*, 241:680–689, 2013.

[8] A.A. Franco. Multiscale modelling and numerical simulation of rechargeable Lithium ion batteries: concepts, methods and challenges. *RSC ADVANCES*, 3(13027), 2013.

[9] M. Landstorfer and T. Jacob. Mathematical modeling of intercalation batteries at the cell level and beyond. *CHEM SOC REV*, 42:3234–3252, 2013.

[10] D. Doerffel and S.A. Sharkh. A critical review of using the Peukert equation for determining the remaining capacity of lead-acid and Lithium-ion batteries. *J POWER SOURCES*, 155(2):395–400, 2006.

[11] W Peukert. Über die abhängigkeit der kapazität von der entladestromstärke bei bleiakkumulatoren. *Elektrotech Z*, 1897.

[12] M. Chen and G. Rincon-Mora. Accurate electrical battery model capable of predicting runtime and IV performance. *IEEE T ENERGY CONVER*, 21(2):504–511, 2006.

[13] R. L. Fares and M.E. Webber. Combining a dynamic battery model with high-resolution smart grid data to assess microgrid islanding lifetime. *APPL ENERG*, 137:482–489, 2015.

[14] P. Rong, S. Member, and M. Pedram. An analytical model for predicting the remaining battery capacity of Lithium-ion batteries. *IEEE T VLSI SYST*, 14(5):441–451, 2006.

[15] M.T. von Srbik, M. Marinescu, R.F. Martinez-Botas, and G.J. Offer. A physically meaningful equivalent circuit network model of a Lithium-ion battery accounting for local electrochemical and thermal behaviour, variable double layer capacitance and degradation. *J POWER SOURCES*, 325:171 – 184, 2016.

[16] W.D. Widanage, A. Barai, G.H. Chouchelamane, K. Uddin, A. McGordon, J. Marco, and P. Jennings. Design and use of multisine signals for Li-ion battery equivalent circuit modelling. Part II: Model estimation. *J POWER SOURCES*, 324:61 – 69, 2016.

[17] H. He, R. Xiong, and J. Fan. Evaluation of Lithium-ion battery equivalent circuit models for state of charge estimation by an experimental approach. *Energies*, 4:582–598, 2011.

[18] L. Gao, S. Liu, and R.A. Dougal. Dynamic Lithium-ion battery model for system simulation. *IEEE T COMPON PACK T*, 25(3):495–505, 2002.

[19] S. Buller and M. Thele. Impedance-based simulation models of supercapacitors and Li-ion batteries for power electronic applications. *IEEE T IND APPL*, 41(3):742–747, 2005.

[20] S. Gold. A PSPICE macromodel for Lithium-ion batteries. In *The 12*[th] *annual battery conference on applications and advances.*, pages 215–222, 1997.

[21] A. Fotouhi, D.J. Auger, K. Propp, S. Longo, and M. Wild. A review on electric vehicle battery modelling: From Lithium-ion toward Lithium–sulphur. *RENEW SUST ENERG REV*, 56:1008 – 1021, 2016.

[22] S.R. De Groot and P. Mazur. *Non-Equilibrium Thermodynamics*. Dover, 1984.

[23] R. DeHoff. *Thermodynamic in material science*. CRC Press - Taylor and Francis, 2006.

[24] M.E. Gurtin, E. Fried, and L. Anand. *The Mechanics and Thermodynamics of Continua*. Cambridge University Press, 2010.

[25] S. Shell. *Thermodynamics and statistical mechanics: an integrated approach*. Cambridge University Press, 2015.

[26] E.B. Tadmor, R.E. Miller, and R.S. Elliott. *Continuum Mechanics and Thermodynamics: From Fundamental Concepts to Governing Equations*. Cambridge University Press, 2011.

[27] P. Tagade, K.S. Hariharan, S. Basu, M.K.S. Verma, S.M. Kolake, T. Song, D. Oh, T. Yeo, and S.K. Doo. Bayesian calibration for electrochemical thermal model of Lithium-ion cells. *J POWER SOURCES*, 320:296 – 309, 2016.

[28] C. Edouard, M. Petit, C. Forgez, J. Bernard, and R. Revel. Parameter sensitivity analysis of a simplified electrochemical and thermal model for Li-ion batteries aging. *J POWER SOURCES*, 325:482 – 494, 2016.

[29] A.J Bard and L.R. Faulkner. *Electrochemical Methods: Fundamentals and Applications*. Wiley, 2nd edition, 2000.

[30] A.F. Bower, P.M. Guduru, and V.A. Sethuraman. A finite strain model of stress, diffusion, plastic flow and electrochemical reactions in a Lithium-ion half-cell. *J MECH PHYS SOLIDS*, 59:804–828, 2011.

[31] A. Aurbach. The role of surface films on electrodes in Li-ion batteries. In W. van Schalkwijk and B. Scrosati, editors, *Advances in Lithium-ion batteries*. Kluwer Academic, New York, 2002.

[32] A.F. Bower, P.R. Guduru, and E. Chason. Analytical solutions for composition and stress in spherical elastic–plastic Lithium-ion electrode particles containing a propagating phase boundary. *INT J SOLIDS STRUCT*, 69-70:328–342, 2015.

[33] M.J. Chon, V.A. Sethuraman, A. McCormick, V. Srinivasan, and P.R. Guduru. Real-time measurement of stress and damage evolution during initial lithiation of crystalline silicon. *PHYS REV LETT*, 107:045503, 2011.

[34] P. Arora, R.E. White, and M. Doyle. Capacity fade mechanisms and side reactions in lithium-ion batteries. *J ELECTROCHEM SOC*, 145(10):3647–3667, 1998.

[35] R. Marom, S.F. Amalraj, N. Leifer, D. Jacob, and D. Aurbach. A review of advanced and practical Lithium battery materials. *J MATER CHEM*, 21:9938–9954, 2011.

[36] G. Sarre, P. Blanchard, and M. Broussely. Aging of Lithium-ion batteries. *J POWER SOURCES*, 127:65–71, 2004.

[37] J. Vetter, P. Novak, M.R. Wagner, C. Veit, K.C. Moeller, J.O. Besenhard, M. Winter, M. Wohlfahrt-Mehrens, C. Vogler, and A. Hammouche. Ageing mechanisms in Lithium-ion batteries. *J POWER SOURCES*, 147(1-2):269–281, 2005.

[38] M. Wohlfart-Mehrens, C. Vogler, and J. Garche. Aging mechanism of Lithium cathode materials. *J POWER SOURCES*, 127:58–64, 2004.

[39] J.G. Swallow, W.H. Woodford, F.P. McGrogan, N. Ferralis, Y.M. Chiang, and K.J. Van Vliet. Effect of electrochemical charging on elastoplastic properties and fracture toughness of Li_xCoO_2. *J ELECTROCHEM SOC*, 161(11):F3084–F3090, 2014.

[40] J.G. Swallow, W.H. Woodford, Y. Chen, Q. Lu, J.J. Kim, D. Chen, Y.M. Chiang, W.C. Carter, B. Yildiz, H.L. Tuller, and K.J. Van Vliet. Chemomechanics of ionically conductive ceramics for electrical energy conversion and storage. *J ELECTROCERAM*, 32:3–27, 2014.

[41] W.I.F. David, M.M. Thackeray, L.A. De Picciotto, and J.B. Goodenough. Structure refinement of the spinel-related phases $Li_2Mn_2O_4$ and $Li_{0.2}Mn_2O_4$. *J SOLID STATE CHEM*, 67(2):316–323, 1987.

[42] T. Ohzuku, Y. Iwakoshi, and K. Sawai. Formation of Lithium-graphite intercalation compounds in nonaqueous electrolytes and their application as a negative electrode for a Lithium ion (shuttlecock) cell. *J ELECTROCHEM SOC*, 140(9):2490–2498, 1993.

[43] T. Ohzuku, N. Matoba, and K. Sawai. Direct evidence on anomalous expansion of graphite-negative electrodes on first charge by dilatometry. *J POWER SOURCES*, 97-98:73–77, 2001. Proceedings of the 10th International Meeting on Lithium Batteries.

[44] H. Wang, Y.I. Jang, B. Huang, D.R. Sadoway, and Y.M. Chiang. TEM study of electrochemical cycling-induced damage and disorder in $LiCoO_2$ cathodes for rechargeable Lithium batteries. *J ELECTROCHEM SOC*, 146(2):473–480, 1999.

[45] M.C. Tucker, J.A. Reimer, and E.J. Cairns. A study of capacity fade in metal-substituted Lithium manganese oxide spinels. *J ELECTROCHEM SOC*, 149(5):A574–A585, 2002.

[46] M.R. Lim, W.I. Cho, and K.B. Kim. Preparation and characterization of gold-codeposited $LiMn_2O_4$ electrodes. *J POWER SOURCES*, 92(1-2):168–176, 2001.

[47] D. Wang, X. Wu, Z. Wang, and L. Chen. Cracking causing cyclic instability of $LiFePO_4$ cathode material. *J POWER SOURCES*, 140(1):125–128, 2005.

[48] H. Gabrisch, J. Wilcox, and M. M. Doeff. TEM study of fracturing in spherical and plate-like $LiFePO_4$ particles. *ELECTROCHEM SOLID ST*, 11(3):A25–A29, 2008.

[49] R. Kostecki and F. McLarnon. Microprobe study of the effect of Li intercalation on the structure of graphite. *J POWER SOURCES*, 119-121:550–554, 2003. Selected papers presented at the 11th International Meeting on Lithium Batteries.

[50] L.J. Hardwick, M. Marcinek, L. Beer, J.B. Kerr, and R. Kostecki. An investigation of the effect of graphite degradation on irreversible capacity in Lithium-ion cells. *J ELECTROCHEM SOC*, 155(6):A442–A447, 2008.

[51] E. Markervich, G. Salitra, M.D. Levi, and D. Aurbach. Capacity fading of lithiated graphite electrodes studied by a combination of electroanalytical methods, raman spectroscopy and SEM. *J POWER SOURCES*, 146(1-2):146–150, 2005. Selected papers presented at the 12th International Meeting on Lithium Batteries12th International Meeting on Lithium Batteries.

[52] L. Y. Beaulieu, K. W. Eberman, R. L. Turner, L. J. Krause, and J. R. Dahn. Colossal reversible volume changes in Lithium alloys. *ELECTROCHEM SOLID ST*, 4(9):A137–A140, 2001.

[53] M. Tang, P. Albertus, and J. Newman. Two-dimensional modeling of Lithium deposition during cell charging. *J ELECTROCHEM SOC*, 156:A390–A399, 2009.

[54] D. P. Finegan, M. Scheel, J. B. Robinson, B. Tjaden, I. Hunt, T. J. Mason, J. Millichamp, M. Di Michiel, G. J. Offer, G. Hinds, D. J. L. Brett, and P. R. Shearing. In-operando high-speed tomography of Lithium-ion batteries during thermal runaway. *NAT COMMUN*, 6, 04 2015.

[55] A. Salvadori, D. Grazioli, M.G.D. Geers, D. Danilov, and P.H.L Notten. A novel approach in modeling ionic transport in the electrolyte of (Li-ion) batteries. *J POWER SOURCES*, 293:892–911, 2015.

[56] A. Salvadori, D. Grazioli, M. Magri, M.G.D. Geers, D. Danilov, and P.H.L. Notten. On the role of saturation in modeling ionic transport in the electrolyte of (Li-ion) batteries. *J POWER SOURCES*, 294:696–710, 2015.

[57] S.S. Zhang. A review on the separators of liquid electrolyte Li-ion batteries. *J POWER SOURCES*, 164:351–364, 2007.

[58] W. Wu, X. Xiao, X. Huang, and S. Yan. A multiphysics model for the in situ stress analysis of the separator in a Lithium-ion battery cell. *COMP MATER SCI*, 83:127–136, 2014.

[59] L.R. Valoen and J.N Reimers. Transport properties of $LiPF_6$-based Li-ion battery electrolytes. *J ELECTROCHEM SOC*, 152(5):A882–A891, 2005.

[60] G. Bauer, V. Gravemeier, and W.A Wall. A 3D finite element approach for the coupled numerical simulation of electrochemical systems and fluid flow. *INT J NUMER METH ENG*, 86:1339–1359, 2011.

[61] G. Bauer, V. Gravemeier, and W.A Wall. A stabilized finite element method for the numerical simulation of multi-ion transport in electrochemical systems. *COMPUT METHOD APPL M*, 223-224:199–210, 2012.

[62] A. Latz and J. Zausch. Multiscale modeling of Li-ion batteries: thermal aspects. *BEILSTEIN J NANOTECHNOL*, 6:987–1007, 2015.

[63] D. Danilov and P.H.L. Notten. Mathematical modeling of ionic transport in the electrolyte of Li-ion batteries. *ELECTROCHIM ACTA*, 53:5569–5578, 2008.

[64] J. Newman and K.E. Thomas-Alyea. *Electrochemical systems*. John Wiley and Sons B.V., 2004.

[65] M.Z. Bazant, K.T. Chu, and B.J. Bayly. Current-voltage relations for elecrochemical thin films. *SIAM J APPL MATH*, 65:1463–1484, 2005.

[66] E.J.F. Dickinson, J.G. Limon-Petersen, and R.G. Compton. The electroneutrality approximation in electrochemistry. *J SOLID STATE ELECTR*, 15:1335–1345, 2011.

[67] A. Salvadori, E. Bosco, and D. Grazioli. A computational homogenization approach for Li-ion battery cells. Part 1 - Formulation. *J MECH PHYS SOLIDS*, 65:114–137, 2014.

[68] A. Salvadori, D. Grazioli, and M.G.D. Geers. Governing equations for a two-scale analysis of Li-ion battery cells. *INT J SOLIDS STRUCT*, 59:90–109, 2015.

[69] D. Djian, F. Alloin, S. Martinet, H. Lignier, and J.Y. Sanchez. Lithium-ion batteries with high charge rate capacity: Influence of the porous separator. *J POWER SOURCES*, 172:416–421, 2007.

[70] X. Huang. Separator technologies for Lithium-ion batteries. *J SOLID STATE ELECTR*, 15:649–662, 2011.

[71] K.M.E Abraham. Directions in secondary lithium battery research and development. *ELECTROCHIM ACTA*, 38:1233–1248, 1993.

[72] D.A.G. Bruggeman. Berechnung verschiedener physikallischer konstanten von heterogenen substanzen. *ANN PHYS-LEIPZIG*, 24:636–664, 1935.

[73] R.B. MacMullin and G.A. Muccini. Characteristics of porous beds and structures. *AICHE J*, 2:393–403, 1956.

[74] K.K. Patel, J.M. Paulsen, and J. Desilvestro. Numerical simulation of porous networks in relation to battery electrodes and separators. *J POWER SOURCES*, 122:144–152, 2003.

[75] I.V. Thorat, D.E. Stephenson, N.A. Zacharias, K. Zaghib, J.N. Harb, and D.R. Wheeler. Quantifying tortuosity in porous Li-ion battery materials. *J POWER SOURCES*, 188:592–600, 2009.

[76] X. Xiao, W. Wu, and X. Huang. A multi-scale approach for the stress analysis of polymeric separators in a Li-ion battery. *J POWER SOURCES*, 195:7649–7660, 2010.

[77] M.B. Pinson and M.Z. Bazant. Theory of SEI formation in rechargeable batteries: Capacity fade, accelerated aging and lifetime prediction. *J ELECTROCHEM SOC*, 160(2):A243–A250, 2013.

[78] J.W. Long, B. Dunn, D.R. Rolison, and H.S. White. Three-dimensional battery architectures. *CHEM REV*, 104:4463–4492, 2004.

[79] J.G. Kim, B. Son, S. Mukherjee, N. Schuppert, A. Bates, O. Kwon, M.J. Choi, H.Y. Chung, and S. Park. A review of lithium and non-lithium based solid state batteries. *J POWER SOURCES*, 282:299 – 322, 2015.

[80] A.L. Robinson. Solid-state batteries enter EV fray. *MRS BULL*, 39:1046–1047, 2014.

[81] B. Scrosati and C.A. Vincent. Polymer electrolytes: the key to Lithium polymer batteries. *MRS BULL*, March:28–30, 2000.

[82] M. Park, X. Zhang, M. Chung, G.B. Less, and A.M. Sastry. A review of conduction phenomena in Li-ion batteries. *J POWER SOURCES*, 195(24):7904–7929, 2010.

[83] S.D. Fabre, D. Guy-Bouyssou, P. Bouillon, F. Le Cras, and C. Delacourta. Charge/discharge simulation of an all-solid-state thin-film battery using a one-dimensional model. *J ELECTROCHEM SOC*, 159(2):A104–A115, 2012.

[84] V. Thangadurai, S. Narayanan, and D. Pinzaru. Garnet-type solid-state fast li ion conductors for li batteries: critical review. *CHEM SOC REV*, 43:4714–4727, 2014.

[85] N.J. Dudney and B.J. Neudecker. Solid state thin-film lithium battery systems. *CURR OPIN SOLID ST M*, 4:479–482, 1999.

[86] D. Danilov, R.A.H. Niessen, and P.H.L. Notten. Modeling all-solid-state Li-ion batteries. *J ELECTROCHEM SOC*, 158(3):A215–A222, 2011.

[87] Y. Wang, B. Liu, Q. Li, S. Cartmell, S. Ferrara, Z.D. Deng, and J. Xiao. Lithium and lithium ion batteries for applications in microelectronic devices: A review. *J POWER SOURCES*, 286:330 – 345, 2015.

[88] Watanabe and Ogata. Ionic conductivity of polymer electrolytes and future applications. *BRIT POLYM J*, 20(3):181–192, 1988.

[89] D.T. Hallinan Jr and N.P. Balsara. Polymer electrolytes. *ANNU REV MATER RES*, 43:503–525, 2013.

[90] P. Johansson. Computational modelling of polymer electrolytes: What do 30 years of research efforts provide us today? *ELECTROCHIM ACTA*, 175:42–46, 2015.

[91] P.P. Natsiavas, K. Weinberg, D. Rosato, and M. Ortiz. Effect of prestress on the stability of electrode–electrolyte interfaces during charging in Lithium batteries. *J MECH PHYS SOLIDS*, 95:92 – 111, 2016.

[92] Giovanna Bucci, Yet-Ming Chiang, and W. Craig Carter. Formulation of the coupled electrochemical–mechanical boundary-value problem, with applications to transport of multiple charged species. *ACTA MATER*, 104:33 – 51, 2016.

[93] K.E. Thomas, J. Newman, and R.M. Darling. Matematical modeling of Lithium batteries. In W. van Schalkwijk and B. Scrosati, editors, *Advances in Lithium-ion batteries*. Kluwer Academic, New York, 2002.

[94] J.S. Newman and C.W. Tobias. Theoretical analysis of current distribution in porous electrodes. *J ELECTROCHEM SOC*, 109(12):1183–1191, 1962.

[95] J. Newman and W.M. Tiedemann. Porous-electrode theory with battery applications. *AICHE J*, 21(1):25–41, 1975.

[96] M. Doyle and J. Newman. The use of mathematical modeling in the design of Lithium/polymer battery systems. *ELECTROCHIM ACTA*, 40(13):2191–2196, 1995.

[97] M. Doyle, T.F. Fuller, and J. Newman. Modeling of galvanostatic charge and discharge of the Lithium/polymer/insertion cell. *J ELECTROCHEM SOC*, 140:1526–1533, 1993.

[98] T.F. Fuller, M. Doyle, and J. Newman. Simulation and optimization of the dual Lithium ion insertion cell. *J ELECTROCHEM SOC*, 141(1):1–10, 1994.

[99] R.E. Garcia, Y.M. Chiang, W.C. Carter, P. Limthongkul, and C.M. Bishop. Microstructural modeling and design of rechargeable Lithium-ion batteries. *J ELECTROCHEM SOC*, 152:255–263, 2005.

[100] K. West, T. Jacobsen, and S. Atlung. Modeling of porous insertion electrodes with liquid electrolyte. *J ELECTROCHEM SOC*, 129(7):1480–1485, 1982.

[101] J. Christensen. Modeling diffusion-induced stress in Li-ion cells with porous electrodes. *J ELECTROCHEM SOC*, 157:366–380, 2010.

[102] V. Ramadesigan, P.W.C. Northrop, S. De, S. Santhanagopalan, R.D. Braatz, and V.R. Subramanian. Modeling and simulation of Lithium-ion batteries from a systems engineering perspective. *J ELECTROCHEM SOC*, 159(3):R31–R45, 2012.

[103] S. Atlung, K. West, and T. Jacobsen. Dynamic aspects of solid solution cathodes for electrochemical power sources. *J ELECTROCHEM SOC*, 126(8):1311–1321, 1979.

[104] M. Doyle, J. Newman, A. S. Gozdz, C. N. Schmutz, and J.M. Tarascon. Comparison of modeling predictions with experimental data from plastic Lithium ion cells. *J ELECTROCHEM SOC*, 143(6):1890–1903, 1996.

[105] P. Arora, M. Doyle, A.S. Gozdz, R.E. White, and J.Newman. Comparison between computer simulations and experimental data for high-rate discharges of plastic lithium-ion batteries. *J POWER SOURCES*, 88(2):219 – 231, 2000.

[106] J. Smekens, J. Paulsen, W. Yang, N. Omar, J. Deconinck, A. Hubin, and J. Van Mierlo. A modified multiphysics model for Lithium-ion batteries with a $Li_xNi_{1/3}Mn_{1/3}Co_{1/3}O_2$ electrode. *ELECTROCHIM ACTA*, 174:615–624, 2015.

[107] A. Mukhopadhyay and B.V. Sheldon. Deformation and stress in electrode materials for Li-ion batteries. *PROG MATER SCI*, 63:58–116, 2014.

[108] T.F. Fuller, M. Doyle, and J. Newman. Relaxation phenomena in Lithium-ion-insertion cells. *J ELECTROCHEM SOC*, 141(4):982–990, 1994.

[109] M. Doyle and Y. Fuentes. Computer simulations of a Lithium-ion polymer battery and implications for higher capacity next-generation battery designs. *J ELECTROCHEM SOC*, 150(6):A706–A713, 2003.

[110] S. Pramanik and S. Anwar. Electrochemical model based charge optimization for Lithium-ion batteries. *J POWER SOURCES*, 313:164 – 177, 2016.

[111] K.E. Thomas and J. Newman. Thermal modeling of porous insertion electrodes. *J ELECTROCHEM SOC*, 150(2):A176–A192, 2003.

[112] S. Renganathan, G. Sikha, S. Santhanagopalan, and R. E. White. Theoretical analysis of stresses in a Lithium ion cell. *J ELECTROCHEM SOC*, 157:155–163, 2010.

[113] H. Arunachalam, S. Onori, and I. Battiato. On veracity of macroscopic Lithium-ion battery models. *J ELECTROCHEM SOC*, 10:A1940–A1951, 2015.

[114] R. E. Garcia and Y.M. Chiang. Spatially resolved modeling of microstructurally complex battery architectures. *J ELECTROCHEM SOC*, 154(9):A856–A864, 2007.

[115] C.W. Wang and A.M. Sastry. Mesoscale modeling of a Li-ion polymer cell. *J ELECTROCHEM SOC*, 154:A1035–A1047, 2007.

[116] R.T. Purkayastha and R.M. McMeeking. An integrated 2-D model of a Lithium ion battery: the effect of material parameters and morphology on storage particle stress. *COMPUT MECH*, 50:209–227, 2012.

[117] O. Stern. Zur theorie der elektrolytischen doppelschicht. *Z Elektrochem*, 30(508-516), 1924.

[118] D.L. Chapman. A contribution to the theory of electrocapillarity. *PHILOS MAG*, 25:475–481, 1913.

[119] M. Gouy. Sur la constitution de la charge electrique a la surface d'un electrolyte. *J PHYS THEOR APPL*, 9(1):457–468, 1910.

[120] C.H. Hamann, A. Hamnett, and W. Vielstich. *Electrochemistry*. Wiley, 2007.

[121] M.Z. Bazant, M.S. Kilic, B. Storey, and A. Ajdari. Towards an understanding of induced-charge electrokinetics at large applied voltages in concentrated solutions. *ADV COLLOID INTERFAC*, 152:48–88, 2009.

[122] P.M. Biesheuvel, M. van Soestbergenb, and M.Z. Bazant. Imposed currents in galvanic cells. *ELECTROCHIM ACTA*, 54:4857–4871, 2009.

[123] J. Marcicki, A.T. Conlisk, and G. Rizzoni. A Lithium-ion battery model including electrical double layer effects. *J POWER SOURCES*, 125:157–169, 2014.

[124] M.Z. Bazant, K. Thornton, and A. Ajdari. Diffuse-charge dynamics in electrochemical systems. *PHYS REV E*, 70:021506, 2004.

[125] A. Frumkin, O. Petry, and B. Damaskin. The notion of the electrode charge and the Lippmann equation. *J ELECTROANAL CHEM*, 27(1):81 – 100, 1970.

[126] J.M. Rubi and S. Kjelstrup. Mesoscopic nonequilibrium thermodynamics gives the same thermodynamic basis to Butler-Volmer and Nernst equations. *J PHYS CHEM B*, 107:13471–13477, 2003.

[127] A.F. Bower and P.M. Guduru. A simple finite element model of diffusion, finite deformation, plasticity and fracture in Lithium ion insertion electrode materials. *MODELLING SIMUL MATER SCI ENG*, 20:045004, 2012.

[128] G. Bucci, S.P.V. Nadimpalli, V.A. Sethuraman, A.F. Bower, and P.R. Guduru. Measurement and modeling of the mechanical and electrochemical response of amorphous Si thin film electrodes during cyclic lithiation. *J MECH PHYS SOLIDS*, 62:276–294, 2014.

[129] T.S. Dao, C.P. Vyasarayani, and J. McPhee. Simplification and order reduction of Lithium-ion battery model based on porous-electrode theory. *J POWER SOURCES*, 198:329–337, 2012.

[130] I. Streeter and R.G. Compton. Numerical simulation of potential step chronoamperometry at low concentrations of supporting electrolyte. *J PHYS CHEM-US*, 112:13716–13728, 2008.

[131] W. Dreyer, C. Guhlke, and M. Landstorfer. A mixture theory of electrolytes containing solvation effects. *ELECTROCHEM COMMUN*, 43:75–78, 2014.

[132] A. Gillman, G. Amadio, K. Matouš, and T.L. Jackson. Third-order thermo-mechanical properties for packs of platonic solids using statistical micromechanics. *P R SOC A*, 471, 2015.

[133] Y.T. Cheng and M.W. Verbrugge. Evolution of stress within a spherical insertion electrode particle under potentiostatic and galvanostatic operation. *J POWER SOURCES*, 190:453–460, 2009.

[134] Y.T. Cheng and M.W. Verbrugge. Diffusion-induced stress, interfacial charge transfer, and criteria for avoiding crack initiation of electrode particles. *J ELECTROCHEM SOC*, 4:508–516, 2010.

[135] J. Christensen and J. Newman. Stress generation and fracture in Lithium insertion materials. *J SOLID STATE ELECTR*, 10:293–319, 2006.

[136] Z. Cui, F. Gao, and J. Qu. A finite deformation stress-dependent chemical potential and its applications to Lithium ion batteries. *J MECH PHYS SOLIDS*, 60:1280–1295, 2012.

[137] R. Deshpande, Y.T. Cheng, and M.W. Verbrugge. Modeling diffusion-induced stress in nanowire electrode structures. *J POWER SOURCES*, 195:5081–5088, 2010.

[138] R. Deshpande, Y.T Cheng, M.W. Verbrugge, and A. Timmons. Diffusion induced stresses and strain energy in a phase-transforming spherical electrode particle. *J ELECTROCHEM SOC*, 158(6):A718–A724, 2011.

[139] S. Golmon, K. Maute, S.H. Lee, and M.L. Dunn. Stress generation in silicon particles during Lithium insertion. *APPL PHYS LETT*, 97:033111, 2010.

[140] C. Miehe and H. Dal. Computational electro-chemo-mechanics of Lithium-ion battery electrodes at finite strains. *COMPUT MECH*, 55:303–325, 2015.

[141] R.T. Purkayastha and R.M. McMeeking. A parameter study of intercalation of Lithium into storage particles in a Lithium-ion battery. *COMP MATER SCI*, 80:2–14, 2013.

[142] X. Zhang, A.M. Sastry, and W. Shyy. Intercalation-induced stress and heat generation within single Lithium-ion battery chatode particles. *J ELECTROCHEM SOC*, 155(7):A542–A552, 2008.

[143] X. Zhang, W. Shyy, and A.M. Sastry. Numerical simulation of intercalation-induced stress in Li-ion battery electrode particles. *J ELECTROCHEM SOC*, 154:A910–A916, 2007.

[144] K. Zhao, M. Pharr, S. Cai, J.J. Vlassak, and Z. Suo. Large plastic deformation in high-capacity Lithium-ion batteries caused by charge and discharge. *J AM CERAM SOC*, 94(S1):S226–S235, 2011.

[145] A. Awarke, S. Lauer, M. Wittler, and S. Pischinger. Quantifying the effects of strains on the conductivity and porosity of LiFePO$_4$ based Li-ion composite cathodes using a multi-scale approach. *COMP MATER SCI*, 50(3):871–879, 2011.

[146] A. Gupta, J. H. Seo, X. Zhang, W. Du, A.M. Sastry, and W. Shyy. Effective transport properties of LiMn$_2$O$_4$ electrode via particle-scale modeling. *J ELECTROCHEM SOC*, 158(5):A487–A497, 2011.

[147] S.A. Roberts, V.E. Brunini, K.N. Long, and A.M. Grillet. A framework for three-dimensional mesoscale modeling of anisotropic swelling and mechanical deformation in Lithium-ion electrodes. *J ELECTROCHEM SOC*, 161(11):F3052–F3059, 2014.

160

[148] A.J. Stershic, S. Simunovic, and J. Nanda. Modeling the evolution of Lithium-ion particle contact distributions using a fabric tensor approach. *J POWER SOURCES*, 297:540–550, 2015.

[149] M. Ender, J. Joos, T. Carraro, and E. Ivers-Tiffee. Three dimensional reconstruction of a composite cathode for Lithium-ion cells. *ELECTROCHEM COMMUN*, 13(2):166–168, 2011.

[150] T. Hutzenlaub, S. Thiele, R. Zengerle, and C. Ziegler. Three-dimensional reconstruction of a $LiCoO_2$ Li-ion battery cathode. *ELECTROCHEM SOLID ST*, 15(3):A33–A36, 2012.

[151] T. Hutzenlaub, S. Thiele, R. Paust, R.M. Spotnitz, R. Zengerle, and C. Walchshofer. Three dimensional electrochemical Li-ion battery modeling featuring a focused ion-beam/scanning electrode microscopy based three-phase reconstruction of a $LiCoO_2$ cathode. *ELECTROCHIM ACTA*, 115:131–139, 2014.

[152] V. Malave, J. Berger, H. Zhu, and R.J. Kee. A computational model of the mechanical behavior within reconstructed Li_xCoO_2 Li-ion battery cathode particles. *ELECTROCHIM ACTA*, 130:707–717, 2014.

[153] V. Malave, J.R. Berger, and P.A. Martin. Concentration-dependent chemical expansion in Lithium-ion battery cathode particles. *J APPL MECH*, 81(9), 2014.

[154] D.E. Stephenson, E.M. Hartman, J.N. Harb, and D.R. Wheeler. Modeling of particle-particle interactions in porous cathodes for Lithium-ion batteries. *J ELECTROCHEM SOC*, 154:A1146–A1155, 2007.

[155] Christian Wieser, Torben Prill, and Katja Schladitz. Multiscale simulation process and application to additives in porous composite battery electrodes. *J POWER SOURCES*, 277:64–75, 2015.

[156] S.K. Babu, A.I. Mohamed, J.F. Whitacre, and S. Litster. Multiple imaging mode X-ray computed tomography for distinguishing active and inactive phases in Lithium-ion battery cathodes. *J POWER SOURCES*, 283:314–319, 2015.

[157] P.R. Shearing, L.E. Howard, P. Jorgensen, N.P. Brandon, and S.J. Harris. Characterization of the 3-dimensional microstructure of a graphite negative electrode from a Li-ion battery. *ELECTROCHEM COMMUN*, 12(3):374 – 377, 2010.

[158] L. Zielke, T. Hutzenlaub, D.R. Wheeler, I. Manke, T. Arlt, N. Paust, R. Zengerle, and S. Thiele. A combination of X-Ray tomography and carbon binder modeling: reconstructing the three phases of $LiCoO_2$ Li-ion battery cathodes. *ADV ENERGY MATER*, 4(8):1301617, 2014.

[159] L. Zielke, T. Hutzenlaub, D.R. Wheeler, C.W. Chao, I. Manke, A. Hilger, N. Paust, R. Zengerle, and S. Thiele. Three-phase multiscale modeling of a $LiCoO_2$ cathode: combining the advantages of FIB-SEM imaging and X-Ray tomography. *ADV ENERGY MATER*, 5:1401612, 2015.

[160] J.R. Wilson, J.S. Cronin, S.A. Barnett, and S.J. Harris. Measurements of three-dimensional microstructure in a $LiCoO_2$ positive electrode. *J POWER SOURCES*, 196:3443–3447, 2011.

[161] Z. Liu, J.S. Cronin, Y. Chen-Wiegart, J.R. Wilson, K.J. Yakal-Kremski, J. Wang, K.T. Faber, and S.A. Barnett. Three-dimensional morphological measurements of $LiCoO_2$ and $LiCoO_2/Li(Ni_{1/3}Mn_{1/3}Co_{1/3})O_2$ Lithium-ion battery cathodes. *J POWER SOURCES*, 227:267–274, 2013.

[162] A.H. Wiedemann, G.M. Goldin, S.A. Barnett, H. Zhu, and R.J. Kee. Effects of three-dimensional cathode microstructure on the performance of Lithium-ion battery cathodes. *ELECTROCHIM ACTA*, pages 580–588, 2013.

[163] Z. Liu, Y. Chen-Wiegart, J. Wang, S.A. Barnett, and K.T. Faber. Three-phase 3d reconstructions of a $LiCoO_2$ cathode via FIB-SEM tomography. *MICROSC MICROANAL*, 22:140–148, 2016.

[164] J. Newman and W.M. Tiedemann. Temperature rise in a battery module with constant heat generation. *J ELECTROCHEM SOC*, 142(4):1054–1057, 1995.

[165] C.R. Pals and J. Newman. Thermal modeling of the Lithium/polymer battery. *J ELECTROCHEM SOC*, 142(10):3274–3281, 1995.

[166] L. Rao and J. Newman. Heat-generation rate and general energy balance for insertion battery systems. *J ELECTROCHEM SOC*, 144(8):2697–2704, 1997.

[167] C.Y. Jhua, Y.W. Wang, C.Y. Wen, and C.M. Shu. Thermal runaway potential of $LiCoO_2$ and $Li(Ni_{1/3}Co_{1/3}Mn_{1/3})O_2$ batteries determined with adiabatic calorimetry methodology. *APPL ENERG*, 100(127–131), 2012.

[168] S. Abada, G. Marlair, A. Lecocq, M. Petit, V. Sauvant-Moynot, and F. Huet. Safety focused modeling of lithium-ion batteries: A review. *J POWER SOURCES*, 306:178 – 192, 2016.

[169] M. Fleckenstein, O. Bohlen, M.A. Roscher, and B. Baeker. Current density and state of charge inhomogeneities in Li-ion battery cells with $LiFePO_4$ as cathode material due to temperature gradients. *J POWER SOURCES*, 196:4769–4778, 2011.

[170] A. Latz and J. Zausch. Thermodynamic consistent transport theory of Li-ion batteries. *J POWER SOURCES*, 196:3296–3302, 2011.

[171] S. Rothe, J.H. Schmidt, and S. Hartmann. Analytical and numerical treatment of electro-thermo-mechanical coupling. *ARCH APPL MECH*, 85:1245–1264, 2015.

[172] I. Baghdadi, O. Briat, J.Y. Delétage, P. Gyan, and J.M. Vinassa. Lithium battery aging model based on Dakin's degradation approach. *J POWER SOURCES*, 325:273 – 285, 2016.

[173] R. Darling and J. Newman. Modeling side reactions in composite $Li_y Mn_2O_4$ electrodes. *J ELECTROCHEM SOC*, 145(3):990–998, 1998.

[174] J.R. Belt, C.D. Ho, C.G. Motloch, T.J. Miller, and T.Q. Duong. A capacity and power fade study of Li-ion cells during life cycle testing. *J POWER SOURCES*, 123(2):241–246, 2003.

[175] I. Bloom, B.W. Cole, J.J. Sohn, S.A. Jones, E.G. Polzin, V.S. Battaglia, G.L. Henriksen, C. Motloch, R. Richardson, T. Unkelhaeuser, D. Ingersoll, and H.L. Case. An accelerated calendar and cycle life study of Li-ion cells. *J POWER SOURCES*, 101(2):238–247, 2001.

[176] K. Asakura, M. Shimomura, and T. Shodai. Study of life evaluation methods for Li-ion batteries for backup applications. *J POWER SOURCES*, 119-121:902–905, 2003. Selected papers presented at the 11th International Meeting on Lithium Batteries.

[177] M. Safari and C. Delacourt. Simulation-based analysis of aging phenomena in a commercial graphite/$LiFePO_4$ cell. *J ELECTROCHEM SOC*, 158(12):A1436–A1447, 2011.

[178] Y.P. Wu, E. Rahm, and R. Holze. Carbon anode materials for Lithium ion batteries. *J POWER SOURCES*, 114(2):228–236, 2003.

[179] R. Fong, U. von Sacken, and J. R. Dahn. Studies of Lithium intercalation into carbons using nonaqueous electrochemical cells. *J ELECTROCHEM SOC*, 137(7):2009–2013, 1990.

[180] J. Christensen and J. Newman. A mathematical model for the Lithium-ion negative electrode solid electrolyte interphase. *J ELECTROCHEM SOC*, 151(11):A1977–A1988, 2004.

[181] J. Deng, G.J. Wagner, and R.P. Muller. Phase field modeling of solid electrolyte interface formation in Lithium ion batteries. *J ELECTROCHEM SOC*, 160(3):A487–A496, 2013.

[182] D. Li, D. Danilov, Z. Zhang, H. Chen, Y. Yang, and P.H.L Notten. Modeling the SEI-formation on graphite electrodes in $LiFePO_4$ batteries. *J ELECTROCHEM SOC*, 162(6):A858–A869, 2015.

[183] L. Liu, J. Park, X. Lin, A.M. Sastry, and W. Lu. A thermal-electrochemical model that gives spatial-dependent growth of solid electrolyte interphase in a Li-ion battery. *J POWER SOURCES*, 268:482–490, 2014.

[184] M. Nie, D. Chalasani, D.P. Abraham, Y. Chen, A. Bose, and B.L. Lucht. Lithium ion battery graphite solid electrolyte interphase revealed by microscopy and spectroscopy. *J PHYS CHEM-US*, 117:1257–1267, 2013.

[185] H.J. Ploehn, P. Ramadass, and R.E. White. Solvent diffusion model for aging of Lithium-ion battery cells. *J ELECTROCHEM SOC*, 151(3):A456–A462, 2004.

[186] E. Rejovitzky, C.V. Di Leo, and L. Anand. A theory and a simulation capability for the growth of a solid electrolyte interphase layer at an anode particle in a Li-ion battery. *J MECH PHYS SOLIDS*, 78(210-230), 2015.

[187] H. Shin, J. Park, S. Han, A.M. Sastry, and W. Lu. Component-/structure-dependent elasticity of solid electrolyte interphase layer in Li-ion batteries: Experimental and computational studies. *J POWER SOURCES*, 277:169–179, 2015.

[188] H. Shin, J. Park, A.M. Sastry, and W. Lu. Degradation of the solid electrolyte interphase induced by the deposition of manganese ions. *J POWER SOURCES*, 284:416–427, 2015.

[189] M. Tang, S. Lu, and J. Newman. Experimental and theoretical investigation of solid-electrolyte-interphase formation mechanisms on glassy carbon. *J ELECTROCHEM SOC*, 159(11):A1775–A1785, 2012.

[190] Y. Xie, J. Li, and C. Yuan. Multiphysics modeling of Lithium ion battery capacity fading process with solid-electrolyte interphase growth by elementary reaction kinetics. *J POWER SOURCES*, 248:172–179, 2014.

[191] H. Ekström and G. Lindbergh. A model for predicting capacity fade due to SEI formation in a commercial graphite/LiFePO$_4$ cell. *J ELECTROCHEM SOC*, 162(6):A1003–A1007, 2015.

[192] D. Bothe. On the Maxwell-Stefan approach to multicomponent diffusion. *PROG NONLIN*, 80:81–93, 2011.

[193] S.H. Lam. Multicomponent diffusion revisited. *PHYSICS OF FLUIDS*, 18:073101, 2006.

[194] Y.T. Cheng and M.W. Verbrugge. The influence of surface mechanics on diffusion induced stresses within spherical nanoparticles. *J APPL PHYS*, 104:083521, 2008.

[195] K. Higa and V. Srinivasan. Stress and strain in silicon electrode models. *J ELECTROCHEM SOC*, 162(6):A1111–A1122, 2015.

[196] R.A. Huggins and W.D. Nix. Decrepitation model for capacity loss during cycling of alloys in rechargeable electrochemical systems. *IONICS*, 6:57–63, 2000.

[197] K. Zhao, M. Pharr, S. Cai, J.J. Vlassak, and Z. Suo. Fracture of electrodes in Lithium-ion batteries caused fast charging. *J APPL PHYS*, 108:073517, 2010.

[198] K.E. Aifantis and J.P. Dempsey. Stable crack growth in nanostructured Li-batteries. *J POWER SOURCES*, 143:203–211, 2005.

[199] K.E. Aifantis, S.A. Hackney, and J.P. Dempsey. Design criteria for nanostructured Li-ion batteries. *J POWER SOURCES*, 165:874–879, 2007.

[200] Y. Hu, X. Zhao, and Z. Suo. Averting cracks caused by insertion reaction in Lithium-ion batteries. *J MATER RES*, 25(6):1007–1010, 2010.

[201] I. Ryu, J. W. Choi, Y. Cui, and W.D. Nix. Size-dependent fracture of si nanowire battery anodes. *J MECH PHYS SOLIDS*, 59:1717–1730, 2011.

[202] H. Woodford, Y.M. Chiang, and W.C. Carter. Electrochemical shock of intercalation electrodes: A fracture mechanics analysis. *J ELECTROCHEM SOC*, 157(10):A1052–A1059, 2010.

[203] K. Zhao, M. Pharr, J.J. Vlassak, and Z. Suo. Inelastic hosts as electrodes for high-capacity Lithium-ion batteries. *J APPL PHYS*, 109:016110, 2011.

[204] A. Salvadori. A plasticity framework for (linear elastic) fracture mechanics. *J MECH PHYS SOLIDS*, 56:2092–2116, 2008.

[205] A. Salvadori. Crack kinking in brittle materials. *J MECH PHYS SOLIDS*, 58:1835–1846, 2010.

[206] A. Salvadori and F. Fantoni. Minimum theorems in 3D incremental linear elastic fracture mechanics. *INT J FRACTURE*, 184(1):57–74, 2013.

[207] A. Salvadori and F. Fantoni. Fracture propagation in brittle materials as a standard dissipative process: general theorems and crack tracking algorithms. *J MECH PHYS SOLIDS*, 95:681–696, 2016.

[208] A. Salvadori and A. Giacomini. The most dangerous flaw orientation in brittle materials and structures. *INT J FRACTURE*, 183(1):19–28, 2013. DOI: 10.1007/s10704-013-9872-x.

[209] T.K. Bhandakkar and H. Gao. Cohesive modeling of crack nucleation under diffusion induced stresses in a thin strip: Implications on the critical size for flaw tolerant battery electrodes. *INT J SOLIDS STRUCT*, 47:1424–1434, 2010.

[210] T.K. Bhandakkar and H. Gao. Cohesive modeling of crack nucleation in a cylindrical electrode under axisymmetric diffusion induced stresses. *INT J SOLIDS STRUCT*, 48:2304–2309, 2011.

[211] C. Miehe, L.M. Schaenzel, and H. Ulmer. Phase field modeling of fracture in multi-physics problems. Part I. balance of crack surface and failure criteria for brittle crack propagation in thermo-elastic solids. *COMPUT METHOD APPL M*, 294:449–485, 2015.

[212] C. Miehe, M. Hofacker, L.M. Schaenzel, and F. Aldakheel. Phase field modeling of fracture in multi-physics problems. Part II. coupled brittle-to-ductile failure criteria and crack propagation in thermo-elastic–plastic solids. *COMPUT METHOD APPL M*, 294:486–522, 2015.

[213] C. Miehe, H. Dal, and A. Raina. A phase field model for chemo-mechanical induced fracture in Lithium-ion battery electrode particles. *INT J NUMER METH ENG*, 106(9):683–711, 2016.

[214] P. Zuo and Y.P. Zhao. A phase field model coupling Lithium diffusion and stress evolution with crack propagation and application in Lithium ion batteries. *PHYS CHEM CHEM PHYS*, 17:287–297, 2015.

[215] C. Miehe and S. Mauthe. Phase field modeling of fracture in multi-physics problems. Part III. crack driving forces in hydro-poro-elasticity and hydraulic fracturing of fluid-saturated porous media. *COMPUT METHOD APPL M*, 304:619–655, 2016.

[216] Y. Zhao, B.X. Xu, P. Stein, and D. Gross. Phase-field study of electrochemical reactions at exterior and interior interfaces in Li-ion battery electrode particles. *COMPUT METHOD APPL M*, pages –, 2016.

[217] M. Klinsmann, D. Rosato, M. Kamlah, and R.M. McMeeking. Modeling crack growth during Li extraction in storage particles using a fracture phase field approach. *J ELECTROCHEM SOC*, 163(2):A102–A118, 2016.

[218] D.T. O'Connor, M.J. Welland, W.K. Liu, and P.V. Voorhees. Phase transformation and fracture in single Li_xFePO_4 cathode particles: a phase-field approach to Li-ion intercalation and fracture. *MODELLING SIMUL MATER SCI ENG*, 24(3):035020, 2016.

[219] M. Klinsmann, D. Rosato, M. Kamlah, and R.M. McMeeking. Modeling crack growth during Li insertion in storage particles using a fracture phase field approach. *J MECH PHYS SOLIDS*, 92:313 – 344, 2016.

[220] J. Christensen and J. Newman. A mathematical model of stress generation and fracture in Lithium manganese oxide. *J ELECTROCHEM SOC*, 153(6):A1019–A1030, 2006.

[221] M.W. Verbrugge and Y.T. Cheng. Stress and strain-energy distributions within diffusion- controlled insertion-electrode particles subjected to periodic potential excitations. *J ELECTROCHEM SOC*, 156:A927–A937, 2009.

[222] Y.F. Gao and M. Zhou. Strong stress-enhanced diffusion in amorphus Lithium alloy nanowire electrodes. *J APPL PHYS*, 109:014310, 2011.

[223] J.C.M. Li. Physical chemistry of some microstructural phenomena. *METALL TRANS*, 9A:1353–1380, 1978.

[224] S. Prussin. Generation and distribution of dislocations by solute diffusion. *J APPL PHYS*, 32(10):1876–1881, 1961.

[225] S. Lee, W.L. Wang, and J.R. Chen. Diffusion-induced stresses in a hollow cylinder: Constant surface stresses. *MATER CHEM PHYS*, 64(2):123 – 130, 2000.

[226] F. Yang. Interaction between diffusion and chemical stresses. *MATER SCI ENG A*, 409:153–159, 2005.

[227] F. Larche and J.W. Cahn. A linear theory of thermochemical equilibrium under stress. *ACTA METALL MATER*, 21:1051–1063, 1973.

[228] F. Larche and J.W. Cahn. Non linear theory of thermochemical equilibrium under stress. *ACTA METALL MATER*, 26:53–60, 1978.

[229] R.T. Purkayastha and R.M. McMeeking. A linearized model for Lithium ion batteries and maps for their performance and failure. *J APPL MECH*, 79:1–16, 2012.

[230] J.H. Seo, M. Chung, M. Park, S.W. Han, X. Zhang, and A.M. Sastry. Generation of realistic structures and simulations of internal stress: A numerical/AFM study of $LiMn_2O_4$ particles. *J ELECTROCHEM SOC*, 158(4):A434–A442, 2011.

[231] C.H. Wu. The role of Eshelby stress in composition-generated and stress-assisted diffusion. *J MECH PHYS SOLIDS*, 49(8):1771–1794, 2001.

[232] H. Haftbaradaran, J. Song, W.A. Curtin, and H. Gao. Continuum and atomistic models of strongly coupled diffusion, stress, and solute concentration. *J POWER SOURCES*, 196:361–370, 2011.

[233] J. W. Wang, Y. He, F. Fan, X.H. Liu, S. Xia, Y. Liu, C.T. Harris, H. Li, J.Y. Huang, S.X. Mao, and T. Zhu. Two-phase electrochemical lithiation in amorphous silicon. *NANO LETT*, 13(2):709–715, 2013.

[234] L. Brassart, K. Zhao, and Z. Suo. Cyclic plasticity and shakedown in high-capacity electrodes of Lithium-ion batteries. *INT J SOLIDS STRUCT*, 50:1120–1129, 2013.

[235] V.A. Sethuraman, V. Srinivasan, A. F. Bower, and P.R. Guduru. In situ measurements of stress-potential coupling in lithiated silicon. *J ELECTROCHEM SOC*, 157:1253–1261, 2010.

[236] J. Wang, Y. Chen-Wiegart, and J. Wang. In operando tracking phase transformation evolution of Lithium iron phosphate with hard X-ray microscopy. *NAT COMMUN*, 5, 2014.

[237] G. Chen, X. Song, and T.J. Richardson. Electron microscopy study of the $LiFePO_4$ to $FePO_4$ phase transition. *ELECTROCHEM SOLID ST*, 9:A295, 2006.

[238] L. Laffont, C. Delacourt, P. Gibot, M. Wu, P. Kooyman, C. Masquelier, and J. Tarascon. Study of the $LiFePO_4/FePO_4$ two-phase system by high-resolution electron energy loss spectroscopy. *CHEM MATER*, 18(23):5520–5529, 2006.

[239] J.W. Cahn and J. E. Hilliard. Free energy of a nonuniform system. I. interfacial free energy. *J CHEM PHYS*, 28:258–267, 1958.

[240] K. Thornton, J. Agren, and P.W. Voorhees. Modelling the evolution of phase boundaries in solids at the meso- and nano-scales. *ACTA MATER*, 51(19):5675 – 5710, 2003.

[241] V. Srinivasan and J. Newman. Discharge model for the Lithium iron-phosphate electrode. *J ELEC-TROCHEM SOC*, 151(10):A1517–A1529, 2004.

[242] V. R. Subramanian, H. J. Ploehn, and R. E. White. Shrinking core model for the discharge of a metal hydride electrode. *J ELECTROCHEM SOC*, 147(8):2868–2873, 2000.

[243] Q. Zhang and R.E. White. Moving boundary model for the discharge of a $LiCoO_2$ electrode. *J ELECTROCHEM SOC*, 154(6):A587–A596, 2007.

[244] F. Gao and W. Hong. Phase-field model for the two-phase lithiation of silicon. *J MECH PHYS SOLIDS*, 94:18 – 32, 2016.

[245] G.K. Singh, G. Ceder, and M.Z. Bazant. Intercalation dynamics in rechargeable battery materials: General theory and phase-transformation waves in $LiFePO_4$. *ELECTROCHIM ACTA*, 53:7599–7613, 2008.

[246] D. Burch, G.K. Singh, G. Ceder, and M.Z. Bazant. Phase-transformation wave dynamics in $LiFePO_4$. *SOLID STATE PHENOM*, 139:95–100, 2008.

[247] B.C. Han, A. Van der Ven, D. Morgan, and G. Ceder. Electrochemical modeling of intercalation processes with phase field models. *ELECTROCHIM ACTA*, 49(26):4691 – 4699, 2004.

[248] M. Tang, W. Craig Carter, J.F. Belak, and Y.M. Chiang. Modeling the competing phase transition pathways in nanoscale olivine electrodes. *ELECTROCHIM ACTA*, 56(2):969 – 976, 2010.

[249] M. Tang, H.-Y. Huang, N. Meethong, Y.-H. Kao, W. C. Carter, and Y.-M. Chiang. Model for the particle size, overpotential, and strain dependence of phase transition pathways in storage electrodes: Application to nanoscale olivines. *CHEM MATER*, 21(8):1557–1571, 2009.

[250] D.A. Cogswell and M.Z. Bazant. Coherency strain and the kinetics of phase separation in $LiFePO_4$ nanoparticles. *ACS NANO*, 6(3):2215–2225, 2012.

[251] L. Anand. A Cahn-Hilliard-type theory for species diffusion coupled with large elastic-plastic deformations. *J MECH PHYS SOLIDS*, 60(12):1983–2002, 2012.

[252] C. Di Leo, E. Rejovitzky, and L. Anand. A Cahn-Hilliard-type phase-field theory for species diffusion coupled with large elastic deformations: Application to phase-separating Li-ion electrode materials. *J MECH PHYS SOLIDS*, 70:1–29, 2014.

[253] P. Areias, E. Samaniego, and T. Rabczuk. A staggered approach for the coupling of Cahn-Hilliard type diffusion and finite strain elasticity. *COMPUT MECH*, 57(2):339–351, 2016.

[254] S. Huang, F. Fan, J. Li, S. Zhang, and T. Zhu. Stress generation during lithiation of high-capacity electrode particles in Lithium ion batteries. *ACTA MATER*, 61:4354–4364, 2013.

[255] H. Yang, F. Fan, W. Liang, X. Guo, T. Zhu, and S. Zhang. A chemo-mechanical model of lithiation in silicon. *J MECH PHYS SOLIDS*, 70:349–361, 2014.

[256] A.D. Drozdov. A model for the mechanical response of electrode particles induced by Lithium diffusion in Li-ion batteries. *ACTA MECH*, 225:2987–3005, 2014.

[257] A.D. Drozdov. Viscoplastic response of electrode particles in Li-ion batteries driven by insertion of Lithium. *INT J SOLIDS STRUCT*, 51:690–705, 2014.

[258] Z. Cui, F. Gao, and J. Qu. Interface-reaction controlled diffusion in binary solids with applications to lithiation of silicon in Lithium ion batteries. *J MECH PHYS SOLIDS*, 61:293–310, 2013.

[259] K. Zhao, M. Pharr, Q. Wan, W.L. Wang, E. Kaxiras, J.J. Vlassak, and Z. Suo. Concurrent reaction and plasticity during initial lithiation of crystalline silicon in Lithium-ion batteries. *J ELECTROCHEM SOC*, 159:A238–A243, 2012.

[260] H. Yang, S. Huang, X. Huang, F. Fan, W. Liang, X.H. Liu, L.Q. Chen, J.Y. Huang, J. Li, T. Zhu, and S. Zhang. Orientation-dependent interfacial mobility governs the anisotropic swelling in lithiated silicon nanowires. *NANO LETT*, 12(4):1953–1958, 2012.

[261] W.J. Drugan and J.R. Willis. A micromechanics-based nonlocal constitutive equation and estimates of representative volume element size for elastic composites. *J MECH PHYS SOLIDS*, 44(4):497 – 524, 1996.

[262] Z. Shan and A. M. Gokhale. Representative volume element for non-uniform micro-structure. *COMP MATER SCI*, 24(3):361 – 379, 2002.

[263] S. Swaminathan, S. Ghosh, and N. J. Pagano. Statistically equivalent representative volume elements for unidirectional composite microstructures: Part I - without damage. *J COMPOS MATER*, 40(7):583–604, 2006.

[264] S. Torquato. *Random Heterogeneous Materials: Microstructure and Macroscopic Properties*. Springer, 2002.

[265] J.R. Willis. *Elasticity Theory of Composites*. Defense Technical Information Center, 1980.

[266] D. E. Stephenson, B. C. Walker, C. B. Skelton, E. P. Gorzkowski, D J. Rowenhorst, and D. R. Wheeler. Modeling 3D microstructure and ion transport in porous Li-ion battery electrodes. *J ELECTROCHEM SOC*, 158:A781–A789, 2011.

[267] T.R. Ferguson and M.Z. Bazant. Nonequilibrium thermodynamics of porous electrodes. *J ELECTROCHEM SOC*, 159(12):A1967–A1985, 2012.

[268] M. Schmuck and M.Z. Bazant. Homogenization of the Poisson-Nernst-Planck equations for ion transport in charged porous media. *SIAM J APPL MATH*, 75(3):1369–1401, 2015.

[269] S. Lee, A.M. Sastry, and J. Park. Study on microstructures of electrodes in Lithium-ion batteries using variational multi-scale enrichment. *J POWER SOURCES*, 315:96 – 110, 2016.

[270] S. Golmon, K. Maute, and M.L. Dunn. Numerical modeling of electrochemical-mechanical interactions in Lithium polymer batteries. *COMPUT STRUCT*, 87:1567–1579, 2009.

[271] S. Golmon, K. Maute, and M.L. Dunn. Multiscale design optimization of Lithium ion batteries using adjoint sensitivity analysis. *INT J NUMER METH ENG*, 92:475–494, 2012.

[272] S. Golmon, K. Maute, and M.L. Dunn. A design optimization methodology for Li^+ batteries. *J POWER SOURCES*, 253:239–250, 2014.

[273] S. Allu, S. Kalnaus, S. Simunovic, J. Nanda, J.A. Turner, and S. Pannala. A three-dimensional meso-macroscopic model for Li-ion intercalation batteries. *J POWER SOURCES*, 325:42 – 50, 2016.

[274] P.M. Suquet. Local and global aspects in the mathematical theory of plasticity. In A. Sawczuk and G. Bianchi, editors, *Plasticity today: modeling, methods and applications*, pages 279–310. Elsevier Applied Science Publishers, London, 1985.

[275] M.G.D. Geers, V.G. Kouznetsova, and Brekelmans W.A.M. Multi-scale computational homogenization: trends and challenges. *J COMPUT APPL MATH*, 234:2175–2182, 2010.

[276] A. Kovetz. *The principles of electromagnetic theory*. Cambridge University Press, 1989.

[277] R.A. Huggins. *Energy storage*. Springer, 2010.

[278] A.A. Franco, M.L. Doublet, and W.G.B. Bessler, editors. *Physical Multiscale Modeling and Numerical Symulation of Electrochemical Devices for Energy Conversion and Storage.* Springer, London, 2016.

[279] M.A. Rahman, S. Anwar, and A. Izadian. Electrochemical model parameter identification of a Lithium-ion battery using particle swarm optimization method. *J POWER SOURCES*, 307:86 – 97, 2016.

[280] K. Takahashi, K. Higa, S. Mair, M. Chintapalli, N. Balsara, and V. Srinivasan. Mechanical degradation of graphite/PVDF composite electrodes: A model-experimental study. *J ELECTROCHEM SOC*, 163(3):A385–A395, 2016.

[281] J. Larsson. Electromagnetics from a quasistatic perspective. *AM J PHYS*, 75(3):230–239, 2007.

[282] A. McNabb and P.K. Foster. A new analysis of the diffusion of hydrogen in iron and ferritic steels. *T METALL SOC AIME*, 227:618–627, 1963.

[283] Oriani R.A. The diffusion and trapping of hydrogen in steel. *ACTA METALL MATER*, 18(1):147–157, 1970.

[284] J.P. Hirth. Effects of hydrogen on the properties of iron and steel. *METALL TRANS A*, 11A:861–876, 1980.

[285] A.J. Kumnick and H.H Johnson. Deep trapping states for hydrogen in deformed iron. *ACTA METALL MATER*, 28:33–39, 1980.

[286] P. Sofronis and R.M. McMeeking. Numerical analysis of hydrogen transport near a blunting crack tip. *J MECH PHYS SOLIDS*, 37(317-350), 1989.

[287] A.H.M. Krom, R.W.J Koers, and A. Bakker. Hydrogen transport near a blunting crack tip. *J MECH PHYS SOLIDS*, 47:971–992, 1999.

[288] A.H.M. Krom and A. Bakker. Hydrogen trapping models in steel. *METALL MATER TRANS B*, 31B:1475–1482, 2000.

[289] J. Toribio and V. Kharin. A generalised model of hydrogen diffusion in metals with multiple trap types. *PHILOS MAG*, 95(31):3429–3451, 2015.

[290] M. Pharr, K. Zhao, X. Wang, Z. Suo, and J.J. Vlassak. Kinetics of initial lithiation of crystalline silicon electrodes of lithium-ion batteries. *NANO LETT*, 12:5039–5047, 2012.

[291] X.H. Liu, J.W. Wang, S. Huang, F. Fan, X. Huang, Y. Liu, S. Krylyuk, J. Yoo, S.A. Dayeh, A.V. Davydov, S.X. Mao, S.T. Picraux, S. Zhang, J. Li, T. Zhu, and J.Y. Huang. In situ atomic-scale imaging of electrochemical lithiation in silicon. *NAT NANOTECHNOL*, 7:749–756, 2012.

[292] M.T. McDowell, S.W. Lee, J.T. Harris, B.A. Korgel, C. Wang, W.D. Nix, and Y. Cui. In situ TEM of two-phase lithiation of amorphous silicon nanospheres. *NANO LETT*, 13(2):758–764, 2013.

[293] G. Holzapfel. *Nonlinear Solid Mechanics: A Continuum Approach for Engineering.* John Wiley & Sons, Ltd., 2001.

[294] S. Paolucci. *Continuum Mechanics and Thermodynamics of Matter.* Cambridge University Press, 2016.

[295] V.A. Lubarda. Consitutive theories based on the multiplicative decomposition of deformation gradient: Thermoelasticity, elastoplasticity, and biomechanics. *APPL MECH REV*, 57(2):95–108, 2004.

[296] J.C. Simo. A framework for finite strain elastoplasticity based on maximum plastic dissipation and the multiplicative decomposition: Part i. continuum formulation. *COMPUT METHODS IN APPL MECH ENG*, 66(2):199 – 219, 1988.

[297] J.C. Simo. A framework for finite strain elastoplasticity based on maximum plastic dissipation and the multiplicative decomposition. part ii: Computational aspects. *COMPUT METHODS IN APPL MECH ENG*, 68(1):1 – 31, 1988.

[298] I. Prigogine. Nobel lecture: Time, structure and fluctuations., 1977.

[299] P. Rosakis, A.J. Rosakis, G. Ravichandran, and J. Hodowany. A thermodynamic internal variable model for the partition of plastic work into heat and stored energy in metals. *J MECH PHYS SOLIDS*, 48:581–607, 2000.

[300] E. Bohn, T. Eckl, M. Kamlah, and R. McMeeking. A model for Lithium diffusion and stress generation in an intercalation storage particle with phase change. *J ELECTROCHEM SOC*, 160(10):A1638–A1652, 2013.

[301] J. Lemaitre and J.L. Chaboche. *Mechanics of solid materials*. Cambridge University Press, 2000.

[302] K. Hackl and F.D. Fischer. On the relation between the principle of maximum dissipation and inelastic evolution given by dissipation potentials. *P R SOC A*, 464(2089):117–132, 2008.

[303] J.P. Thomas and C.E. Chopin. Modeling of coupled deformation-diffusion in non-porous solids. *INT J ENG SCI*, 37:1–24, 1999.

[304] V. Deshpande, M. Mrksich, R.M. Mc Meeking, and A.G. Evans. A bio-mechanical model for coupling cell contractility with focal adhesion formation. *J MECH PHYS SOLIDS*, 56:1484–1510, 2008.

[305] C. Di Leo and L. Anand. Hydrogen in metals: a coupled theory for species diffusion and large elastic-plastic deformations. *INT J PLASTICITY*, 43:42–69, 2013.

[306] J.C. Simo and T.J.R. Hughes. *Computational inelasticity*. Springer-Verlag, New York, 1998.

[307] L. Anand. A thermo-mechanically-coupled theory accounting for hydrogen diffusion and large elastic-viscoplastic deformations of metals. *INT J SOLIDS STRUCT*, 48:962–971, 2011.

[308] A. Villani, E. P. Busso, K. Ammar, S. Forest, and M. G. D. Geers. A fully coupled diffusional-mechanical formulation: numerical implementation, analytical validation, and effects of plasticity on equilibrium. *ARCH APPL MECH*, 84:1647–1664, 2014.

[309] K. Mizushima, P.C. Jones, P.J. Wiseman, and J.B. Goodenough. Li_xCoO_2: A new cathode material for batteries of high energy density. *MRS BULLETIN*, 15(6):783 – 789, 1980.

[310] J.N. Reimers and J.R. Dahn. Electrochemical and in situ X-ray diffraction studies of lithium intercalation in Li_xCoO_2. *J ELECTROCHEM SOC*, 139(8):2091–2097, 1992.

[311] G.G. Amatucci, J.M. Tarascon, and L.C. Klein. CoO_2, the end member of the Li_xCoO_2 solid solution. *J ELECTROCHEM SOC*, 143(3):1114–1123, 1996.

[312] A. Van der Ven, M.K. Aydinol, G. Ceder, G. Kresse, and J. Hafner. First-principles investigation of phase stability in Li_xCoO_2. *PHYS REV B*, 58:2975–2987, 1998.

[313] G. Ceder and A. Van der Ven. Phase diagrams of lithium transition metal oxides: investigations from first principles. *ELECTROCHIM ACTA*, 45(1–2):131 – 150, 1999.

[314] H. Xia, L. Lu, and G. Ceder. Li diffusion in Li_xCoO_2 thin films prepared by pulsed laser deposition. *J POWER SOURCES*, 159(2):1422 – 1427, 2006.

[315] P.J. Bouwman, B.A. Boukamp, H.J.M. Bouwmeester, and P.H.L. Notten. Influence of diffusion plane orientation on electrochemical properties of thin film Li_xCoO_2 electrodes. *J ELECTROCHEM SOC*, 149(6):A699–A709, 2002.

[316] L. Wu and J. Zhang. Ab initio study of anisotropic mechanical properties of Li_xCoO_2 during lithium intercalation and deintercalation process. *J APPL PHYS*, 118(22):225101, 2015.

[317] L. Wu, W.H. Lee, and J. Zhang. First principles study on the electrochemical, thermal and mechanical properties of Li_xCoO_2 for thin film rechargeable battery. *MATER TODAY*, 1(1):82 – 93, 2014.

[318] V. Malav, M.K. Jangid, I. Hait, and A. Mukhopadhyay. In situ monitoring of stress developments and mechanical integrity during galvanostatic cycling of $LiCoO_2$ thin films. *ECS ELECTROCHEM LETT*, 4(12):A148–A150, 2015.

[319] D. Grazioli, M. Magri, and A. Salvadori. Computational modeling of li-ion batteries. *COMPUT MECH*, 58(6):889–909, 2016.

[320] A.F. Bower, P.R. Guduru, and E. Chason. A continuum model of deformation, transport and irreversible changes in atomic structure in amorphous Lithium–silicon electrodes. *ACTA MATER*, 98:229–241, 2015.

[321] H.C. Shin and S. Pyun. The kinetics of lithium transport through $Li_{1-\delta}CoO_2$ by theoretical analysis of current transient. *ELECTROCHIM ACTA*, 45(3):489 – 501, 1999.

[322] A. Salvadori, R.M. Mc Meeking, D. Grazioli, and M. Magri. A coupled model of transport-reaction-mechanics with trapping. part I - small strain analysis. Under review, 2017.

[323] E.D.S. Neto, D. Peric, and D. Owens. *Computational methods for plasticity: theory and applications.* John Wiley & Sons Ltd, 2008.

[324] W. Dreyer and R. Guhlke, C.and Muller. Modeling of electrochemical double layers in thermodynamic non-equilibrium. *PHYS CHEM CHEM PHYS*, 17:27176–27194, 2015.

[325] W. Dreyer, C. Guhlke, and R. Muller. A new perspective on the electron transfer: recovering the butler-volmer equation in non-equilibrium thermodynamics. *PHYS CHEM CHEM PHYS*, 18:24966–24983, 2016.

[326] E. A. Brandes and G. B. Brook. *Smithells Metals Reference Book.* Butterworth Einemann, 1998.

[327] K. Park and G.H. Paulino. Computational implementation of the ppr potential-based cohesive model in abaqus: Educational perspective. *ENG FRACT MECH*, 93(Supplement C):239–262, 2012.